VAAL UNIVERSITY OF TECHNOLOGY

PLASMON CATALYST DISPERSED ON CARBONISED PINECONE FOR ENHANCED DEGRADATION OF ORGANIC CONTAMINANTS

By

SANNI SAHEED OLALEKAN
(211127817)

Thesis submitted to the Department of Chemistry,

Vaal University of Technology

In Partial Fulfillment of the Requirements

For the Degree of Doctor in Chemistry

Promoter: Prof. Augustine Ofomaja

Co-Promoter: Dr Elvera Viljoen

Declaration

I hereby confirm that the thesis submitted is my own work and to the best of my knowledge, which I hereby submit for the qualification of Doctor of Technology in Chemistry. Furthermore, the thesis has not been submitted in any previous application for a degree. The contribution of the candidate and co-authors' work have been explicitly indicated below. The candidate, as lead author, was solely responsible for all experimentation, laboratory data analysis and writing of the papers. Co-authors provided guidance, support on the scope and design of the project, the analyses performed and contributed to the editing of the manuscript.

Signed

Date

Sanni Saheed

November 2020

Abstract

Aromatic organic contaminants are difficult to biodegrade, and thus effective green technologies are required to remove these pollutants from the ecosystem. Tetracycline antibiotic, an organic water pollutant, can be degraded by heterogeneous photocatalysis using an appropriate catalyst, with capability in converting the visible light energy into active species. The thesis focused on silver nanoparticles anchored on silver bromide (Ag/AgBr) as a plasmonic catalyst dispersed on activated carbon (ACK), were used as a photocatalyst (AABR-ACK) in tetracycline removal. The aim is to develop a catalyst that is active in low intensity visible light, whilst the addition of activated carbon will increase the light absorption and separate the charge pairs, after the photocatalyst has been excited by the visible light.

The activated carbons were derived from pinecone pyrolyzed in a microwave. The pinecone mass to potassium hydroxide impregnation ratio and microwave pyrolysis time influenced the activated carbon properties. An impregnation ratio of 2.24 and microwave pyrolysis time of 16 minutes at constant microwave power of 400 W yielded the activated carbon with the best-developed porous structure and electrochemical properties. This activated carbon was used during the optimisation of the Ag/AgBr activated carbon (AABR-ACK) catalysts preparation using a thermal polyol precipitation method and response surface methodology. The most active catalyst was the AABR-ACK 11 obtained by a preparation temperature of 140 ºC, time (17.50 minutes), mass of surfactant and activated carbon (0.26 g and 0.03 g) respectively. This catalyst had an ordered nanospheres morphology, reduced electron-hole recombination rate, better electrochemical properties and exhibited enhanced activity on the tetracycline antibiotic removal

in comparison to other Ag/AgBr activated carbon catalysts. A percentage degradation of 92% was obtained in 180 minutes were obtained with the AABR-ACK 11 catalyst.

The photocatalyst prepared using the best activated carbon derived from pinecone developed in this study was compared to photocatalysts prepared using commercial activated carbon and biochar. The Ag/AgBr activated carbon catalysts using pinecone-derived activated carbon degraded the tetracycline to 92%, which is significantly higher than the percentage degradations (80% and 74%) for the catalyst prepared using commercial activated carbon and biochar catalysts respectively. The higher activity of the Ag/AgBr activated carbon catalysts using pinecone-derived activated carbon was due to the conductive attributes of the catalyst support for accelerated transfer of photo-induced electrons. The Ag/AgBr activated carbon catalysts using pinecone-derived activated carbon also exhibited better performance on tetracycline removal when compared to photocatalysts reported in literature.

Two catalyst preparation methods, thermal polyol and deposition precipitation, were compared. The thermal polyol method yielded a more active catalyst for the degradation of the tetracycline in comparison to the deposition precipitation method.

The degradation reaction conditions such as pH, light intensity and degradation temperature influenced the rate of the reaction. The highest rate of degradation was obtained at a pH of seven, white light and 40 ºC temperature.

The intermediate products formed because of hydroxylation, deamination, demethylation and dehydration during the photocatalytic degradation of tetracycline antibiotics were identified using liquid chromatography mass spectrometer. Quenching experiments with hydroxyl, hole, and superoxide anion species showed that the most important radical responsible for the tetracycline degradation was the superoxide anion radical.

Acknowledgments

I would like to express my deepest gratitude to my supervisor and co-supervisor Prof. Augustine Ofomaja and Dr Elvera Viljoen for their guidance, encouragement, support, and patience during the doctorate work at Chemistry Department, Vaal University of Technology.

Further, thanks must go to Dr Mena Oseghe, Dr Isiaka Lawal, Dr Samsom Akpotu, Dr Chukwunonso Okoli, Dr Martins Omorogie, Dr Paul Diagboya, Dr Peter Ejidike, Dr Bamidele Okoli, Dr Reddy Prasad, Dr Adeniyi Osikoya and Dr Omoruyi for their much-appreciated time to provide advice, training, and assistance throughout the doctorate programme. I also want to thank my incredible research colleagues (Neo, Ouma, Wanda, Attah-Daniel, Benton) in chemistry department who gave valuable contributions towards the completion of this thesis.

I am thankful to the National Research Foundation of South Africa and Sasol University Collaboration Program who has provided full scholarships for the doctorate programme. My sincere gratitude goes to my mother, Mrs Sanni for her innumerable sacrifice, prayers, and support for her children. Finally, my kindest regards and thanks would go to all of my family: my father, my wonderful sisters, brother and friends here in South Africa. Their interest and support have been of great comfort to me.

Publications and Presentations

Publications

Sanni S.O., Viljoen, E.L, Ofomaja A.E, Design of Ordered Ag/AgBr Nanostructures Coupled Activated Carbon with Enhanced Charge Carriers Separation Efficiency for Photodegradation of Tetracycline under Visible Light, **Journal of Molecular Liquids**, 2019, 112032.

Sanni S.O., Viljoen, E.L, Ofomaja A.E, Accelerated Electron Transport and Improved Photocatalytic Activity of Ag/AgBr Under Visible Light Irradiation Based on Conductive Carbon Derived Biomass, **Catalysis Letters**, 149 3027-3040, 2019.

Sanni S.O., Viljoen, E.L, Ofomaja A.E, Controlled Microstructure of Ag/AgBr-AC Synergistic Enhancement on Photocatalytic Degradation of Tetracycline: A Synthesis Approach Comparison, **Proceeding of International Conference on Pure and Applied Chemistry**, Chemistry for a Clean and Healthy Planet 1-17, 2018.

Sanni S.O., Reddy Prasad, P., Ofomaja A.E, Novel microwave synthesis carbon dots from pine bark and its application for heavy metal sensing, **Proceeding of Emerging Technologies in Clean Energy 2016** - Topical Conference at the 2016 AIChE Spring Meeting and 12th Global Congress on Process Safety, 109-119.

Sanni S.O., Viljoen, E.L, Ofomaja A.E, Three-Dimensional Hierarchical Porous Carbon Structure Derived from Pinecone as Potential Catalyst Support in Catalytic Remediation of Antibiotics (**Manuscript Accepted @ RSC Advances, C9RA10638C**).

Sanni S.O., Viljoen, E.L, Ofomaja A.E, Controllable Synthesis of Regulated Ag/AgBr Nanostructures on Activated Carbon with Enhanced Photocatalytic Degradation Activity for Tetracycline Removal (**Manuscript in preparation**).

Presentations

Sanni S.O., Viljoen, E.L, Ofomaja A.E, Methylene blue adsorption by KOH treated activated carbon produced via microwave synthesis, 42nd National Convention of the South African Chemical Institute, 2015, Durban, **Oral Presentation.**

Sanni S.O., Viljoen, E.L, Ofomaja A.E, Synthesis of $ZnCl_2$-Activated Carbon Produced from Pinecone by Microwave Pyrolysis: Characterization and Methylene blue Adsorption, International Conference on Pure and Applied Chemistry (ICPAC), 2016, Mauritius, **Oral Presentation.**

Sanni S.O., Viljoen, E.L, Ofomaja A.E, Controllable synthesis of efficient Ag/AgBr nanocomposite supported on pinecone activated carbon for the degradation of Tetracycline, Catalysis Society of South Africa (CATSA), 2016, Drakensberg, **Oral Presentation.**

Sanni S.O., Viljoen, E.L, Ofomaja A.E, Preparation of Ag/AgBr-AC by template-assisted method for photocatalytic degradation of Tetracycline as a pharmaceutical pollutant, Catalysis Society of South Africa (CATSA), 2017, Kwa Maritane Bush Lodge, Pilanesberg, **Oral Presentation.**

Sanni S.O., Viljoen, E.L, Ofomaja A.E, Morphological control and photocatalytic properties of Ag/AgBr-AC synthesized by thermal polyol: Response surface methodology approach, 5th Nano Today Conference, 2017, Hawaii, USA, **Poster Presentation.**

Sanni S.O., Viljoen, E.L, Ofomaja A.E, Morphology control of Ag/AgBr-AC with enhanced visible light catalytic properties for organic pollutants removal, The 10th International Conference on Environmental Catalysis, 2018, Tianjin, China, **Oral Presentation.**

Table of Contents

List of Abbreviations and symbols

Abbreviations

AOPs Advanced oxidation processes

AOTs Advanced oxidation technologies

TOC Total organic carbon

AC Activated carbon

MOS Metal oxide semiconductor

SPR Surface plasmon resonance

SEM Scanning Electron Microscope

TC Tetracycline hydrochloride

UV Ultraviolet

Ag/AgBr Silver -silver bromide

Ag/AgCl Silver -silver chloride

Ag/AgI Silver –silver iodide

3D Three Dimensional

UV-DRS Ultraviolet visible diffuse reflectance spectrophotometry

RSM Response Surface Methodology

ANOVA Analysis of variance

PL Photoluminescence microscopy

LED Light-emitting diode

PPCPs Pharmaceutical and Personal Care Products

WWTPs Wastewater treatment plants

XRD X-ray diffraction

IR Impregnation ratio

AgX Silver halide

XPS X-ray photoelectron spectroscopy

TEM Transmission electron microscopy

HRTEM High-resolution transmission electron microscopy

XPS X-ray photoelectron spectroscopy

JCPDS Joint committee on powder diffraction standards

CNT Carbon nanotube

pH-$_{PZC}$ Point of zero charge

GCE Glassy carbon electrode

EIS Electrochemical impedance spectroscopy

MB Methylene Blue

IN Iodine number

MPT Microwave pyrolysis time

TGA Thermogravimetry analysis

DTA Differential thermal analysis

CB Conduction band

VB Valence band

BET Brunauer–Emmett–Teller

Symbols

λ Wavelength

e^- Electron

h^+ Hole

β Affinity coefficient

α Absorption coefficient

T Temperature

List of Tables

List of Figures

Chapter 1. Introduction

1.1 Background

Environmental pollution and energy shortage represent a great hindrance to the sustainable development of modern human society (Nadimi & Tokimatsu 2018; Shahsavari & Akbari 2018). Pollution of water, air, and soil are becoming an increasingly serious problem, they are attributed to rapid population explosion, wastes derived from industrial expansion and industrial sources (Liu, Adams, Cote, Geng & Li 2018). These non-biodegradable pollutants present in wastewaters and air are toxic, carcinogenic in nature, which pose serious hazards to aquatic life and human health worldwide (Ozdemir 2004; Huang 2010). In South Africa context, some of these organic pollutants from the wastewaters emanate from textiles, pharmaceuticals, steel mills, chemical and fertilizer plants, refining and petrochemical operations (Rimayi, Odusanya, Weiss, de Boer & Chimuka 2018). Detecting and treating these existing organic contaminants especially the non-biodegradable pharmaceutical compounds aimed at prevention of pharmaceutical drug resistance in microorganisms is crucial (Gao, Li, Zhang, Huang, Hu, Shah & Su 2012; Agunbiade & Moodley 2014; Xiao, Tang, Yang, Tang, Zhou & Zou 2018). Among these pharmaceutical drug, tetracycline hydrochloride (TC) is of particular focus to be treated, because of its prevalent usage by humans and in veterinary medicines (Ji, Wan, Zheng & Zhu 2011; Daghrir & Drogui 2013). It's crucial to treat TC wastewater before its released into the water bodies.

The conventional water treatment processes for the elimination of TC such as adsorption, membrane separation, electrolysis, and microbial decomposition have proven to be ineffective (Jiang, Xiao, Shao, Li & Chen 2017). They lead into the generation of secondary pollution; as a

result the demand for treatment of TC antibiotics effectively is required. Hence, advanced wastewater treatment technologies are desired to remove this recalcitrant pharmaceutical pollutant effectively without leaving any secondary product in the final output of water. Advanced oxidation processes (AOPs) is an efficient treatment technologies that employ stronger oxidant such as $^{\cdot}O_2^-$,$^{\cdot}OH$ and O_3 radicals. These radicals are generated either by a UV light source, Fenton reagent, or UV light source and a catalyst (Vora 2009; Ahmed 2011) thereby reducing the contaminants into mineralized products such as CO_2 and H_2O during the oxidation process. The heterogeneous photo-catalytic approach using a combination of a light source and photocatalyst material is widely employed under AOPs as good technology in degrading recalcitrant pharmaceuticals pollutants effectively (Li & Shi 2016; Lofrano, Libralato, Adinolfi, Siciliano, Iannece, Guida, Giugni, Ghirardini & Carotenuto 2016). The application of visible light photocatalyst materials aimed at effective degradation of TC antibiotics outperformed conventional TiO_2 catalyst material (Jodeyri, Haghighi & Shabani 2019). Among the visible light photocatalysts, the plasmonic silver/silver bromide (Ag/AgBr) material is of interest due to their intrinsic catalytic performance (Hou, Wang, Yang, Zhou, Jiao & Zhu 2013). The high activity is caused by the surface plasmon resonance (SPR) effect of metallic silver particles anchor on AgBr resulting in enhanced absorption in the visible light region (Li & Ding 2010).

The controlled microstructure, visible light absorption, reduced electron-hole recombination, stability and reusability of the Ag/AgBr catalyst can be significantly improved through immobilization (Slimen 2011; Sohrabnezhad 2013) on porous adsorbent materials. The carbonaceous materials attribute as catalyst support for metal oxide semiconductor (MOS) dispersion includes mechanical strength, pore size distribution, thermal stability and abundance oxygenated functional groups for MOS uniform distribution (Jafri, Rajalakshmi & Ramaprabhu

2010; Kong, Chen & Chen 2014; Lam 2014). This synergistic interaction with Ag/AgBr catalyst is desirable for high activity on the removal of TC. Activated carbon (AC), an excellent carbonaceous material has shown immense attributes in gas purification, energy storage, and water remediation due to its excellent adsorption properties (Lillo-Ródenas, Marco-Lozar, Cazorla-Amorós & Linares-Solano 2007). The characteristics properties of produced AC from biomass as catalyst support will depend on its hierarchical porous structure, surface chemistry, and electrochemical attributes (Wang, Xu, Liu, Zhang, Zhu, Xia & Li 2017).

1.2 Problem statement

The challenges of energy crisis and environmental pollution are becoming increasingly threats to our lives. Wastewater generated annually from industrial sectors contains huge amount of harmful and recalcitrant organic contaminants, especially the antibiotics which are been detected in groundwater and municipal wastewater treatment in South Africa (Agunbiade & Moodley 2014). Tetracycline (TC) antibiotics have been used in treatment of human and animal infections. The presence of TC in the environment at very low concentration could cause antibiotic resistance problem, which poses a serious threat to the well-being of human and animals (Chen, Yang, Wang, Yao, Sun, Wang, Zhang, Li, Niu & Wang 2017). Therefore, a need to find an efficient method to remove TC antibiotics from surface water is urgent.

To deal with TC antibiotic residuals, various conventional treatment methods have been widely investigated. The hetero-aromatic stable structure and recalcitrance nature make TC very difficult to be removed by conventional treatment processes. Photocatalysis-a green technology with semiconductor photocatalyst is considered an efficient approach for TC antibiotic treatment due

to its low-cost, environment-friendly and energy-conservation (Li, Yu, Dong, Wang, Wu, Zhang, Chen & Liu 2018). Although host of photocatalysts has been designed for TC remediation from groundwater, there is still a need to design highly-efficient and durable photocatalysts that can efficiently operate under low-intensity visible light of solar spectrum (Liu, Guo, Chen, Zhang & Fang 2016, Hezam, Namratha, Drmosh, Yamani & Byrappa 2017).

The plasmonic silver-silver bromide (Ag/AgBr) have been established as potential photocatalyst that can effectively operate in visible light of solar spectrum in degradation of organic pollutants (Sohrabnezhad 2013). However, the photocatalytic efficiency of Ag/AgBr catalyst is still low, due to irregular morphology, insufficient charge carrier separation and poor photochemical stability of the photocatalyst after degradation process. The dispersion of Ag/AgBr catalyst on carbonized low cost agricultural material is a good approach in addressing the challenges highlighted with Ag/AgBr catalyst. The interconnected hierarchical carbon structure of carbonized biomass will enhance the photocatalytic properties of Ag/AgBr catalyst under low intensity of visible light, in effective removal of tetracycline.

1.3 Research objectives

The overall objective of this thesis is focused on the dispersion of the plasmonic silver-silver bromide (Ag/AgBr) nanoparticles on carbonized pinecone, aimed at efficient removal and mineralization of tetracycline antibiotic from the aqueous solution. The scope of this work are highlighted as follows:

1. Preparation and optimization of preparation parameters on activated carbon from chemically activated pinecone biomass through microwave pyrolysis, capable of performance as catalyst support.
2. Characterization of prepared ACs physicochemical properties by Fourier transform spectroscopy (FTIR), Raman spectroscopy, X-ray diffraction (XRD), nitrogen (N_2) sorption analysis, transmission electron microscopy (TEM), and electrochemical studies.
3. Synthesis of heterostructure nanocomposites based on the dispersion of Ag/AgBr on optimized carbonized pinecone through thermal polyol and deposition precipitation route.
4. The synthesis parameters for Ag/AgBr composites from the thermal polyol route will be model using a response surface methodology (RSM) approach.
5. Understand the relationship between the prepared catalyst structures, morphologies, optical properties, and electronic properties' significant impact on the degradation of tetracycline antibiotics under a visible LED light.
6. Evaluation of the photocatalytic activity of the prepared photocatalyst on the degradation of TC under visible LED light by varying different parameters including pH, different LED light source, inorganic anions influence, and degradation temperature. The stability of the prepared catalysts will also be investigated by recycling use.

1.4 Thesis organization

The background, problem statement and research objectives of this thesis are described here in Chapter 1. Chapter 2 focuses on the literature survey on activated carbon attributes as potential catalyst support, Ag/AgBr heterojunctions used for visible-light-active photocatalysis, tetracycline

imminent threat to the environment and need to eliminate them using heterogeneous photocatalysis approach. Chapter 3 highlights the promising attributes of activated carbon prepared from pinecone biomass as good catalyst support for dispersion of Ag/AgBr. The porous structure, surface chemistry, and electrochemical attributes of these prepared ACs were discussed in detail. Chapter 4 describes the design of Ag/AgBr-activated carbon heterostructures through response surface methodology approach, also understanding their synergistic characteristics on the photocatalytic activity of TC removal. In addition to experimental observations of TC photocatalysis, and reaction mechanism of the optimized photocatalyst from the RSM model is also discussed. In Chapter 5, a heterostructure composite made between Ag/AgBr catalyst and different carbon materials (carbon from pinecone biomass, commercial source, and biochar) is discussed by considering their charge carriers attributes on the degradation of tetracycline antibiotics. Chapter 6 explores the preparation, characterization, and application of Ag/AgBr-activated carbon heterostructure using two different synthetic approaches (thermal polyol and deposition precipitation route) on TC removal. The significant impact of reactive oxidative species produced by the prepared catalysts during the catalytic process will also be studied. In Chapter 7, describe the overall conclusions from the study performed in this thesis and provide recommendations for future work in the field of heterogeneous photocatalysis.

1.5 References

AGUNBIADE, F.O. & MOODLEY, B. 2014. Pharmaceuticals as emerging organic contaminants in Umgeni River water system, KwaZulu-Natal, South Africa. *Environmental Monitoring Assessment,* 186, 7273-7291.

AHMED, S., RASUL, M. G., BROWN, R., HASHIB M. A. 2011. Influence of parameters on the heterogeneous photocatalytic degradation of pesticides and phenolic contaminants in wastewater: A short review. *Journal of Environmental Management,* 92, 311-330.

CHEN, F., YANG, Q., WANG, S., YAO, F., SUN, J., WANG, Y., ZHANG, C., LI, X., NIU, C. & WANG, D. 2017. Graphene oxide and carbon nitride nanosheets co-modified silver chromate nanoparticles with enhanced visible-light photoactivity and anti-photocorrosion properties towards multiple refractory pollutants degradation. *Applied Catalysis B: Environmental*, 209, 493-505.

DAGHRIR, R. & DROGUI, P. 2013. Tetracycline antibiotics in the environment: a review. *Environmental Chemistry Letters,* 11, 209-227.

GAO, Y., LI, Y., ZHANG, L., HUANG, H., HU, J., SHAH, S.M. & SU, X. 2012. Adsorption and removal of tetracycline antibiotics from aqueous solution by graphene oxide. *Journal of Colloid and Interface Science* 368, 540-546.

HEZAM, A., NAMRATHA, K., DRMOSH, Q., YAMANI, Z. & BYRAPPA, K. 2017. Synthesis of heterostructured Bi_2O_3–CeO_2–ZnO photocatalyst with enhanced sunlight photocatalytic activity. *Ceramics International*, 43, 5292-5301.

HOU, J., WANG, Z., YANG, C., ZHOU, W., JIAO, S. & ZHU, H. 2013. Hierarchically plasmonic Z-scheme photocatalyst of Ag/AgCl nanocrystals decorated mesoporous single-crystalline metastable $Bi_{20}TiO_{32}$ nanosheets. *The Journal of Physical Chemistry C,* 117, 5132-5141.

HUANG, J.H., CUI, Y. J., WANG, X. C. 2010. Visible light-sensitive ZnGe Oxynitride catalysts for the decomposition of organic pollutants in water. *Environmental Science and Technology*, 44, 3500–3504.

JAFRI, R.I., RAJALAKSHMI, N. & RAMAPRABHU, S. 2010. Nitrogen doped graphene nanoplatelets as catalyst support for oxygen reduction reaction in proton exchange membrane fuel cell. *Journal of Materials Chemistry,* 20, 7114-7117.

JI, L., WAN, Y., ZHENG, S. & ZHU, D. 2011. Adsorption of tetracycline and sulfamethoxazole on crop residue-derived ashes: implication for the relative importance of black carbon to soil sorption. *Environmental Science Technology*, 45, 5580-5586.

JIANG, D., XIAO, P., SHAO, L., LI, D. & CHEN, M. 2017. RGO-promoted all-solid-state g-C_3N_4/$BiVO_4$ Z-scheme heterostructure with enhanced photocatalytic activity toward the degradation of antibiotics. *Industrial Engineering Chemistry Research,* 56, 8823-8832.

JODEYRI, M., HAGHIGHI, M. & SHABANI, M. 2019. Enhanced-photoreduction deposition of Ag over sono-dispersed C_3N_4-Clinoptilolite used as nanophotocatalyst for efficient photocatalytic degradation of tetracycline antibiotic under simulated solar-light. *Journal of Materials Science: Materials in Electronics*, 30, 13877-13894.

KONG, X.-K., CHEN, C.-L. & CHEN, Q.-W. 2014. Doped graphene for metal-free catalysis. *Chemical Society Reviews,* 43, 2841-2857.

LAM, E., LUONG, J. H. T., 2014. Carbon Materials as Catalyst Supports and Catalysts in the Transformation of Biomass to Fuels and Chemicals. *ACS Catalysis,* 4, 3393−3410.

LI, D. & SHI, W. 2016. Recent developments in visible-light photocatalytic degradation of antibiotics. *Chinese Journal of Catalysis,* 37, 792-799.

LI, Y. & DING, Y. 2010. Porous AgCl/Ag nanocomposites with enhanced visible light photocatalytic properties. *The Journal of Physical Chemistry C,* 114, 3175-3179.

LI, C., YU, S., DONG, H., WANG, Y., WU, H., ZHANG, X., CHEN, G. & LIU, C. 2018. Mesoporous ferriferrous oxide nanoreactors modified on graphitic carbon nitride towards improvement of physical, photoelectrochemical properties and photocatalytic performance. *Journal of Colloid Interface Science*, 531, 331-342.

LILLO-RÓDENAS, M., MARCO-LOZAR, J., CAZORLA-AMORÓS, D. & LINARES-SOLANO, A. 2007. Activated carbons prepared by pyrolysis of mixtures of carbon precursor/alkaline hydroxide. *Journal of Analytical Applied Pyrolysis,* 80, 166-174.

LIU, Z., ADAMS, M., COTE, R.P., GENG, Y. & LI, Y. 2018. Comparative study on the pathways of industrial parks towards sustainable development between China and Canada. *Resources, Conservation Recycling,* 128, 417-425.

LIU, Q., GUO, Y., CHEN, Z., ZHANG, Z. & FANG, X. 2016. Constructing a novel ternary Fe (III)/graphene/g-C_3N_4 composite photocatalyst with enhanced visible-light driven photocatalytic activity via interfacial charge transfer effect. *Applied Catalysis B: Environmental,* 183, 231-241.

LOFRANO, G., LIBRALATO, G., ADINOLFI, R., SICILIANO, A., IANNECE, P., GUIDA, M., GIUGNI, M., GHIRARDINI, A.V. & CAROTENUTO, M. 2016. Photocatalytic degradation of the antibiotic chloramphenicol and effluent toxicity effects. *Ecotoxicology Environmental Safety,* 123, 65-71.

NADIMI, R. & TOKIMATSU, K. 2018. Energy use analysis in the presence of quality of life, poverty, health, and carbon dioxide emissions. *Energy,* 153, 671-684.

OZDEMIR, O., ARMAGAN, B., TURAN, M., CELIK, M. S. 2004. Comparison of the adsorption characteristics of azo-reactive dyes on mesoporous minerals. *Dyes Pigments,* 62, 49–60.

RIMAYI, C., ODUSANYA, D., WEISS, J.M., DE BOER, J. & CHIMUKA, L. 2018. Contaminants of emerging concern in the Hartbeespoort Dam catchment and the uMngeni River estuary 2016 pollution incident. South Africa. *Science of the Total Environment,* 627, 1008-1017.

SHAHSAVARI, A. & AKBARI, M. 2018. Potential of solar energy in developing countries for reducing energy-related emissions. *Renewable Sustainable Energy Reviews,* 90, 275-291.

SLIMEN, H., HOUAS, A., NOGIER, J. P. 2011. Elaboration of stable anatase TiO_2 through activated carbon addition with high photocatalytic activity under visible light. *Journal of Photochemistry and Photobiology A: Chemistry,* 221, 13–21.

SOHRABNEZHAD, S., REZAEI, A. 2013. Plasmonic photocatalyst system using Ag/AgBr/mordenite nanocrystal under visible light. *Superlattices and Microstructures,* 55, 168–179.

VORA, J.J., CHAUHAN, S. K., PARMAR, K. C., VASAVA, S. B., SHARMA, S., BHUTADIYA, L. S. 2009. Kinetic study of application of ZnO as a photocatalyst in heterogeneous medium. *E Journal of Chemistry,* 6, 531-536.

WANG, B., XU, L., LIU, G., ZHANG, P., ZHU, W., XIA, J. & LI, H. 2017. Biomass willow catkin-derived Co_3O_4/N-doped hollow hierarchical porous carbon microtubes as an effective tri-functional electrocatalyst. *Journal of Materials Chemistry A,* 5, 20170-20179.

XIAO, T., TANG, Z., YANG, Y., TANG, L., ZHOU, Y. & ZOU, Z. 2018. In situ construction of hierarchical WO_3/g-C_3N_4 composite hollow microspheres as a Z-scheme photocatalyst for the degradation of antibiotics. *Applied Catalysis B: Environmental,* 220, 417-428.

Chapter 2. Literature review

2.1 Water crisis worldwide

Water is an essential source for human existence, as required for basic human needs, agricultural and industrial applications. Though, the water crisis caused by rapid industrialization is a major threat to the current and ever-growing population, as more than 13% of the world population access this water from unprotected sources (WHO 2008). Presently in the world, access to adequate sanitation is not available to 2.5 billion people in the world, while 1.2 billion lack access to good sanitation facilities (WHO 2008). As ongoing exposure to this water continues, a host of life-threatening water diseases such as malnutrition, schistosomiasis, malaria, diarrhea, intestinal nematode infections, arsenic and fluoride poisoning have occurred due to the presence of these non-biodegradable organics, pathogens, heavy metals and pharmaceutical and personal care products (PPCPs) (Efftaxias 2002; Erlanger, Keiser, De Castro, Bos, Singer, Tanner & Utzinger 2005). The detection of emerging contaminants like pharmaceutical and personal care products (PPCPs) at lower concentration levels has serious effects on ecosystem and human health (Lapworth, Baran, Stuart & Ward 2012; Zhang, Yang, Huang, Zhao & Sun 2016). It's imperative to clean-up these PPCPs from the environment, as such extensive research is focused on development of efficient and cost-effective technologies.

Moreover, conventional approaches such as classical physico-chemical treatment, physical processes, and biological treatment have been utilized for the treatment of pollutants in the environment but have their limitations. Classical physico-chemical treatments such as chlorination create disinfection byproducts, which possess major health risks to the populace (Hamidin, Yu &

Connell 2008; Hrudey 2009). The case of ozonolysis and UV irradiation are hindered by high selectivity and slow kinetics. Though the application of conventional biological treatment (aerobic and anaerobic digestion) shows promising attributes, recalcitrant organic pollutants are resistant to this treatment approach (Forster 1985). Physical processes such as adsorption, coagulation, and membrane filtration change the pollutants' phases without necessarily removing or degrading them completely, thus the creation of toxic by-products that require safe storage (Chong, Jin, Chow & Saint 2010; Gao, Sun, Wan, Yu & Li 2013). The conventional treatment is not environmentally acceptable due to these limitations; invariably the development of alternative and sustainable technologies in addressing water remediation issues in the world is desirable.

2.2 Advanced oxidation technologies

Advanced oxidation technologies (AOT) have proven to be highly efficient for wastewater treatment that has proven challenging to be treated with conventional technologies. These technologies show great potential to be utilized alone, as pre-treatment, complementary methods with other conventional techniques. Heterogeneous catalysis as an AOT has attracted attention to operates at ambient temperature and pressure water conditions, which also simultaneously generates reactive radicals in breaking down the pollutants (Maldonado, Passarinho, Oller, Gernjak, Fernández, Blanco & Malato 2007).

Heterogeneous photocatalytic treatment is an excellent technology for the treatment of water and air pollutants (Vohra, Goswami, Deshpande & Block 2006; Wang, Hu, Chen, Zhao, Liu & Wen 2009). As organic pollutants present in water with high total organic carbon (TOC) can be effectively, mineralize to subtle products with this technology in comparison to conventional

techniques. This technique operates uniquely as compared to other AOTs, with the presence of a solid reusable catalyst under constant illumination of light irradiation and no addition of any other strong oxidants. This technology added merit includes:

- operation at ambient temperature and pressure,
- utilization of atmospheric oxygen and no need for costly oxidizing chemical,
- the technologies operate in a green way as degradation products show low toxicity,
- photocatalyst materials are non-hazardous, stable, insoluble under most conditions and recyclable,
- Process operational at low concentrations of pollutants.

From these technologies' advantages, this process offers a cost-effective route for environmental remediation and quality water generation from wastewater. Moreover, the heterogeneous metal oxide semiconductor (MOS) applied as photocatalyst in environmental remediation includes TiO_2, (Rodriguez & Fernández-García 2007) ZnO, WO_3, (Szilágyi, Fórizs, Rosseler, Szegedi, Németh, Király, Tárkányi, Vajna, Varga-Josepovits & László 2012; Tian, Zhang, Wu, Jiang, Liang, Jiang & Fu 2012). The TiO_2 MOS is widely utilized for photocatalytic activity in a wider range of environmental applications due to its strong oxidizing power, low toxicity, and long-term photostability (Fujishima, Rao & Tryk 2000; Li, Li, Li & Yin 2006; Zheng, Liu, Ye, Zhao, Waclawik & Zhu 2010). However, the application of TiO_2 MOS at large scale operation has been hinder by low quantum efficiency (below 5%) due to electron-hole pairs recombination, poor harvesting of solar spectrum and poor stability after repeated degradation activities due to its nanosized structure (Sopyan, Watanabe, Murasawa, Hashimoto & Fujishima 1996; Liu, Nakata,

Zhao, Ochiai, Murakami & Fujishima 2011). The poor absorption in the visible light region of the solar spectrum is ascribed to the high band gap energy of TiO_2 MOS (3.2 eV). As the TiO_2 MOS can only be excited in the ultraviolet region (wavelength < 400 nm) which is 3-5 % of the solar spectrum, while the visible light region comprises 43 % of the solar spectrum. The aspect of separation of TiO_2 MOS from aqueous solution can be challenging, as the powder aggregate at high concentrations (Arana, Melián, Rodrıguez, Dıaz, Viera, Pena, Sosa & Jiménez 2002; Arana, Doña-Rodrí, Rendón, i Cabo, González-Dí, Herrera-Melián, Pérez-Peña, Colón & Naví 2003).

These challenges have prompted a host of approaches aimed at improving the photocatalytic efficiency of TiO_2 MOS through photocatalyst development, for effective performance in the visible region of solar radiation. Some of the strategies include bandgap fine-tuning through changing the electronic structure of photocatalyst or extension of excitation wavelengths with the application of photosensitizers (Chen, Wang & Fu 2009; Devi, Kottam, Murthy & Kumar 2010; Devi, Murthy & Kumar 2010). The reduction rate of electron-hole pairs recombination and acceleration of reaction system using another MOS (Xi & Ye 2010) or a support material, which eventually facilitates the pollutant transfer to the active sites of the photocatalyst (Leary & Westwood 2011). Based on the inherent shortcomings associated with these approaches, the immobilization of MOS nanoparticles on suitable support material is a promising avenue to overcome the challenges of MOS for practical application of recovery and reuse of the catalyst (Mozia & Morawski 2012). Carbonaceous materials are excellent materials with strong light-absorbing potential, textural features, improved mass transfer, and interfacial electronic properties, which have contributed significantly to the improvement of the catalytic activity of MOS upon immobilization (Puma, Bono, Krishnaiah & Collin 2008).

2.3 Carbonaceous materials

The higher specific surface area, high porosity, excellent electron conductivity, more effective adsorption sites, and their relative chemical inertness are some of the advantages for dispersion of photocatalysts on carbonaceous materials (Fan, Zhao, Yang, Shan, Yang, Zhang, Li & Gao 2012). These carbonaceous materials enhanced degradation rates of organic pollutants based on their high adsorption capacity and reduced the electron-hole recombination rate on the surface of the composite material (Matos, Laine & Hermann 1998; Slimen, Houas & Nogier 2011). These carbonaceous materials possess high mechanical strength, chemical and thermal stability for preventing the agglomeration of MOS nanoparticles (Machek, Hanika, Sporka, Růžička & Kunz 1981). The physical and chemical properties of the most utilized carbonaceous materials (Lam & Luong 2014) for dispersion of MOS photocatalyst are highlighted in Table 1 with their individual characteristics.

Table 2.1: Carbonaceous materials applied as catalyst support and their physical properties (Lam & Luong 2014).

Carbonaceous materials	Specific surface area ($m^2 g^{-1}$)	Pore Volume ($cm^3 g^{-1}$)	Density ($g\ cm^{-3}$)	Electrical conductivity ($S\ cm^{-1}$)	Cost
Activated Carbon	1000-3500	0.6-2	0.4-0.7	0.1-1	Low
Templated porous carbon	500-3000	0.7-2	0.5-1	0.3-10	High
Carbon fibers	1000-3000	0.3-0.7	0.3-0.8	5-10	Medium
Carbon nanotubes	120-500	2.5	0.6	10^4-10^5	High
Carbon aerogel	400-1000	2-6	0.5-0.7	1-10	Low
Graphite	10-1000	0.01-0.1	2.26	104	Low
Graphene	1500-2500	2-3.5	>1	106	High

Production cost, selection of an abundant, inexpensive matrix with complementary non-toxicity attributes are primary importance for a good selection of desirable carbonaceous material for MOS photocatalyst immobilization. Among the carbonaceous materials listed in **Table 4**, activated carbon (AC) is desirable as a catalyst support in gas and water remediation due to these excellent properties described above (Matos, Laine, Herrmann, Uzcategui & Brito 2006; Liu, Chen & Chen 2007).

2.4 Activated carbon

Activated carbon (AC) is a non-graphitizable carbon that possesses a highly disordered microstructure. The Egyptians recognized this material around 3750 B.C as a good material for metals reduction in the bronze manufacturing process and smokeless fuel (Przepiórski 2006). Though, the first application of AC for adsorption of gases was carried out in 1773 by Scheele (Dietz 1944). Then, the industrial production of AC in 1900 was established and subsequently used to replace bone char in sugar refining processes (Bansal & Goyal 2005). Activated carbon application in recent years are ascribed to its host of physicochemical properties, such as lightweight, exciting electronic properties, tunable porosity, chemical and thermal stability (Wang, Li, Chen & Huang 2001; Budarin, Clark, Hardy, Luque, Milkowski, Tavener & Wilson 2006; Poonjarernsilp, Sano & Tamon 2014). AC have been exploited for host of applications in catalysis (Tawalbeh, Allawzi & Kandah 2005; Azargohar & Dalai 2006), environmental science (Zhang 2014), absorbent (Mubarak, Sahu, Abdullah & Jayakumar 2014) in environmental industry, petrochemical industry, pharmaceutical, drug delivery (Fraczek-Szczypta 2014). ACs have been utilized also in food industry, electrode materials (Vikkisk, Kruusenberg, Joost, Shulga, Kink & Tammeveski 2014) and batteries, fuel cells (Shah, Jan, Mabood & Shahid 2006), energy storage (Yang, Yu, Yan, Tu & Dahlquist 2013) in automobile industry. The AC can also be employed as a stationary phase in the chromatography system (Takeba, Matsumoto, Shida & Nakazawa 1990) in chemical industry.

The exceptional attributes of AC are from a combination of the developed porous framework (surface areas and pore volumes) and abundance of heteroatoms functionalities groups on their surface inclusive (Marsh & Reinoso 2006). The porous framework of AC is created during the activation process, whereby the spaces between the aromatic sheets become unobstructed of carbonaceous material and disorganized carbon. The process continues with the exposure of aromatic sheets to the activating agent and further enhancement of the porous structure. With respect to the activation process, the AC pores are more opened which pave access for previously inaccessible pores and thus modifies the surface of the carbon. This porous framework comprises of pore diameter, which are classified into either as micropore (pore size < 2 nm), mesopore (2nm < pore size < 50 nm) or macropore (pore size > 50 nm) (Everett 1972) as shown in Figure 2.1. The porous fissures extend well within the AC structure, which improves overall surface area and promotes fast electrical conductivity.

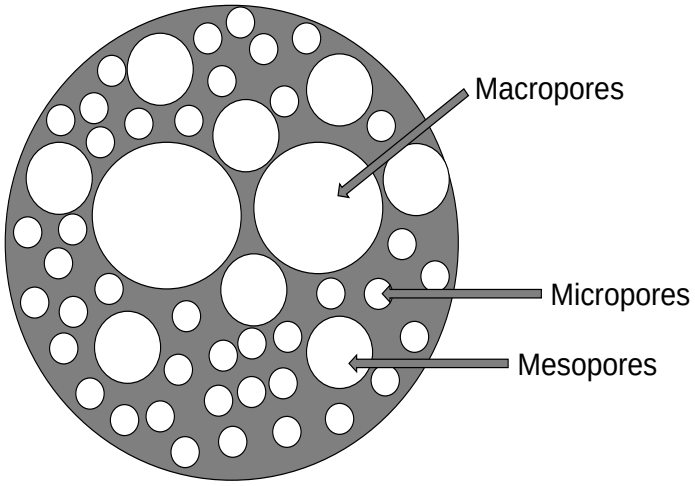

Figure 2.1: Pore structure identification in activated carbon.

The activation process, activating agent and reaction conditions influence the porous framework formation, characteristic catalytic attributes, and surface chemistry in activated carbons (Sentorun-Shalaby, Uçak-Astarlıoglu, Artok & Sarıcı 2006; Wu & Tseng 2006). The activation process begins with the elimination of the disorganized carbon produced during the carbonization process and the opening of the blocked pores. The activation process can be achieved through either physical or chemical means (Rodriguez-Reinoso 1997; Kyotani 2000), or a combination of the two using different precursors. Both activation routes are desirable for AC production based on the conditions, though the quality of AC generated from the 2 methods will not be the same.

Physical activation also known as thermal activation and gas activation, which requires elevated temperatures near 900 ^{o}C and suitable oxidizing gases such as steam or carbon dioxide (CO_2) in the activation process for generating activated carbon with high porosity (Rodrıgues-Reinoso, Heintz & Marsh 1997; Rodrıguez-Reinoso & Molina-Sabio 1998). Air, oxygen, flue gases are rarely used as oxidizing gases in combination with carbon, due to challenging control of activation with these gases. The porosity in AC is not well developed with above described oxidizing gases, as the carbon particles get burn away forming carbon dioxide and carbon monoxide (Rodríguez-Reinoso 1997; Rodríguez-Reinoso 2002).

The chemical activation route is very important for the industrial process aimed at producing highly microporous ACs, where the carbonization and activation occur simultaneously. This route operates through impregnating the precursor with a chemical agent, heating in an inert atmosphere, and then washing any chemical remnant from the produced AC out with acid/base and water. In

the chemical activation route, the chemical agent dehydrates the sample, inhibits the tar formation and volatile compounds evolution, which also enhances the yield of the carbonization process (Rodriguez-Reinoso 1997; Williams & Reed 2004). In contrast to physical activation, chemical activation occurs at lower temperatures and at shorter times with well-developed porosity. The energy required for AC production is lower, as well this route offers well and controlled porosity development. The most utilized activating agents include potassium hydroxide (KOH), phosphoric acid (H_3PO_4) (Bandosz 2006; Marsh & Rodríguez-Reinoso 2006) and zinc chloride ($ZnCl_2$) (McEnaney 2002). The reaction mechanism for the above mentioned activating agents differs from each other, though their advantages outweigh that of physical activation.

AC produced from chemical activation using $ZnCl_2$ activating agents is dominantly microporous, though with significant mesopores which are augmented by an increase in the impregnation ratio ($ZnCl_2$/precursor) (McEnaney 2002). Zinc chloride activation also has its limitations such as low recovery efficiencies, corrosion problems, the presence of residual zinc in the carbon structure, which is of environmental concerns (Bandosz 2006). Concerning phosphoric acid activation, the reaction occurs with acid-catalyzed dehydration and partial depolymerization of the hemicelluloses and lignin. This promotes bond cleavage (separation of the cellulose fibers) and the formation of cross-links (with cyclisation and condensation reactions) (Hayashi, Kazehaya, Muroyama & Watkinson 2000; Molina-Sabio & Rodrıguez-Reinoso 2004). The recovery of phosphoric acid in large amounts which is carried out through multiple stage extraction (Bandosz 2006; Marsh & Rodríguez-Reinoso 2006) is a major concern.

In the case of potassium hydroxide (KOH) impregnation of raw material, no reaction will occur until the heat treatment is applied, making the chemical act as a dehydrating agent on the precursor and it does not prevent the shrinkage of the particles upon heat treatment. The reaction condition for the impregnated KOH precursor is desirable at a high temperature above 700 ^{o}C, well-developed porosity on AC is obtained from good impregnation of the raw material. KOH activation occur through a redox reaction where carbon is oxidized to CO or CO_2. The reduction of potassium to a metal ion (hydrogen, metallic potassium), which intercalates between the graphene layers of the carbon structure and expands the structural graphene layers. The destructive removal of this metal ion occurs when the carbon is progressively heated, creating new pores by disrupting the graphene structure as it exits (Molina-Sabio & Rodrıguez-Reinoso 2004). The reaction mechanism in accordance with literature is described as follows:

$$6KOH + 2C \rightarrow 2K + 3H_2 + 2K_2CO_3 \qquad 2.1$$

$$2KOH + 2C \rightarrow 2K + 2CO + H_2 \qquad 2.2$$

The proposed reactions described here also proceed with the decomposition of the potassium carbonate further to form potassium oxide and carbon dioxide. Activated carbon with highly developed microstructure, along with high surface area more than 3000 m^2/g, have been produced through KOH chemical activation (McEnaney 2002; Robau-Sánchez, Aguilar-Elguézabal & Aguilar-Pliego 2005).

2.4.1 Microwave heating method

The conventional heating method is widely utilized for ACs preparations (Noor & Nawi 2008; Gimba, Salihu, Kagbu, Turoti, Itodo & Sariyya 2010), which involves the generation of energy by an electric furnace, requires high energy consumptions and long processing times. This process poses limitations for the biomass material, as the heat transfer through the material is governed by conduction through individual articles with reduced convective heat transfer within the voids. This heating mode has been in existence for many years still has its challenge due to slow heating rates with large material and imprecise heating of the workspace surface that affects the overall yield of produced material. Invariably, heat transfer remains a primary challenge with conventional heating method especially with bioenergy and bio-derived products. The need for an exceptional heating method that can match the quality of biomass derivatives aside from conventional heating is highly desirable.

In order to overcome the challenges of conventional heating methods, an alternative heating method have been developed, also utilized in the science and technology field. Microwave heating exhibits potential attributes as compared to conventional heating methods due to its improved heating efficiencies. Microwave heating has since found vast applications in the food industry, pasteurization and sterilization, crude oil exploration and processing, vacuum drying, (Kaatze & Hübner 2010) specifically due to the overcoming of heat transfer limitations. Microwaves heat volumetrically due to the presence of an electric field within the processed material and do selective heating to the material, which is more efficient as compared to conventional heating (Lei,

Ren & Julson 2009). Microwave pyrolysis selectively heating the targeted material, a more uniform temperature profile, while a higher yield of desired end products can be achieved (Fernández, Arenillas, Bermúdez & Menéndez 2010; Zuo, Tian & Ren 2011). Microwave heating is easy, rapidly initiated and terminated, help in reducing the quantity of heating required to achieve a particular end, and with it the associated energy use and costs (Menéndez, Domınguez, Inguanzo & Pis 2004). The application of microwave pyrolysis on different biomass materials such as waste tea (Yagmur, Ozmak & Aktas 2008), rice straw (Huang, Kuan, Lo & Lin 2008), wood (Miura, Kaga, Sakurai, Kakuchi & Takahashi 2004), micro-algae (Budarin, Zhao, Gronnow, Shuttleworth, Breeden, Macquarrie & Clark 2011), coffee hulls and wheat straw (Budarin, Clark, Lanigan, Shuttleworth, Breeden, Wilson, Macquarrie, Milkowski, Jones & Bridgeman 2009) have been used a starting material for AC production.

2.4.2 Pinecone biomass as AC source

AC has a worldwide huge demand in the market around an estimate of 1,000,000 tonnes per year. AC is also cheap and readily available with the earth's crust in form of fossil-based sources. Their production from fossil-based requires sophisticated and energy-consuming processes for their production, which also generates a host of toxic gases and chemicals during the production process. In the limelight of these challenges involved using fossil-based precursors for AC synthesis, attention is shifted on the application of alternative, most resourceful, cost-effective and non-cyclic cropping sources for AC production. AC preparation from renewable sources (biomass) is a good approach in terms of availability, economic and application purposes. These biomass are widely available as a renewable source on the earth's surface with an estimate growth amount of 118 billion tons/year, dried (Bobleter 1994). Green chemistry also affords these biomass wastes to

serves a double purpose by utilizing the unwanted, surplus wastes as a starting precursor for vitamins, colorants, polymers, pharmaceuticals, chemicals, and surfactants (Anastas & Kirchhoff 2002) and also reduce the environmental nuisance of these biomass. Moreover, biomass usage as a precursor for AC preparation reduces the demand for non-renewable activated carbon feedstock (coal) and limits global warming by converting these biodegradable waste materials into solid carbon char.

Pinecone (Pinus radiata) is another abundant, inexpensive agricultural biomass material that is widely abundant in South Africa. This material has been employed as pine based adsorbent for removal of heavy metals and phenolics from wastewater by other researchers (Tseng, Wu & Juang 2003; Ofomaja & Naidoo 2011). The pinecone is rich in carbon and low in ash contents, and also possesses huge potential to be converted into activated carbon if pyrolyzed under controlled conditions or with vital chemical treatment (Zhang, Zhang, Li & Chen 2007; Duman, Onal, Okutucu, Onenc & Yanik 2009). The proximate analysis and the calorific value measurements of pinecone determined according to ASTM standards and results (Haykiri-Acma & Yaman 2007) are given in **Table 2.2**. The ultimate analyses of pinecone were conducted using EuroEA3000 model elemental analyzer are shown in **Table 2.3**. The chemical composition of the pinecone are shown in **Table 2.4** respectively.

Table 2.2: Proximate analysis (%, on the original basis) and gross calorific value results of the pinecone (Haykiri-Acma & Yaman 2007).

Material	Moisture	Volatile matter	Fixed carbon	Ash	Gross calorific value (MJ/kg)
Pinecone	9.4	69.0	20.9	0.7	18.6

Table 2.3: Ultimate analysis results of the pinecone (%, on the dry-ash-free basis) (Haykiri-Acma & Yaman 2007).

Material	C	H	N	O
Pinecone	44.1	5.9	0.01	50.0

Table 2.4: Chemical compositions of the pinecone (%, on the original basis) (Haykiri-Acma & Yaman 2007).

Material	Alcohol/benzene extractives	Holocellulose	Lignin	α-Cellulose
Pinecone	15.4	46.5	37.4	18.8

The carbonized pinecone has been applied as a low-cost material for the removal of pollutants from water and also as anode lithium secondary batteries (Zhang et al. 2007; Duman et al. 2009). However, the preparation of AC and optimization of preparation parameters through microwave-assisted pyrolysis of chemically (KOH) activated pinecone biomass, as a potential catalyst support has not been reported before. The dispersion of most MOS photocatalyst on AC is limited by either poor catalytic activities in the visible light region of the solar spectrum (Byrappa, Subramani, Ananda, Rai, Sunitha, Basavalingu & Soga 2006; Sobana, Muruganandam & Swaminathan 2008). The need to develop a photocatalyst that can effectively utilize the solar spectrum well, it must be active under low intensity of visible light region and possess high efficiency to remove different types of organic pollutants from the environment.

2.5 Plasmonic silver/silver halides photocatalyst

Plasmonic photocatalysts are promising materials that can harness visible sunlight in photocatalytic processes. These noble-metal such as Au, Ag, Pt, and Cu, possess unique attributes which is ascribed to excitation of resonant collective oscillations of the conduction electrons (Figure 2.2) by electromagnetic radiation–the surface plasmon resonance (SPR) (Awazu, Fujimaki, Rockstuhl, Tominaga, Murakami, Ohki, Yoshida & Watanabe 2008; Zhang, Li, Lu, Tang & Lu 2012). The SPR phenomenon can be influenced by the metal type, material composition, particle size, shape and the dielectric constant of the surrounding medium (Jones, Osberg, Macfarlane, Langille & Mirkin 2011). The SPR band is stronger with Ag and Au as compared to other noble metals (Tang & Lu 2012). The anchor semiconductor catalyst with the

Ag noble metal tends to possess intense degradation performance as a result of good interaction with the electronic environment of supported semiconductor (Tian & Tatsuma 2005; Linic, Christopher & Ingram 2011). These attributes paved the way for harnessing their properties for the creation of efficient visible-light-driven plasmonic photocatalysts, due to their excellent absorption in the visible region of the solar spectrum.

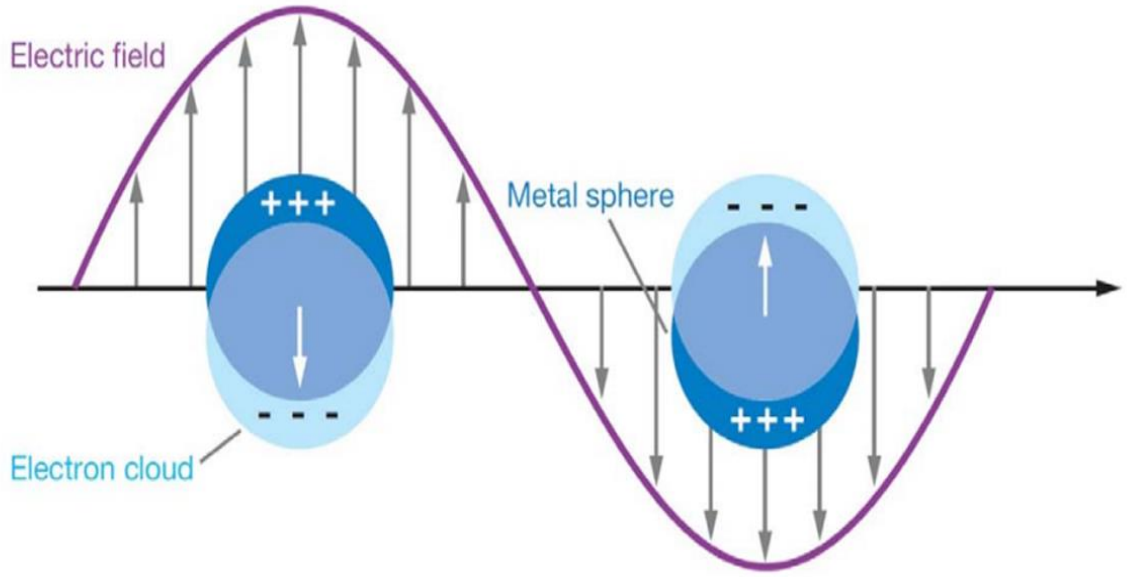

Figure 2.2: Schematic illustration of surface plasmon resonance in plasmonic nanoparticles (Fujishima, Zhang & Tryk 2008).

The silver halide (AgX, X = Cl, Br or I) species are good material source applied as photographic film, which are unstable upon illumination. The metallic Ag anchor with the silver halide results in the formation of silver/silver halide (Ag/AgX, X = Cl, Br or I) nanoparticles. In a synergistic manner, the Ag^{o} on the surface of AgX with plasmon attributes induced photostability and efficient visible-light photocatalyst for environmental remediation (Ng & Fan 2007; Wang, Huang, Qin, Zhang, Dai, Wei & Whangbo 2008). The metallic Ag on the surface of AgX material also aids the effective separation of electron-hole pairs by forming a Schottky barrier. This Schottky barrier enhances the catalytic performance of silver/silver halide nanoparticles and also their stability after degradation activities (Hu, Lan, Qu, Hu & Wang 2006). Since the discovery of Ag/AgCl plasmonic photocatalysts (Lou, Huang, Qin, Zhang, Cheng, Liu, Wang, Wang & Dai 2012), there has been continued interest on the application of the plasmonic Ag/AgX for environmental remediation (Zhu, Ke, Yang, Sarina & Liu 2010). Though, the overall performance of Ag/AgX (X = Cl, Br, I) materials is dependent on their morphological structures that evolve from their synthesis approaches. Huang and his co-workers pioneered the synthesis of Ag/AgCl through ion-exchange approach (Zhang, Lima, Lee, Zaera, Chi & Yin 2011) and as such a host of methods have been utilized for Ag/AgX (X = Cl, Br, I) synthesis with different morphologies (Li & Ding 2010).

The plasmonic Ag/AgX (X = Cl, Br and I) nanomaterials possess excellent catalytic performance on the degradation of organic pollutants from wastewater under visible light irradiation (Zhou, Hu, Hu, Peng & Qu 2010). Much attention is focused on the synthesis of Ag/AgCl, though the Ag/AgBr photocatalyst possesses more increased visible light absorption than Ag/AgCl (Zhang, Chen, Liu & Tsai 2013). The AgBr has an indirect bandgap of 2.6 eV

(Wang, Huang, Zhang, Qin, Jin, Dai, Wang, Wei, Zhan & Wang 2009) as compared to narrow bandgap of 2.4 eV for AgI (2.4 eV for α - AgI and 2.8 eV for β – AgI) (Victora 1997) and wide bandgap of 3.25 eV for AgCl. Invariably, both Ag/AgBr and Ag/AgI possess the capability in absorbing visible light effectively by not using metallic Ag nanoparticles alone, but also with their intrinsic absorption of adjacent silver halide. Though, the Ag/AgBr has more catalytic properties more than Ag/AgCl by a factor of 1.5 (Hou, Wang, Yang, Zhou, Jiao & Zhu 2013). Another attribute of Ag/AgBr is related to the electron affinity of Br, which is lower as compared to Cl (324 vs 348 kJ mol-1). The reduced electron affinity of Br paves way for it to combine with hole faster than Cl., this step is crucial for enhancing catalytic reaction process as the holes combine with X^{-I} forming X^{o} (oxidant radical) that degrade the pollutant. However, the Ag/AgI photocatalyst is less focused on due to lower catalytic performance which is ascribed to the weak oxidation power of iodine (Hu, Peng, Hu, Nie, Zhou, Qu & He 2009). The focus of attention in this doctorate thesis will be on the plasmonic Ag/AgBr due to its higher catalytic activity than Ag/AgCl and Ag/AgI photocatalyst.

However, most pure Ag/AgX material are not very efficient for high catalytic performance due to their large particles size and irregular morphology which emanates from the rapid reaction kinetics between the silver and halide ions (Ng & Fan 2007; Wang, Huang, Zhang, Zhang, Qin, Dai, Zhan, Yu, Liu & Lou 2010). The AgX nucleates rapidly and aggregate in solution due to rapid reactions, thus the need to control the particle size and shape of nanosized silver halides. Also, irregular morphology results in recombination of electron-hole pairs, which affect the catalytic activities (Hou, Wang, Yang, Zhou, Jiao & Zhu 2013). With the case of the plasmonic Ag/AgBr, host of synthetic approaches have been employed in controlled size and shape. Routes such as

hydrothermal, photoreduction, solvothermal, sacrificial template-directed, microwave-assisted, deposition-precipitation and thermal polyol method have been utilised (Lee, Kim & Kim 2010; Choi, Byun, Bae & Lee 2013; Yan, Zhang, Luo, Ma, Lin & You 2013; Chen, Li, Huang, Guo, Qiao, Qiu, Wang, Jiang & Yuan 2015; Xiao, Ge, Han, Li, Zhao, Xin, Fang, Wu & Qiu 2015). It should be noted that most of these methods described have utilized a lot of organic reagents, amphiphilic surfactants, ionic liquids, or polymers as templates in the synthesis process for guiding the formation of anisotropic growth of different Ag/AgBr. However, removal of these templates after the reaction process can be challenging and also have no participation in the degradation process, which invariably decrease the active sites of the photocatalyst (Chen, Su, Wu, Yang, Zhuang, Wang & Chen 2012; Wang, Lang, Gao, Liu, Wu, Wu, Guo & Li 2012). The need to develop morphology controlled Ag/AgX photocatalyst with a clean surface structure that also works as a functional template and catalyst promoter, which will improve high photocatalytic activities and stability of the overall composite.

Controlled morphology of plasmonic Ag/AgX with AC from commercial source have been reported, by promoting the spontaneous formation of plasmonic Ag and act as surfactant to affect the growth of AgX particles (McEvoy, Cui & Zhang 2014; McEvoy & Zhang 2014; McEvoy & Zhang 2016). However, no report in the literature on the utilization of AC from pinecone biomass as a catalyst support in the dispersion of Ag/AgBr have been described before, through synthesis of the composite via thermal polyol and deposition-precipitation method. The synthesis parameters in preparation of Ag/AgX play important roles in the morphology, structural and electrical properties. Among them, the control of temperature, reaction time, support material mass, and surfactant affect the product formation and their intrinsic performance on targeted pollutants.

However, there are several limitations (Chen et al. 2015) with conventional one synthesis parameter at a time approach, as it fails to clearly identify the actual parameters responsible for exceptional characteristic properties of Ag/AgBr composite on targeted pollutant. The process response is assumed to be a direct function of a single variable parameter, as the interactive influence of different parameters is not taken into consideration, which makes the experimental design time consuming and less efficient (Gunst 1996). As such, a statistical model of synthesis parameters in preparation of Ag/AgBr composite in correlation with organic pollutant removal is required for better understanding.

2.6 Response surface methodology

The traditional design experimental focusses on the investigation of the effect of a single parameter at a time by changing that parameter and keeping others constant. A statistical tool called Response Surface Methodology (RSM) has been employed to carry out a multiple regression analysis and optimization of data from properly designed experiments. This statistical tool allows good designing of experiments and optimization purposes through investigation of interactions between factors. Response Surface Methodology (RSM) as a design of experiment tools utilizes a combination of statistical and mathematical skills to plan, develop, improve and optimize processes with efficient conclusions (Gunst 1996). This statistical tool is a commonly used method in the optimisation of industrial processes, especially when there are several input variables that can be influential on the performance or quality characteristics of a product or process (i.e. response) (Gunst 1996). RSM first application by Box and Wilson in 1951 within the chemistry field for process optimization, while the tool showed promising attributes especially in areas where experiments are sequential with rather small errors (Box & Wilson 1992). The

exceptional attributes of this design have been put to usage by different types of industrial processes for investigation of the behavior of materials, optimization of the process and selection of operating conditions for specific objectives (Yan, Qin, Kong, Zhi, Sun, Shen & Li 2016; Zhang, Li, Liu, Chen, Ma & An 2019).

RSM does a multiple regression analysis of the data from properly designed experiments, which results in a mathematical relationship between the response and process independent variables. The regression models show the individual and interactive influence of the test variables on the process, which are from one of the three classes described here: (i) first-order polynomial (indicative of main effects only), (ii) first-order polynomial enhanced with two-factor interactions and (iii) second-order models which considers complete quadratic effects (Gunst 1996; Banks 1998). Moreover, the response surface is depicted in the form of three-dimensional (3D) plots or by contour plots as shown in **Figure 2.**3. There is also a need to explore RSM to correlates the relationship between synthesis parameters with the physicochemical properties of the prepared composite using analytical means such as X-ray diffraction (XRD), UV-vis diffuse reflectance spectrophotometry (DRS), Fourier transform spectroscopy (FTIR), scanning electron microscope-(SEM), Photoluminescence microscopy (PL), and electrochemical spectroscopy on degradation of organic pollutants.

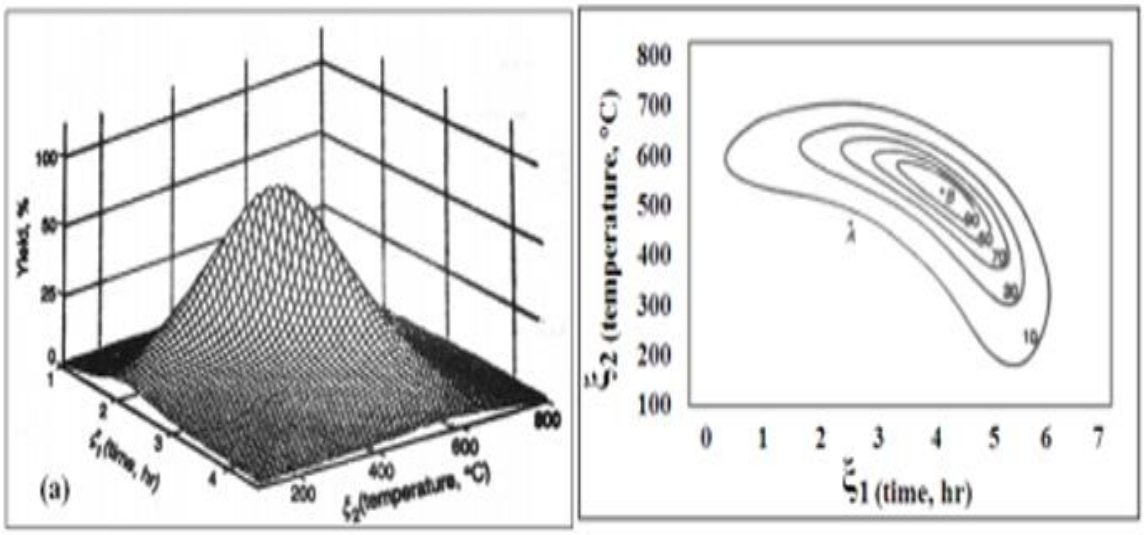

Figure 2.3: Description of response surface as a function of two factors (a) 3D plot, (b) Contour plot (Gunst 1996).

2.7 Pharmaceuticals in the environment

Pharmaceutical and personal care products (PPCPs) include groups of complex organic molecules with different physicochemical, biological properties and functionalities in human and animal health care (Daughton & Ternes 1999; Kümmerer 2008). Many of these compounds are extensively employed as anti-inflammatories, lipid regulators, analgesics, antibiotics, anti-epileptics, antiseptics and disinfectants (Kolpin, Furlong, Meyer, Thurman, Zaugg, Barber & Buxton 2002). These PPCPs presence in the surface waters, wastewaters and drinking waters are critical concerns for the ecosystem at large (Oulton, Kohn & Cwiertny 2010). These PPCPs enters through the sewage systems from incomplete metabolism during therapeutic usage and also through excreta from human and animals in an unchanged form (Hirsch, Ternes, Haberer & Kratz 1999). The disposal of unused drugs into the sewer by health officials and veterinary services

(Diaz-Cruz, Lopez de Alda & Barcelo 2003; Kummerer 2003) are potential sources for the large occurrence of these PPCPs in the environment. These PPCPs also occur in surface, ground and drinking waters (Gros, Petrovic´, Ginebreda & Barceló 2010) as well in river sediments and wastewater sludge, especially in the case of antibiotics (Jelic´, Petrovic´ & Barceló 2009). However, antibiotic drugs are major PPCPs that need close attention (Watkinson, Murbyc & Costanzo 2007) due to the impending threat towards the function of the ecosystem (Costanzo, Murby & Bates 2005). Routine monitoring of the levels of PPCPs released from wastewater treatment plants (WWTPs) is largely neglected by regulatory authorities (Verlicchi, Al Aukidy & Zambello 2012) as the importance of such releases for humans and biota has not been fully established . Increased antibiotics resistance by bacteria and the spread of the antibiotic resistance genes (Gros et al. 2010) are major concerns that warrant complete removal.

2.7.1 Tetracycline antibiotic

Among these antibiotics drug commonly consumed for both human therapy and agricultural purposes over the years is Tetracycline (TC) antibiotics for their antimicrobial activity against a host of bacteria (Mathers, Flick & Cox Jr 2011). This antibiotic is also employed as a food additive to accelerate the growth rate of animals, which is ascribed to their activity, oral availability, low cost. TC production wide world is estimated to be around thousands of tons annually (Michalova, Novotna & Schlegelova 2004). TC has a high molecular weight of (444 g mol^{-1}) with a chemical structure comprising several carbonyls, amino and hydroxyl functional groups as depicted in **Figure 2.4**.

Over the past years, the utilization of TC in the environment has accelerated the wide release of the antibiotic into the ecosystem via water discharges from the manufacture and formulation of drugs, animal farms and disposal of unused or expired pharmaceutical products by accidental release. The release of TC into the environment contaminates the soil and groundwater through leaching and runoff from improper handling by humans and also TC residues can also be found in wastewater treatment plants (Lin, Yu & Lateef 2009). These TC residues found in the TC antibiotics have been detected at concentrations ranging from 0.11 to 4.20 g/L in surface waters. The TC concentrations in effluents from wastewater treatment plants ranged from 46 to 1300 ng/L for tetracycline, 270 to 970 ng/L for chlortetracycline, and 240 ng/L for oxytetracycline (Lin et al. 2009; Gao, Mao, Luo, Wang, Xu & Xu 2012). The TC presence in drinking water has resulted in vomiting, diarrhea, gastrointestinal irritation, and renal failure (Deblonde, Cossu-Leguille & Hartemann 2011). A reduction in bone growth rate can occur from stable calcium complex in bone, due to the absorption of TC into the bones (Thi & Lee 2017). Studies also showed that too much of TC in an animal can impair the development of the fetus (Phillips, Eastwood, Curtis, Gower & De Wardener 1974). The need to develop appropriate, efficient and cost-effective treatment technologies to eliminate the tetracycline antibiotics before releasing to the environment.

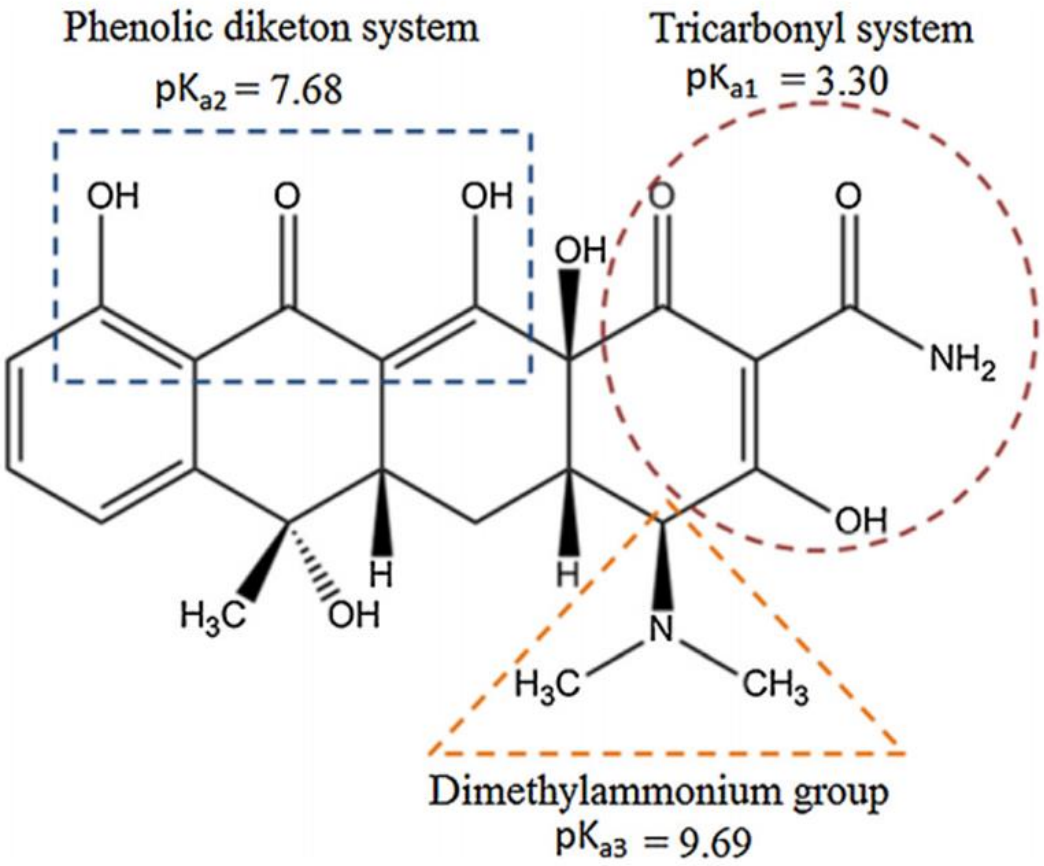

Figure 2.4: Chemical structure of Tetracycline ($C_{22}H_{24}N_2O_8$).

Up till now, various treatment techniques have been applied to remove these antibiotics, which comprises of adsorption (Wu, Li & Hong 2013), photocatalysis (Yan, Wang, Gu, Wu, Yan, Hu, Che, Han, Yang & Fan 2015), microbial decomposition (Gómez-Pacheco, Sánchez-Polo, Rivera-Utrilla & López-Peñalver 2011) electrolysis (Yu, Gao, Lu, Liu, Huo, Liu, Wu & Yan 2013), and membrane separation (Wang, Yuan, Wu, Huang, Peng, Zeng, Zhong, Liang & Ren 2013). According to literature, the most effective treatment for TC wastewater remediation is heterogeneous photocatalysis due to the environmentally friendly and easily handled method for the removal of antibiotics and other organic pollutants from water. In recent years the application of plasmonic Ag/AgBr alone, or in conjunction with other hetero-junction (Z-scheme), Ag/AgBr dispersed on catalyst support as visible light photocatalyst have been employed for oxidation of TC (Chen, Yang, Li, Zeng, Wang, Niu, Zhao, An, Xie & Deng 2017; Rimoldi, Meroni, Cappelletti & Ardizzone 2017; Thi & Lee 2017; Yin, Fang, Luo, Zhang & Shi 2017). The degradation of TC using the plasmonic Ag/AgBr dispersed on the catalyst support showed enhanced degradation within shorter times under visible light irradiation. This case shows that these plasmonic composite have potential to operate in large scale for TC elimination from the ecosystem (Wang, Yang, Zi, Zhou, Ye, Li, Guan, Lv, Huo & Yan 2016; Shi, Lv, Yuan, Huang, Liu & Kang 2017). Also from the HLPC-MS spectra, the detection of less toxic intermediates generated during the TC degradation process using the plasmonic Ag/AgBr was identified (Thi & Lee 2017). The aromatic ring and amino group of cationic and zwitterionic TC were destroyed by the reactive oxidative species such as $\cdot O_2$ and h^+ through the ring-opening reactions and the cleavage of the main carbon bond (Liu, Hou, Xi, Li, Hu & Yu 2016). This shows the potential attributes of the catalyst for antibiotics removal.

Aside from the utilization of the Ag/AgBr catalyst material, other operating factors can also play a role in the photocatalytic degradation of TC in wastewater along with the applied catalyst. These include different light intensity, initial concentration, and catalyst loading, initial pH of the reaction medium and presence of ionic components in solution. The optimization of these factors is also crucial from the angle of an efficient design and the application of the photocatalytic degradation process to enhanced tetracycline removal. Also, the desire for the prepared Ag/AgBr composite to work effectively at low intensity of visible light region. To the best of our knowledge, no investigation has been carried out using AC from pinecone biomass as catalyst support for the dispersion of Ag/AgBr (AABR-ACK). The synthesis of the composite is carried out through thermal polyol, whilst the synthesis parameters model using RSM as an experimental design approach. The most active AABR-ACK photocatalyst from the thermal polyol route, characteristics attribute will be further compared with the AABR-ACK composite prepared through a deposition-precipitation method in this thesis. The prepared composites (Ag/AgBr-ACK) was applied for the degradation of tetracycline antibiotics under low-cost visible light-emitting diode (LED) irradiation, which has not been reported before.

2.8 References

AHMED, M.J. & THEYDAN, S.K. 2013. Microporous activated carbon from Siris seed pods by microwave-induced KOH activation for metronidazole adsorption. *Journal of Analytical and Applied Pyrolysis*, 99, 101-109.

AL-OTHMAN, Z.A., ALI, R. & NAUSHAD, M. 2012. Hexavalent chromium removal from aqueous medium by activated carbon prepared from peanut shell: adsorption kinetics, equilibrium and thermodynamic studies. *Chemical Engineering Journal*, 184, 238-247.

ANASTAS, P.T. & KIRCHHOFF, M.M. 2002. Origins, current status, and future challenges of green chemistry. *Accounts of Chemical Research*, 9, 686-694.

ANTOLINI, E. 2016. Nitrogen-doped carbons by sustainable N-and C-containing natural resources as nonprecious catalysts and catalyst supports for low temperature fuel cells. *Renewable Sustainable Energy Reviews*, 58, 34-51.

ARANA, J., DOÑA-RODRí, J., RENDÓN, E.T., I CABO, C.G., GONZÁLEZ-Dí, O., HERRERA-MELIÁN, J., PÉREZ-PEÑA, J., COLÓN, G. & NAVí, J. 2003. TiO_2 activation by using activated carbon as a support: part I. Surface characterisation and decantability study. *Applied Catalysis B: Environmental*, 2, 161-172.

ARANA, J., MELIÁN, J.H., RODRıGUEZ, J.D., DıAZ, O.G., VIERA, A., PENA, J.P., SOSA, P.M. & JIMÉNEZ, V.E. 2002. TiO_2-photocatalysis as a tertiary treatment of naturally treated wastewater. *Catalysis Today*, 2, 279-289.

ATCHUDAN, R., EDISON, T.N.J.I., PERUMAL, S. & LEE, Y.R. 2017. Green synthesis of nitrogen-doped graphitic carbon sheets with use of Prunus persica for supercapacitor applications. *Applied Surface Science*, 393, 276-286.

AWAZU, K., FUJIMAKI, M., ROCKSTUHL, C., TOMINAGA, J., MURAKAMI, H., OHKI, Y., YOSHIDA, N. & WATANABE, T. 2008. A plasmonic photocatalyst consisting of silver nanoparticles embedded in titanium dioxide. *Journal of the American Chemical Society,* 130, 1676-1680.

AZARGOHAR, R. & DALAI, A. 2006. Biochar as a precursor of activated carbon. *Applied Biochemistry and Biotechnology,* 131, 762-773.

BANDOSZ, T.J. 2006. Activated carbon surfaces in environmental remediation. *7*. Elsevier.

BANKS, J. 1998. Handbook of Simulation: Modelling, Estimation and Control. Wiley & Sons.

BANSAL, R.C. & GOYAL, M. 2005. Activated carbon adsorption. CRC press.

BARZEGAR, F., BELLO, A., DANGBEGNON, J.K., MANYALA, N. & XIA, X. 2017. Asymmetric supercapacitor based on activated expanded graphite and pinecone tree activated carbon with excellent stability. *Applied Energy,* 207, 417-426.

BOBLETER, O. 1994. Hydrothermal degradation of polymers derived from plants. *Progress in Polymer Science,* 19, 797-841.

BOX, G.E. & WILSON, K.B. 1992. On the experimental attainment of optimum conditions. *Breakthroughs in Statistics.* Springer. 270-310.

BUDARIN, V., CLARK, J.H., HARDY, J.J., LUQUE, R., MILKOWSKI, K., TAVENER, S.J. & WILSON, A.J. 2006. Starbons: New starch-derived mesoporous carbonaceous materials with tunable properties. *Angewandte Chemie International Edition,* 45, 3782-3786.

BUDARIN, V.L., CLARK, J.H., LANIGAN, B.A., SHUTTLEWORTH, P., BREEDEN, S.W., WILSON, A.J., MACQUARRIE, D.J., MILKOWSKI, K., JONES, J. & BRIDGEMAN, T. 2009. The preparation of high-grade bio-oils through the controlled, low temperature microwave activation of wheat straw. *Bioresource Technology,* 100, 6064-6068.

BUDARIN, V.L., ZHAO, Y., GRONNOW, M.J., SHUTTLEWORTH, P.S., BREEDEN, S.W., MACQUARRIE, D.J. & CLARK, J.H. 2011. Microwave-mediated pyrolysis of macro-algae. *Green Chemistry,* 13, 2330-2333.

BYRAPPA, K., SUBRAMANI, A., ANANDA, S., RAI, K.L., SUNITHA, M., BASAVALINGU, B. & SOGA, K. 2006. Impregnation of ZnO onto activated carbon under hydrothermal conditions and its photocatalytic properties. *Journal of Materials Science,* 41, 1355-1362.

CAO, Q., XIE, K.-C., LV, Y.-K. & BAO, W.-R. 2006. Process effects on activated carbon with large specific surface area from corn cob. *Bioresource Technology,* 97, 110-115.

CHANDRA, T.C., MIRNA, M., SUDARYANTO, Y. & ISMADJI, S. 2007. Adsorption of basic dye onto activated carbon prepared from durian shell: Studies of adsorption equilibrium and kinetics. *Chemical Engineering Journal,* 127, 121-129.

CHEN, F., YANG, Q., LI, X., ZENG, G., WANG, D., NIU, C., ZHAO, J., AN, H., XIE, T. & DENG, Y. 2017. Hierarchical assembly of graphene-bridged Ag_3PO_4/Ag/$BiVO_4$ (040) Z-scheme photocatalyst: An efficient, sustainable and heterogeneous catalyst with enhanced visible-light photoactivity towards tetracycline degradation under visible light irradiation. *Applied Catalysis B: Environmental,* 200, 330-342.

CHEN, G., LI, F., HUANG, Z., GUO, C.-Y., QIAO, H., QIU, X., WANG, Z., JIANG, W. & YUAN, G. 2015. Facile synthesis of Ag/AgBr/RGO nanocomposite as a highly efficient sunlight plasmonic photocatalyst. *Catalysis Communications,* 59, 140-144.

CHEN, X., SU, B., WU, G., YANG, C.J., ZHUANG, Z., WANG, X. & CHEN, X. 2012. Platinum nanoflowers supported on graphene oxide nanosheets: their green synthesis, growth mechanism, and advanced electrocatalytic properties for methanol oxidation. *Journal of Materials Chemistry,* 22, 11284-11289.

CHEN, X., WANG, X. & FU, X. 2009. Hierarchical macro/mesoporous TiO_2/SiO_2 and TiO_2/ZrO_2 nanocomposites for environmental photocatalysis. *Energy Environmental Science and Technology,* 2, 872-877.

CHOI, W.S., BYUN, G.Y., BAE, T.S. & LEE, H.-J. 2013. Evolution of AgX Nanowires into Ag Derivative Nano/microtubes for Highly Efficient Visible-Light Photocatalysts. *ACS Applied Materials and Interfaces,* 5, 11225-11233.

CHONG, M.N., JIN, B., CHOW, C.W. & SAINT, C. 2010. Recent developments in photocatalytic water treatment technology: a review. *Water Research,* 44, 2997-3027.

COSTANZO, S.D., MURBY, J. & BATES, J. 2005. Ecosystem response to antibiotics entering the aquatic environment. *Marine Pollution Bulletin,* 51, 218–223.

DAUGHTON, C.G. & TERNES, T. 1999. Pharmaceuticals and personal care products in the environment: agents of subtle change? *Environmental Health Perspectives,* 107, 907–938.

DEBLONDE, T., COSSU-LEGUILLE, C. & HARTEMANN, P. 2011. Emerging pollutants in wastewater: a review of the literature. *International Journal of Hygiene and Environmental Health,* 214, 442-448.

DEMIR, M., KAHVECI, Z., AKSOY, B., PALAPATI, N.K., SUBRAMANIAN, A., CULLINAN, H.T., EL-KADERI, H.M., HARRIS, C.T. & GUPTA, R.B. 2015. Graphitic biocarbon from metal-catalyzed hydrothermal carbonization of lignin. *Industrial Engineering Chemistry Research,* 54, 10731-10739.

DENG, H., LI, G., YANG, H., TANG, J. & TANG, J. 2010. Preparation of activated carbons from cotton stalk by microwave assisted KOH and K_2CO_3 activation. *Chemical Engineering Journal,* 163, 373-381.

DEVI, L.G., KOTTAM, N., MURTHY, B.N. & KUMAR, S.G. 2010. Enhanced photocatalytic activity of transition metal ions Mn^{2+}, Ni^{2+} and Zn^{2+} doped polycrystalline titania for the degradation of Aniline Blue under UV/solar light. *Journal of Molecular Catalysis A: Chemical,* 328, 44-52.

DEVI, L.G., MURTHY, B.N. & KUMAR, S.G. 2010. Photocatalytic activity of TiO_2 doped with Zn^{2+} and V^{5+} transition metal ions: influence of crystallite size and dopant electronic configuration on photocatalytic activity. *Materials Science and Engineering: B,* 166, 1-6.

DIAZ-CRUZ, M.S., LOPEZ DE ALDA, M.J. & BARCELO, D. 2003. Environmental behavior and analysis of veterinary and human drugs in soils, sediments and sludge. *Trends in Analytical Chemistry,* 22, 340-351.

DIETZ, A.A. 1944. Distribution of bone marrow, bone, and bone-ash in rabbits. *Proceedings of the Society for Experimental Biology and Medicine,* 57, 60-62.

DONG, T., GAO, D., MIAO, C., YU, X., DEGAN, C., GARCIA-PÉREZ, M., RASCO, B., SABLANI, S.S. & CHEN, S. 2015. Two-step microalgal biodiesel production using acidic catalyst generated from pyrolysis-derived bio-char. *Energy Conversion Management,* 105, 1389-1396.

DUMAN, G., ONAL, Y., OKUTUCU, C., ONENC, S. & YANIK, J. 2009. Production of activated carbon from pinecone and evaluation of its physical, chemical, and adsorption properties. *Energy and Fuels,* 23, 2197-2204.

EFFTAXIAS, A. 2002. Catalytic Wet Air Oxidation of Phenol in a Trickle Bed Reactor: Kinetics and Reactor Modeling. *Ph. D. Thesis, Universitat Rovirai Virgili.*

ERLANGER, T.E., KEISER, J., DE CASTRO, M.C., BOS, R., SINGER, B.H., TANNER, M. & UTZINGER, J. 2005. Effect of water resource development and management on lymphatic

filariasis, and estimates of populations at risk. *The American Journal of Tropical Medicine and Hygiene,* 73, 523-533.

ESMAEILI, A. & ENTEZARI, M.H. 2016. Sonosynthesis of an Ag/AgBr/Graphene-oxide nanocomposite as a solar photocatalyst for efficient degradation of methyl orange. *Journal of Colloid and Interface Science,* 466, 227-237.

ESPINOSA, J.C., MANICKAM-PERIYARAMAN, P., BERNAT-QUESADA, F., SIVANESAN, S., ÁLVARO, M., GARCÍA, H. & NAVALÓN, S. 2019. Engineering of activated carbon surface to enhance the catalytic activity of supported cobalt oxide nanoparticles in peroxymonosulfate activation. *Applied Catalysis B: Environmental,* 249, 42-53.

EVERETT, D. 1972. Manual of symbols and terminology for physicochemical quantities and units, appendix II: Definitions, terminology and symbols in colloid and surface chemistry. *Pure and Applied Chemistry*, 31, 577-638.

FAN, H., ZHAO, X., YANG, J., SHAN, X., YANG, L., ZHANG, Y., LI, X. & GAO, M. 2012. ZnO-graphene composite for photocatalytic degradation of methylene blue dye. *Catalysis Communications,* 29, 29–34.

FERNÁNDEZ, Y., ARENILLAS, A., BERMÚDEZ, J.M. & MENÉNDEZ, J. 2010. Comparative study of conventional and microwave-assisted pyrolysis, steam and dry reforming of glycerol for syngas production, using a carbonaceous catalyst. *Journal of Analytical and Applied Pyrolysis,* 88, 155-159.

FOO, K. & HAMEED, B. 2011. Preparation of oil palm (Elaeis) empty fruit bunch activated carbon by microwave-assisted KOH activation for the adsorption of methylene blue. *Desalination,* 275, 302-305.

FOO, K.Y. & HAMEED, B.H. 2012. Microwave-assisted preparation and adsorption performance of activated carbon from biodiesel industry solid reside: Influence of operational parameters. *Bioresource Technology,* 103, 398-404.

FORSTER, C.F. 1985. Biotechnology and wastewater treatment. Cambridge University Press.

FRACZEK-SZCZYPTA, A. 2014. Carbon nanomaterials for nerve tissue stimulation and regeneration. *Materials Science and Engineering: C,* 34, 35-49.

FU, X., LI, D., CHEN, J., ZHANG, Y., HUANG, W., ZHU, Y., YANG, J. & ZHANG, C. 2013. A microalgae residue based carbon solid acid catalyst for biodiesel production. *Bioresource Technology,* 146, 767-770.

FUJISHIMA, A., RAO, T.N. & TRYK, D.A. 2000. Titanium dioxide photocatalysis. *Journal of Photochemistry and Photobiology C: Photochemistry Reviews,* 1, 1-21.

FUJISHIMA, A., ZHANG, X. & TRYK, D.A. 2008. TiO_2 photocatalysis and related surface phenomena. *Surface Science Reports,* 63, 515-582.

GAO, L., SUN, L., WAN, S., YU, Z. & LI, M. 2013. Degradation kinetics and mechanism of emerging contaminants in water by dielectric barrier discharge non-thermal plasma: The case of 17β-Estradiol. *Chemical Engineering Journal,* 228, 790-798.

GAO, P., MAO, D., LUO, Y., WANG, L., XU, B. & XU, L. 2012. Occurrence of sulfonamide and tetracycline-resistant bacteria and resistance genes in aquaculture environment. *Water Research,* 46, 2355-2364.

GIMBA, C., SALIHU, A.A., KAGBU, J., TUROTI, M., ITODO, A. & SARIYYA, A. 2010. Study of pesticide (Dichlorvos) removal from aqueous medium by Arachis hypogaea (groundnut shell) using GC/MS. *World Rural Observations* 2, 1-9.

GIRALDO, L. & MORENO-PIRAJÁN, J.C. 2012. Synthesis of activated carbon mesoporous from coffee waste and its application in adsorption zinc and mercury ions from aqueous solution. *Journal of Chemistry,* 9, 938-948.

GÓMEZ-PACHECO, C., SÁNCHEZ-POLO, M., RIVERA-UTRILLA, J. & LÓPEZ-PEÑALVER, J. 2011. Tetracycline removal from waters by integrated technologies based on ozonation and biodegradation. *Chemical Engineering Journal,* 178, 115-121.

GROS, M., PETROVIC´, M., GINEBREDA, A. & BARCELÓ, D. 2010. Removal of pharmaceuticals during wastewater treatment and environmental risk assessment using hazard index. *Environment International,* 36, 15–26.

GUAN, Y., WANG, S., WANG, X., SUN, C., HUANG, Y., LIU, C. & ZHAO, H. 2017. In situ self-assembled synthesis of Ag-AgBr/Al-MCM-41 with excellent activities of adsorption-photocatalysis. *Applied Catalysis B: Environmental,* 209, 329-338.

GUESH, K., MÁRQUEZ-ÁLVAREZ, C., CHEBUDE, Y. & DÍAZ, I. 2016. Enhanced photocatalytic activity of supported TiO_2 by selective surface modification of zeolite Y. *Applied Surface Science,* 378, 473-478.

GUNST, R.F. 1996. Response surface methodology: process and product optimization using designed experiments. *Technometrics,* 38, 284-286.

DENG, H., LI, G. X., YAN, H. B., TANG, J. P. &. TANG, J. G. 2010. Preparation of activated carbons from cotton stalk by microwave assisted KOH and K_2CO_3 activation. *Chemical Engineering Journal,* 163, 373-381.

HAYKIRI-ACMA, H. & YAMAN, S. 2007. Interpretation of biomass gasification yields regarding temperature intervals under nitrogen–steam atmosphere. *Fuel Processing Technology,* 88, 417-425.

HAMEED, B. & DAUD, F. 2008. Adsorption studies of basic dye on activated carbon derived from agricultural waste: Hevea brasiliensis seed coat. *Chemical Engineering Journal,* 139, 48-55.

HAMIDIN, N., YU, Q.J. & CONNELL, D.W. 2008. Human health risk assessment of chlorinated disinfection by-products in drinking water using a probabilistic approach. *Water Research,* 42, 3263-3274.

HAYASHI, J.I., KAZEHAYA, A., MUROYAMA, K. & WATKINSON, A.P. 2000. Preparation of activated carbon from lignin by chemical activation. *Carbon,* 38, 1873-1878.

HIRSCH, R., TERNES, T., HABERER, K. & KRATZ, K.L. 1999. Occurrence of antibiotics in the aquatic environment. *Science of the Total Environment* 225, 109-118.

HOU, J., WANG, Z., YANG, C., ZHOU, W., JIAO, S. & ZHU, H. 2013. Hierarchically plasmonic Z-scheme photocatalyst of Ag/AgCl nanocrystals decorated mesoporous single-crystalline metastable $Bi_{20}TiO_{32}$ nanosheets. *The Journal of Physical Chemistry C,* 117, 5132-5141.

HRUDEY, S.E. 2009. Chlorination disinfection by-products, public health risk tradeoffs and me. *Water Research,* 43, 2057-2092.

HU, C., LAN, Y., QU, J., HU, X. & WANG, A. 2006. $Ag/AgBr/TiO_2$ visible light photocatalyst for destruction of azodyes and bacteria. *The Journal of Physical Chemistry B,* 110, 4066-4072.

HU, C., PENG, T., HU, X., NIE, Y., ZHOU, X., QU, J. & HE, H. 2009. Plasmon-induced photodegradation of toxic pollutants with $Ag- AgI/Al_2O_3$ under visible-light irradiation. *Journal of the American Chemical Society,* 132, 857-862.

HUANG, Y.F., KUAN, W., LO, S. & LIN, C. 2008. Total recovery of resources and energy from rice straw using microwave-induced pyrolysis. *Bioresource Technology,* 99, 8252-8258.

JELIC´, A., PETROVIC´, M. & BARCELÓ, D. 2009. Multi-residue method for trace level determination of pharmaceuticals in solid samples using pressurized liquid extraction followed by liquid chromatography/quadrupole-linear ion trap mass spectrometry. *Talanta,* 80, 363–371.

JI, T., CHEN, L., MU, L., YUAN, R., KNOBLAUCH, M., BAO, F.S., SHI, Y., WANG, H. & ZHU, J. 2016. Green processing of plant biomass into mesoporous carbon as catalyst support. *Chemical Engineering Journal,* 295, 301-308.

JIANG, L., YUAN, X., ZENG, G., LIANG, J., CHEN, X., YU, H., WANG, H., WU, Z., ZHANG, J. & XIONG, T. 2018. In-situ synthesis of direct solid-state dual Z-scheme WO_3/g-C_3N_4/Bi_2O_3 photocatalyst for the degradation of refractory pollutant. *Applied Catalysis B: Environmental,* 227, 376-385.

JIANG, Z., ZHANG, X., YUAN, Z., CHEN, J., HUANG, B., DIONYSIOU, D.D. & YANG, G. 2018. Enhanced photocatalytic CO_2 reduction via the synergistic effect between Ag and activated carbon in TiO_2/AC-Ag ternary composite. *Chemical Engineering Journal,* 348, 592-598.

JONES, M.R., OSBERG, K.D., MACFARLANE, R.J., LANGILLE, M.R. & MIRKIN, C.A. 2011. Templated techniques for the synthesis and assembly of plasmonic nanostructures. *Chemical Reviews,* 111, 3736-3827.

KAATZE, U. & HÜBNER, C. 2010. Electromagnetic techniques for moisture content determination of materials. *Measurement Science and Technology,* 21 082001.

KAUR, B., GUPTA, R.K. & BHUNIA, H. 2019. Chemically activated nanoporous carbon adsorbents from waste plastic for CO_2 capture: Breakthrough adsorption study. *Microporous Mesoporous Materials,* 282, 146-158.

KOLPIN, D.W., FURLONG, E.T., MEYER, M.T., THURMAN, E.M., ZAUGG, S.D., BARBER, L.B. & BUXTON, H.T. 2002. Pharmaceuticals, hormones, and other organics waste water

contaminants in U.S. streams, 1999–2000: a national reconnaissance. *Environmental Science and Technology,* 36, 1202–1211.

KUMAR, J., MALLAMPATI, R., ADIN, A. & VALIYAVEETTIL, S. 2014. Functionalized carbon spheres for extraction of nanoparticles and catalyst support in water. *ACS Sustainable Chemistry Engineering,* 2, 2675-2682.

KUMMERER, K. 2003. Significance of antibiotics in the environment. *Journal of Antimicrobial Chemotherapy,* 52, 5-7.

KÜMMERER, K. 2008. Pharmaceuticals in the Environment: Sources, Fate and Risks. *Springer-Verlag, Berlin, Heidelberg.*

KUNDU, A., GUPTA, B.S., HASHIM, M., SAHU, J., MUJAWAR, M. & REDZWAN, G. 2015. Optimisation of the process variables in production of activated carbon by microwave heating. *RSC Advances,* 5, 35899-35908.

KYOTANI, T. 2000. Control of pore structure in carbon. *Carbon,* 38, 269-286.

L. W. MUNIANDY, F. ADAMA, A. R. MOHAMED & E. POHNG. 2014. The synthesis and characterization of high purity mixed microporous/mesoporous activated carbon from rice husk using chemical activation with NaOH and KOH. *Microporous and Mesoporous Materials,* 197, 316-323.

LAM, E. & LUONG, J.H.T. 2014. Carbon Materials as Catalyst Supports and Catalysts in the Transformation of Biomass to Fuels and Chemicals. *ACS Catalysis,* 4, 3393−3410.

LAM, S.S., LIEW, R.K., WONG, Y.M., AZWAR, E., JUSOH, A. & WAHI, R. 2017a. Activated carbon for catalyst support from microwave pyrolysis of orange peel. *Waste Biomass Valorization* 8, 2109-2119.

LAM, S.S., LIEW, R.K., WONG, Y.M., YEK, P.N.Y., MA, N.L., LEE, C.L. & CHASE, H.A. 2017b. Microwave-assisted pyrolysis with chemical activation, an innovative method to convert orange peel into activated carbon with improved properties as dye adsorbent. *Journal of Cleaner Production,* 162, 1376-1387.

LAPWORTH, D., BARAN, N., STUART, M. & WARD, R. 2012. Emerging organic contaminants in groundwater: a review of sources, fate and occurrence. *Environmental Pollution,* 163, 287-303.

LEARY, R. & WESTWOOD, A. 2011. Carbonaceous nanomaterials for the enhancement of TiO_2 photocatalysis. *Carbon,* 49, 741-772.

LEE, K., KIM, M. & KIM, H. 2010. Catalytic nanoparticles being facet-controlled. *Journal of Materials Chemistry,* 20, 3791-3798.

LEI, H., REN, S. & JULSON, J. 2009. The effects of reaction temperature and time and particle size of corn stover on microwave pyrolysis. *Energy & Fuels,* 23, 3254-3261.

LEI, X., WANG, M., LAI, Y., HU, L., WANG, H., FANG, Z., LI, J. & FANG, J. 2017. Nitrogen-doped micropore-dominant carbon derived from waste pinecone as a promising metal-free electrocatalyst for aqueous zinc/air batteries. *Journal of Power Sources,* 365, 76-82.

LI, J., LIU, W., XIAO, D. & WANG, X. 2017. Oxygen-rich hierarchical porous carbon made from pomelo peel fiber as electrode material for supercapacitor. *Applied Surface Science,* 416, 918-924.

LI, Y. & DING, Y. 2010. Porous AgCl/Ag nanocomposites with enhanced visible light photocatalytic properties. *The Journal of Physical Chemistry C,* 114, 3175-3179.

LI, Y., LI, X., LI, J. & YIN, J. 2006. Photocatalytic degradation of methyl orange by TiO_2-coated activated carbon and kinetic study. *Water Research,* 40, 1119-1126.

LI, Y., SAMAD, Y.A., POLYCHRONOPOULOU, K., ALHASSAN, S.M. & LIAO, K. 2014. From biomass to high performance solar–thermal and electric–thermal energy conversion and storage materials. *Journal of Materials Chemistry A,* 2, 7759-7765.

LIEW, R.K., CHONG, M.Y., OSAZUWA, O.U., NAM, W.L., PHANG, X.Y., SU, M.H., CHENG, C.K., CHONG, C.T. & LAM, S.S. 2018. Production of activated carbon as catalyst support by microwave pyrolysis of palm kernel shell: a comparative study of chemical versus physical activation. *Research on Chemical Intermediates,* 44, 3849-3865.

LIN, A.Y.-C., YU, T.-H. & LATEEF, S.K. 2009. Removal of pharmaceuticals in secondary wastewater treatment processes in Taiwan. *Journal of Hazardous Materials,* 167, 1163-1169.

LINIC, S., CHRISTOPHER, P. & INGRAM, D.B. 2011. Plasmonic-metal nanostructures for efficient conversion of solar to chemical energy. *Nature Materials,* 10, 911.

LIU, B., NAKATA, K., ZHAO, X., OCHIAI, T., MURAKAMI, T. & FUJISHIMA, A. 2011. Theoretical kinetic analysis of heterogeneous photocatalysis: the effects of surface trapping and bulk recombination through defects. *The Journal of Physical Chemistry C,* 115, 16037-16042.

LIU, M., HOU, L.-A., XI, B.-D., LI, Q., HU, X. & YU, S. 2016. Magnetically separable Ag/AgCl-zero valent iron particles modified zeolite X heterogeneous photocatalysts for tetracycline degradation under visible light. *Chemical Engineering Journal,* 302, 475-484.

LIU, S.X., CHEN, X.Y. & CHEN, X. 2007. A TiO2/AC composite photocatalyst with high activity and easy separation prepared by a hydrothermal method. *Journal of Hazardous Materials,* 143, 257–263.

LIU, X., LIU, X., SUN, B., ZHOU, H., FU, A., WANG, Y., GUO, Y.-G., GUO, P. & LI, H. 2018. Carbon materials with hierarchical porosity: Effect of template removal strategy and study on their electrochemical properties. *Carbon,* 130, 680-691.

LONG, C., CHEN, X., JIANG, L., ZHI, L. & FAN, Z. 2015. Porous layer-stacking carbon derived from in-built template in biomass for high volumetric performance supercapacitors. *Nano Energy,* 12, 141-151.

LOU, Z., HUANG, B., QIN, X., ZHANG, X., CHENG, H., LIU, Y., WANG, S., WANG, J. & DAI, Y. 2012. One-step synthesis of AgCl concave cubes by preferential overgrowth along< 111> and< 110> directions. *Chemical Communications,* 48, 3488-3490.

LU, J., HU, H., YANG, S., SHANMUGAM, P., WEI, W., SELVARAJ, M. & XIE, J. 2018. ZnS@carbonaceous aerogel composites fabricated in production of hydrogen and for removal of organic pollutants. *Journal of Materials Science: Materials in Electronics,* 29, 8523-8534.

M. KıLıÇ, E. APAYDıN-VAROL & A. E. PÜTÜN. 2010. Preparation and surface characterization of activated carbons from Euphorbia rigida by chemical activation with $ZnCl_2$, K_2CO_3, NaOH and H_3PO_4. *Applied Surface Science,* 261, 247-254.

MACHEK, V., HANIKA, J., SPORKA, K., RŮŽIČKA, V. & KUNZ, J. 1981. Relation between the distribution of platinum, its dispersion, and activity of catalysts prepared by impregnation of activated carbon with chloroplatinic acid solutions. *Collection of Czechoslovak Chemical Communications,* 46, 3270– 3277.

MADEJOVA, J. 2003. FTIR techniques in clay mineral studies. *Vibrational Spectroscopy,* 1-10.

MALDONADO, M., PASSARINHO, P., OLLER, I., GERNJAK, W., FERNÁNDEZ, P., BLANCO, J. & MALATO, S. 2007. Photocatalytic degradation of EU priority substances: a comparison between TiO_2 and Fenton plus photo-Fenton in a solar pilot plant. *Journal of Photochemistry and Photobiology A: Chemistry,* 185, 354-363.

MARSH, H. & REINOSO, F.R. 2006. *Activated carbon.* Elsevier.

MARSH, H. & RODRÍGUEZ-REINOSO, F. 2006. CHAPTER 2-Activated Carbon (Origins). *Activated Carbon,* 13-86.

MATHERS, J.J., FLICK, S.C. & COX JR, L.A. 2011. Longer-duration uses of tetracyclines and penicillins in US food-producing animals: indications and microbiologic effects. *Environment International,* 37, 991-1004.

MATOS, J., LAINE, J. & HERMANN, J.M. 1998. Synergy effect in the photocatalytic degradation of phenol on a suspended mixture of titania and activated carbon. *Applied Catalysis B: Environmental,* 18, 281–291.

MATOS, J., LAINE, J., HERRMANN, J.M., UZCATEGUI, D. & BRITO, J.L. 2006. Influence of activated carbon upon titania on aqueous photocatalytic consecutive runs of phenol photomineralization. *Applied Catalysis B: Environmental,* 70, 461–469.

MCENANEY, B. 2002. Handbook of Porous Solids. Wiley-VCH Verlag GmbH, Weinheim, Germany.

MCEVOY, J.G., CUI, W. & ZHANG, Z. 2014. Synthesis and characterization of Ag/AgCl–activated carbon composites for enhanced visible light photocatalysis. *Applied Catalysis B: Environmental,* 144, 702-712.

MCEVOY, J.G. & ZHANG, Z. 2014. Synthesis and characterization of magnetically separable Ag/AgCl–magnetic activated carbon composites for visible light induced photocatalytic detoxification and disinfection. *Applied Catalysis B: Environmental,* 160, 267-278.

MCEVOY, J.G. & ZHANG, Z. 2016. Synthesis and characterization of Ag/AgBr–activated carbon composites for visible light induced photocatalytic detoxification and disinfection. *Journal of Photochemistry Photobiology A: Chemistry,* 321, 161-170.

MENÉNDEZ, J., DOMıNGUEZ, A., INGUANZO, M. & PIS, J. 2004. Microwave pyrolysis of sewage sludge: analysis of the gas fraction. *Journal of Analytical and Applied Pyrolysis,* 71, 657-667.

MICHALOVA, E., NOVOTNA, P. & SCHLEGELOVA, J. 2004. Tetracyclines in veterinary medicine and bacterial resistance to them. *Veterinarni Medicina-Praha-,* 49, 79-100.

MIURA, M., KAGA, H., SAKURAI, A., KAKUCHI, T. & TAKAHASHI, K. 2004. Rapid pyrolysis of wood block by microwave heating. *Journal of Analytical and Applied Pyrolysis,* 71, 187-199.

MOHAMMED, A.A., CHEN, C. & ZHU, Z. 2019. Low-cost, high-performance supercapacitor based on activated carbon electrode materials derived from baobab fruit shells. *Journal of Colloid Interface Science,* 538, 308-319.

MOHAMMED, A.A., CHEN, C., ZHU, Z.J.J.O.C. & SCIENCE, I. 2019. Low-cost, high-performance supercapacitor based on activated carbon electrode materials derived from baobab fruit shells. *Journal of Colloid and Interface Science*, 538, 308-319.

MOHAMMED, J., NASRI, N.S., ZAINI, M.A.A., HAMZA, U.D. & ANI, F.N. 2015. Adsorption of benzene and toluene onto KOH activated coconut shell based carbon treated with NH_3. *International Biodeterioration Biodegradation,* 102, 245-255.

MOLINA-SABIO, M. & RODRıGUEZ-REINOSO, F. 2004. Role of chemical activation in the development of carbon porosity. *Colloids and Surfaces A: Physicochemical and Engineering Aspects,* 241, 15-25.

MOMODU, D., OKAFOR, C., MANYALA, N., BELLO, A., ZEBAZEKANA, M.G. & NTSOENZOK, E. 2019. Transformation of Plant Biomass Waste into Resourceful Activated

Carbon Nanostructures for Mixed-Assembly Type Electrochemical Capacitors. *Waste Biomass Valorization,* 10, 1741-1753.

MOZIA, S. & MORAWSKI, A.W. 2012. The performance of a hybrid photocatalysis–MD system for the treatment of tap water contaminated with ibuprofen. *Catalysis Today,* 193, 213-220.

MUBARAK, N., SAHU, J., ABDULLAH, E. & JAYAKUMAR, N. 2014. Removal of heavy metals from wastewater using carbon nanotubes. *Separation and Purification Reviews,* 43, 311-338.

NAITO, K., TACHIKAWA, T., FUJITSUKA, M. & MAJIMA, T. 2008. Single-molecule observation of photocatalytic reaction in TiO_2 nanotube: importance of molecular transport through porous structures. *Journal of the American Chemical Society,* 131, 934-936.

NANDA, S., GONG, M., HUNTER, H.N., DALAI, A.K., GÖKALP, I. & KOZINSKI, J.A. 2017. An assessment of pinecone gasification in subcritical, near-critical and supercritical water. *Fuel Processing Technology,* 168, 84-96.

NG, C.H.B. & FAN, W.Y. 2007. Controlled synthesis of β-AgI nanoplatelets from selective nucleation of twinned Ag seeds in a tandem reaction. *The Journal of Physical Chemistry C,* 111, 2953-2958.

NOOR, A.B.M. & NAWI, M.A.B.M. 2008. Textural characteristics of activated carbons prepared from oil palm shells activated with $ZnCl_2$ and pyrolysis under nitrogen and carbon dioxide. *Journal of Physical Science,* 19, 93-104.

OFOMAJA, A. & NAIDOO, E. 2011. Biosorption of copper from aqueous solution by chemically activated pinecone: a kinetic study. *Chemical Engineering Journal,* 175, 260-270.

OULTON, R.L., KOHN, T. & CWIERTNY, D.M. 2010. Pharmaceuticals and personal care products in effluent matrices: a survey of transformation and removal during wastewater treatment

and implications for wastewater management. *Journal of Environmental Monitoring,* 12, 1956-1978.

PENG, L., LIANG, Y., DONG, H., HU, H., ZHAO, X., CAI, Y., XIAO, Y., LIU, Y. & ZHENG, M. 2018. Super-hierarchical porous carbons derived from mixed biomass wastes by a stepwise removal strategy for high-performance supercapacitors. *Journal of Power Sources,* 377, 151-160.

PHILLIPS, M., EASTWOOD, J., CURTIS, J., GOWER, P. & DE WARDENER, H. 1974. Tetracycline poisoning in renal failure. *British Medical Journal,* 2, 149-151.

POONJARERNSILP, C., SANO, N. & TAMON, H. 2014. Hydrothermally sulfonated single-walled carbon nanohorns for use as solid catalysts in biodiesel production by esterification of palmitic acid. *Applied Catalysis B: Environmental,* 147, 726-732.

PRAHAS, D., KARTIKA, Y., INDRASWATI, N. & ISMADJI, S. 2008. Activated carbon from Jack fruit peel waste by H_3PO_4 chemical activation: pore structure and surface chemistry characterization. *Chemical Engineering Journal,* 140, 32-42.

PRZEPIÓRSKI, J. 2006. Activated carbon filters and their industrial applications. *Interface Science and Technology,* 7, 421-474.

PUMA, G.L., BONO, A., KRISHNAIAH, D. & COLLIN, J.G. 2008. Preparation of titanium dioxide photocatalyst loaded onto activated carbon support using chemical vapor deposition: a review paper. *Journal of Hazardous Materials,* 157, 209-219.

PUZIY, A., PODDUBNAYA, O., MARTıNEZ-ALONSO, A., SUÁREZ-GARCıA, F. & TASCÓN, J. 2002. Synthetic carbons activated with phosphoric acid: I. Surface chemistry and ion binding properties. *Carbon,* 40, 1493-1505.

RAZA, W., ALI, F., RAZA, N., LUO, Y., KWON, E.E., YANG, J., KUMAR, S., MEHMOOD, A. & KIM, K.-H. 2018. Recent advancements in supercapacitor technology. *Nano Energy,* 52, 441-473.

RIMOLDI, L., MERONI, D., CAPPELLETTI, G. & ARDIZZONE, S. 2017. Green and low cost tetracycline degradation processes by nanometric and immobilized TiO_2 systems. *Catalysis Today,* 281, 38-44.

ROBAU-SÁNCHEZ, A., AGUILAR-ELGUÉZABAL, A. & AGUILAR-PLIEGO, J. 2005. Chemical activation of Quercus agrifolia char using KOH: evidence of cyanide presence. *Microporous and Mesoporous Materials,* 85, 331-339.

RODRıGUES-REINOSO, F., HEINTZ, E. & MARSH, H. 1997. Introduction to carbon technologies. *Publicaciones de la Universidad de Alicante, Spain.*

RODRÍGUEZ-REINOSO, F. 1997. Activated carbon: structure, characterization, preparation and applications. *Introduction to Carbon Technologies,* 35, 291–297.

RODRıGUEZ-REINOSO, F. & MOLINA-SABIO, M. 1998. Textural and chemical characterization of microporous carbons. *Advances in Colloid and Interface Science,* 76, 271-294.

RODRÍGUEZ-REINOSO, F. 2002. Production and applications of activated carbons. *Handbook of Porous Solids,* 1766-1827.

RODRIGUEZ, J.A. & FERNÁNDEZ-GARCÍA, M. 2007. Synthesis, properties, and applications of oxide nanomaterials. John Wiley and Sons.

SENTORUN-SHALABY, Ç., UÇAK-ASTARLıOGLU, M.G., ARTOK, L. & SARıCı, Ç. 2006. Preparation and characterization of activated carbons by one-step steam pyrolysis/activation from apricot stones. *Microporous and Mesoporous Materials,* 88, 126-134.

SHAH, J., JAN, M.R., MABOOD, F. & SHAHID, M. 2006. Conversion of waste tyres into carbon black and their utilization as adsorbent. *Journal of the Chinese Chemical Society,* 53, 1085-1089.

SHEN, J., HUANG, G., AN, C., XIN, X., HUANG, C. & ROSENDAHL, S. 2018. Removal of Tetrabromobisphenol A by adsorption on pinecone-derived activated charcoals: Synchrotron FTIR, kinetics and surface functionality analyses. *Bioresource technology,* 247, 812-820.

SHI, W., LV, H., YUAN, S., HUANG, H., LIU, Y. & KANG, Z. 2017. Near-infrared light photocatalytic ability for degradation of tetracycline using carbon dots modified Ag/AgBr nanocomposites. *Separation and Purification Technology,* 174, 75-83.

SINGH, Y.D., MAHANTA, P. & BORA, U. 2017. Comprehensive characterization of lignocellulosic biomass through proximate, ultimate and compositional analysis for bioenergy production. *Renewable Energy,* 103, 490-500.

SLIMEN, H., HOUAS, A. & NOGIER, J.P. 2011. Elaboration of stable anatase TiO_2 through activated carbon addition with high photocatalytic activity under visiblelight. *Journal of Photochemistry and Photobiology A: Chemistry,* 221, 13-21.

SOBANA, N., MURUGANANDAM, M. & SWAMINATHAN, M. 2008. Characterization of AC–ZnO catalyst and its photocatalytic activity on 4-acetylphenol degradation. *Catalysis Communications,* 9, 262-268.

SOPYAN, I., WATANABE, M., MURASAWA, S., HASHIMOTO, K. & FUJISHIMA, A. 1996. An efficient TiO_2 thin-film photocatalyst: photocatalytic properties in gas-phase acetaldehyde degradation. *Journal of Photochemistry and Photobiology A: Chemistry,* 98, 79-86.

SUN, J., NIU, J., LIU, M., JI, J., DOU, M. & WANG, F. 2018. Biomass-derived nitrogen-doped porous carbons with tailored hierarchical porosity and high specific surface area for high energy and power density supercapacitors. *Applied Surface Science,* 427, 807-813.

SUN, L., ZHANG, Y., YE, X., LIU, H., ZHANG, H., WU, A. & WU, Z. 2017. Removal of I– from aqueous solutions using a biomass carbonaceous aerogel modified with KH-560. *ACS Sustainable Chemistry Engineering,* 5, 7700-7708.

SZILÁGYI, I.M., FÓRIZS, B., ROSSELER, O., SZEGEDI, Á., NÉMETH, P., KIRÁLY, P., TÁRKÁNYI, G., VAJNA, B., VARGA-JOSEPOVITS, K. & LÁSZLÓ, K. 2012. WO_3 photocatalysts: influence of structure and composition. *Journal of Catalysis,* 294, 119-127.

TAKEBA, K., MATSUMOTO, M., SHIDA, Y. & NAKAZAWA, H. 1990. Determination of phenol in honey by liquid chromatography with amperometric detection. *Journal-Association of Official Analytical Chemists,* 73, 602-604.

TAN, I., AHMAD, A. & HAMEED, B. 2008. Preparation of activated carbon from coconut husk: optimization study on removal of 2, 4, 6-trichlorophenol using response surface methodology. *Journal of Hazardous Materials,* 153, 709-717.

TANG, Y.-B., LIU, Q. & CHEN, F.-Y. 2012. Preparation and characterization of activated carbon from waste ramulus mori. *Chemical Engineering Journal,* 203 19-24.

TAWALBEH, M., ALLAWZI, M.A. & KANDAH, M.I. 2005. Production of Activated Carbon from Jojoba Seed Residue by Chemical Activation Residue Using a Static Bed Reactor. *Journal of Applied Sciences,* 5, 482-487.

THI, V.H.T. & LEE, B.-K. 2017. Great improvement on tetracycline removal using ZnO rod-activated carbon fiber composite prepared with a facile microwave method. *Journal of Hazardous Materials,* 324, 329-339.

THOMMES, M., KANEKO, K., NEIMARK, A.V., OLIVIER, J.P., RODRIGUEZ-REINOSO, F., ROUQUEROL, J. & SING, K.S. 2015. Physisorption of gases, with special reference to the

evaluation of surface area and pore size distribution (IUPAC Technical Report). *Pure Applied Chemistry,* 87, 1051-1069.

TIAN, C., ZHANG, Q., WU, A., JIANG, M., LIANG, Z., JIANG, B. & FU, H. 2012. Cost-effective large-scale synthesis of ZnO photocatalyst with excellent performance for dye photodegradation. *Chemical Communications,* 48, 2858-2860.

TIAN, Y. & TATSUMA, T. 2005. Mechanisms and applications of plasmon-induced charge separation at TiO_2 films loaded with gold nanoparticles. *Journal of the American Chemical Society,* 127, 7632-7637.

TITIRICI, M.-M. & ANTONIETTI, M. 2010. Chemistry and materials options of sustainable carbon materials made by hydrothermal carbonization. *Chemical Society Reviews,* 39, 103-116.

TSENG, R.-L., WU, F.-C. & JUANG, R.-S. 2003. Liquid-phase adsorption of dyes and phenols using pinewood-based activated carbons. *Carbon,* 41, 487-495.

VERLICCHI, P., AL AUKIDY, M. & ZAMBELLO, E. 2012. Occurrence of pharmaceutical compounds in urban wastewater: removal, mass load and environmental risk after a secondary treatment—a review. *Science of the Total Environment,* 429, 123-155.

VICTORA, R. 1997. Calculated electronic structure of silver halide crystals. *Physical Review B,* 56 4417.

VIKKISK, M., KRUUSENBERG, I., JOOST, U., SHULGA, E., KINK, I. & TAMMEVESKI, K. 2014. Electrocatalytic oxygen reduction on nitrogen-doped graphene in alkaline media. *Applied Catalysis B: Environmental,* 147, 369-376.

VOHRA, A., GOSWAMI, D., DESHPANDE, D. & BLOCK, S. 2006. Enhanced photocatalytic disinfection of indoor air. *Applied Catalysis B: Environmental,* 64, 57-65.

W. W. ROBBINS, T. E. WEIER & C. R. STOCKING. 1957. Botany an Introduction to Plant Science. *Wiley* 495-496.

WAN MAHARI, W., ZAINUDDIN, N., WAN NIK, W., CHONG, C. & LAM, S.J.E. 2016. Pyrolysis recovery of waste shipping oil using microwave heating. *Energies* 9, 780.

WANG, H., LANG, X., GAO, J., LIU, W., WU, D., WU, Y., GUO, L. & LI, J. 2012. Polyhedral AgBr Microcrystals with an Increased Percentage of Exposed {111} Facets as a Highly Efficient Visible-Light Photocatalyst. *Chemistry-A European Journal*, 18, 4620-4626.

WANG, H., LIU, H., WANG, S., LI, L. & LIU, X. 2018. Influence of tunable pore size on photocatalytic and photoelectrochemical performances of hierarchical porous TiO_2/C nanocomposites synthesized via dual-Templating. *Applied Catalysis B: Environmental*, 224, 341-349.

WANG, H., LIU, X., WANG, S. & LI, L. 2018. Dual templating fabrication of hierarchical porous three-dimensional ZnO/carbon nanocomposites for enhanced photocatalytic and photoelectrochemical activity. *Applied Catalysis B: Environmental*, 222, 209-218.

WANG, H., YANG, X., ZI, J., ZHOU, M., YE, Z., LI, J., GUAN, Q., LV, P., HUO, P. & YAN, Y. 2016. High photocatalytic degradation of tetracycline under visible light with Ag/AgCl/activated carbon composite plasmonic photocatalyst. *Journal of Industrial and Engineering Chemistry*, 35, 83-92.

WANG, H., YUAN, X., WU, Y., HUANG, H., PENG, X., ZENG, G., ZHONG, H., LIANG, J. & REN, M. 2013. Graphene-based materials: fabrication, characterization and application for the decontamination of wastewater and wastegas and hydrogen storage/generation. *Advances in Colloid Interface Science*, 195, 19-40.

WANG, J., DUAN, X., DONG, Q., MENG, F., TAN, X., LIU, S. & WANG, S. 2019. Facile synthesis of N-doped 3D graphene aerogel and its excellent performance in catalytic degradation of antibiotic contaminants in water. *Carbon,* 144, 781-790.

WANG, P., HUANG, B., QIN, X., ZHANG, X., DAI, Y., WEI, J. & WHANGBO, M.H. 2008. Ag@ AgCl: a highly efficient and stable photocatalyst active under visible light. *Angewandte Chemie International Edition,* 47, 7931-7933.

WANG, P., HUANG, B., ZHANG, Q., ZHANG, X., QIN, X., DAI, Y., ZHAN, J., YU, J., LIU, H. & LOU, Z. 2010. Highly efficient visible light plasmonic photocatalyst Ag@Ag(Br, I). *Chemistry-A European Journal,* 16, 10042-10047.

WANG, P., HUANG, B., ZHANG, X., QIN, X., JIN, H., DAI, Y., WANG, Z., WEI, J., ZHAN, J. & WANG, S. 2009. Highly Efficient Visible-Light Plasmonic Photocatalyst Ag@AgBr. *Chemistry-A European Journal,* 15, 1821-1824.

WANG, Q., LI, H., CHEN, L. & HUANG, X. 2001. Monodispersed hard carbon spherules with uniform nanopores. *Carbon,* 39, 2211-2214.

WANG, X., HU, Z., CHEN, Y., ZHAO, G., LIU, Y. & WEN, Z. 2009. A novel approach towards high-performance composite photocatalyst of TiO_2 deposited on activated carbon. *Applied Surface Science,* 255, 3953-3958.

WATANIYAKUL, P., BOONNOUN, P., QUITAIN, A.T., KIDA, T., LAOSIRIPOJANA, N. & SHOTIPRUK, A. 2018. Preparation of hydrothermal carbon acid catalyst from defatted rice bran. *Industrial Crops Products,* 117, 286-294.

WATKINSON, A.J., MURBYC, E.J. & COSTANZO, S.D. 2007. Removal of antibiotics in conventional and advanced wastewater treatment: implications for environmental discharge and wastewater recycling. *Water Research,* 41, 4164-4176.

WEN, X.-J., NIU, C.-G., ZHANG, L., LIANG, C. & ZENG, G.-M. 2018. A novel Ag_2O/CeO_2 heterojunction photocatalysts for photocatalytic degradation of enrofloxacin: possible degradation pathways, mineralization activity and an in depth mechanism insight. *Applied Catalysis B: Environmental,* 221, 701-714.

WEN, Y., ZHANG, L., LIU, J., WEN, X., CHEN, X., MA, J., TANG, T. & MIJOWSKA, E. 2019. Hierarchical porous carbon sheets derived on a MgO template for high-performance supercapacitor applications. *Nanotechnology,* 30, 295703.

WHO 2008. *Progress on drinking-water and sanitation.* World health organization.

WILLIAMS, P.T. & REED, A.R. 2004. High grade activated carbon matting derived from the chemical activation and pyrolysis of natural fibre textile waste. *Journal of Analytical and Applied Pyrolysis,* 71, 971-986.

WU, F.C. & TSENG, R.L. 2006. Preparation of highly porous carbon from fir wood by KOH etching and CO_2 gasification for adsorption of dyes and phenols from water. *Journal of Colloid and Interface Science,* 294, 21-30.

WU, Q., LI, Z. & HONG, H. 2013. Adsorption of the quinolone antibiotic nalidixic acid onto montmorillonite and kaolinite. *Applied Clay Science,* 74, 66-73.

XI, G. & YE, J. 2010. Synthesis of bismuth vanadate nanoplates with exposed {001} facets and enhanced visible-light photocatalytic properties. *Chemical Communications,* 46, 1893-1895.

XIANG, Q., YU, J. & JARONIEC, M. 2012. Graphene-based semiconductor photocatalysts. *Chemical Society Reviews,* 41, 782-796.

XIAO, X., GE, L., HAN, C., LI, Y., ZHAO, Z., XIN, Y., FANG, S., WU, L. & QIU, P. 2015. A facile way to synthesize Ag@ AgBr cubic cages with efficient visible-light-induced photocatalytic activity. *Applied Catalysis B: Environmental,* 163, 564-572.

XIE, X., LI, S., ZHANG, H., WANG, Z. & HUANG, H. 2019. Promoting charge separation of biochar-based Zn-TiO_2/pBC in the presence of ZnO for efficient sulfamethoxazole photodegradation under visible light irradiation. *Science of The Total Environment,* 659, 529-539.

XING, X., JIANG, W., LI, S., ZHANG, X. & WANG, W. 2019. Preparation and analysis of straw activated carbon synergetic catalyzed by $ZnCl_2$-H_3PO_4 through hydrothermal carbonization combined with ultrasonic assisted immersion pyrolysis. *Waste Management,* 89, 64-72.

NUHOGLU, Y. & OGUZ, E. 2003. Removal of copper(II) from aqueous solutions by biosorption on the cone biomass of Thuja orientalis. *Process Biochemistry,* 38, 1627-1638.

YAGMUR, E., OZMAK, M. & AKTAS, Z. 2008. A novel method for production of activated carbon from waste tea by chemical activation with microwave energy. *Fuel,* 87, 3278-3285.

YAN, L., QIN, J., KONG, L., ZHI, H., SUN, M., SHEN, G. & LI, L.J.R.A. 2016. Optimized synthesis of $CuInS_2$/ZnS: Al–TiO_2 nanocomposites for 1, 3-dichloropropene photodegradation. *RSC Advances,* 6, 77777-77785.

YAN, T., ZHANG, H., LUO, Q., MA, Y., LIN, H. & YOU, J. 2013. Controllable synthesis of plasmonic Ag/AgBr photocatalysts by a facile one-pot solvothermal route. *Chemical Engineering Journal,* 232, 564-572.

YAN, X., WANG, X., GU, W., WU, M., YAN, Y., HU, B., CHE, G., HAN, D., YANG, J. & FAN, W. 2015. Single-crystalline AgIn $(MoO_4)_2$ nanosheets grafted Ag/AgBr composites with enhanced plasmonic photocatalytic activity for degradation of tetracycline under visible light. *Applied Catalysis B: Environmental,* 164, 297-304.

YANG, H., YAN, R., CHEN, H., LEE, D.H. & ZHENG, C. 2007. Characteristics of hemicellulose, cellulose and lignin pyrolysis. *Fuel,* 86, 1781-1788.

YANG, J., YU, X., YAN, J., TU, S.-T. & DAHLQUIST, E. 2013. Effects of SO_2 on CO_2 capture using a hollow fiber membrane contactor. *Applied Energy,* 112, 755-764.

YANG, S., FENG, X., WANG, X. & MÜLLEN, K. 2011. Graphene-based carbon nitride nanosheets as efficient metal-free electrocatalysts for oxygen reduction reactions. *Angewandte Chemie International Edition,* 50, 5339-5343.

YANG, Y., CHIANG, K. & BURKE, N. 2011. Porous carbon-supported catalysts for energy and environmental applications: A short review. *Catalysis Today,* 178, 197-205.

YIN, B., FANG, Z., LUO, B., ZHANG, G. & SHI, W. 2017. Facile Preparation of $Bi_{24}O_{31}Cl_{10}$ Nanosheets for Visible-Light-Driven Photocatalytic Degradation of Tetracycline Hydrochloride. *Catalysis Letters,* 147, 2167-2172.

YU, X., GAO, X., LU, Z., LIU, X., HUO, P., LIU, X., WU, D. & YAN, Y. 2013. Preparation and photodegradation properties of transition metal ion–poly-o-phenylenediamine/TiO_2/fly-ash cenospheres by ion imprinting technology. *RSC Advances,* 3, 14807-14813.

YU, Y., ZHU, Z., FAN, W., LIU, Z., YAO, X., DONG, H., LI, C. & HUO, P. 2018. Making of a metal-free graphitic carbon nitride composites based on biomass carbon for efficiency enhanced tetracycline degradation activity. *Journal of the Taiwan Institute of Chemical Engineers,* 89, 151-161.

YUAN, D., ZHANG, T., GUO, Q., QIU, F., YANG, D. & OU, Z. 2018. Recyclable biomass carbon@ SiO_2@ MnO_2 aerogel with hierarchical structures for fast and selective oil-water separation. *Chemical Engineering Journal,* 351, 622-630.

YUAN, X., JIANG, L., LIANG, J., PAN, Y., ZHANG, J., WANG, H., LENG, L., WU, Z., GUAN, R. & ZENG, G. 2019. In-situ synthesis of 3D microsphere-like In_2S_3/$InVO_4$ heterojunction with

efficient photocatalytic activity for tetracycline degradation under visible light irradiation. *Chemical Engineering Journal,* 356, 371-381.

ZHAI, Y., DOU, Y., LIU, X., PARK, S.S., HA, C.-S. & ZHAO, D. 2011. Soft-template synthesis of ordered mesoporous carbon/nanoparticle nickel composites with a high surface area. *Carbon,* 49, 545-555.

ZHANG, G., SONG, A., DUAN, Y. & ZHENG, S. 2018. Enhanced photocatalytic activity of TiO_2/zeolite composite for abatement of pollutants. *Microporous Mesoporous Materials,* 255, 61-68.

ZHANG, H., FAN, X., QUAN, X., CHEN, S. & YU, H. 2011. Graphene sheets grafted Ag@ AgCl hybrid with enhanced plasmonic photocatalytic activity under visible light. *Environmental Science and Technology,* 45, 5731-5736.

ZHANG, Q., LIMA, D.Q., LEE, I., ZAERA, F., CHI, M. & YIN, Y. 2011. A highly active titanium dioxide based visible-light photocatalyst with nonmetal doping and plasmonic metal decoration. *Angewandte Chemie International Edition,* 50, 7088-7092.

ZHANG, R., YANG, Y., HUANG, C.-H., ZHAO, L. & SUN, P. 2016. Kinetics and modeling of sulfonamide antibiotic degradation in wastewater and human urine by UV/H_2O_2 and UV/PDS. *Water Research,* 103, 283-292.

ZHANG, W., LI, G., LIU, H., CHEN, J., MA, S. & AN, T. 2019. Micro/nano-bubble assisted synthesis of Au/TiO_2@ CNTs composite photocatalyst for photocatalytic degradation of gaseous styrene and its enhanced catalytic mechanism. *Environmental Science: Nano,* 6, 948-958.

ZHANG, X., CHEN, Y.L., LIU, R.-S. & TSAI, D.P. 2013. Plasmonic photocatalysis. *Reports on Progress in Physics,* 76, 046401.

ZHANG, X., LI, J., LU, X., TANG, C. & LU, G. 2012. Visible light induced CO_2 reduction and Rh B decolorization over electrostatic-assembled AgBr/palygorskite. *Journal of Colloid and Interface Science,* 377, 277-283.

ZHANG, Y., ZHANG, F., LI, G.-D. & CHEN, J.-S. 2007. Microporous carbon derived from pinecone hull as anode material for lithium secondary batteries. *Materials Letters,* 61, 5209-5212.

ZHANG, Y.F. 2014. Research on low-carbon architectural development based on green life cycle. *In Applied Mechanics and Materials*. Trans Tech Publ, 263-267.

ZHENG, Z., LIU, H., YE, J., ZHAO, J., WACLAWIK, E.R. & ZHU, H. 2010. Structure and contribution to photocatalytic activity of the interfaces in nanofibers with mixed anatase and TiO_2 (B) phases. *Journal of Molecular Catalysis A: Chemical,* 316, 75-82.

ZHOU, X., HU, C., HU, X., PENG, T. & QU, J. 2010. Plasmon-assisted degradation of toxic pollutants with Ag− AgBr/Al2O3 under visible-light irradiation. *The Journal of Physical Chemistry C,* 114, 2746-2750.

ZHU, H., KE, X., YANG, X., SARINA, S. & LIU, H. 2010. Reduction of nitroaromatic compounds on supported gold nanoparticles by visible and ultraviolet light. *Angewandte Chemie,* 122, 9851-9855.

ZHU, M., CHEN, P. & LIU, M. 2011. Graphene oxide enwrapped Ag/AgX (X= Br, Cl) nanocomposite as a highly efficient visible-light plasmonic photocatalyst. *ACS Nano,* 4529-4536.

ZUO, W., TIAN, Y. & REN, N. 2011. The important role of microwave receptors in bio-fuel production by microwave-induced pyrolysis of sewage sludge. *Waste Management,* 31, 1321-1326.

Chapter 3. Three-dimensional hierarchical porous carbon structure derived from pinecone as potential catalyst support in catalytic remediation

Abstract

In this chapter, pinecone was converted via two stage pyrolysis to produce low cost activated carbon. Furnace pyrolysis was used in the first step to convert pinecone to biochar, followed by microwave pyrolysis of the biochar activated with KOH to obtain activated carbon (ACK) materials as a suitable catalyst support. The resulting ACKs materials were characterized by morphology, structural, adsorption, and electrochemical properties. The optimized ACK 2.24-16 prepared from the pinecone had a complex three-dimensional (3D)-hierarchical network structure with an abundance of micropores and mesopores than other ACKs samples judging from the iodine number (1900 mg/g) and the methylene blue number (4000 mg/g) adsorption capacity. The optimized 3D ACK hierarchical material had the highest current response and least charge transfer resistance, along with a high surface area (427 m^2/g) which gives it great potential as a photocatalyst support in heterogeneous photocatalysis. The morphology, structural and electrochemical analysis shows that 3D ACK hierarchical network structure will significantly benefits catalyst dispersion, facilitate reactant transport, enhance visible light absorption and fast interfacial charge transfer. This work highlights exciting avenue of utilizing pinecone, which is a

biowaste to produce low-cost and effective carbon-based photocatalyst support materials for environmental remediation.

Keywords: Catalyst support material, Pinecone, KOH-activation, Microwave pyrolysis, hierarchical network structure

3.1. Introduction

Heterogeneous photocatalysis utilizing metal-semiconductor materials as catalyst under light exposure at relatively low temperature has received considerable attention for the efficient removal of pollutant in wastewater (Wen, Niu, Zhang, Liang & Zeng 2018). However, the application of these photocatalysts for enhanced performance is hindered by aggregation and agglomeration of the catalyst materials during preparation, weak light-harvesting efficiency, inefficient separation and fast recombination rate of photoexcited charge carriers, and poor recovery from solution after degradation activities (Jiang, Yuan, Zeng, Liang, Chen, Yu, Wang, Wu, Zhang & Xiong 2018; Espinosa, Manickam-Periyaraman, Bernat-Quesada, Sivanesan, Álvaro, García & Navalón 2019; Yuan, Jiang, Liang, Pan, Zhang, Wang, Leng, Wu, Guan & Zeng 2019). The immobilization of the catalytic active phase on high surface area insoluble materials as a cocatalyst in the degradation process is a promising approach in obtaining highly efficient and stable photocatalytic composite (Zhang, Fan, Quan, Chen & Yu 2011; Zhu, Chen & Liu 2011; Xiang, Yu & Jaroniec 2012; Esmaeili & Entezari 2016; Ji, Chen, Mu, Yuan, Knoblauch, Bao, Shi, Wang & Zhu 2016; Guan, Wang, Wang, Sun, Huang, Liu & Zhao 2017).

The higher specific surface area, excellent electron conductivity, active binding sites for catalyst dispersion and their relative chemical inertness are exceptional attributes for utilizing carbonaceous materials (graphene, graphene oxide, carbon nanotube and activated carbon) (Fan, Zhao, Yang, Shan, Yang, Zhang, Li & Gao 2012; Dong, Gao, Miao, Yu, Degan, Garcia-Pérez, Rasco, Sablani & Chen 2015; Antolini 2016) as supports in comparison to other support materials (Guesh, Márquez-Álvarez, Chebude & Díaz 2016; Guan et al. 2017; Zhang, Song, Duan & Zheng 2018). Low cost of production, abundance, inexpensive matrix with nontoxicity are key factors towards the selection of activated carbon (AC) among these carbonaceous materials for catalyst

dispersion (Yu, Zhu, Fan, Liu, Yao, Dong, Li & Huo 2018; Xie, Li, Zhang, Wang & Huang 2019). In the optimization of activated carbon (AC) as a catalyst support, the desire should not only be based on a high specific surface area for effective adsorption-desorption of solution and abundant functional groups for catalyst dispersion judging from previous works (Yang, Chiang & Burke 2011; Zhai, Dou, Liu, Park, Ha & Zhao 2011; Kumar, Mallampati, Adin & Valiyaveettil 2014). The AC must also have exceptional interconnected porous channel with accessible space, favorable for light-harvesting, aid electrons transfer after generation and assist separation of photo-generated charge carriers, as well high adsorption and diffusion of targeted pollutants (Naito, Tachikawa, Fujitsuka & Majima 2008; Chen, Wang & Fu 2009; Wang, Liu, Wang & Li 2018).

The AC porous channels in form of 3D hierarchical network structures have shown promising attributes in fuel cells, supercapacitors and environmental remediation (Li, Samad, Polychronopoulou, Alhassan & Liao 2014; Jiang, Zhang, Yuan, Chen, Huang, Dionysiou & Yang 2018; Raza, Ali, Raza, Luo, Kwon, Yang, Kumar, Mehmood & Kim 2018; Yuan, Zhang, Guo, Qiu, Yang & Ou 2018). However, previous works devoted in the development of these 3D AC hierarchical structures rely on utilization of high-price templates, requirement of energy-intensive routes, and the usage of corrosive chemicals, which pose huge concerns on environmental sustainability and production costs (Zhai et al. 2011; Ji et al. 2016). A more sustainable approach to develop 3D AC hierarchical structure exploring sustainable resources like biowaste is crucial to alleviate the preparation cost, environmental impact and also enhance the value of the biowaste material (Titirici & Antonietti 2010; Demir, Kahveci, Aksoy, Palapati, Subramanian, Cullinan, El-Kaderi, Harris & Gupta 2015). Previous works have explored agricultural biomasses, waste residues and wood as renewable precursors for generating 3D AC hierarchical network structure materials as catalyst support for pollutant removal with high activity (Ji et al. 2016; Lam, Liew,

Wong, Azwar, Jusoh & Wahi 2017a; Liew, Chong, Osazuwa, Nam, Phang, Su, Cheng, Chong & Lam 2018). The unique 3D AC interconnected porous channel potential as catalyst support depends strongly on the type of agricultural biomass precursor, the activation methods and the heating method during carbonization.

Particularly, pinecone biomass is abundantly available throughout the world, a valuable product in waste remediation (Nuhoglu & Oguz 2003) due to its excellent chemical composition (Haykiri-Acma & Yaman 2007). Ovulate pinecones are rich in cellulose, hemicellulose, lignin, resin and tannins (Robbins, Weier & Stocking 1957), that serve as the biomass source for AC synthesis. Host of carbon materials from pinecone have shown good performances in many fields such as supercapacitors, energy production, adsorbent and electrocatalysts (Barzegar, Bello, Dangbegnon, Manyala & Xia 2017; Lei, Wang, Lai, Hu, Wang, Fang, Li & Fang 2017; Nanda, Gong, Hunter, Dalai, Gökalp & Kozinski 2017; Shen, Huang, An, Xin, Huang & Rosendahl 2018). Activated carbon, from various agricultural sources, have been used as catalyst supports (Li, Tie, Li, Guo, Liu, Liu, Liu, Feng & Zhao 2018; Liew et al. 2018).

Regarding activation condition, AC produced via mixing of the precursor with chemical activating agent especially potassium hydroxide (KOH) has shown potential for good formation of 3D hierarchical network structure with large surface area (Mohammed, Chen & Zhu 2019). This emanates from interaction of the potassium atom with the carbon structure of the AC by means of dehydration and degradation (Giraldo & Moreno-Piraján 2012; Li, Liu, Xiao & Wang 2017). Microwave-assisted pyrolysis instead of conventional oven heating has shown promising attributes for the generation of 3D AC interconnected porous channels. This may be ascribed to the microwave's exceptional fast, efficient and selective heating mechanism (Wan Mahari, Zainuddin, Wan Nik, Chong & Lam 2016). There is no reports in literature regarding the optimization of

different preparation parameters on activated carbon produced from pinecone, as a catalyst support in heterogeneous catalysis field.

Inspired by these facts, the focus of this study was to construct 3D AC hierarchical porous structure through microwave pyrolysis of KOH impregnated pinecone and test it as photocatalyst support (ACK). The characteristic properties of 3D AC hierarchical porous structures with abundant oxygenated functional groups were established, along with their efficient adsorption attributes is also discussed in this chapter.

3.2. Materials and method

3.2.1. Materials

Agricultural biomass pinecones were collected from Vaal University parking space, South Africa and will serve as the precursor for carbon production. The pinecones were washed to remove impurities such as sand and leaves from the material. The washed cone was dried in a conventional oven at 90 ^{o}C for 48 hr. The scales on the cones were removed and crushed using a pulverizer to make a fine powder with particle size less than 1 mm. Analytical grade chemicals such as potassium hydroxide (KOH) was purchased from Merck, while hydrochloric acid (HCl, 99%), sodium hydroxide (NaOH, 99%), iodine (I_2) sodium thiosulfate ($Na_2S_2O_3 \cdot 5H_2O$), potassium iodide (KI) and methylene blue ($C_{16}H_{18}ClN_3S$, 99%) were purchased from Sigma Aldrich. All the reagents were used as received and the water used in all these experiments was purified with a Millipore system.

3.2.2. Activated carbon preparation

This work adopts the established two-stage pyrolysis method for preparing AC (Yang, Liu, Liang, Chen, Ma, Li, Liu, Tu, Lan & Chen 2019). The pinecone powder (approximately 15 g) weighed in an aluminum foil and, was placed in a tubular furnace reactor (Carbolite Gero, MTF 12/38/250). Nitrogen gas was passed through the furnace for about 10 minutes to eliminate air from the reactor, before heating up the furnace. The material was using a heating rate of 10 °C/min and carbonized at 600 °C for 2 h under an inert atmosphere of nitrogen flow (50 mL/min) to obtain the biochar (BCR). The BCR was allowed to cool, washed repeatedly with distilled water and dried overnight at 80 °C. A yield of about 40 wt% was obtained for the biochar, which was further subjected to chemical activation for conversion into activated carbon. The chemical activation of the BCR (5 g) with a particle size of fewer than 300 μm was carried out with a 25 mL KOH solution at different mass ratio of KOH to biochar or impregnation ratio (IR) (0.56 - 3.36). The prepared mixtures were impregnated for 24 hr and the solution was dried in oven at 80 ^{o}C for 12 hr to remove any remaining moisture present in the material. The dried sample placed in Duran bottle and flushed with nitrogen atmosphere flow (50 mL/min) for 30 min. Thereafter the bottle was closed with a lid; with a pin-hole to prevent pressure build up during pyrolysis. The biochar was pyrolyzed in the microwave reactor (model LG MH8042GM, maximum power of 1000 W at a frequency of 2450 MHz) at a constant power of 400 W for different times (8 -24 min) with 4 minutes difference interval. The produced activated carbon samples were cooled to room temperature, washed with 0.1 M hydrochloric acid and hot distilled water to remove the excess potassium and any impurities until the pH is between 6-7. The ACs were further dried at 105 ^{o}C

overnight, and named as ACK-a-b, where a represents mass ratio of KOH to biochar (impregnation ratio) and b is the microwave pyrolysis time during the microwave process.

3.2.3. Characterization

The percentage yield (Genovese, Jiang, Lian & Holm) was calculated as the ratio of the dry weight of produced pinecone-activated carbon (W_{ACK}) to weight of the biochar (W_{BCR}) (Prahas, Kartika, Indraswati & Ismadji 2008; Kılıç, Apaydın-Varol & Pütün 2012) as depicted below:

$$Y\ \% = \frac{W_{ACK}}{W_{BCR}}\ X\ 100 \qquad 3.1$$

The morphology of BCR and ACKs samples were determined by scanning electron microscope (Zeiss EVO 50 XVP). The ACKs functional groups were investigated by Fourier transform infrared spectrometer (Perkin Elmer spectrum 400) within the range of 600–4000 cm^{-1}. X-ray diffraction (XRD) patterns were obtained by using Bruker diffractometer AXS with Cukα radiation source (source light at a wavelength of 0.1541 nm) with scan range of 10 to 80°. Thermal analysis on each sample was carried out using Perkin Elmer STA 6000 thermal simultaneous analyzer at heating rate of 5 °C/min from 30 to 900 °C under nitrogen purge stream of 20 mL/min. The BET surface area, average pore size distribution was estimated by N_2 adsorption at 77 K using a Micromeritics (Australia) Tristar 3000 analyzer coupled to a VacPrep 061 degassing unit. The sample was degassed at a temperature of 105 °C for 24 hours and cooled down to 30 °C before the analysis, to eliminate any adsorbed moisture on the surface of the sample. The Raman spectra for ACK material was performed using a T64000 series II triple spectrometer system from HORIBA scientific, Jobin Yvon Technology. The Raman spectra were generated using argon/krypton laser

with an excitation wavelength of 514 nm through an Olympus microscope with a 50x objective lens and laser power of 1.48 mW. The Raman spectra were acquired in the Raman shift range from 200 cm^{-1} to 1800 cm^{-1}.

The point of zero charge (pH-PZC) was determined using 6 points experiment. The optimized ACK sample (100 mg) along with 50 mL of 0.1 M potassium nitrate (KNO_3) solution was agitated at 25 C for 48 h to allow it to reach the equilibrium state (Xing, Jiang, Li, Zhang & Wang 2019). The initial pH of KNO_3 solution (2, 4, 6, 8, 10 and 12) was adjusted using 0.1 M HCl and 0.1 M NaOH. After shaking for 48 h, the final pH was measured using a Hach pH meter.

The quantification of the oxygenated functional groups was done by Boehm titration (Bardestani & Kaliaguine 2018). According to this method, activated carbon sample (0.1 g) was equilibrated with separate solution of 50 mL of 0.1 M $NaHCO_3$, Na_2CO_3, NaOH, and HCl solution, then sealed and shaken at room temperature for 48 hr. Afterward, 10 mL of each filtrate was back-titrated with 0.1 M HCl using phenolphthalein indicator to detect the end point. The determination of the numbers and types of acidic sites, certain considerations were made. NaOH neutralizes carboxylic, lactone and phenolic groups; Na_2CO_3 neutralizes carboxylic and lactonic groups, while $NaHCO_3$ neutralizes only carboxylic groups (Goertzen, Thériault, Oickle, Tarasuk & Andreas 2010). The total basic surface sites were determined with a similar titration technique using 0.1 M HCl solution and back titrating with 0.1 M NaOH. All experiments were done in triplicate.

The electrochemical properties for prepared ACK samples were conducted in a standard three-electrode workstation (Biologic SP 240 potentiostat). A glassy carbon electrode (GCE, 5mm in diameter) was utilized as the working electrode, while platinum wire and Ag/AgCl (in saturated 4M KCl) were used as the counter electrode and a reference electrode respectively. Before surface modification, the glassy carbon electrode (diameter of 6 mm) was polished with 0.0.5 and 0.3 µm

alumina powder for 3 min, rinsed thoroughly with distilled water. The washed GCE further sonicated in equal volume of water and ethanol solution for 10 min, then dried under 100 W infrared lamp for 5 min. The ACKs samples suspension was prepared by dispersing 5 mg of material into 0.5 ml DMF solution followed by ultrasonication for 1 h to obtain ACK ink. A volume of 20 μL of the ACK suspension was dropped onto the surface of clean GCE by using a micropipette and then dried at room temperature. The cyclic voltammetry (CV) method was performed in 6 M KOH solution at a scan rate of 50 mV S^{-1} from -0.8 V to +0.2 V. The electrochemical impedance spectroscopy (EIS) was tested between frequency range of 100 KHz to 10 mHz with a perturbation amplitude of 5 mV.

3.2.4. Methylene blue and iodine adsorption capacity for ACK

The methylene blue adsorption capacity also called methylene blue number (MBN) is defined as the maximum amount of dye adsorbed on 1.0 g of adsorbent. The MBN is a measure of mesopores content (2 – 5 nm) present in produced ACK samples. The batch adsorption of MB was conducted in a set of 100 mL plastic bottles containing 0.01 g ACK along with 40 mL dye solution at various initial concentrations (10, 25, 50, 100, 250, 500, and 1000 mg/L) at a pH of 12. The bottles were agitated in a shaker at room temperature with a shaking speed of 120 rpm until the equilibrium was reached after 2 hrs. The samples were filtered and the residual concentration of MB in the supernatant solution was analyzed using a double beam UV–Vis spectrophotometer at 665 nm. The amount of MB uptake per unit mass of adsorbent at equilibrium, qe (mg/g), was calculated by:

$$Q_e = \frac{(C_O - C_e)}{W} V \qquad 3.2$$

where Co and Ce (mg/L) is the liquid-phase concentrations of MB dye at initial and equilibrium, respectively. V (L) is the volume of the solution, and W (g) is the mass of ACK used. The initial pH of the dye solution was adjusted by addition of 0.1 M of HCl or NaOH. Langmuir isotherm which assumes homogenous monolayer adsorption, was employed to determine the monolayer. The monolayer adsorption capacity was determined using a plot of q_{eq} versus C_e as presented in Appendix (Figure A3). The calculated monolayer adsorption capacity is best reported as the methylene blue number and corresponding Freundlich isotherm also describe below:

$$q_e = \frac{q_{max}.K_L.C_e}{1+K_L.C_e} \quad 3.3$$

$$q_e = K_F.C_e^{1/n} \quad 3.4$$

where the qe is the amount of MB dye adsorbed at equilibrium time (mg/g), Langmuir parameters such as q_{max} (mg/g) is monolayer adsorption capacity in Langmuir model, K_L (L/mg) is isotherm constants of Langmuir equation, Ce is the equilibrium concentration of MB dye in solution (mg/L), K_F is the capacity of the adsorbent and 1/n is the intensity of adsorption constant for Freundlich equation. **Table A 1** and **A 2** (**Appendix A**) presents the maximum sorption capacities of the ACK samples studied towards methylene blue (MB) adsorption as calculated from the Langmuir and Freundlich isotherm for the ACK samples.

The iodine adsorption capacity represented as iodine number (IN) is a good measure of microporosity of the AC (up to 2 nm). The IN indicates milligrams of iodine adsorbed by a gram

of activated carbon (mg/g), is determined by using the ASTM D4607-94 method for characterizing ACK samples. A mass of 0.1 g ACK samples were placed in a dry 100 mL volumetric flask, then fully wetted with 10 mL of HCl (5 wt%). The mixture was boiled on the hot plate for about 30s and allowed to cool. After cooling down to room temperature, 100 mL of iodine standard solution (0.1 mol/L) was added, and then shake for 5 min. The resulting mixture was filtered, then 50 mL of the filtrate were transferred with a pipette into a 250 mL volumetric flask, and further titrated with sodium thiosulfate (0.1 mol/L) until the solution became pale yellow. A volume of 2 mL of starch indicator solution (5 g/L) was added and the titration was continued with sodium thiosulfate until the solution became colorless (Xing et al. 2019). The amount of iodine adsorbed in milligrams per gram of carbon at a residual iodine concentration of 0.02 N is represented as the iodine number. The X/M and C values are calculated by the equations below:

$$\frac{X}{M} = \frac{\left[(\mathrm{N}_1 \ \mathrm{X}\ 126.93\ \mathrm{X}\ V_1) - \left[\frac{V_1 + V_{HCl}}{V_F}\right] X \left(N_{Na_2S_2O_3} X 126.93\ X\ V_{Na_2S_2O_3}\right)\right]}{M_C} \qquad 3.5$$

$$C = \quad (N_{Na_2S_2O_3}\ X\ V_{Na_2S_2O_3}\ ) \qquad 3.6$$

where N_I is the iodine solution normality, V_I is the added volume of iodine solution, V_{HCl} is the added volume of 5% HCl, V_F is the filtrate volume used in titration, $N_{Na2S2O3}$ is the sodium thiosulfate solution normality, VN_{a2S2O3} is the consumed volume of sodium thiosulfate solution and MC is the mass of activated carbon.

3.3. Results and discussion

3.3.1. Yield and characteristics properties of carbon samples

The high carbon and low ash content of pinecone (PC) biomass (Haykiri-Acma & Yaman 2007) makes the pinecone an ideal precursor for the production of activated carbon. The influence of impregnation ratio (IR) of the chemical activating agent and the microwave pyrolysis time (MPT) plays a major role in the final yield of the produced activated carbon. The chemical activating agent (KOH) acts as dehydrating agents, whereby they penetrate deep into the biochar structure (Deng, Li, Yang, Tang & Tang 2010; Muniandy, Adam, Mohamed & Ng 2014), which results to decomposition of the large organic molecules present in the biomass to smaller molecules. Moreover, active surface sites for catalyst dispersion, open channel for light penetration and high surface are formed from influence of KOH at different IR under microwave activation.

The ACKs yield decreases from 91 to 39% as the IR increases from 0.56 to 3.36 (**Figure 3.1a**), while an increase in MPT from 8 to 24 min at IR of 2.24 results in decrease in yield from 66 to 41% (**Figure 3.1b**). The yield of ACK reduces with increasing IR and MPT, as huge amount of carbon is burn-off, though the yield of ACK shows no significant changes when IR is 1.68 to 3.36. The yield variation of ACK from MPT at 8 to 24 min is significant, highlighting MPT as variable is more dominant to IR in obtaining high yield of ACK. High ACK yield is obtained at low IR and MPT, which is ascribed to weak elimination of volatiles from the BCR due to poor activation from activating agent and short microwave pyrolysis time (Lam, Liew, Wong, Yek, Ma, Lee & Chase 2017b). Herein at higher IR and microwave time, decomposition of cellulose, hemicellulose and lignin in BCR results to producing more volatiles, which explains lower yield of ACK. The eliminated volatile matters paves access for good channel formations from inaccessible channel,

as intense gasification of surface carbon atoms occurs with fast weight loss at higher IR and MPT (Kundu, Gupta, Hashim, Sahu, Mujawar & Redzwan 2015; Lam et al. 2017b).

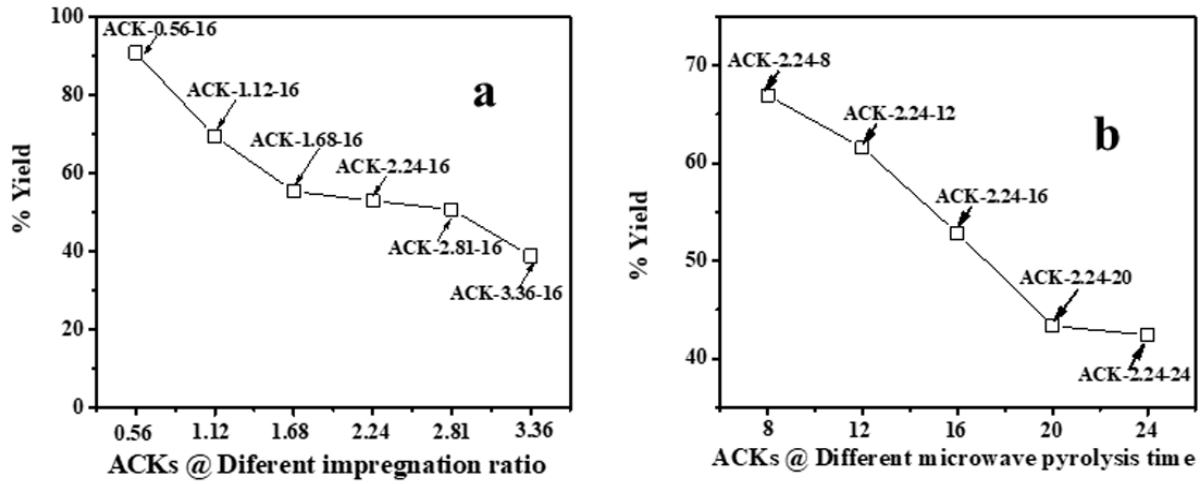

Figure 3.1: % Yield of ACK at different (a) impregnation ratio and (b) microwave pyrolysis time.

The surface morphology of produced ACKs at different IR and MPT are further shown in **Figure 3.2** and **Figure 3.3**. Biochar as shown in **Appendix A (Figure A 1)** has small open channel, however upon impregnation with KOH and subjected to microwave activation, the porous structural channel becomes pronounced in produced ACKs samples in **Figure 3.2**. During microwave activation, volatile matters are released along with formation of small rudimentary channel, as they are less developed at lower IR (0.56 – 1.12) in **Figure 3.2**, which could adversely affect their adsorption and catalytic properties. The porous structural channel in form of three-dimensional (3D) hierarchical like network becomes evident at IR of 1.68 – 3.36, which is due to elimination of excess volatile matters during the activation process (Li et al. 2017; Kaur, Gupta &

Bhunia 2019). The 3D hierarchical like framework is well developed with ACK-2.2.4-16 sample, as well will favours high IN and MBN adsorption capacity (*as further discussed in adsorption experiment*). The 3D hierarchical like framework of the ACK is also crucial for boosting the photocatalytic reaction because of the large number of porous structural channels that aid photocatalyst uniform dispersion without agglomeration (Wang, Duan, Dong, Meng, Tan, Liu & Wang 2019). The 3D hierarchical framework would also promote light harvesting of photocatalyst material, interfacial charge carrier mobility and facilitate reactant transport into the catalyst's inner surface (Wang, Liu, Wang, Li & Liu 2018; Momodu, Okafor, Manyala, Bello, ZebazeKana & Ntsoenzok 2019).

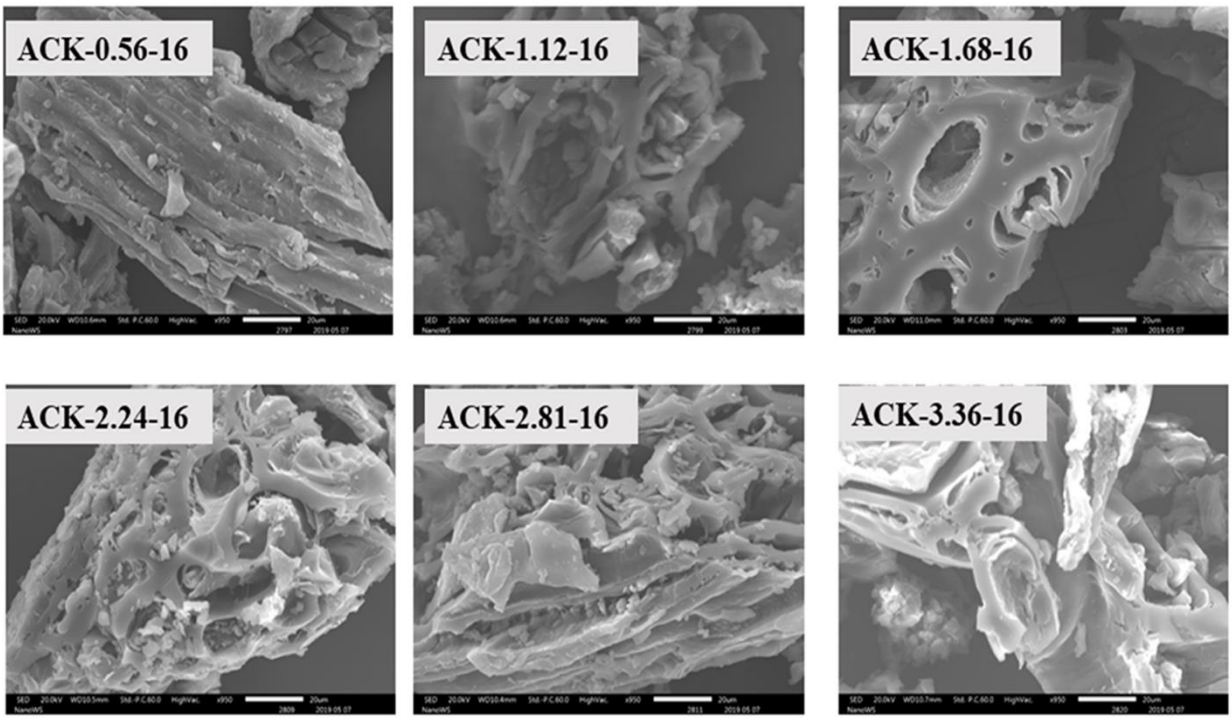

Figure 3.2: SEM images of ACKs at different impregnation ratio.

From **Figure 3.3**, the porous channels of ACK at low MPT (ACK-2.24-8) are not well developed, depicting incomplete formation of ACK sample. However, the channel development becomes pronounced with an increment in MPT from 12 – 20 min, as surface impurities are eliminated from the surface of ACK. The 3D hierarchical porous structure with active sites formation favors enhanced adsorption and catalytic support properties of the ACK. However, an augmentation in microwave time to 24 min causes the existing channel to be destroyed due to over gasification that is unfavorable for adsorption and as catalyst support properties. Hence, it can be inferred that KOH activation with microwave pyrolysis aided in better development of porous structural channels for ACK samples. The TEM image of ACK-2.24-16 sample is presented in **Figure 3.3,** with a well-developed porous structure that are attributed to presence to micropores and mesopores resulting from the chemical activation of KOH. Corresponding SEM images of optimized ACK-2.24-16 sample at different magnification and biochar image are shown in **Appendix A** (**Figure A 1).**

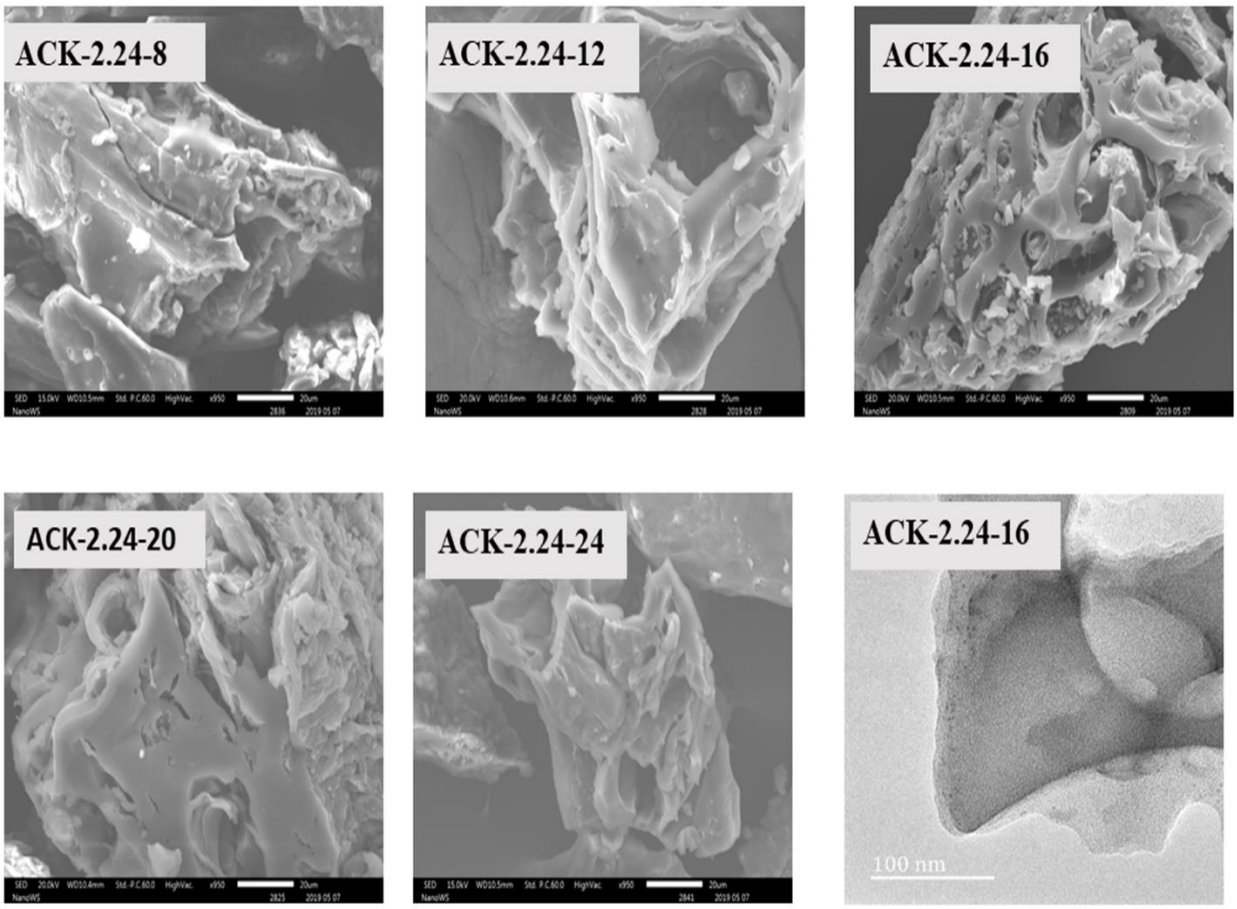

Figure 3.3: SEM images of ACKs prepared by microwave pyrolysis at various microwave pyrolysis time and TEM image of optimized ACK sample.

The XRD pattern of ACK prepared at different IR and MPT are depicted in **Figure 3.4 a and b**. A broaden peak is observed between range of 22.3º, while a sharp peak at 43.5º is also prominent and these two peaks are ascribed to the 002 and 100 diffraction planes of carbon pattern. Herein, the prepared ACKs at 002 lattice plane are indication of amorphous carbon with carbon rings that are disorderly stack up (Tang, Liu & Chen 2012) and this characteristic plane for ACK samples significantly decreases slightly with an increase in IR and MPT respectively (Gao, Li, Jin, Wang, Yuan, Wei, Chen, Ge & Lu 2015). The ACKs at 100 plane are composed of turbostatic structure with minute presence of graphite like microcrytsallites (Tang et al. 2012; Long, Chen, Jiang, Zhi & Fan 2015) which is good for electrical conductivity of ACK (Atchudan, Edison, Perumal & Lee 2017). Corresponding XRD plot of optimized ACK-2.24-16 sample and biochar shown in **Appendix A (Figure A 2).**

The FTIR spectra of ACKs at different IR and MPT are shown in **Figure 3.4 c and d**, respectively. The broad peaks around 3420 cm^{-1} is ascribed to stretching vibrations of OH bonds from the water molecules adsorbed on the surface of prepared ACK (Kaur et al. 2019). The two bands at 2946 and 2815 cm^{-1} are attributed to aliphatic C-H stretching vibrations (Luo, Chen, Li, Zhang, Zhao & Fan 2018). The bands at 1698, 1582 and 1427 cm^{-1} are all ascribed to C=O stretching of the carboxylate and carbonyl groups (Genovese et al. 2015), C=C of the aromatic groups that is highly conjugated to carbonyl groups and –OH bending (Puziy, Poddubnaya, Martınez-Alonso, Suárez-Garcıa & Tascón 2002; Madejova 2003). The stretching vibration of C-O-C bonds of esters, phenol, carboxylic and ethers (Fu, Li, Chen, Zhang, Huang, Zhu, Yang & Zhang 2013; Wataniyakul, Boonnoun, Quitain, Kida, Laosiripojana & Shotipruk 2018) are prominent at 1150 – 1079 cm^{-1}, indicative that the produced carbon samples have abundance

oxygen moieties on the surface of ACK samples (Kaur et al. 2019). The weak peak at 2300 and 870 - 750 cm^{-1} are ascribed to the C-H sp^3 stretching present in the lignin (Kaur et al. 2019) and out-of-plane bending vibration of C-H in the aromatic rings (Sun, Zhang, Ye, Liu, Zhang, Wu & Wu 2017). Moreover, the peaks of aliphatic C-H stretching and stretching vibration of C-O-C bonds were decreased slightly with increasing IR and MPT, highlighting the dehydrating influence of KOH (Heidarinejad, Rahmanian, Fazlzadeh & Heidari 2018) and intense microwave heating during activation process (Hu, Nango, Bao, Li, Hasan & Li 2019). The prepared ACKs samples possess abundance of oxygenated functional groups on their surface, which offers promising route for extensive functionalization. These functional groups makes the ACKs samples more hydrophilic in nature, in turn aid uniform dispersion catalyst nanoparticles on the ACK surface. The hydrophobic nature from these functional groups from the prepared ACKs samples ensures the good stability between carbon and the supported catalyst (Lu, Hu, Yang, Shanmugam, Wei, Selvaraj & Xie 2018). Corresponding FTIR plot of optimized ACK-2.24-16 sample and biochar is shown in **Appendix A (Figure A 2).**

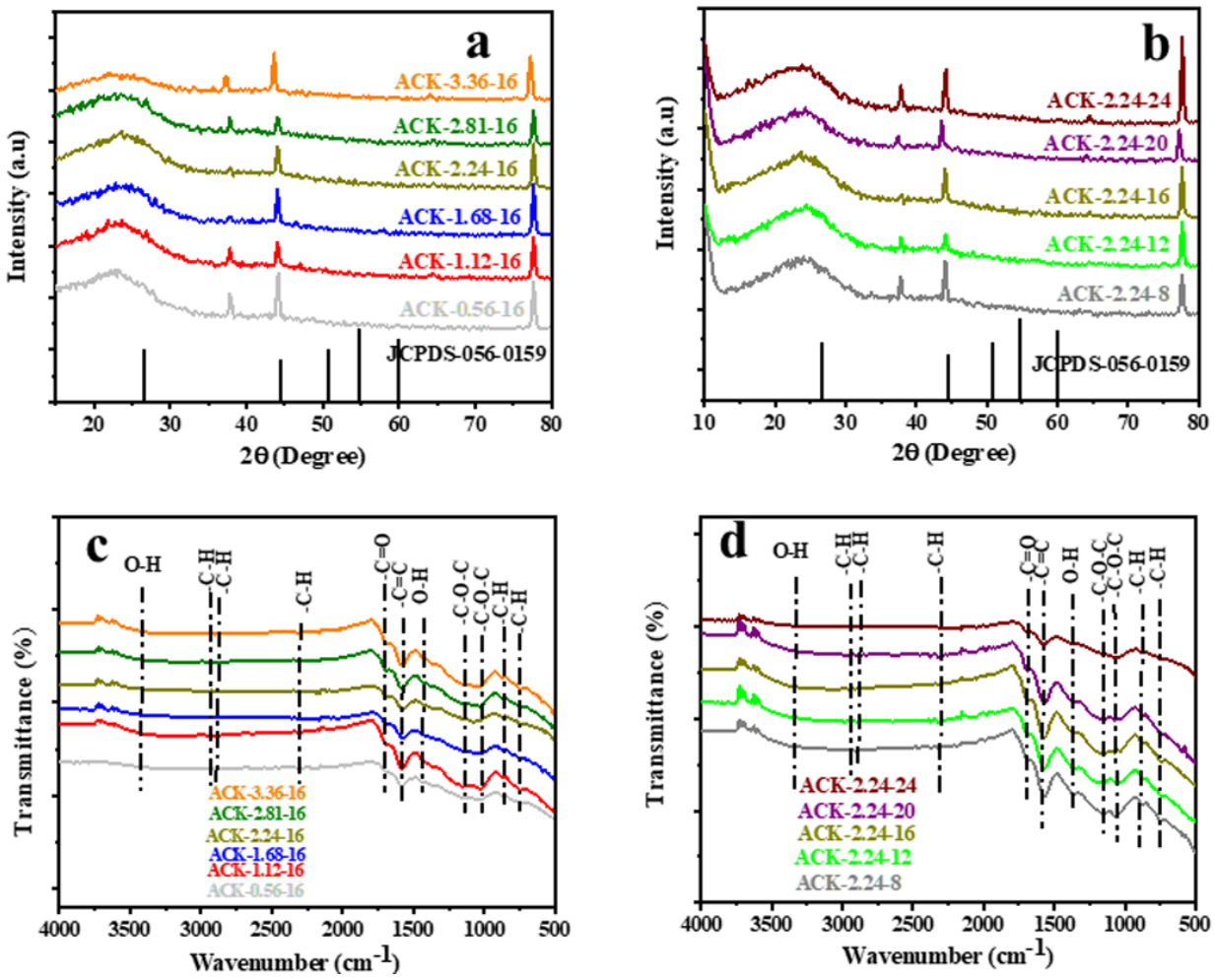

Figure 3.4: X-ray diffraction pattern and FTIR spectra of ACKs at different (a, c) Impregnation ratio and (b, d) Microwave pyrolysis time.

Raman spectroscopy was used to establish the structural of the ACK-2.24-16 and biochar sample. Two characteristic peaks can be assigned to carbon material in **Figure 3.5**, D band (1320 – 1361 cm^{-1}) and G band (1589 - 1598 cm^{-1}) respectively. The D band corresponds with structural defects and disordered structures of the sp^2 domains (Kudin, Ozbas, Schniepp, Prud'Homme, Aksay & Car 2008), and the G band is associated with the first-order scatting of the E2g phonon for sp^2-bonded graphitic carbon structures (Shimodaira & Masui 2002). The intensity of D band and G band (I_D/I_G) is used to estimate the degree of structural disorder and graphitic properties for carbon materials, which is calculated to be 0.85 (ACK-2.24-16) and 0.83 (BCR-600) for in this work. This indicates that ACK-2.24-26 is more disorder and have higher graphitic level than BCR-600, which can provide extra active sites for both adsorption and catalysis.

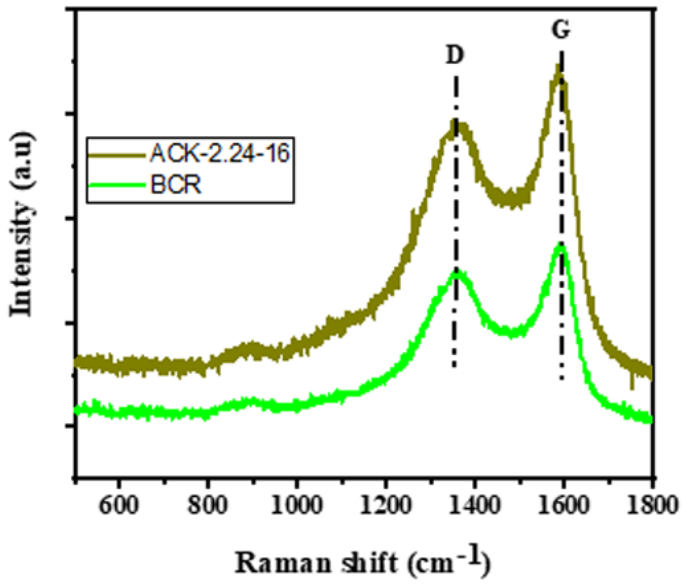

Figure 3.5: Raman spectra of ACK-2.24-16 and BCR.

The TGA and DTA analysis of ACK-2.24-16 sample is shown in **Figure 3.6**. The ACK sample was conducted in N_2 atmosphere at temperature range between 35 to 850 ºC and showed three-weight loss in **Figure 3.6**. The first weight loss occurs between 30 - 154 ºC with loss of 3%, which is ascribed to decomposition of water molecules adsorbed on the carbon surface (Yang, Yan, Chen, Lee & Zheng 2007). The second weight loss (8%) for the ACK happens between 154 - 480 ºC, which is due to decomposition of hemicellulose, cellulose and lignin structure in form of volatile matters and inorganic matrix elimination (Singh, Mahanta & Bora 2017). The last stage of weight loss occurs between 480 and 680 ºC with weight losses from 12%, is attributed to decomposition of extra residual carbonaceous skeleton.

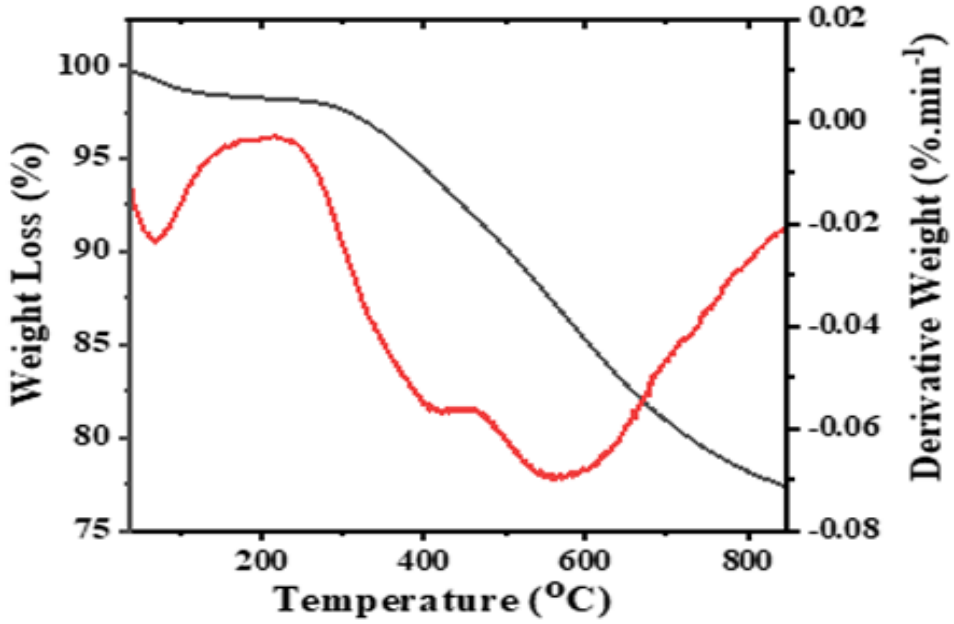

Figure 3.6: Thermogravimetric and differential thermal analysis plot of optimized ACK.

Figure 3.7 shows that the pHPZC of ACK-2.24-16 is equal to 8.5. Invariably, for pH values lower than 8.5, ACK-2.24-26 sample will have positive charge on its surface and negative charge for pH values higher than pHPZC. It should be highlighted that the basic attributes of ACK-2.24-16 is ascribed to presence of carbonyl, pyrone and chromene groups (Suárez, Menéndez, Fuente & Montes-Morán 1999) present on the AC surface and is in agreement with FTIR result (**Figure 3.4c and d**). The adsorption capacity of the cationic methylene blue in activated carbon increases with pH due to the basic surface groups via electrostatic interactions (Khasri, Bello & Ahmad 2018) and form the basis for carrying out adsorption experiment at pH 12 (*as stated above in adsorption studies*). These basic functionalities on AC surface have also shown potential to enhance electrochemical activity in a carbonaceous material (Genovese et al. 2015).

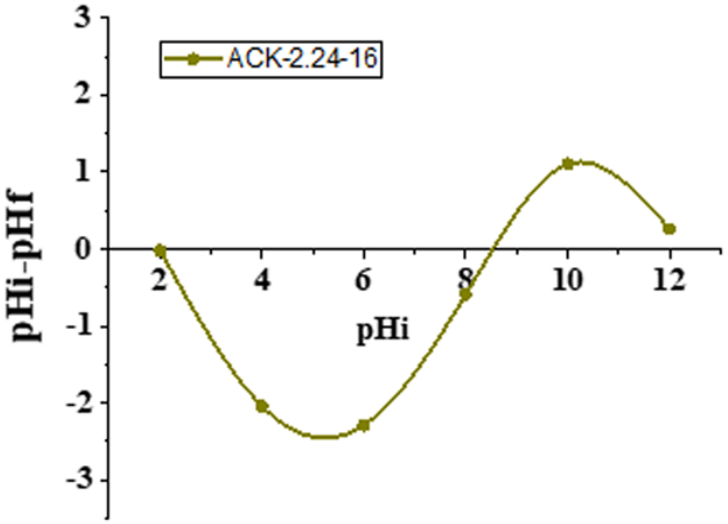

Figure 3.7: The pH-PZC of ACK-2.24-16 sample.

The Boehm technique indicated the surface chemical properties of the prepared ACK samples. **Table A 3 (Appendix A)** presents a summary of the properties of the surface functional groups (acidic and basic). The basic group value was much higher than the acidic group indicating, that the prepared ACKs sample surface is predominantly basic made up of chromene-type structures and pyrone-type oxides (Jaramillo, Álvarez & Gómez-Serrano 2010), due to activation using KOH as the activating agent. The ACK-2.24-16 sample possessed higher basic oxygen functional groups than other ACK samples, which aligns with pH-pzc observation.

3.3.2 Adsorption studies on prepared ACK samples

The adsorption experiment studies via iodine number and methylene blue number capacity for the prepared ACK samples are further presented in **Figure 3.8a-d.** From **Figure 3.8a and b**, the IR microwave time have more significance on the iodine number (IN) adsorption capacity compared to MPT. The IN adsorption is significantly reduced at lower IR (0.56 - 1.12) and MPT (8 - 12 min) with IN capacity range from 797.10 to 1188.06 mg/g. Herein, an incomplete open channel (**From Figure 3.2 and 3.3**) with low active sites results from insufficient reaction between the biochar and activating agent (KOH). At low IR, more MPT is required for development of porous channel (micropores) to aid IN adsorption. Increasing IR from 1.68 - 2.24 and MPT to 16 min results into an increment of IN adsorption, as the optimum IN capacity of 1900 mg/g for ACK-2.24-16 as shown in **Figure 3.8a and b.** The porous channels along with the 3D hierarchical network structure is evident with ACK-2.24-16 sample from **Figure 3.2** for high IN capacity, as

volatile matters that are detrimental to formation of this porous channel (micropores and mesopores) are been eliminated (Tan, Ahmad & Hameed 2008). Further increment in IR from 2.81 - 3.36 and MPT from 20 - 24 min after the optimum ACK sample results in decrease in IN adsorption in **Figure 3.8a and b**. This reduction in IN capacity is attributed to destruction of porous channel (formation of macropores) (**as seen in Figure 3.2 and 3.3**) and results to blockage of the porous channels (Cao, Xie, Lv & Bao 2006). The IN capacity of optimized ACK is also compared with biochar as presented in **Appendix A (Figure A 3).**

The methylene blue number (MBN) capacity for the ACK samples is shown in **Figure 3.8c and d**, the effect of IR was more dominant on MBN adsorption capacity as compared to MPT. The MBN capacity is reduced at lower IR (0.56 - 1.68) and MPT (8 - 12 min) as shown in **Figure 3.8c and d**. However, an increment in IR to 2.24 and MPT at 16 min results into higher MBN adsorption capacity up to 4000 mg/g. The optimum MBN capacity of 4000 mg/g was obtained for ACK-2.24-16 sample as shown in **Figure 3.8c and d**. The porous channel for ACK-2.24-16 along with increase active sites are factors for higher MBN adsorption capacity. However, an increase above this condition results into decrease in MBN adsorption capacity for ACK. Herein, the increment in both factors above the optimum condition causes excessive dehydration and collapse of porous channels (macropores formation), which reduces the adsorption efficiency of ACK. Corresponding Langmuir isotherm plot of prepared ACK samples at different IR, MPT, and biochar are shown in **Appendix A (Figure A 3).**

There is a relation between the yield of the activated carbon with the IN and MBN as shown in **Figure A 4 and A 5**. The yield decreases as the mass ratio of KOH to biochar mass increases, while both IN and MBN capacity tends to increase up to 2.24 of IR, then reduces with further increment in IR (**Figure A 4)**. Similar trend is also observable with the ACKs at different MPT at

constant IR of 2.24 (**Figure A 5**), where increasing MPT results to the yield of ACK to decrease, and the IN and MBN capacity increases. Similar observation have been reported by other studies utilizing biomass material for activated carbon synthesis (Ge, Ma, Wu, Xiao & Yan 2015, Duan, Srinivasakannan, Wang, Wang & Liu 2017, Chen, Chen, Sun, Zheng & Fu 2016). A decrease in yield might explain that pinecone with high volatile matter provided more sites for the 3D hierarchical porous formation.

The optimized ACK 2.24-16 sample with highest IN and MBN capacity was further compared with other AC produced from agricultural biomass using microwave and conventional route with KOH chemical impregnation as presented in **Table 3.1**. Such differences in the yield of activated carbon can be attributed to the different pyrolysis conditions and precursor types used. The higher IN and MBN adsorption capacity for ACK shows that pinecone is an efficient biomass source for good carbon production with well- developed porous structure. Sample ACK-2.24-16 with good porous channel (abundant micropores and mesopores, less of macropores), will offer enormous interspace for mass transport and pollutant adsorption (Wang et al. 2019). The 3D hierarchical network structure for ACK-2.24-16 sample with abundant micropores and mesopores, will also enhance charge carrier transport that will results to exceptional electrochemical attributes (Momodu et al. 2019) for a supported catalyst as further discussed in the electrochemical studies for the prepared ACK samples.

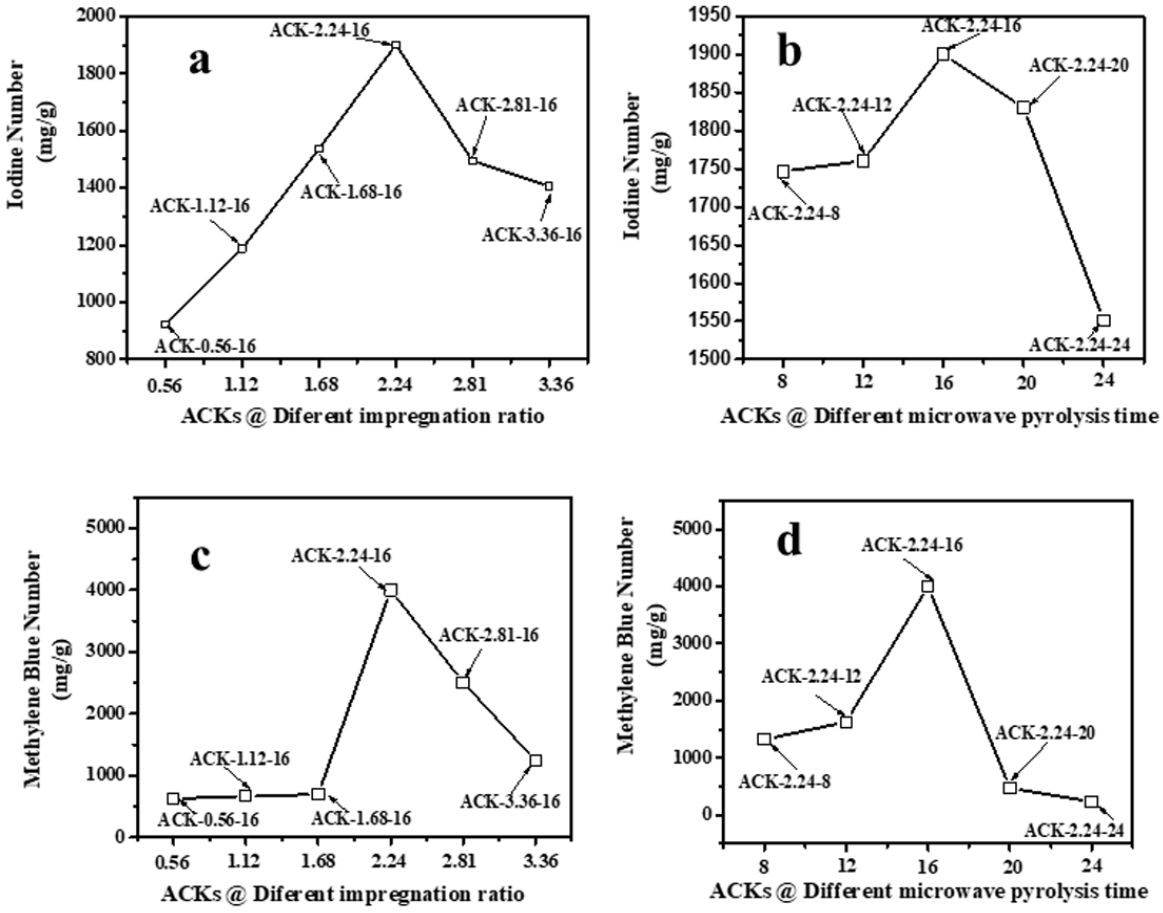

Figure 3.8: Iodine number and methylene blue number capacity of ACKs at different (a, c) impregnation ratio and (b, d) microwave pyrolysis time.

Table 3.1: Comparison of percentage yield, iodine number and methylene blue number adsorption capacity based on different biomass derived carbons.

Biomass Material	Heating Method	% Yield	Iodine Number (mg/g)	Methylene Blue Number (mg/g)	Reference
Pinecone	Microwave	53	1900	4000	**This Study**
Oil palm fiber	Microwave	32	n.m.	382	(Foo & Hameed 2012)
Oil palm residues	Microwave	73	n.m.	395	(Foo & Hameed 2011)
Cotton Stalk	Microwave	n.m.	285	294	(Deng et al. 2010)
Siris seed pods	Microwave	22	1760		(Ahmed & Theydan 2013)
Hevea seed coat	Conventional	n.m.	n.m.	22	(Hameed & Daud 2008)
Durian shell	Conventional	n.m.	n.m.	289	(Chandra, Mirna, Sudaryanto & Ismadji 2007)
Pistachio shells	Microwave	n.m	1276	331	(Baytar, Şahin, Saka & Ağrak 2018)
Sesame seed shells	Microwave and conventional	n..m	1199	103	(Sharif, Saka, Baytar & Şahin 2018)

n.m.: not mentioned

3.3.3 Electrochemical properties of ACK samples

The electrochemical properties of ACKs were further evaluated in a three-electrode system with 6 M KOH as an aqueous electrolyte and the results are shown in **Figure 3.9a-d**. The cyclic voltammetry (CV) curves of ACKs electrode at different IR and MPT (**Figure 3.9a and b**) collected at scan rate of 50 mV s^{-1}, exhibited a quasi-rectangular shape with bumps (caused by redox reactions). It observed from the CV curves, that the ACK-2.24-16 sample shows the largest current response demonstrating the best electrochemical properties among other samples (**Figure 3.9a and b)**. The high current response for ACK-2.24-16 is attributed to the 3D hierarchical network structure (with abundant micropore and mesopores) which can effectively absorb the electrolyte and minimize the diffusion resistance of the ion transport (Sun, Niu, Liu, Ji, Dou & Wang 2018; Wen, Zhang, Liu, Wen, Chen, Ma, Tang & Mijowska 2019).

Figure 3.9c and d shows the Nyquist plots of ACKs electrodes in a frequency range from 10 kHz to 10 mHz. All the samples exhibit small semicircle in the high frequency and almost vertical-line feature in the low frequency, which are ascribed to charge transfer and Warburg resistance, respectively (Liu, Liu, Sun, Zhou, Fu, Wang, Guo, Guo & Li 2018). Sample ACK-2.24-16 presents smallest semicircle and shortest Warburg-type line among all the samples (**Figure 3.9c and d)**, which correlates with good interfacial charge transfer resistance (Rct) and faster ion transportation from the electrolyte to the inner mesopores (Peng, Liang, Dong, Hu, Zhao, Cai, Xiao, Liu & Zheng 2018; Mohammed et al. 2019). Overall, hierarchical porous structure channels of ACK-2.24-16 is a key factor for good electrochemical properties for this material amongst the prepared ACKs samples.

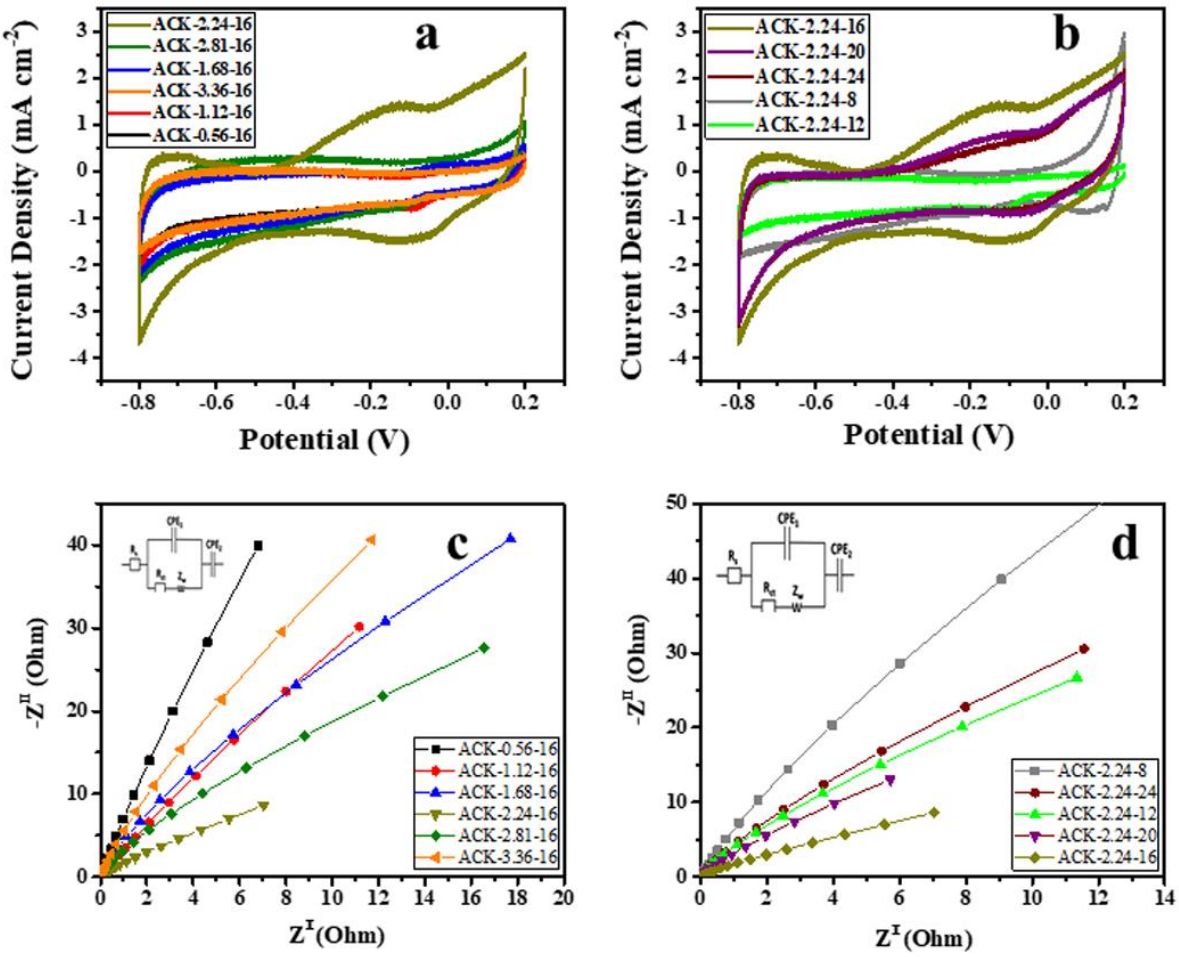

Figure 3.9: Cyclic Voltammetry curves, Electrochemical impedance spectroscopy of ACK at (a, c) different impregnation ratio and (b, d) different microwave times.

3.3.3 Surface area of optimized ACK

The N_2 adsorption-desorption isotherm for the optimized ACK-2.24-16 is shown in **Figure 3.10a**. The samples have a typical type IV isotherm, which indicates that they have mesoporous materials (Yang, Feng, Wang & Müllen 2011), with a contribution of micropores which correlates with the IN and MBN adsorption studies. ACK-2.24-16 samples also presented type H4 hysteresis loop in line with IUPAC nomenclature showing the presence of slit-shaped pores (Thommes, Kaneko, Neimark, Olivier, Rodriguez-Reinoso, Rouquerol & Sing 2015). The Brunauer–Emmett–Teller (BET) surface area calculated from the N_2 sorption isotherms is 427 m^2/g for ACK-2.24-16 with total pore volume are 0.203 cm^3/g respectively. Corresponding BJH adsorption pore size distribution of ACK-2.24-16 is between 2.68 – 16.5 nm indicating substantial amounts of mesopores present in the material (**Figure 3.10b**).

The prepared ACK-2.24-16 sample obtained in this study present considerable moderate BET surface area (427 m^2/g) in comparison to other AC produced from Peanut shell (96 m^2/g) (Al-Othman, Ali & Naushad 2012), Coconut coir (205 m^2/g) (Banerjee & Sharma 2013), Yellow mombin fruit stones (167 m^2/g) (Brito, Veloso, Santos, Bonomo & Fontan 2018) and coconut shell (478 m^2/g) (Mohammed, Nasri, Zaini, Hamza & Ani 2015). Though, the surface area is lower compared to carbon produced from other biomass through KOH activation, which includes empty fruit bunch (2114 m^2/g) (Egbosiuba, Abdulkareem, Kovo, Afolabi, Tijani, Auta & Roos 2020) and Onion (1914 m^2/g) (Zhang, Xu, Hou, Yin, Liu, He & Lin 2018). This further suggest that KOH activation of pinecone along with microwave pyrolysis approach is a good route to produce activated carbon as potential photocatalyst support.

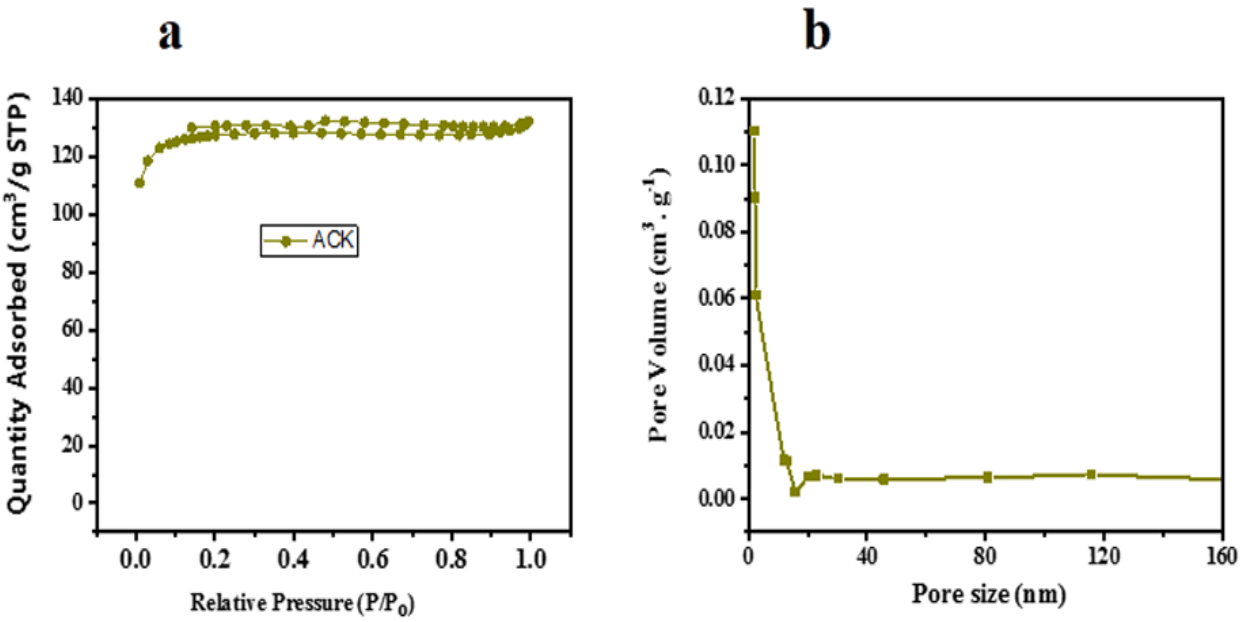

Figure 3.10: Nitrogen adsorption -desorption isotherms and pore size distribution of optimized ACK (ACK-2.24-16).

The ACK-2.24-16 sample with complex formation of 3D hierarchical structure, highest current response and least charge transfer resistance was chosen as the optimized carbon sample to disperse the visible light Ag-AgBr catalyst, for efficient photocatalytic activity on the removal of tetracycline antibiotic in this thesis. Also in this work, the contribution of ACK as catalyst support in the dispersion of silver-silver bromide composite (Ag-AgBr ACK) prepared via thermal polyol route (**Chapter 4**) and deposition-precipitation route (**Chapter 6**) was investigated.

3.4 Summary and concluding remarks

ACKs were synthesized from pinecone biomass through microwave pyrolysis and chemical activation route using KOH. The pinecone biomass was utilised for the first time as green carbon source to create environmentally friendly, highly efficient catalyst support material and two-stage pyrolysis increased the yield. The ACKs possesses 3D hierarchical network structure with abundant micropores and mesopores have plentiful oxygenated functional groups on their surface along with good electrochemical properties making the ACKs a promising catalyst support material for photocatalysis. ACK-2.24-16 sample had the highest iodine number and methylene blue number capacity (1900 mg/g and 4000 mg/g) among the prepared ACKs samples due to its excellent hierarchical structure. Meanwhile, the iodine and methylene blue adsorption of ACK-2.24-16 was much higher than that of other activated carbons from literature. Results from FTIR, boehm titration and pHPZC revealed the presence of a large number of basic groups on the surface of the optimized ACK. The optimized ACK-2.24-16 hierarchical network structure had a moderate surface area of 427 m^2/g. The ACK-2.24-16 hierarchical structure will significantly boost the characteristic properties of photocatalytic material (Ag/AgBr, which will be further discussed in **Chapter 4**) as a potential catalyst support based on its unique attributes. AC as vital catalyst support will improve the fast adsorption of pollutant towards the photocatalyst, thus enhancing activity and stability in the field of heterogeneous catalysis. Overall, this study offers an interesting perspective on the application of agricultural biomass as precursor in activated carbon production, as catalyst support in heterogeneous catalysis field for environmental remediation.

3.5 References

AHMED, M.J. & THEYDAN, S.K. 2013. Microporous activated carbon from Siris seed pods by microwave-induced KOH activation for metronidazole adsorption. *Journal of Analytical and Applied Pyrolysis*, 99, 101-109.

AL-OTHMAN, Z.A., ALI, R. & NAUSHAD, M. 2012. Hexavalent chromium removal from aqueous medium by activated carbon prepared from peanut shell: adsorption kinetics, equilibrium and thermodynamic studies. *Chemical Engineering Journal,* 184, 238-247.

ANTOLINI, E. 2016. Nitrogen-doped carbons by sustainable N-and C-containing natural resources as nonprecious catalysts and catalyst supports for low temperature fuel cells. *Renewable Sustainable Energy Reviews,* 58, 34-51.

ATCHUDAN, R., EDISON, T.N.J.I., PERUMAL, S. & LEE, Y.R. 2017. Green synthesis of nitrogen-doped graphitic carbon sheets with use of Prunus persica for supercapacitor applications. *Applied Surface Science,* 393, 276-286.

BANERJEE, S. & SHARMA, Y.C. 2013. Equilibrium and kinetic studies for removal of malachite green from aqueous solution by a low cost activated carbon. *Journal of Industrial Engineering Chemistry,* 19, 1099-1105.

BARDESTANI, R. & KALIAGUINE, S. 2018. Steam activation and mild air oxidation of vacuum pyrolysis biochar. *Biomass and Bioenergy,* 108, 101-112.

BARZEGAR, F., BELLO, A., DANGBEGNON, J.K., MANYALA, N. & XIA, X. 2017. Asymmetric supercapacitor based on activated expanded graphite and pinecone tree activated carbon with excellent stability. *Applied Energy,* 207, 417-426.

BAYTAR, O., ŞAHIN, Ö., SAKA, C. & AĞRAK, S. 2018. Characterization of microwave and conventional heating on the pyrolysis of pistachio shells for the adsorption of methylene blue and iodine. *Analytical Letters,* 51, 2205-2220.

BRITO, M.J.P., VELOSO, C.M., SANTOS, L.S., BONOMO, R.C.F. & FONTAN, R.D.C.I. 2018. Adsorption of the textile dye Dianix® royal blue CC onto carbons obtained from yellow mombin fruit stones and activated with KOH and H_3PO_4: kinetics, adsorption equilibrium and thermodynamic studies. *Powder Technology,* 339, 334-343.

CAO, Q., XIE, K.-C., LV, Y.-K. & BAO, W.-R. 2006. Process effects on activated carbon with large specific surface area from corn cob. *Bioresource Technology,* 97, 110-115.

CHANDRA, T.C., MIRNA, M., SUDARYANTO, Y. & ISMADJI, S. 2007. Adsorption of basic dye onto activated carbon prepared from durian shell: Studies of adsorption equilibrium and kinetics. *Chemical Engineering Journal,* 127, 121-129.

CHEN, X., WANG, X. & FU, X. 2009. Hierarchical macro/mesoporous TiO_2/SiO_2 and TiO_2/ZrO_2 nanocomposites for environmental photocatalysis. *Energy Environmental Science and Technology,* 2, 872-877.

CHEN, D., CHEN, X., SUN, J., ZHENG, Z. & FU, K. 2016. Pyrolysis polygeneration of pine nut shell: quality of pyrolysis products and study on the preparation of activated carbon from biochar. *Bioresource Technology,* 216, 629-636.

DUAN, X., SRINIVASAKANNAN, C., WANG, X., WANG, F. & LIU, X. 2017. Synthesis of activated carbon fibers from cotton by microwave induced H_3PO_4 activation. *Journal of the Taiwan Institute of Chemical Engineers,* 70 374-381.

DEMIR, M., KAHVECI, Z., AKSOY, B., PALAPATI, N.K., SUBRAMANIAN, A., CULLINAN, H.T., EL-KADERI, H.M., HARRIS, C.T. & GUPTA, R.B. 2015. Graphitic biocarbon from metal-catalyzed hydrothermal carbonization of lignin. *Industrial Engineering Chemistry Research,* 54, 10731-10739.

DENG, H., LI, G., YANG, H., TANG, J. & TANG, J. 2010. Preparation of activated carbons from cotton stalk by microwave assisted KOH and K_2CO_3 activation. *Chemical Engineering Journal,* 163, 373-381.

DONG, T., GAO, D., MIAO, C., YU, X., DEGAN, C., GARCIA-PÉREZ, M., RASCO, B., SABLANI, S.S. & CHEN, S. 2015. Two-step microalgal biodiesel production using acidic catalyst generated from pyrolysis-derived bio-char. *Energy Conversion Management,* 105, 1389-1396.

EGBOSIUBA, T., ABDULKAREEM, A., KOVO, A., AFOLABI, E., TIJANI, J., AUTA, M. & ROOS, W. 2020. Ultrasonic enhanced adsorption of methylene blue onto the optimized surface area of activated carbon: Adsorption isotherm, kinetics and thermodynamics. *Chemical Engineering Research Design*, 153, 315-336.

ESMAEILI, A. & ENTEZARI, M.H. 2016. Sonosynthesis of an Ag/AgBr/Graphene-oxide nanocomposite as a solar photocatalyst for efficient degradation of methyl orange. *Journal of Colloid and Interface Science*, 466, 227-237.

ESPINOSA, J.C., MANICKAM-PERIYARAMAN, P., BERNAT-QUESADA, F., SIVANESAN, S., ÁLVARO, M., GARCÍA, H. & NAVALÓN, S. 2019. Engineering of activated carbon surface to enhance the catalytic activity of supported cobalt oxide nanoparticles in peroxymonosulfate activation. *Applied Catalysis B: Environmental*, 249, 42-53.

FAN, H., ZHAO, X., YANG, J., SHAN, X., YANG, L., ZHANG, Y., LI, X. & GAO, M. 2012. ZnO-graphene composite for photocatalytic degradation of methylene blue dye. *Catalysis. Communication*, 29, 29–34.

FOO, K. & HAMEED, B. 2011. Preparation of oil palm (Elaeis) empty fruit bunch activated carbon by microwave-assisted KOH activation for the adsorption of methylene blue. *Desalination,* 275, 302-305.

FOO, K.Y. & HAMEED, B.H. 2012. Microwave-assisted preparation and adsorption performance of activated carbon from biodiesel industry solid reside: Influence of operational parameters. *Bioresource Technology,* 103, 398-404.

FU, X., LI, D., CHEN, J., ZHANG, Y., HUANG, W., ZHU, Y., YANG, J. & ZHANG, C. 2013. A microalgae residue based carbon solid acid catalyst for biodiesel production. *Bioresource Technology,* 146, 767-770.

GAO, Y., LI, L., JIN, Y., WANG, Y., YUAN, C., WEI, Y., CHEN, G., GE, J. & LU, H. 2015. Porous carbon made from rice husk as electrode material for electrochemical double layer capacitor. *Applied Energy,* 15, 341-47.

GE, X., MA, X., WU, Z., XIAO, X. & YAN, Y. 2015. Modification of coal-based activated carbon with nitric acid using microwave radiation for adsorption of phenanthrene and naphthalene. *Research on Chemical Intermediates*, 41, 7327-7347.

GENOVESE, M., JIANG, J., LIAN, K. & HOLM, N. 2015. High capacitive performance of exfoliated biochar nanosheets from biomass waste corn cob. *Journal of Materials Chemistry A,* 3, 2903-2913.

GIRALDO, L. & MORENO-PIRAJÁN, J.C. 2012. Synthesis of activated carbon mesoporous from coffee waste and its application in adsorption zinc and mercury ions from aqueous solution. *Journal of Chemistry,* 9, 938-948.

GOERTZEN, S.L., THÉRIAULT, K.D., OICKLE, A.M., TARASUK, A.C. & ANDREAS, H.A. 2010. Standardization of the Boehm titration. Part I. CO_2 expulsion and endpoint determination. *Carbon,* 48, 1252-1261.

GUAN, Y., WANG, S., WANG, X., SUN, C., HUANG, Y., LIU, C. & ZHAO, H. 2017. In situ self-assembled synthesis of Ag-AgBr/Al-MCM-41 with excellent activities of adsorption-photocatalysis. *Applied Catalysis B: Environmental,* 209, 329-338.

GUESH, K., MÁRQUEZ-ÁLVAREZ, C., CHEBUDE, Y. & DÍAZ, I. 2016. Enhanced photocatalytic activity of supported TiO_2 by selective surface modification of zeolite Y. *Applied Surface Science,* 378, 473-478.

HAMEED, B. & DAUD, F. 2008. Adsorption studies of basic dye on activated carbon derived from agricultural waste: Hevea brasiliensis seed coat. *Chemical Engineering Journal,* 139, 48-55.

HAYKIRI-ACMA, H. & YAMAN, S. 2007. Interpretation of biomass gasification yields regarding temperature intervals under nitrogen–steam atmosphere. *Fuel Processing Technology,* 88, 417-425.

HEIDARINEJAD, Z., RAHMANIAN, O., FAZLZADEH, M. & HEIDARI, M. 2018. Enhancement of methylene blue adsorption onto activated carbon prepared from Date Press Cake by low frequency ultrasound. *Journal of Molecular Liquids,* 264, 591-599.

HU, X., NANGO, K., BAO, L., LI, T., HASAN, M.M. & LI, C.-Z. 2019. High yields of solid carbonaceous materials from biomass. *Green chemistry,* 21, 1128-1140.

JARAMILLO, J., ÁLVAREZ, P. & GÓMEZ-SERRANO, V. 2010. Preparation and ozone-surface modification of activated carbon. Thermal stability of oxygen surface groups. *Applied Surface Science,* 256, 5232-5236.

JI, T., CHEN, L., MU, L., YUAN, R., KNOBLAUCH, M., BAO, F.S., SHI, Y., WANG, H. & ZHU, J. 2016. Green processing of plant biomass into mesoporous carbon as catalyst support. *Chemical Engineering Journal,* 295, 301-308.

JIANG, L., YUAN, X., ZENG, G., LIANG, J., CHEN, X., YU, H., WANG, H., WU, Z., ZHANG, J. & XIONG, T. 2018. In-situ synthesis of direct solid-state dual Z-scheme WO_3/g-C_3N_4/Bi_2O_3 photocatalyst for the degradation of refractory pollutant. *Applied Catalysis B: Environmental,* 227, 376-385.

JIANG, Z., ZHANG, X., YUAN, Z., CHEN, J., HUANG, B., DIONYSIOU, D.D. & YANG, G. 2018. Enhanced photocatalytic CO_2 reduction via the synergistic effect between Ag and activated carbon in TiO_2/AC-Ag ternary composite. *Chemical Engineering Journal,* 348, 592-598.

KAUR, B., GUPTA, R.K. & BHUNIA, H. 2019. Chemically activated nanoporous carbon adsorbents from waste plastic for CO_2 capture: Breakthrough adsorption study. *Microporous Mesoporous Materials,* 282, 146-158.

KHASRI, A., BELLO, O.S. & AHMAD, M.A. 2018. Mesoporous activated carbon from Pentace species sawdust via microwave-induced KOH activation: optimization and methylene blue adsorption. *Research on Chemical Intermediates,* 44, 5737-5757.

KıLıÇ, M., APAYDıN-VAROL, E. & PÜTÜN, A.E. 2012. Preparation and surface characterization of activated carbons from Euphorbia rigida by chemical activation with $ZnCl_2$, K_2CO_3, NaOH and H_3PO_4. *Applied Surface Science,* 261, 247-254.

KUDIN, K.N., OZBAS, B., SCHNIEPP, H.C., PRUD'HOMME, R.K., AKSAY, I.A. & CAR, R. 2008. Raman spectra of graphite oxide and functionalized graphene sheets. *Nano Letters,* 8, 36-41.

KUMAR, J., MALLAMPATI, R., ADIN, A. & VALIYAVEETTIL, S. 2014. Functionalized carbon spheres for extraction of nanoparticles and catalyst support in water. *ACS Sustainable Chemistry Engineering,* 2, 2675-2682.

KUNDU, A., GUPTA, B.S., HASHIM, M., SAHU, J., MUJAWAR, M. & REDZWAN, G. 2015. Optimisation of the process variables in production of activated carbon by microwave heating. *RSC Advances,* 5, 35899-35908.

LAM, S.S., LIEW, R.K., WONG, Y.M., AZWAR, E., JUSOH, A. & WAHI, R. 2017a. Activated carbon for catalyst support from microwave pyrolysis of orange peel. *Waste Biomass Valorization,* 8, 2109-2119.

LAM, S.S., LIEW, R.K., WONG, Y.M., YEK, P.N.Y., MA, N.L., LEE, C.L. & CHASE, H.A. 2017b. Microwave-assisted pyrolysis with chemical activation, an innovative method to convert orange peel into activated carbon with improved properties as dye adsorbent. *Journal of Cleaner Production,* 162, 1376-1387.

LEI, X., WANG, M., LAI, Y., HU, L., WANG, H., FANG, Z., LI, J. & FANG, J. 2017. Nitrogen-doped micropore-dominant carbon derived from waste pinecone as a promising metal-free electrocatalyst for aqueous zinc/air batteries. *Journal of Power Sources,* 365, 76-82.

LI, J., LIU, W., XIAO, D. & WANG, X. 2017. Oxygen-rich hierarchical porous carbon made from pomelo peel fiber as electrode material for supercapacitor. *Applied Surface Science,* 416, 918-924.

LI, Y., SAMAD, Y.A., POLYCHRONOPOULOU, K., ALHASSAN, S.M. & LIAO, K. 2014. From biomass to high performance solar–thermal and electric–thermal energy conversion and storage materials. *Journal of Materials Chemistry A,* 2, 7759-7765.

LI, X., TIE, K., LI, Z., GUO, Y., LIU, Z., LIU, X., LIU, X., FENG, H. & ZHAO, X.S. 2018. Nitrogen-doped hierarchically porous carbon derived from cherry stone as a catalyst support for purification of terephthalic acid. *Applied Surface Science,* 447, 57-62.

LIEW, R.K., CHONG, M.Y., OSAZUWA, O.U., NAM, W.L., PHANG, X.Y., SU, M.H., CHENG, C.K., CHONG, C.T. & LAM, S.S. 2018. Production of activated carbon as catalyst support by microwave pyrolysis of palm kernel shell: a comparative study of chemical versus physical activation. *Research on Chemical Intermediates*, 44, 3849-3865.

LIU, X., LIU, X., SUN, B., ZHOU, H., FU, A., WANG, Y., GUO, Y.-G., GUO, P. & LI, H. 2018. Carbon materials with hierarchical porosity: Effect of template removal strategy and study on their electrochemical properties. *Carbon,* 130, 680-691.

LONG, C., CHEN, X., JIANG, L., ZHI, L. & FAN, Z. 2015. Porous layer-stacking carbon derived from in-built template in biomass for high volumetric performance supercapacitors. *Nano Energy,* 12, 141-151.

LU, J., HU, H., YANG, S., SHANMUGAM, P., WEI, W., SELVARAJ, M. & XIE, J. 2018. ZnS@carbonaceous aerogel composites fabricated in production of hydrogen and for removal of organic pollutants. *Journal of Materials Science: Materials in Electronics,* 29, 8523-8534.

LUO, L., CHEN, T., LI, Z., ZHANG, Z., ZHAO, W. & FAN, M. 2018. Heteroatom self-doped activated biocarbons from fir bark and their excellent performance for carbon dioxide adsorption. *Journal of CO_2 Utilization,* 25, 89-98.

MADEJOVA, J. 2003. FTIR techniques in clay mineral studies. *Vibrational spectroscopy,* 31, 1-10.

MOHAMMED, A.A., CHEN, C. & ZHU, Z. 2019. Low-cost, high-performance supercapacitor based on activated carbon electrode materials derived from baobab fruit shells. *Journal of colloid Interface Science,* 538, 308-319.

MOHAMMED, J., NASRI, N.S., ZAINI, M.A.A., HAMZA, U.D. & ANI, F.N. 2015. Adsorption of benzene and toluene onto KOH activated coconut shell based carbon treated with NH_3. *International Biodeterioration Biodegradation,* 102, 245-255.

MOMODU, D., OKAFOR, C., MANYALA, N., BELLO, A., ZEBAZEKANA, M.G. & NTSOENZOK, E. 2019. Transformation of Plant Biomass Waste into Resourceful Activated Carbon Nanostructures for Mixed-Assembly Type Electrochemical Capacitors. *Waste Biomass Valorization,* 10, 1741-1753.

MUNIANDY, L., ADAM, F., MOHAMED, A.R. & NG, E.-P. 2014. The synthesis and characterization of high purity mixed microporous/mesoporous activated carbon from rice husk using chemical activation with NaOH and KOH. *Microporous Mesoporous Materials,* 197, 316-323.

NAITO, K., TACHIKAWA, T., FUJITSUKA, M. & MAJIMA, T. 2008. Single-molecule observation of photocatalytic reaction in TiO_2 nanotube: importance of molecular transport through porous structures. *Journal of the American Chemical Society,* 131, 934-936.

NANDA, S., GONG, M., HUNTER, H.N., DALAI, A.K., GÖKALP, I. & KOZINSKI, J.A. 2017. An assessment of pinecone gasification in subcritical, near-critical and supercritical water. *Fuel Processing Technology,* 168, 84-96.

NUHOGLU, Y. & OGUZ, E. 2003. Removal of copper (II) from aqueous solutions by biosorption on the cone biomass of Thuja orientalis. *Process Biochemistry*, 38, 1627-1631.

PENG, L., LIANG, Y., DONG, H., HU, H., ZHAO, X., CAI, Y., XIAO, Y., LIU, Y. & ZHENG, M. 2018. Super-hierarchical porous carbons derived from mixed biomass wastes by a stepwise removal strategy for high-performance supercapacitors. *Journal of Power Sources,* 377, 151-160.

PRAHAS, D., KARTIKA, Y., INDRASWATI, N. & ISMADJI, S. 2008. Activated carbon from Jack fruit peel waste by H_3PO_4 chemical activation: pore structure and surface chemistry characterization. . *Chemical Engineering Journal,* 140, 32-42.

PUZIY, A., PODDUBNAYA, O., MARTıNEZ-ALONSO, A., SUÁREZ-GARCıA, F. & TASCÓN, J. 2002. Synthetic carbons activated with phosphoric acid: I. Surface chemistry and ion binding properties. *Carbon,* 40, 1493-1505.

RAZA, W., ALI, F., RAZA, N., LUO, Y., KWON, E.E., YANG, J., KUMAR, S., MEHMOOD, A. & KIM, K.-H. 2018. Recent advancements in supercapacitor technology. *Nano Energy*, 52, 441-473.

ROBBINS, W.W., WEIER, T.E. & STOCKING, C.R. 1957. Botany—An Introduction to Plant Science. *Soil Science,* 84, 180.

SHARIF, Y.M., SAKA, C., BAYTAR, O. & ŞAHIN, Ö. 2018. Preparation and Characterization of Activated Carbon from Sesame Seed Shells by Microwave and Conventional Heating with Zinc Chloride Activation. *Analytical Letters,* 51, 2733-2746.

SHEN, J., HUANG, G., AN, C., XIN, X., HUANG, C. & ROSENDAHL, S. 2018. Removal of Tetrabromobisphenol A by adsorption on pinecone-derived activated charcoals: Synchrotron FTIR, kinetics and surface functionality analyses. *Bioresource Technology,* 247, 812-820.

SHIMODAIRA, N. & MASUI, A. 2002. Raman spectroscopic investigations of activated carbon materials. *Journal of Applied Physics,* 92, 902-909.

SINGH, Y.D., MAHANTA, P. & BORA, U. 2017. Comprehensive characterization of lignocellulosic biomass through proximate, ultimate and compositional analysis for bioenergy production. *Renewable Energy,* 103, 490-500.

SUÁREZ, D., MENÉNDEZ, J.A., FUENTE, E. & MONTES-MORÁN, M.A. 1999. Contribution of pyrone-type structures to carbon basicity: an ab initio study. *Langmuir,* 15, 3897-3904.

SUN, J., NIU, J., LIU, M., JI, J., DOU, M. & WANG, F. 2018. Biomass-derived nitrogen-doped porous carbons with tailored hierarchical porosity and high specific surface area for high energy and power density supercapacitors. *Applied Surface Science,* 427, 807-813.

SUN, L., ZHANG, Y., YE, X., LIU, H., ZHANG, H., WU, A. & WU, Z. 2017. Removal of I– from aqueous solutions using a biomass carbonaceous aerogel modified with KH-560. *ACS Sustainable Chemistry Engineering,* 5, 7700-7708.

TAN, I., AHMAD, A. & HAMEED, B. 2008. Preparation of activated carbon from coconut husk: optimization study on removal of 2, 4, 6-trichlorophenol using response surface methodology. *Journal of Hazardous Materials,* 153, 709-717.

TANG, Y.-B., LIU, Q. & CHEN, F.-Y. 2012. Preparation and characterization of activated carbon from waste ramulus mori. *Chemical Engineering Journal,* 203, 19-24.

THOMMES, M., KANEKO, K., NEIMARK, A.V., OLIVIER, J.P., RODRIGUEZ-REINOSO, F., ROUQUEROL, J. & SING, K.S. 2015. Physisorption of gases, with special reference to the evaluation of surface area and pore size distribution (IUPAC Technical Report). *Pure Applied Chemistry,* 87, 1051-1069.

TITIRICI, M.-M. & ANTONIETTI, M. 2010. Chemistry and materials options of sustainable carbon materials made by hydrothermal carbonization. *Chemical Society Reviews,* 39, 103-116.

WAN MAHARI, W., ZAINUDDIN, N., WAN NIK, W., CHONG, C. & LAM, S.J. 2016. Pyrolysis recovery of waste shipping oil using microwave heating. *Energies,* 9, 780.

WANG, H., LIU, H., WANG, S., LI, L. & LIU, X. 2018. Influence of tunable pore size on photocatalytic and photoelectrochemical performances of hierarchical porous TiO_2/C nanocomposites synthesized via dual-Templating. *Applied Catalysis B: Environmental,* 224, 341-349.

WANG, H., LIU, X., WANG, S. & LI, L. 2018. Dual templating fabrication of hierarchical porous three-dimensional ZnO/carbon nanocomposites for enhanced photocatalytic and photoelectrochemical activity. *Applied Catalysis B: Environmental,* 222, 209-218.

WANG, J., DUAN, X., DONG, Q., MENG, F., TAN, X., LIU, S. & WANG, S. 2019. Facile synthesis of N-doped 3D graphene aerogel and its excellent performance in catalytic degradation of antibiotic contaminants in water. *Carbon,* 144, 781-790.

WATANIYAKUL, P., BOONNOUN, P., QUITAIN, A.T., KIDA, T., LAOSIRIPOJANA, N. & SHOTIPRUK, A. 2018. Preparation of hydrothermal carbon acid catalyst from defatted rice bran. *Industrial Crops Products,* 117, 286-294.

WEN, X.-J., NIU, C.-G., ZHANG, L., LIANG, C. & ZENG, G.-M. 2018. A novel Ag_2O/CeO_2 heterojunction photocatalysts for photocatalytic degradation of enrofloxacin: possible degradation pathways, mineralization activity and an in depth mechanism insight. *Applied Catalysis B: Environmental,* 221, 701-714.

WEN, Y., ZHANG, L., LIU, J., WEN, X., CHEN, X., MA, J., TANG, T. & MIJOWSKA, E. 2019. Hierarchical porous carbon sheets derived on a MgO template for high-performance supercapacitor applications. *Nanotechnology,* 30, 295703.

XIANG, Q., YU, J. & JARONIEC, M. 2012. Graphene-based semiconductor photocatalysts. *Chemical Society Reviews,* 41, 782-796.

XIE, X., LI, S., ZHANG, H., WANG, Z. & HUANG, H. 2019. Promoting charge separation of biochar-based Zn-TiO_2/pBC in the presence of ZnO for efficient sulfamethoxazole photodegradation under visible light irradiation. *Science of The Total Environment,* 659, 529-539.

XING, X., JIANG, W., LI, S., ZHANG, X. & WANG, W. 2019. Preparation and analysis of straw activated carbon synergetic catalyzed by $ZnCl_2$-H_3PO_4 through hydrothermal carbonization combined with ultrasonic assisted immersion pyrolysis. *Waste Management,* 8964-72.

YANG, H., YAN, R., CHEN, H., LEE, D.H. & ZHENG, C. 2007. Characteristics of hemicellulose, cellulose and lignin pyrolysis. *Fuel,* 86, 1781-1788.

YANG, S., FENG, X., WANG, X. & MÜLLEN, K. 2011. Graphene-based carbon nitride nanosheets as efficient metal-free electrocatalysts for oxygen reduction reactions. *Angewandte Chemie International Edition,* 50, 5339-5343.

YANG, Y., CHIANG, K. & BURKE, N. 2011. Porous carbon-supported catalysts for energy and environmental applications: A short review. *Catalysis Today,* 178, 197-205.

YANG, B., LIU, Y., LIANG, Q., CHEN, M., MA, L., LI, L., LIU, Q., TU, W., LAN, D. & CHEN, Y. 2019. Evaluation of activated carbon synthesized by one-stage and two-stage co-pyrolysis from sludge and coconut shell. *Ecotoxicology Environmental Safety*, 170, 722-731.

YU, Y., ZHU, Z., FAN, W., LIU, Z., YAO, X., DONG, H., LI, C. & HUO, P. 2018. Making of a metal-free graphitic carbon nitride composites based on biomass carbon for efficiency enhanced tetracycline degradation activity. *Journal of the Taiwan Institute of Chemical Engineers,* 89, 151-161.

YUAN, D., ZHANG, T., GUO, Q., QIU, F., YANG, D. & OU, Z. 2018. Recyclable biomass carbon@ SiO_2@MnO_2 aerogel with hierarchical structures for fast and selective oil-water separation. *Chemical Engineering Journal,* 351, 622-630.

YUAN, X., JIANG, L., LIANG, J., PAN, Y., ZHANG, J., WANG, H., LENG, L., WU, Z., GUAN, R. & ZENG, G. 2019. In-situ synthesis of 3D microsphere-like In_2S_3/$InVO_4$ heterojunction with efficient photocatalytic activity for tetracycline degradation under visible light irradiation. *Chemical Engineering Journal,* 356, 371-381.

ZHAI, Y., DOU, Y., LIU, X., PARK, S.S., HA, C.-S. & ZHAO, D. 2011. Soft-template synthesis of ordered mesoporous carbon/nanoparticle nickel composites with a high surface area. *Carbon,* 49, 545-555.

ZHANG, G., SONG, A., DUAN, Y. & ZHENG, S. 2018. Enhanced photocatalytic activity of TiO_2/zeolite composite for abatement of pollutants. *Microporous Mesoporous Materials,* 255, 61-68.

ZHANG, H., FAN, X., QUAN, X., CHEN, S. & YU, H. 2011. Graphene sheets grafted Ag@ AgCl hybrid with enhanced plasmonic photocatalytic activity under visible light. *Environmental Science and Technology,* 45, 5731-5736.

ZHANG, W., XU, J., HOU, D., YIN, J., LIU, D., HE, Y. & LIN, H. 2018. Hierarchical porous carbon prepared from biomass through a facile method for supercapacitor applications. *Journal of Colloid Interface Science*, 530, 338-344.

ZHU, M., CHEN, P. & LIU, M. 2011. Graphene oxide enwrapped Ag/AgX (X= Br, Cl) nanocomposite as a highly efficient visible-light plasmonic photocatalyst. *ACS Nano,* 5, 4529-4536.

Chapter 4. Design of ordered Ag/AgBr nanostructures coupled activated carbon with enhanced charge carriers separation efficiency for photodegradation of tetracycline under visible light

Abstract

Oriented design of ordered Ag/AgBr photocatalyst with high separation of photoinduced charge carriers is crucial for high catalytic performance. In this chapter, ordered Ag/AgBr nanostructures were synthesized by facile thermal polyol method in the presence of char-microwave assisted activated carbon (AABR-ACK). The influence of four synthesis key variables comprising of the mass of surfactant, temperature, the mass of catalyst support and time, and their simultaneous interactions on the photodegradation of tetracycline (TC) were investigated using response surface methodology (RSM). The time and temperature had significant influences on the TC photocatalytic removal under visible light, as observed from the RSM model. The analysis of XRD, FTIR, SEM, optical and electrochemical properties for AABR-ACK composites evidenced the formation of ordered nanostructures with enhanced charge carriers separation efficiency. It was found that 92% of TC was decomposed after 180 min by optimized AABR-ACK 11. Furthermore, the inorganic phosphate anion retards the degradation performance of AABR-ACK 11 on TC removal. The AABR-ACK 11 composite also exhibits higher activity and reusability for degradation of TC without any major reduction in the performance. This work provides new insight into engineering ordered Ag/AgBr nanostructures through optimization of synthesis variables, with potential application for degradation of antibiotic pollutants.

Keywords: Ordered Ag/AgBr nanostructures, Thermal polyol, Response surface methodology, Tetracycline, Visible light

4.1. Introduction

Pharmaceutical antibiotics are widely used in the environment to protect human health and promotes livestock growth, whilst partial metabolism by human or animal body results in large fraction of these antibiotics being discharged into the environment by excretion from urine and faeces, thus creates water pollution (Luo, Xu, Rysz, Wang, Zhang & Alvarez 2011; Polesel, Andersen, Trapp & Plósz 2016). Tetracycline (TC), a commonly used antibiotic with bio-refractory properties, pose greater threat to the environment (Jiang, Yuan, Zeng, Chen, Wu, Liang, Zhang, Wang & Wang 2017; Chen, Jing, Teng & Wang 2018). As such, effective removal of TC is crucial to protect the environment and human health. The development of visible-light-driven (VLD) photocatalyst materials with strong catalytic activity in the full solar spectrum is gaining interest for their application in photocatalytic degradation of antibiotic pollutants (Wen, Niu, Zhang, Liang & Zeng 2018; Zhou, Lai, Huang, Zeng, Zhang, Cheng, Hu, Wan, Xiong & Wen 2018). These VLD photocatalysts are viewed as attractive alternatives to the conventional photocatalysts materials which operate only in the ultraviolet region (Dong, Zeng, Tang, Fan, Zhang, He & He 2015). The unique surface plasmon resonance (SPR) of noble-metal nanoparticles (e.g. Ag, Au, Pt) has been attributed to VLD photocatalytic abilities (Hou, Li, Zhao, Chen & Raston 2012b; Shi, Li, Sun, An, Zhao & Wong 2014). A typical example is Ag anchored on the surface of AgX which combines to form a narrow bandgap photocatalyst resulting in a highly efficient visible light response plasmonic photocatalysts (Ag/AgX, X= Cl, Br and I) (Hu, Peng, Hu, Nie, Zhou, Qu & He 2009; Zhang, Li, Wang, Huang, Zeng & Xu 2014). Ag/AgBr catalyst are known to be more efficient than Ag/AgCl due to the lower electron affinity of Br^o atom and small bandgap as compared with Cl^o atoms (Wang, Huang, Zhang, Qin, Jin, Dai, Wang, Wei, Zhan & Wang 2009; Xu, Yan, Xu, Song, Li, Xia, Huang & Wan 2013).

Nevertheless, key challenges of Ag/AgBr for the practical application include high recombination of photo-induced electron-hole pairs and irregular nanostructures, resulting in low photocatalytic activities (Chen, Li, Chen, Gao, Fan, Li, Li, Zhang, Sun & Gao 2012). The coupling of the Ag/AgBr catalyst with carbonaceous support such as graphene oxide, carbon nanotube, and activated carbon is considered an effective approach to overcoming these problems (Zhu, Chen & Liu 2012; Xu, Xu, Yan, Li, Huang, Zhang, Huang & Wan 2013; McEvoy & Zhang 2016; Zhang, Shi, Wang & Hu 2018). Activated carbon (López-Peñalver, Sánchez-Polo, Gómez-Pacheco & Rivera-Utrilla) among these carbonaceous materials, has attracted focus due to its abundance, non-toxicity, low cost, rich oxygenated functional groups and electron conductivity (Huang, Wang, Jiao, Cai, Shen, Zhou, Cao, Lü & Cao 2018). The 3D interconnected carbon structure with high porosity, and the high surface area of AC from renewable source (Zhang, Xu, Hou, Yin, Liu, He & Lin 2018; Khan, Marpaung, Young, Lin, Islam, Alsheri, Ahamad, Alhokbany, Ariga & Shrestha 2019) makes it a promising candidate as a catalyst support. Previous work has shown that the biomass AC support form ordered nanostructure composites with a photocatalyst, which also facilitates the separation of charge carriers and prolongs the lifetime of electron-hole pairs (Gao, Lu, Zhao, Zhu, Wang, Wang, Hua, Li, Huo & Song 2016; Huang et al. 2018; Li, Chen, Yin, Zhu, Li & Ma 2018; Yu, Zhu, Fan, Liu, Yao, Dong, Li & Huo 2018) with high catalytic activities. However, the conventional photo-reduction process for dispersing plasmonic Ag/AgX catalyst on carbonaceous materials results in irregular morphologies, agglomeration, and aggregation of actives sites that affect degradation activities (Zhang, Fan, Quan, Chen & Yu 2011; McEvoy & Zhang 2014; Esmaeili & Entezari 2015).

The synthesis of stable and efficient Ag/AgBr plasmonic photocatalysts with ordered nanostructures have been achieved through a host of synthetic routes (Choi, Byun, Bae & Lee 2013; Li, Wang, Zhang, Hu, Chen & Guo 2013; Yan, Zhang, Luo, Ma, Lin & You 2013; Chen,

Li, Huang, Guo, Qiao, Qiu, Wang, Jiang & Yuan 2015; Xiao, Ge, Han, Li, Zhao, Xin, Fang, Wu & Qiu 2015). Recently, a thermal polyol route has shown exceptional design of isotropically or anisotropically nanostructures of Ag/AgBr (An, Peng & Sun 2010; Chen et al. 2015), that are often difficult to obtain through the traditional photo-reduction process (Wang et al. 2009)**.** The polyol solvent used in this synthetic approach can also influence the nanostructures control, whilst behaving as a reducing agent to achieve metallic Ag particles and still being coherent with other heating approaches (Xu, Shen, Zhou, Qiu, Zhu & Chen 2013; Yan et al. 2013; Gaikwad, Koratti & Mukherjee 2019). Of emphasis is that the preparation main variables such as synthesis time (Xu, X. et al. 2013; Wu, Shen, Ji, Zhu, Zhou, Zang, Yu, Chen, Song & Feng 2017), reaction temperature (Chen et al. 2015; Wu et al. 2017), structural directing agent (Xu, X. et al. 2013; Chen et al. 2015), and catalyst support can also engineer ordered nanostructures with fast interfacial charge separation and enhance the photocatalytic activities of Ag/AgX catalyst. Thus, the optimization of synthesis parameters is desirable to obtain high photocatalytic activities for the Ag/AgBr catalyst materials on organic pollutant removal.

The conventional optimization method (optimizing one preparation variable at a time) was previously employed for preparation factors influencing Ag/AgBr catalytic performance, demand time and cost especially with large amounts of variables (Chen et al. 2015). Response surface methodology (RSM) is an appropriate statistical technique for an experimental design with a large number of variables, evaluation of simultaneous interaction of preparation conditions and optimization of the results to yield the desirable response. However, there have been no reports in the literature on the application of RSM that correlates the relationship between synthesis variables and photocatalytic performance using regulated Ag/AgBr coupled biomass activated carbon (AABR-ACK) composites on TC antibiotic removal.

In this study, AABR-ACK composites were prepared via the thermal polyol route, with the purpose of designing ordered nanostructures and improving their charge carrier's separation efficiency. The ACK with the best characteristics (**see Chapter 3**) was selected to prepare the AABR-ACK composites. RSM experimental design was first applied to investigate and optimize the relevant preparation factors of AABR-ACK composites associated with a removal efficiency of TC in aqueous solution under visible light irradiation. The integral properties of the prepared composites comprising of crystal phase, morphology structure, optical and electrochemical characteristics were investigated in details, based on observation from the RSM findings. The most appropriate photocatalyst (AABR-ACK) exhibited enhanced photocatalytic activity, which was attributed to the ordered nanospheres structure with enhanced separation of photo-induced charge carriers. The ordered AABR-ACK photocatalyst will be a promising choice for antibiotic removal in environmental fields.

4.2. Experimental section

4.2.1 Materials

$AgNO_3$ was obtained from Merck Chemical Company. Hexadecyltrimethylammonium bromide (HTAB, 99%), polyvinylpyrrolidone (PVP, M.W. 58000; K29-32), ethylene glycol was purchased from Acros. Ethanol, sodium hydroxide isopropyl alcohol (IPA), Ethylenediaminetetraacetic acid disodium salt (EDTA 2Na), benzoquinone (BQ) and tetracycline hydrochloride (TC, 99%) were purchased from Sigma Aldrich. All the reagents were used as received and water used in all these experiments was purified with a Millipore system. All glassware was soaked in 5% w/v HNO_3 for at least 2 hours and rinsed with purified water before use. Stock solutions for TC were kept in dark amber bottles when not in use. A 36 W white light-emitting diode (LED) light strip (A-NF1210W12V-120, Wahwang Holdings) equipped with a visible light wavelength ($\lambda > 400$ nm) was used as the light source in all these

studies (**Figure 4.1a**). As presented in the appendix (**Figure 4.1b**), the LED source emits different emission wavelengths.

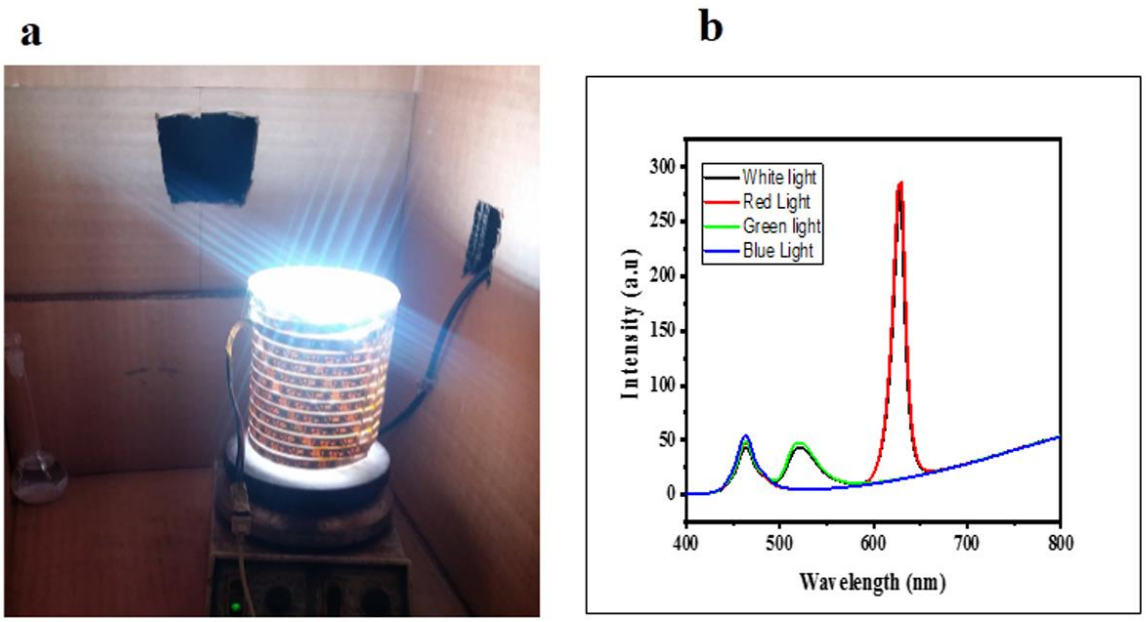

Figure 4.1: (a) LED light in operation; (b) LED Light Spectra.

4.2.2 Preparation of AABR-ACK

The activated carbon (ACK-2.24-16) with the best characteristics, prepared from pinecone biomass is utilized in this section as the catalyst support throughout this work has been described in **Chapter 3 (Section 3.2.2)**. The synthesis of Ag/AgBr on ACK (AABR-ACK) was carried out through a modified thermal polyol route (Chen et al. 2015). Typically, 18 mL of ethylene glycol was poured into a round-bottom flask which was heated at 60℃ for 30 min. Different weight of PVP (0.12, 0.26 and 0.4 g) and 480 mg of HTAB were added to the solution. Different masses of ACK (0.01, 0.03 and 0.06 g) were then added to the mixture. After proper mixing to completely dissolve the PVP and HTAB, 3 ml ethylene glycol solution

containing silver nitrate was slowly added drop-wise to the above mixture. The solution was maintained at 60 °C for an additional 30 min and the mixture was then heated at different temperatures (100, 140 and 180 °C) in line with an experimental design using RSM design. After attainment of the desired temperature, different reaction times of 10, 17.5 and 25 min were used for further generation of metallic Ag particles. The reaction vessel was cooled down to room temperature in the air. The resulting catalyst was collected by centrifugation (REMI benchtop centrifuge-R-8D) and washed thoroughly with ethanol and dried in an oven for 12 hr. In addition, other comparative samples (AABR and AgBr catalyst) were obtained under similar preparation route without ACK and light illumination.

4.2.3 Characterizations

The morphology and composition of the samples and optimized activated carbon (ACK-2.24-16) were recorded by scanning electron microscopy (Zeiss Leo 1430 VP) and energy dispersive X-ray spectrometer (EDS, INCA). The specimen was prepared by spreading sample powder onto a carbon grid, sputter-coated with a ~10 nm thick layer of conductive chromium using 108C Auto Carbon Coater. The structure of the most active catalyst, AABR-ACK 11 was further characterized by transmission electron microscope (TEM, JEOL JEM-2010) at an accelerating voltage of 200 kV. The sample was dispersed in water and dropped onto a copper grid for analysis. The crystal structures and phase data for the AABR-ACK photocatalysts were determined by Shimadzu X-ray 700 (XRD) with Cu Kαradiation in the 2θ range of 20–80 at 40 Kv and 40 mA. X-ray photoelectron spectroscopy (XPS) measurements were conducted using a Thermo Scientific ESCALAB spectrometer. A monochromatic Al Kα ($h\nu = 1486.7$ eV) x-ray beam source was used at a power of 100 W, 15 kV electron beam to analyse different binding energy peaks. The functional group on the samples was investigated by Fourier transform infrared spectrometer (Perkin Elmer spectrum 400) within the range of 600–4000

cm^{-1}. The UV–visible spectrum of the samples was recorded using Ocean Optics high-resolution spectrometer (Maya 2000) equipped with an integrating sphere accessory, using $BaSO_4$ as blank reference within the wavelength range of 350 to 800 nm. The photoluminescence (PL) emission spectra of samples were detected with a Fluorescence spectrophotometer (FP-8600 Spectrofluorometer, Jasco) using a Xenon lamp as the excitation source at room temperature, and the excitation wavelength was 365 nm. Electrochemical impedance spectroscopy (EIS) was carried out in a three-way electrode system using a Biologic SP 240 potentiostat workstation. The working, reference and counter electrode were glassy carbon electrode, Ag/AgCl (in saturated KCl) and platinum wire respectively. The glassy carbon electrode (GCE, 6 mm in diameter) was thoroughly cleaned with 0.3 and 1-micron alumina powder to eliminate impurities, then further washed with double distilled water and ethanol solution. The washed GCE was dried under 100 W infrared lamp for 5 min, then the catalyst material (5 mg) were dispersed into 0.5 ml (Dimethylformamide solution) solution using ultrasonic bath machine (Bransonic CPXH) to obtain a homogenous suspension and 20 µL of it is drop cast on the clean GCE surface. Linear sweep voltammetry was swept linearly from 0.5 to 2.0 V vs SCE at a scan rate of 50 mV s^{-1} using 0.2 M sodium sulphate. The EIS experiments were carried out between frequency ranges of 100 KHz to 10 mHz with a perturbation amplitude of 5 mV in 5 mM ferrocyanide containing 0.1 M KCl solution.

4.2.4 Photocatalytic activity evaluation

The photocatalytic activity of the prepared samples was evaluated by the degradation of Tetracycline (TC) antibiotic in aqueous solution under the irradiation of 36 W white LED light strip wrapped around a quartz photochemical reactor. The initial TC concentration was 15 mg/L and the photocatalyst loading was 0.3g/L in 150 mL of TC solution. Prior to irradiation, the mixed solution was ultrasonicated then mildly stirred in the fabricated reactor for 60 min

in the dark to reach the adsorption/desorption equilibrium of TC on the photocatalyst surface. The adsorbed solution was further subjected to degradation by switching on the LED light under stirring for 3 hr. Sample solution (3 mL) was withdrawn at given time intervals (30 min) and centrifuged at 5000 rpm for 5 mins to remove suspended particles. The concentration of TC was determined by measuring the absorbance of the solution in a UV-visible spectrophotometer at 376 nm. To better understand the advantages of the most active catalyst, AABR-ACK from the RSM design, reference Ag/AgBr (AABR), AgBr and titanium dioxide on dealuminated Clinoptilolite (TiO_2/HCP) photocatalyst from previous work (Saheed, Modise & Sipamla 2013) were used to compare activity on TC. Different radical scavengers were added to TC solution, to determine which radical species were mostly responsible for enhanced activity of active photocatalyst.

Benzoquinone (BQ), isopropanol and disodium ethylenediaminetetraacetic acid (EDTA-Na_2) at one mmole were dispersed in TC solution added photocatalyst to scavenge superoxide radicals ($^{\bullet}O_2^-$), hydroxyl radicals ($^{\bullet}OH$) and holes (h^+), respectively, followed by the photocatalytic activity test. To test the stability and reusability of the most active catalyst, AABR-ACK, the catalyst was utilized in the TC oxidation experiment, then recovered from with centrifugation after 180 min. Dried and dispersed in fresh TC solution, then preceded with degradation activities described above for 5 times.

4.2.5 Response surface methodology

The RSM design known as central composite design (CCD) was used in this study, to estimate the influence and interaction of the synthetic variables on the response (degradation efficiency of TC). The synthetic variables selected as main parameters include a mass of PVP, reaction temperature, the mass of carbon and time. The variables are defined as a districted numeric parameter and studied in three levels as indicated in **Table 4.1**, while the variables chosen were based on literature published in the past (Chen et al. 2015; Wu et al. 2017).

Table 4.1: Experimental levels for independent parameters.

Factor	Name	Units	Low (-1)	Medium (0)	High (+1)
A	Mass of PVP	g	0.12	0.26	0.40
B	Temperature	℃	100	140	180
C	Mass of Carbon	g	0.01	0.06	0.06
D	Time	min	10	17.5	25

The experiment comprises of 30 runs as presented by Design-Expert software (version 7) in **Table 4.2**. The response was utilized to develop an empirical model, which correlated the response to the synthetic process variables using a second-degree polynomial equation as given by Eq. 4.1

$$Y = b_0 + \sum_{i=1}^{4} b_i x_i + \sum_{i=1}^{4} b_{ii} x_i^2 + \sum_{i=1}^{4} \sum_{j=i1}^{4} b_{ij} x_i x_j \qquad 4.1$$

where Y is the predicted response for degradation percentage of TC, b_o is constant coefficient, *bi* the linear coefficient, b_{ij} is factor coefficient, b_{ii} is quadratic coefficient, while x_i and x_{ij} are the variables which determine the response Y.

Table 4.2: Experimental design matrix with the response value of TC degradation efficiency

		Actual Variables				Response Variables
Sample Name	Run	Mass Of PVP (g)	Temperature (°C)	Mass of Carbon (g)	Time (min)	Degradation Efficiency (%)
	1	0.40	100	0.06	10.00	60.90
	2	0.12	100	0.06	10.00	54.41
	3	0.26	140	0.06	17.50	91.91
	4	0.26	140	0.03	17.50	90.44
	5	0.40	180	0.01	10.00	69.51
	6	0.40	180	0.01	25.00	55.98
AABR-ACK 7	7	0.26	140	0.03	10.00	73.71
	8	0.40	100	0.01	10.00	53.33
	9	0.40	100	0.06	25.00	57.39
	10	0.26	140	0.01	17.50	89.31
AABR-ACK 11	11	0.26	140	0.03	17.50	92.08
	12	0.12	140	0.03	17.50	91.90
	13	0.12	180	0.06	25.00	49.00
AABR-ACK 14	14	0.26	140	0.03	25.00	81.98
	15	0.40	180	0.06	10.00	74.50
	16	0.26	140	0.03	17.50	89.82
	17	0.40	140	0.03	17.50	91.01
	18	0.12	180	0.06	10.00	70.74
	19	0.40	180	0.06	25.00	60.05
	20	0.12	100	0.06	25.00	50.54
AABR-ACK 21	21	0.26	180	0.03	17.50	49.44
	22	0.12	100	0.01	25.00	59.35
	23	0.26	140	0.03	17.50	90.48
	24	0.40	100	0.01	25.00	57.37
	25	0.26	140	0.03	17.50	87.58
AABR-ACK 26	26	0.26	100	0.03	17.50	57.26
	27	0.12	100	0.01	10.00	53.38
	28	0.26	140	0.03	17.50	88.08
	29	0.12	180	0.01	10.00	71.23
	30	0.12	180	0.01	25.00	53.51

4.3 Results and Discussions

4.3.1 Model fitting on the degradation of TC

Based on the sequential model sum of squares, the quadratic model was selected as the highest order polynomial where the additional term is significant and the model is not aliased. The regression analysis of the CCD for the quadratic model with the significant terms on degradation percentage (DP) for TC are shown in Eq. 4.2 below:

$$DP = 87.58 + 2.78B - 3.14D - 4.38BD - 32.06B^2 - 7.57D^2 \quad 4.2$$

The linear terms of B, D, the interaction terms of BD and the quadratic terms of B^2 and D^2 were the significant variables for the degradation efficiency for TC, hence insignificant effects were ignored as shown in **Eq. 4.2** and **Table 4.3**. Further details on model authentication from an analysis of variance (ANOVA) are further discussed.

The analysis of variances (ANOVA) employed to evaluate the statistical significance of interactions between the synthesis variables and the response based on the F and p-values. Parameters such as F-value, probability >F and adequate precision, which is a measure of error or the signal-to-noise ratio, were used as the indicators of how the suggested models fit the experimental values. The statistical analysis showed that quadratic model fitted closely with the experimental data with a high F-value of and a probability > F of < 0.0001 for the quadratic models shows that the models are significant. The applicability of the model equations to the experimental data was further evaluated using the correlation coefficient (R^2). The correlation coefficient (R^2) for the response factor yielded a high amount more than 95% that is from the independent variables.

Table 4.3 : Analyisis of Variance of the response surface model for degradation efficieny of Tetracyline.

Source	Sum of Squares	df	Mean Square	F Value	p-value Prob > F	
Model	8008.59	14	572.04	52.06	< 0.0001	Significant
B-Temperature	139.07	1	139.07	6.27	0.0244	
D-Time	177.67	1	177.67	8.01	0.0127	
BD	306.82	1	306.82	13.82	0.0021	
B^2	2663.75	1	2663.75	120.02	< 0.0001	
D^2	148.54	1	148.54	6.69	0.0206	
Residual	332.91	15	22.19			
Lack of Fit	318.97	10	31.9	11.44	0.0275	not significant
Pure Error	13.94	5	2.79			

R-Squared	Adj R-Squared	Pred R-Squared	Adeq Precision
0.9561	0.9151	0.8173	13.678

The highest coefficient values of time and temperature from the regression analysis in **Eq. 4.2** and their high F values from ANOVA (**Table 4.3**), shows their major contributions toward TC degradation. The time determines the size growth of AABR dispersed on the ACK (Xiang Xu, Shen, Hu Zhou, Dezhou Qiu, Guoxing Zhu & Chen 2013), which also ensures strong contact between the components and further reducing migration distance of charge carriers. Meanwhile, the formation of unique morphologies with an intimate contact structure between AABR and ACK will be governed by the reaction temperature (Xu et al. 2013; Chen et al. 2015), which simultaneously enhances separation of electron-hole pairs and promotes radicals formation. Overall, both time and temperature optimization are advantageous towards enhancing the degradation of TC derived from the RSM design.

4.3.2 Variables interaction influence on TC degradation efficiency

Three-dimensional (3D) response surface was used to investigate the influence of the synthesis variables and their interactions on the degradation efficiency of TC removal. The adjusted correlation coefficient value was also more than 91% the response factor was relatively high and close to R^2 value. These values show a good agreement between the experimental and predicted values as depicted in **Figure 4.2a**. The significant interactions of synthesis variables from **Eq. 4.2** on the response are presented in **Figure 4.2b**.

Figure 4.2b shows the influence of temperature and time on degradation efficiency of TC at a fixed mass of carbon and PVP (around 0.03 g and 0.26 g) Increasing both variables simultaneously from 100 - 180 °C and 10 – 25 min, the degradation percentage increases from 49.44 to 92.08% and 81.98 to 92.08% respectively, whilst further increase for both variables decreases to 57.26 and 73.73%. The highest degradation efficiency is achieved when the temperature is maintained at 140 °C and extended time for 17.50 min. From the 3D surface plots finding, the time and temperature play a significant role in the photocatalytic performance of AABR-ACK composites on TC removal. The importance of time and temperature as preparation variables was not been fully realized from previous studies until now. Therefore, in this study, the focus was placed on the characterization of prepared AABR-ACK samples on time and temperature variation to understand how these preparation variables influence the catalytic activity on TC removal (**Table 4.2**).

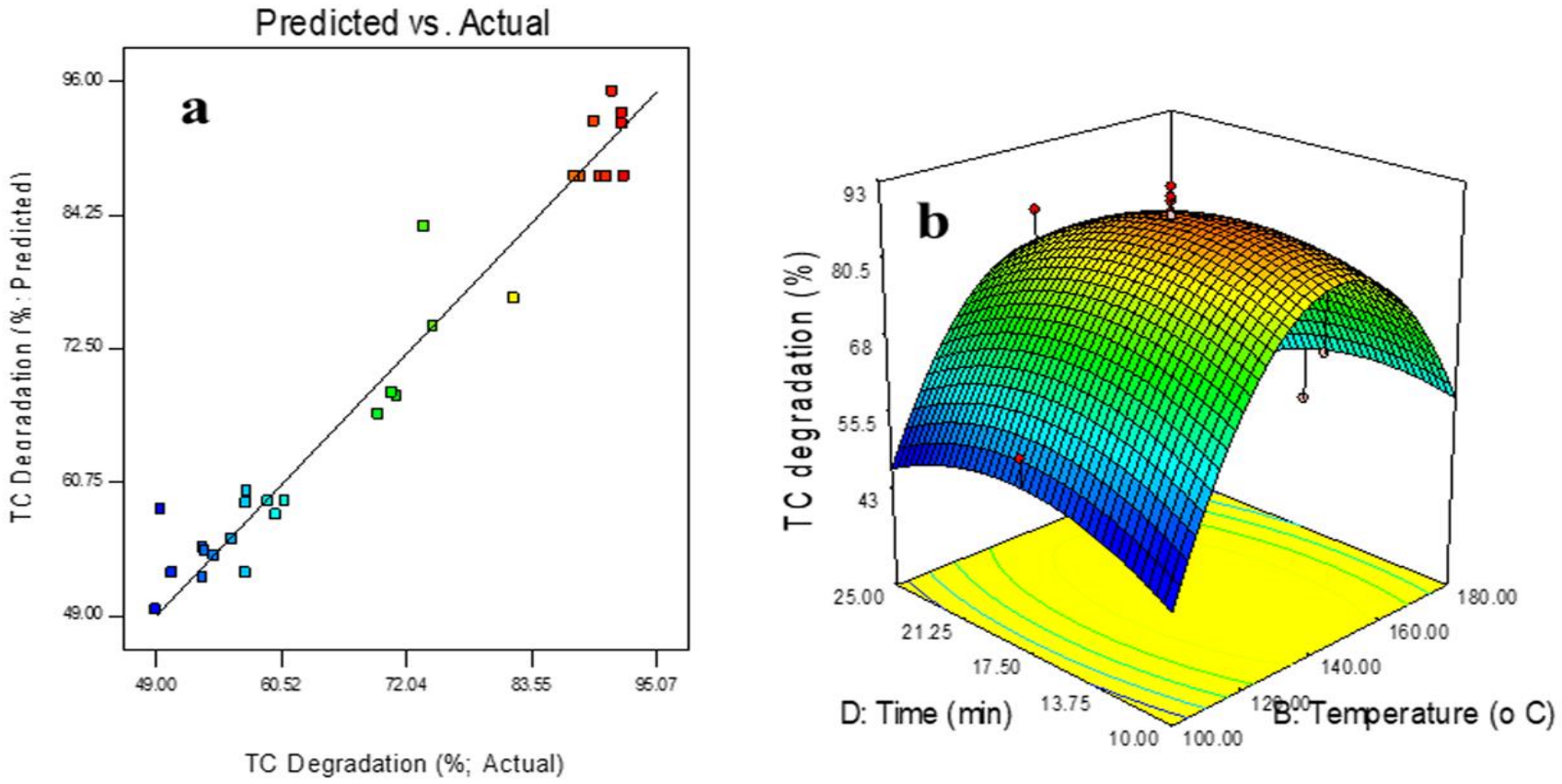

Figure 4.2: (a) Plots of predicted vs. experimental values for degradation efficiency of tetracycline and 3D surface plots of degradation efficiency of tetracycline by AABR-ACK photocatalysts from interactions between (b) temperature and time.

4.4 Characterization

4.4.1 Phase, morphology and surface composition analysis

The XRD patterns of the AABR-ACK composites at different times (AABR-ACK 7, AABR-ACK 11 and AABR-ACK 14) and temperatures (AABR-ACK 21, AABR-ACK 11 and AABR-ACK 26) at the constant mass of PVP and carbon (0.26 and 0.03 g) are shown in **Figure 4.3a-b**. The XRD pattern of the prepared composites comprises of pure face center cubic phase of AgBr with space group: Fm-3m (225) (Zhu, Wang, Lin, Gao, Guo, Du & Xu 2013). The peaks at 2θ values of 26.6, 31.1, 44.3, 54.8, 64.8, and 73.4° are in indexed with planes of (111), (200), (220), (222), (400) and (420) cubic structure of AgBr (JPCDS 079-0148) respectively. The diffraction peaks of metallic cubic Ag at 38.1, 44.2, 64.4 and 77.8^{o} 2θ are ascribed to (111), (200), (220) and (311) planes (JCPDS 071-3762, space group: Fm-3m (225)). In this study, the diffraction peak of Ag at 38.1^{o} is distinct, highlighting the abundance of metallic Ag in the composites as compared to other reports (Chen et al. 2012; Lou, Huang, Qin, Zhang, Cheng, Liu, Wang, Wang & Dai 2012). Metallic Ag peaks at 111, 200, 220 and 311 widen with an increase in time and temperature, which is similar to other reports (Uygur 1997). A further increase in time to 25 min (AABR-ACK-14), results in a negative shift of XRD peaks for AgBr and Ag by 0.2^{o} 2θ, which is ascribed to close interaction between AgBr and metallic Ag (Xu, Li, Xia, Yin, Luo, Liu & Xu 2010). The diffraction peaks of AgBr and metallic Ag were enhanced with AABR-ACK 11 compared to other composites, highlighting the formation of ordered nanostructures along with reduced particle diameter, which is further evidenced with morphology discussion in **Figure 4.4a-f**.

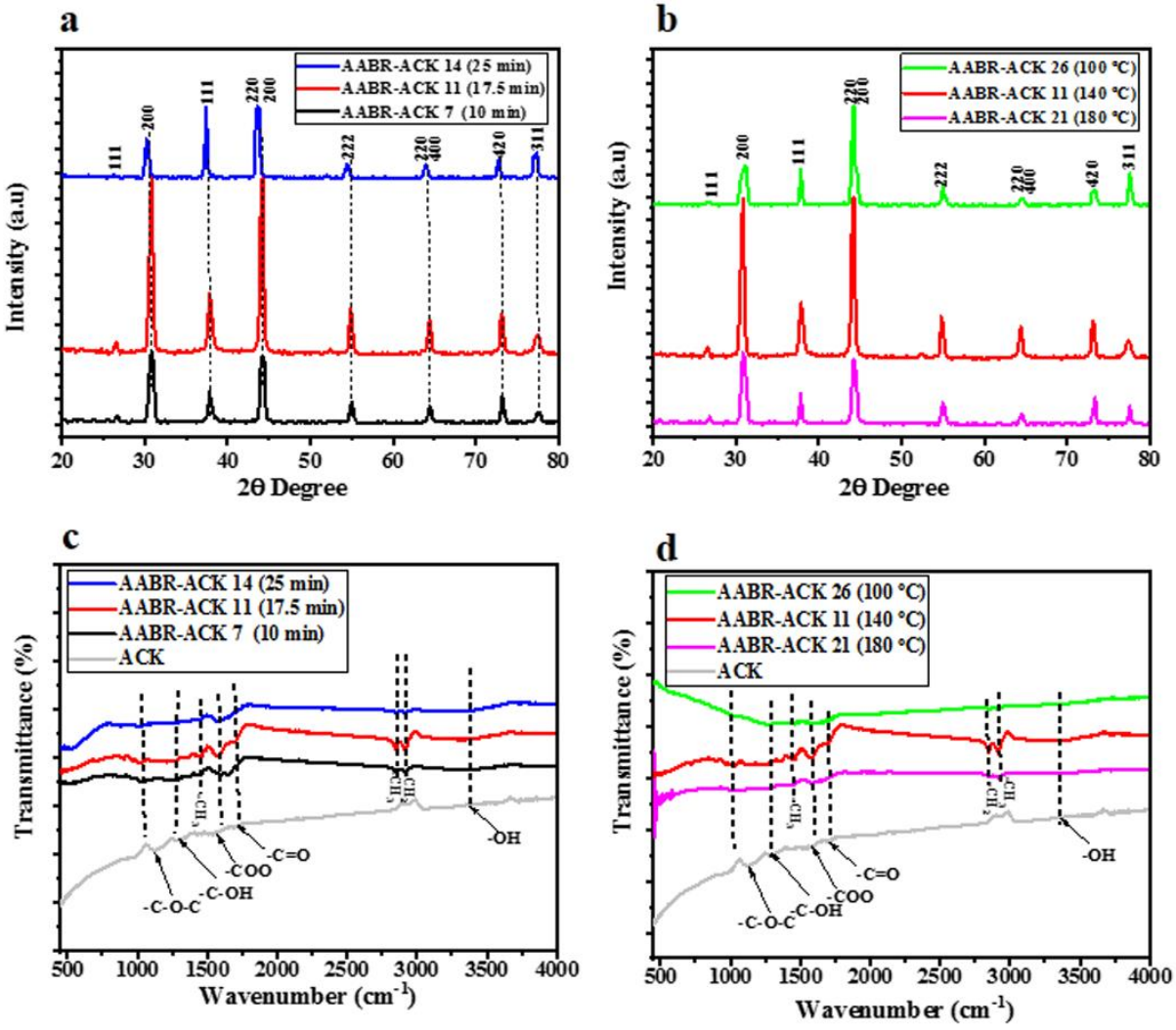

Figure 4.3: XRD pattern and FTIR spectra of AABR-ACK composites synthesized at different (a, c) times and (b, d) temperatures.

The FTIR spectra for AABR-ACK composites at different times (10, 17.5 and 25 min) and temperatures (100, 140 and 180 ºC) as shown in **Figure 4.3c-d**. For ACK, five absorption bands are located at 3340, 1733, 1648, 1341 and 1135 cm^{-1} that are ascribed to -OH stretching, -C=O from carbonyl stretching, -COO from carboxyl stretching, the –C-OH and –C-O-C stretching vibrations (Deng, Li, Yang, Tang & Tang 2010). The –C=O carbonyl stretching, -C-OH and –C-O-C stretching band for ACK shifts to lower wavenumber in the AABR-ACK composites, which confirms the interaction between the AABR particles and ACK. The ACK as our capping molecules with abundance oxygenated functional groups such as -COO, -C-OH and –C-O-C partake in AABR defined nanostructures. This leads to a decrease in agglomeration, a decrease in size distribution and decrease the rate of AABR particle growth. The bands at 2918 and 2839 cm^{-1} that are ascribed to the stretching vibration of C-H bonds in $-CH_3$ and $-CH_2$ groups from the PVP molecules (Gao, Song, Jiang, Liu, Yan, Zhou, Liu, Wang, Yuan & Zhang 2005) are pronounced for AABR-ACK 7, 11, and 14 composites. The band at 1450 cm^{-1} corresponds to anti-symmetric deformation vibration of $-CH_3$ group of the PVP molecules (Cong-Wen, Hai-Tao, Cheng-Min, Zi-An, Huai-Ruo, Fei, Tian-Zhong, Shu-Tang & Hong-Jun 2005) are also present for AABR-ACK composites at a different time (**Figure 4.3c**). The presence of PVP molecules causes a steric effect (Chen, Liu, Chen, Ge, Fan, Wang, Lu, Yang, Zhang & Yan 2014) between the Ag^+ and Br^-, as a result, rapid growth and agglomeration of AgBr crystal particles are prohibited with the formation of ordered nanostructures (as presented in SEM analysis in **Figure 4.4a-c**). However, these mentioned bands ($-CH_3$ and $-CH_2$ groups for the PVP molecules) are weakened for AABR-ACK 21 and AABR-ACK 26 composites (**Figure 4.3d**), due to irregular morphology, agglomeration (evidenced from SEM image in **Figure 4.4d and f**) and PVP polymerization at higher temperature (Inoue, Nakazawa, Mitsuhashi, Shirai & Fluck 1989).

The SEM morphology of the as-prepared AABR-ACK composites prepared at different times (AABR-ACK 7, AABR-ACK 11 and AABR-ACK 14) and temperatures (AABR-ACK 21, AABR-ACK 11 and AABR-ACK 26) are shown in **Figure 4.4a-f.** The SEM images of prepared AABR-ACK composites at different times (10-25 min) are all well-distributed nanospheres morphology (**Figure 4.4a-c**) with an average particle diameter range between 162-201 nm. The morphology of the AABR-ACK 7 is large nanospheres with particle diameter of 201 nm. The AABR-ACK composites nanostructures remain unchanged with the variation of times (from 17.5 to 25 min) as observed with the previous report (Xiang Xu et al. 2013), but the average particle diameter for AABR-ACK 11 and 14 are 162 and 198 nm. The AABR-ACK 26 (100 °C) is comprised of aggregated morphologies of cubes, spheres, and triangles (**Figure 4.4d**) with a particle diameter of 262 nm. When the temperature was increased to 140 °C (AABR-ACK 11), the formation of ordered AABR nanospheres anchored on ACK surface (**Figure 4.4e**) with a particle diameter of 162 nm was formed. A further increase in temperature to 180 °C (AABR-ACK 21) caused the spheres to agglomerate together forming an octahedral morphology (**Figure 4.4f**) with a particle diameter of 586 nm. The uniform nanospheres morphology for AABR-ACK 11 with reduced particle diameter will shorten migration path of the charge carriers and enhanced the degradation activities (Xiang Xu et al. 2013) as presented in **Table 4.2**.

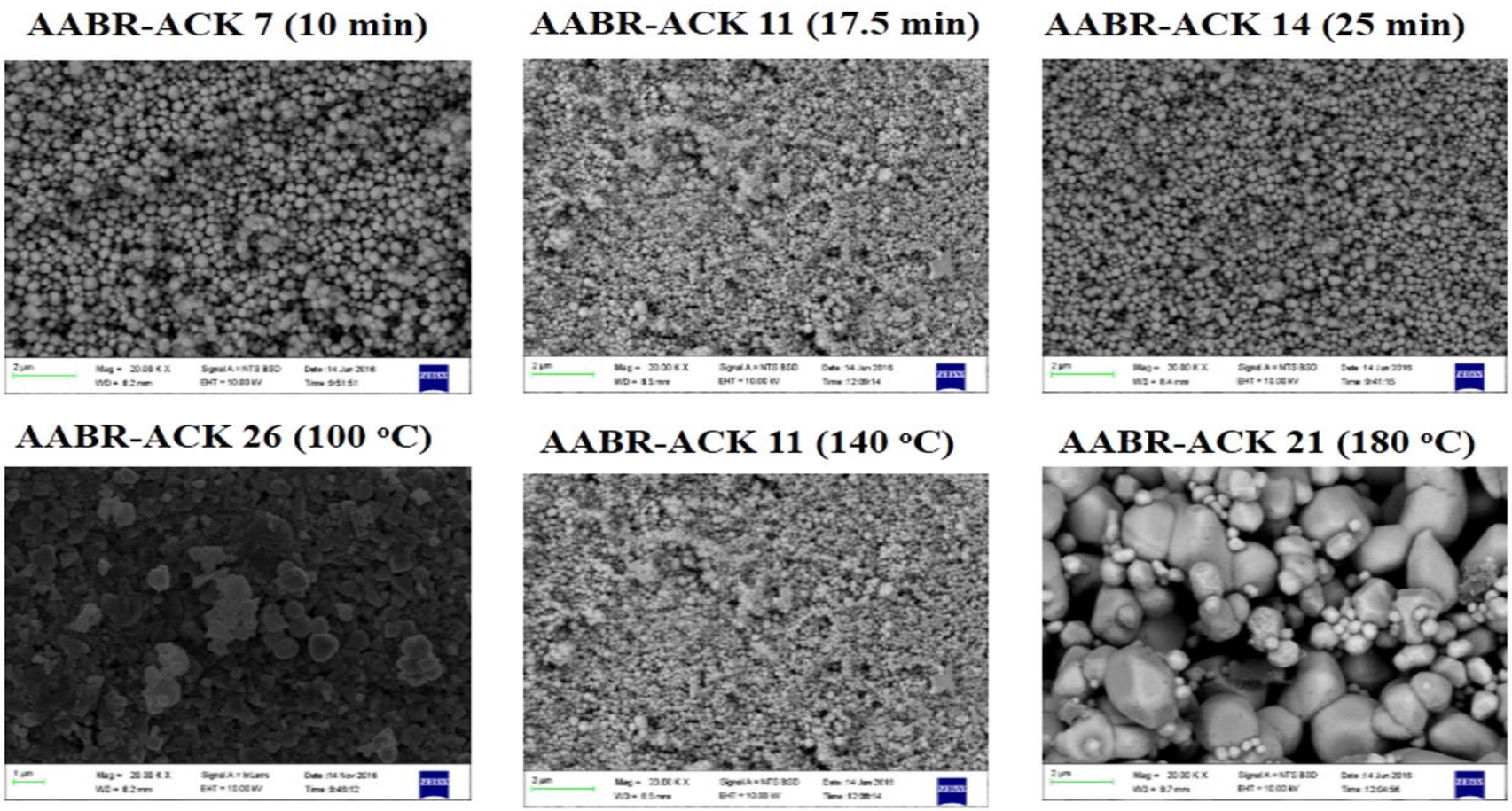

Figure 4.4: SEM images of AABR-ACK composites synthesized at different (a) times (AABR-ACK 7, AABR-ACK 11and AABR-ACK 14) and (b) temperatures (AABR-ACK 26, AABR-ACK 11 and AABR-ACK 21).

The AABR particles without activated carbon (**Figure 4.5a**) are an irregular octahedral shape, aggregated with an average particle diameter of 1.3 μm. Herein, the ACK (**Figure 4.5b**) interconnected carbon network structure with abundance oxygenated functional groups will aid in the favorable immobilization of ordered AABR nanostructure for AABR-ACK composites.

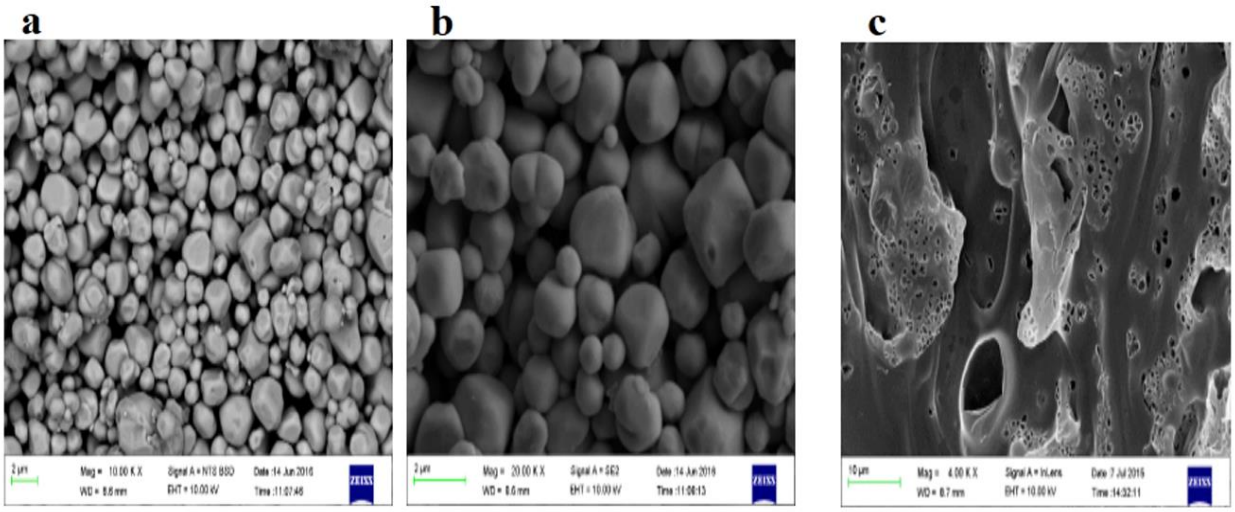

Figure 4.5: SEM image of (a, b) AABR and (c) ACK.

The TEM images of the ACK and AABR-ACK 11 composite are shown in **Figures 4.6a and b**. **Fig. 4.6a** presents the porous ACK material, while Fig. **4.6b** shows the TEM image for AABR-ACK 11 is spheres shaped nanoparticles, in which the AABR particles with a diameter of around 3-5 nm uniformly distributed on the ACK surface. A close inspection of the AABR-ACK 11 nanostructure as observed by HRTEM (**Figure 4.6c**) shows the lattice fringes with an interplanar spacing of 0.238 and 0.285 nm, which are attributed to Ag (111) and AgBr (200) planes. Herein, intimate contact between AABR and ACK was formed for AABR-ACK 11, which favors

accelerated electron migration from the former to the latter, which results in photo-prompted electron-hole pairs separation and enhanced photocatalytic activity.

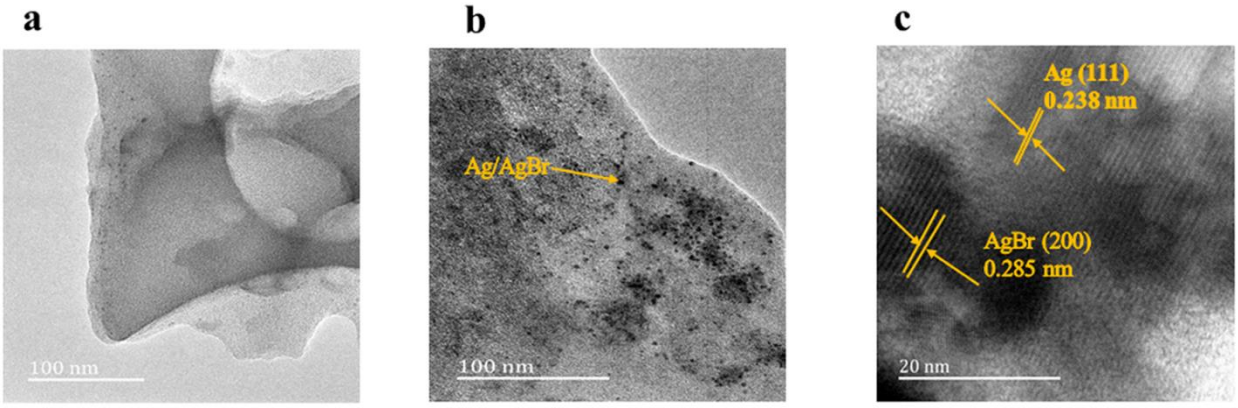

Figure 4.6: TEM images of (a) ACK; (b) AABR-ACK 11 and (c) HRTEM of AABR-ACK 11 composite.

The surface chemical composition and valence states of AABR-ACK 11 composite were analyzed by X-ray photoelectron spectroscopy (XPS) in **Figure 4.7**. The survey scan spectrum (**Figure 4.7a**) indicates the presence of Ag, Br, and C in the sample. However, the high-resolution XPS spectra of Ag 3d (**Figure 4.7b**) has two symmetrical peaks at binding energies of 366.87 eV and 372.80 eV for Ag $3d_{5/2}$ and Ag $3d_{3/2}$ respectively (Zeng, Tian & Zhang 2013). These two peaks are further divided into two different peaks. The peaks at 366.87and 372.80 eV are attributed to Ag^{+}, while the peaks at 366.78 and 372.80 eV could be ascribed to metallic Ag^{o} (Jiang & Zhang 2011; Zhu, Chen & Liu 2011; Xu, Y. et al. 2013). The Br 3d spectra (**Figure 4.7c**) at 67.27 eV and 67.99 eV would be attributed to Br $3d_{5/2}$ and Br $3d_{3/2}$ respectively. (Choi & Kang 2014). **Figure 4.7d** shows the high-resolution XPS spectra of C 1s. The main peak at 284.6 eV is attributed to

the C=C/C-C bond with graphitic carbons (sp^2 orbital), which originate from the amorphous carbon phase (Li, Ma, Ye, Zhou, Wang, Ma, Wang, Huo & Yan 2017). The peaks at 286.1, 287.6 and 289 eV are ascribed to C-C (sp^3 orbital), C-O, and C=O respectively. Based on the observation from XRD, SEM and XPS analysis, these findings show hybridization of AABR with ACK, and the existence of metal Ag°, $Ag^{+,}$ and Br^{-} in the composite.

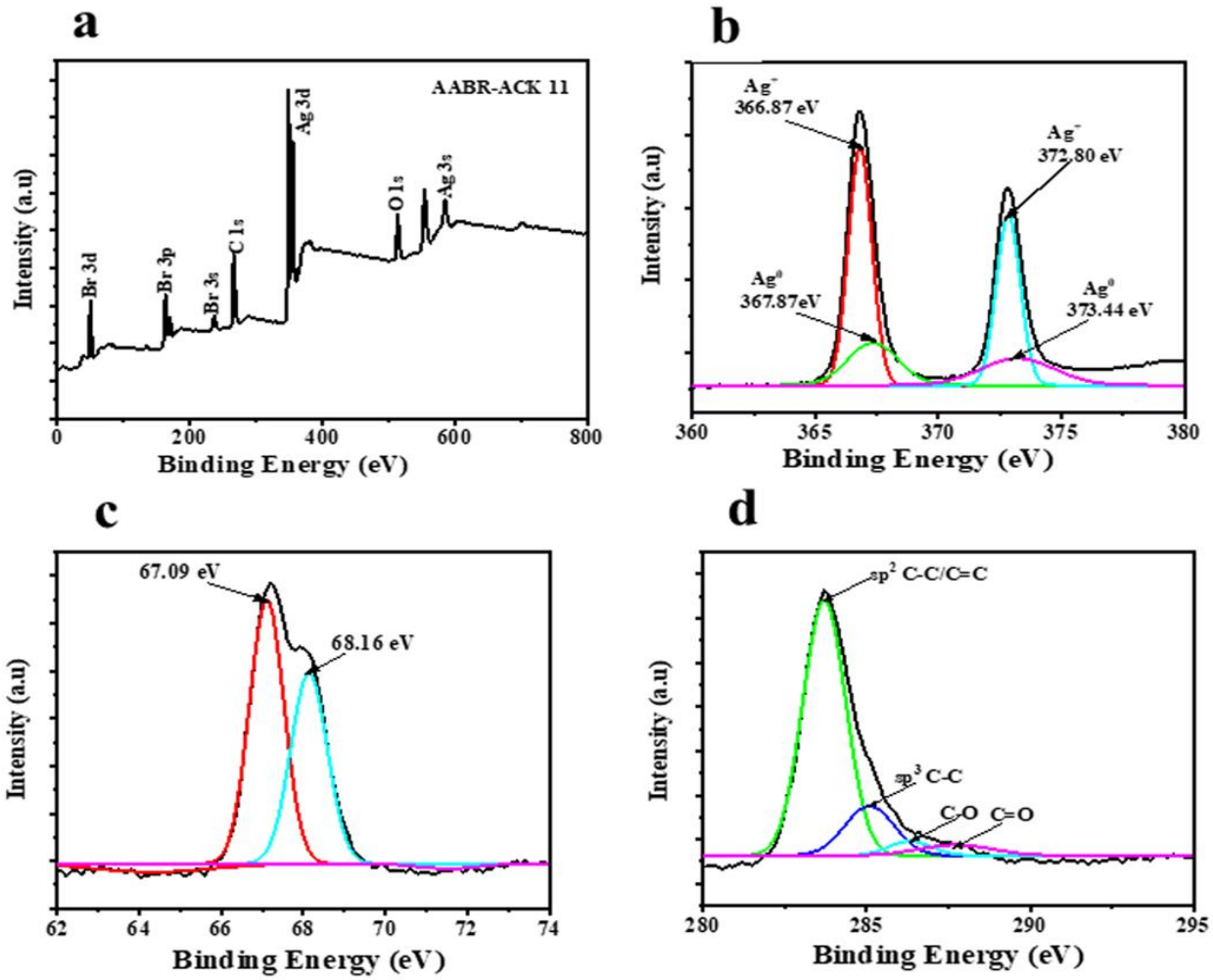

Figure 4.7: (a) The survey XPS spectra of AABR-ACK 11 composite; high resolution spectra of (b) Ag 3d; (c) Br 3d and (d) C 1s.

4.4.2 Optical and electrical properties of AABR-ACK composites

Figure 4.8a-b illustrated the UV–Vis DRS spectra of as-prepared AABR-ACK composites at different times (AABR-ACK 7, AABR-ACK 11 and AABR-ACK 14) and temperatures (AABR-ACK 21, AABR-ACK 11 and AABR-ACK 26). The AABR-ACK composites exhibited a strong absorbance edge in the visible region within the range of 400 to 800 nm. This is ascribed to the intense surface plasmon resonance (SPR) of the metallic Ag particles, caused by a thermal reduction of AgBr by EG (Sun & Xia 2002; Dai, Lu, Dong, Ji, Zhu, Liu, Liu, Zhang, Li & Liang 2013). The SPR of Ag particles is influenced by the ordered nanostructure and particle diameter as evidenced by SEM analysis (**Figure 4.4a-f**). The AABR-ACK X (X =7, 14, 21, 26) composites absorption edges in the visible region were reduced as compared to AABR-ACK 11 (**Figure 4.8a-b**), which endow the latter to efficiently utilize the visible light for enhanced photodegradation of TC (Liu, Dong, Hao, Wang, Ma & Zhang 2017). The strong hybridization between AABR and ACK interconnected carbon network acting as light transmittance channels (Linares, Silvestre-Albero, Serrano, Silvestre-Albero & García-Martínez 2014), also boosted the visible light-harvesting ability of the AABR within the AABR-ACK 11 (**Figure 4.9a).**

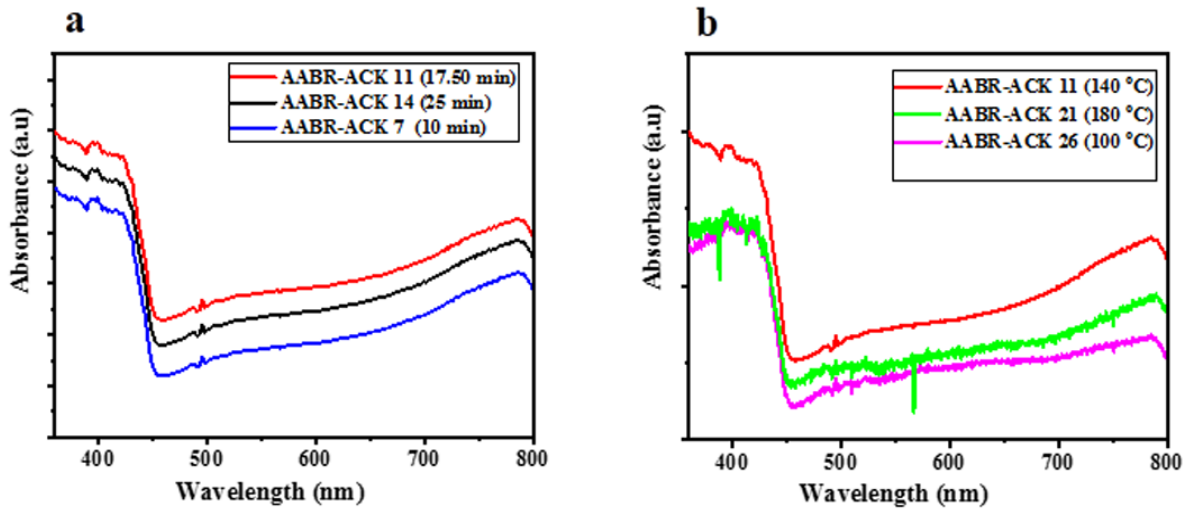

Figure 4.8: UV–vis DRS spectra for AABR-ACK composites synthesized at different (a) times (AABR-ACK 7, AABR-ACK 11and AABR-ACK 14) and (b) temperatures (AABR-ACK 21, AABR-ACK 11 and AABR-ACK 26).

The bandgap energy (Eg) of AABR-ACK and AABR were calculated using the Kubelka-Munk (Zhang, Han, Yu, Zou & Dong 2019a) equation below:

$$\alpha h\nu = A(h\nu - Eg)^{\frac{n}{2}} \qquad 4.3$$

where α, h, υ, A and Eg are the optical absorption coefficient, Plank's constant, light frequency, a constant and bandgap energy. Also n is equal to 1 and 4 for direct and indirect bandgap semiconductor, hence the AgBr catalyst is an indirect bandgap semiconductor (Cao, Luo, Lin &

Chen 2011) and the plot of $(\alpha h\nu)a^2$ versus photon energy ($h\nu$) is shown in **Figure 4.9b**. The corresponding band gap for AABR-ACK 11 and AABR is 2.34 eV and 2.4 eV respectively.

The VB and CB positions for AABR-ACK 11 are determined through the following empirical formula:

$$E_{VB} = X - E_O + 0.5E_g \quad (4.4)$$

$$E_{CB} = E_{VB} - E_g \quad (4.5)$$

where E_{VB} and E_{CB} are the edge potential of the valence band (VB) and conduction band (CB) respectively, and X represents the absolute electronegativity of the semiconductor. The X value for AgBr is calculated at 5.8 eV. E_O is the energy of free electrons on the hydrogen scale (about 4.5 V) (Zhang, Han, Yu, Zou & Dong 2019b) and Eg is the bandgap energy of the semiconductor. The E_{VB} and E_{CB} values of AABR are calculated to be 2.47 and 0.13 V vs. NHE, respectively.

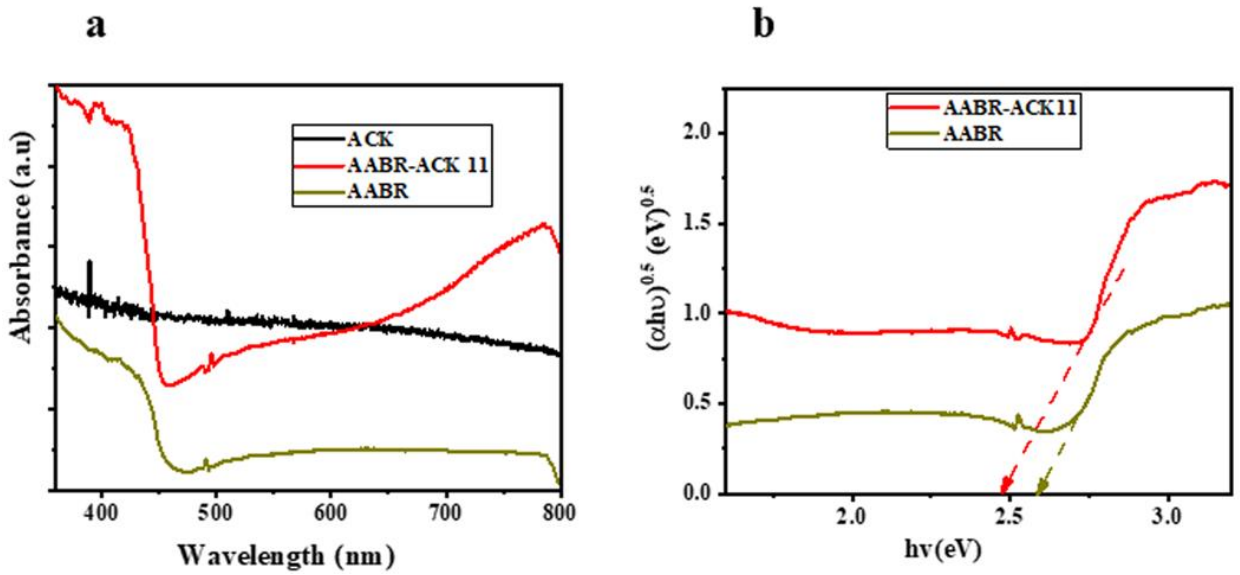

Figure 4.9: (a) UV–vis DRS spectra for ACK, AABR, AABR-ACK composites and (b) corresponding Tauc plots for AABR and AABR-ACK composites.

The recombination of photo-induced electrons and holes pairs (Lei, Wang, Song, Fan, Pang, Tang & Zhang 2010) affects the photocatalytic activity of a photocatalyst. The intensity for AABR-ACK composites according to different times can be ranked as (AABR-ACK 11 < AABR-ACK 14 < AABR-ACK 7; **Figure 4.10a**) and at different temperatures (AABR-ACK 11 < AABR-ACK 26 < AABR-ACK 21; **Figure 4.10b**). AABR-ACK 11 composite exhibits lower intensity, which indicates that the recombination of photo-induced electron-hole pairs was effectively inhibited (Wang, Fang, Zheng, Che, Tao & Chen 2015) and correlates with its enhanced degradation of TC in **Table 4.2**. The ordered nanospheres for AABR-ACK 11 composites retard

the recombination of electron-hole pairs, which further boost the photocatalytic performance. The ACK support also effectively facilitates separation of photo-induced charge carriers from AABR-spheres judging from the PL spectra of AABR and AABR-ACK 11 composite (**Figure 4.10c**).

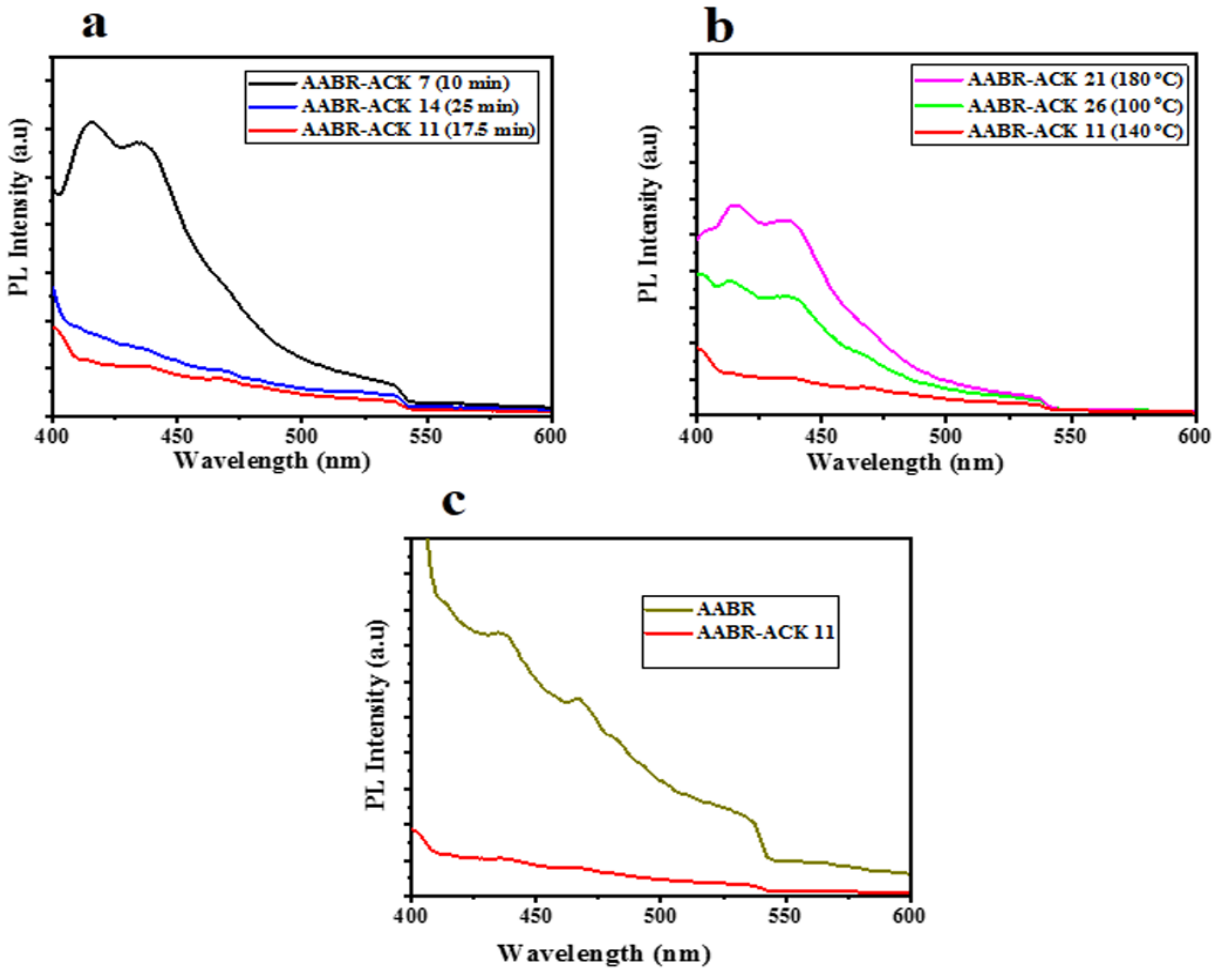

Figure 4.10: PL spectra for AABR-ACK composites synthesized at different (a) times (AABR-ACK 7, AABR-ACK 11and AABR-ACK 14), (b) temperatures (AABR-ACK 21, AABR-ACK 11 and AABR-ACK 26) and (c) AABR and AABR-ACK 11 composite.

To further study the influence of facile tuning AABR-ACK nanostructures on the separation of photo-prompted electron-hole pairs and electron conductivity, photo-electrochemical analysis was also carried out. The photo-electrochemical response as well as the curve under dark are presented in **Figure 4.11a -b**. The photocurrent density-voltage curve was measured in the potential range of 0.5–2.0 V vs SCE. The AABR-ACK 11 composite showed the highest photocurrent density of 1.07 mA/cm^2, which is higher than that of AABR-ACK X relatives (X = 14, 7, 26 and 21) and AABR under visible light irradiation, suggesting its higher electron-hole pairs separation efficiency. The high photocurrent density for AABR-ACK 11 further verifies that the ordered nanostructures of AABR and interconnected network structure of ACK significantly boost the photo-electrochemical performance for high degradation activities.

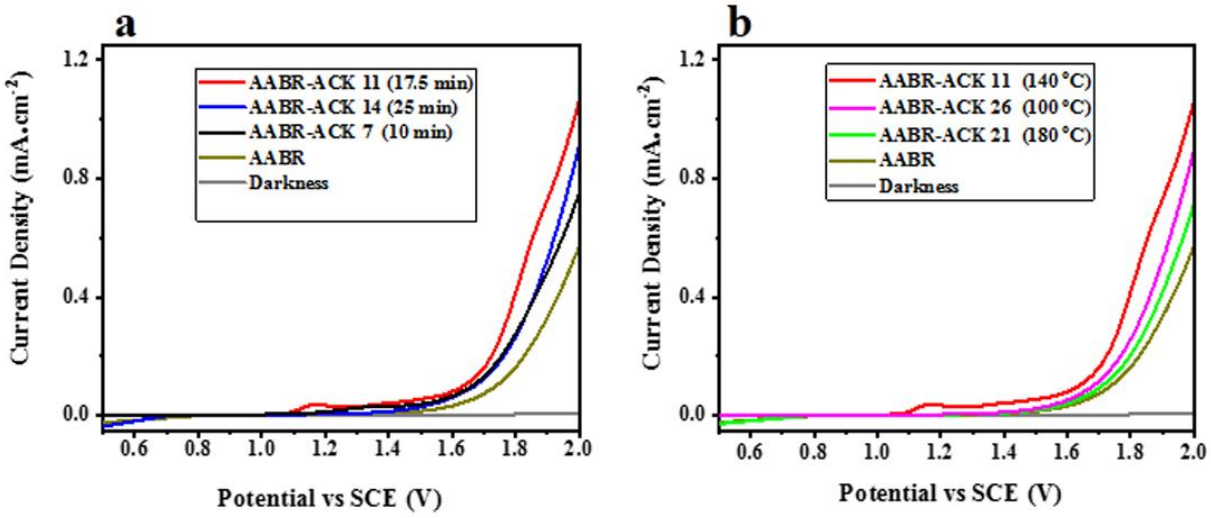

Figure 4.11: Linear sweep voltammetry curves for AABR-ACK composites synthesized at different (a) times (AABR-ACK 7, AABR-ACK 11and AABR-ACK 14) and (b) temperatures (AABR-ACK 21, AABR-ACK 11 and AABR-ACK 26).

The EIS Nyquist plots of AABR-ACK composites are shown in **Figure 4.12a-b**. The rank of smallest semicircle arc radius for the composites at different times are: AABR-ACK 11 < AABR-ACK 14 < AABR-ACK 7, while for temperatures: AABR-ACK 11 < AABR-ACK 26 < AABR-ACK 21. The smallest semicircle arc radius implies effective electron conductivity and enhanced separation efficiency of photo-prompted electron-hole pairs (Wen, Niu, Zhang & Zeng 2017) that occurred with the AABR-ACK 11 nanospheres composite. In addition, the AABR-ACK 11 composite displays smaller arc radius as compared to pure AABR in **Figure 4.12c.** This means an efficient charge carrier separation was actualized via the intimate contact between AABR and ACK support (Nayak, Mohapatra & Parida 2015) for AABR-ACK 11 nanospheres. ACK conductive support in the AABR-ACK 11 composite will also effectively enhances the separation of photoinduced charge carriers and improving the photocatalytic performance (Kandi, Martha, Thirumurugan & Parida 2017).

The corresponding Bode plots in **Figure 4.12d - e** shows much lower |Z| trend for AABR-ACK 11 than that of AABR-ACK relatives and AABR. The lower |Z| trend implies faster electron-hole pairs separation, which confirms that the ordered nanostructure for AABR and the conductive ACK promotes the charge carriers separation properties of AABR. The hybridization of AABR with ACK enhanced the transportation rate of photo-excited electrons through an interfacial interaction between AABR nanospheres and the conductive ACK support [43], prompting reactive species formation for higher photocatalytic activities for AABR-ACK 11 composite.

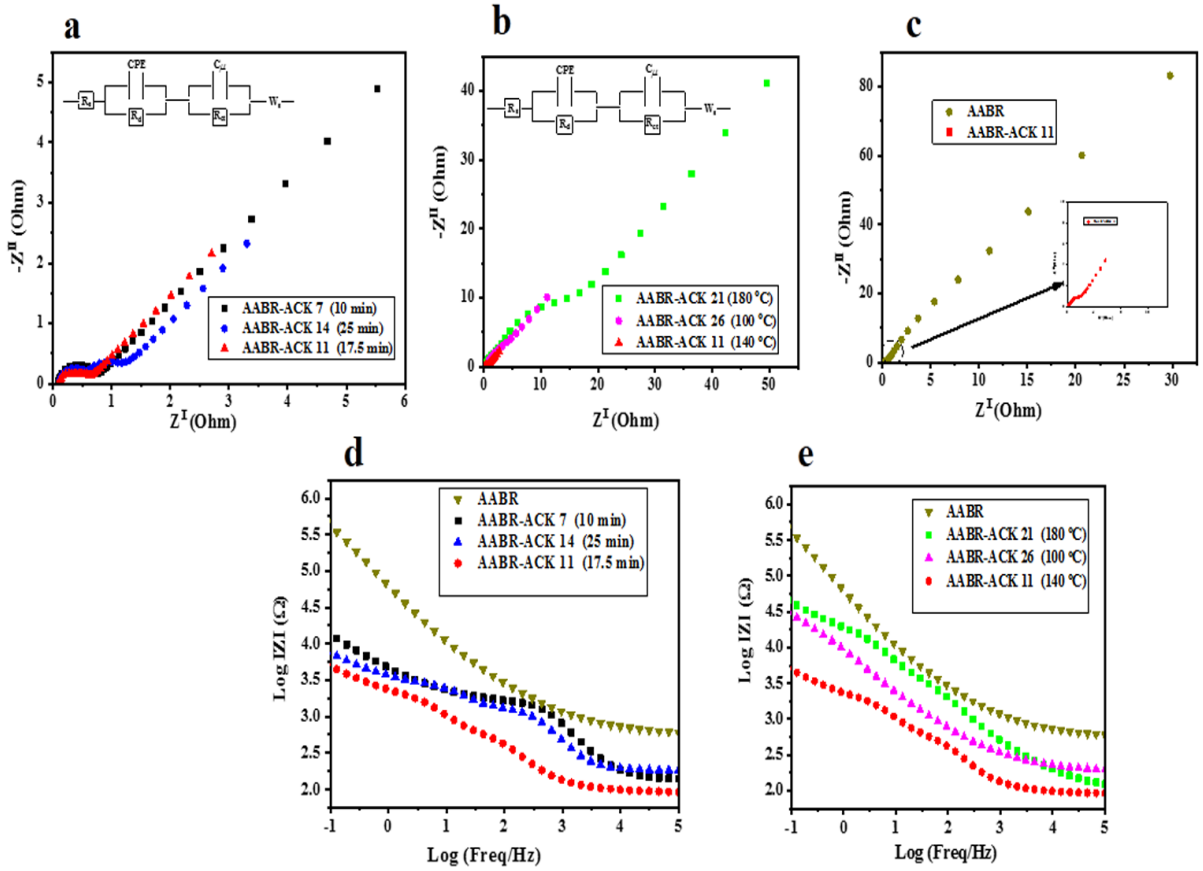

Figure 4.12: EIS Nyquist plots and imaginary bode plots for AABR-ACK composites synthesized at different (a, d) times (AABR-ACK 7, AABR-ACK 11and AABR-ACK 14) and (b, e) temperatures (AABR-ACK 21, AABR-ACK 11 and AABR-ACK 26); and (c) corresponding EIS plot of the most active catalyst AABR-ACK 11 and AABR.

Overall, TC high degradation efficiency using AABR-ACK 11 (temperature - 140 °C, extended time - 17.50 min, mass of carbon - 0.03 g and PVP - 0.26 g) is advanced by ordered nanostructures morphology with strong synergistic interactions between components of the composite. The ordered AABR nanospheres further enhanced visible light harvesting and fast electron transfer in the presence of conductive ACK, along with suppressed recombination rate of charge carriers. The analysis of optical, photo-electrochemical, morphology results and RSM approach evidence that AABR-ACK 11 composite is the active photocatalyst for degradation of TC in this study.

4.4.3 Photocatalytic activities

The visible-light photocatalytic activities of AABR-ACK 11 composite and other as-prepared samples were further investigated on the degradation of TC (15 mg/L, 150 ml), as presented in **Figure 4.13a**. The degradation of TC without photocatalyst under visible light conditions cannot be effectively oxidized as observed in **Figure 4.13a.** The photocatalytic activity of AABR, AgBr, and reference TiO_2/HCP exhibited lower degradation rate less than 60% in 180 min. However, the AABR-ACK 11 showed higher photocatalytic rate of 92.08% within 180 min than AABR and other samples under the same conditions; hence, the close contact of ordered AABR with ACK enhanced the oxidation degradation of TC. To quantitatively evaluate the photodegradation kinetics of TC over the prepared samples, the experiment values were fitted to both pseudo-first-order and pseudo-second-order kinetic features as presented in the equations below (da Silva, Carvalho, Lopes & Ribeiro 2017; Yuan, Lei, Xi, Liu, Qin, Chen & Dong 2019).

$$-In\frac{C_t}{C_o} = kt \quad 4.6$$

$$\frac{1}{C_t} - \frac{1}{C_o} = k_2 t \quad 4.7$$

Here, t is reaction time, Co and Ct are the TC concentrations at reaction time of 0 and t min, k and k2 are the apparent rate constant of pseudo first order and pseudo second order kinetics. The pseudo-second-order model in **Figure 4.13b** fitted better to describe the photocatalytic process of TC removal as compared the pseudo-first-order model (**Figure 4.13c**). This was ascribed to the generated small-molecular intermediates from TC degradation, which further adsorbed on AABR-ACK surface and reacted more easily with active species (Tian, Zhao, Sun, Xiao & Wong 2020). Therefore, both adsorption and photocatalytic activity was the major reason for the enhanced degradation of TC molecule in the AABR-ACK photocatalytic process (Liu, Lv, Yao, Ma, Huo & Yan 2013; Tian, Zhao, Sun, Xiao & Wong 2020).

The degradation rate constant for the as-prepared samples are ranked as: AABR-ACK 11 > AABR > AgBr > TiO_2/HCP. AABR-ACK 11 composite has the highest rate constant (0.0044 L mg^{-1} min^{-1}), which is 9.4 times fold more than AABR (0.0005 L mg^{-1} min^{-1}). The absorption spectra of TC over AABR-ACK 11 composite is shown in **Figure 4.13d,** the main band of TC at 376 nm reduces with an increase in irradiation time up to 180 min during the photocatalytic process. The reduction of TC main band at 376 nm suggests that the phenolic-diketone group is easily broken down (Chen & Huang 2011; Mahamallik, Saha & Pal 2015). This indicates that the AABR-ACK 11 is a promising photocatalyst for the treatment of antibiotic wastewater. The enhanced photocatalytic performance for AABR-ACK 11 is attributed to the design of ordered nanospheres structure, which promotes interfacial charge separation and prolonging the lifetime of photo-carriers (Mou, Song, Zhou, Zhang & Wang 2018; Bafaqeer, Tahir & Amin 2019).

In real water situations, inorganic ions may also be present and therefore their potential influence on the activity of the photocatalyst was investigated. In this work, the influence of inorganic anions on the photocatalytic performance of AABR-ACK 11 composite on the removal of TC was also carried out using several sodium salts of sulfate, sulphite, bicarbonate, chloride, and phosphate at a concentration of 20 mM as presented in **Figure 4.13e**. All the inorganic anions used in this work, have an inhibitory effect on the photocatalyst with the degradation of TC, as the degradation rate reduces from 92% to 49%. This inhibitory effect is attributed to the scavenging of free reactive oxidative species (h^+ and $^{\bullet}OH$) on the photocatalyst surface, which further transforms into inactive oxidative species and lowers the degradation % (Konstantinou & Albanis 2004; Rincon & Pulgarin 2004). The negative effects of these inorganic anions were found to be in the order of phosphate > chloride > bicarbonate > sulphite > sulphate. Among the inorganic anions, the highest inhibitory effect was more with phosphate and chloride ions, which is ascribed to their high potential (Chen & Liu 2017; Kakavandi, Bahari, Kalantary & Fard 2019) to occupy the active sites of AABR-ACK 11 composite as compared to other anions.

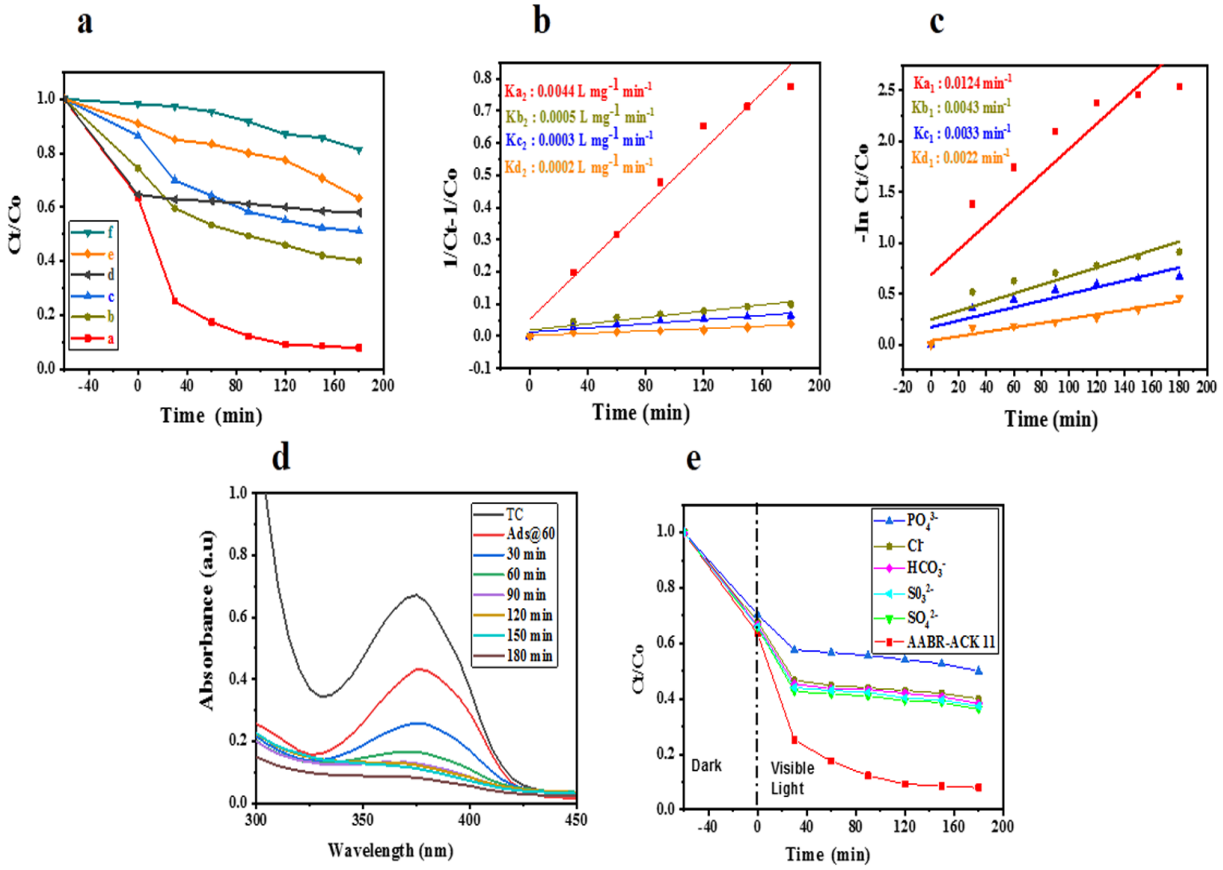

Figure 4.13: (A) Photocatalytic degradation of TC in aqueous solution with respect to time; (B, C) Plot of pseudo second ($1/Ct-1/C_o$) and pseudo first order kinetics ($-In(Ct/C_o)$ against the reaction time for the catalytic degradation of TC using different photocatalysts: (a) AABR-ACK 11, (b) AABR, (c) AgBr, (d) ACK, (e) TiO_2/HCP and (f) photolysis; (D) UV−Vis absorption spectra for the catalytic degradation of TC over AABR-ACK 11 and (E) effects of inorganic anions on the photocatalytic degradation of the TC.

The stability and reusability for a photocatalyst are critical for a cost-efficient commercial process. Therefore, the reusability of the AABR-ACK 11 composite was evaluated for the degradation of TC in five consecutive cycles. After each cycle, the photocatalysts were recovered by centrifugation, washing, drying. **Figure 4.14a.**shows that the degradation % of AABR-ACK 11 exhibited no significant reduction in the catalysts ability to degrade TC, 8.9% loss were observed after 5 cycles, which originated from small catalyst mass losses during washing and drying process. Therefore, the XRD, FTIR and UV-vis DRS spectra (**Figure 4.14b-d**) for the reused AABR-ACK 11 (five cycle times) show that the phase, structural and optical properties remain unchanged after the photocatalytic process. The ordered AABR-ACK 11 nanospheres exhibit higher activity and reusability for degradation of TC under LED visible light illumination, which is of great value in practical application for the antibiotic and other aromatic organic pollutants degradation in wastewater.

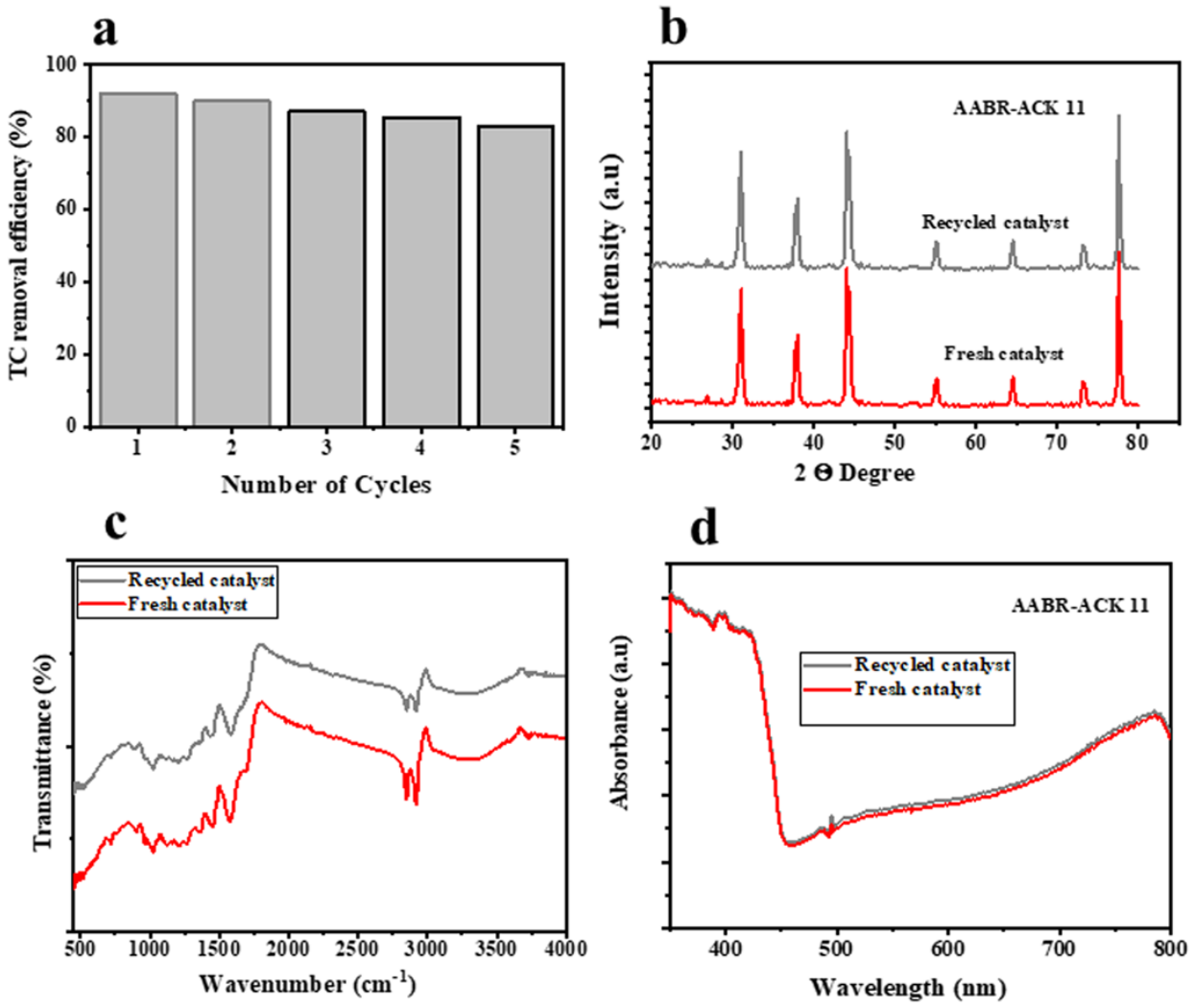

Figure 4.14: (a) Recycling test of AABR-ACK 11; (b-d) XRD, FTIR and UV-DRS spectra of AABR-ACK 11 composite before and recycled catalyst after the degradation activities.

4.4.4 Reaction Mechanism of AABR-ACK

In order to understand the photocatalytic mechanism, active species quenching experiments were performed. The quenchers used in this work comprised of EDTA-Na_2 for h^+, IPA for $^{\bullet}OH$ and BQ for $^{\cdot}O_2^-$ (Chen, Yang, Niu, Li, Zhang, Zhao, Xu, Zhong, Deng & Zeng 2016; Cheng, Yan, Zhou, Chen, Li, Chen & Dong 2016) respectively. As shown in **Figure 4.15**, both BQ and EDTA-Na_2 quenchers greatly inhibited the degradation of TC, and weakly reduced the activities on TC removal after the addition of IPA. It's concluded that the $^{\cdot}O_2^-$ and h^+ are the main active species in the photocatalytic degradation of TC using AABR-ACK 11, while the $^{\bullet}OH$ plays a secondary role. Invariably, O_2^-, h^+, and $^{\bullet}OH$ reactive species all participate in TC degradation (as a mixture).

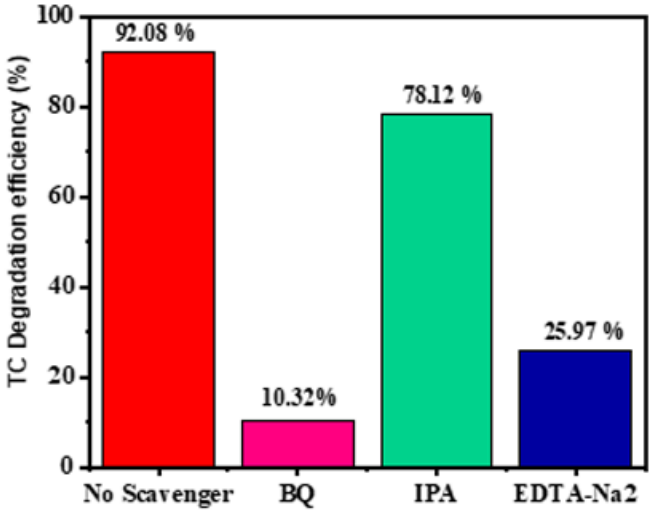

Figure 4.15: Effect of different quencher agents on TC degradation using AABR-ACK 11 composite.

Based on the above quencher experiment, a tentative reaction mechanism for degradation of TC under visible light irradiation using AABR-ACK 11 nanospheres structure is proposed, as presented in **Figure 4.16**. The TC molecules adsorb on the Ag and AgBr particles with close proximity to the ACK through π–π, electrostatic or hydrogen-bonding interactions (Upadhyay, Soin & Roy 2014; Zhu, Gao, Yue, Song, Gao & Xu 2018). Under visible light irradiation, both Ag and AgBr particles in AABR-ACK 11 composite are photoexcited to produce electron-hole pairs (Yu, Dai & Huang 2009; Kuai, Geng, Chen, Zhao & Luo 2010). The energy of excited electrons generated by the Ag SPR effect reached to 1.0–4.0 eV (Linic, Christopher & Ingram 2011), which means that the generated electrons have enough energy to jump onto the CB of AgBr. Injected electrons in the CB of AgBr cannot trap O_2 on its surface, since the CB potential of AgBr (0.13 eV) is more positive than the potential of O_2/O_2^- (-0.33 eV vs NHE) (Zhang, Ai, Li & Jiang 2014) and ACK presence as an acceptor of photo-induced electrons promotes the migration of electrons away from the conduction band (CB) of AgBr. The recombination with photo-excited holes is prevented while allowing the electrons to react with O_2 molecules on the ACK surface to form superoxide radical species and attacks the adsorbed TC directly (Hu et al. 2009; Hou, Wang, Yang, Zhou, Jiao & Zhu 2013). This electron transfer process significantly prolongs the lifetime of photogenerated charge carriers for intimate contact with TC pollutant, which results in elevated photocatalytic activity of AABR-ACK 11 under visible light illumination. The photo-induced holes accumulated at the Ag VB (Zhang, Wong, Chen, Jimmy, Zhao, Hu, Chan & Wong 2009) directly participate in the oxidation of TC. In addition, the photo-induced holes in VB AgBr are more positive to oxidize H2O to form ˙OH radicals (OH^-/OH, 2.4 V vs NHE) (Luo, Xu, Li, Wu, Wu, Shi, Chen & interfaces 2015). This reactive hydroxyl species (˙OH) produced by H_2O with

photo-induced holes also aid in the degradation of TC (Shahzad, Kim & Yu 2016). The positively charged holes on AgBr surface also oxidize Br^- to Br^o, Br^o is a reactive species that can oxidize TC directly due to its high oxidation potential, which is consistent with other reports (Begum, Manna & Rana 2012; Hou, Li, Zhao, Chen & Raston 2012a). Overall, the regulated nanospheres structure for AABR-ACK 11 composite, separation and transfer of photo-induced electron-hole pairs enhanced the photocatalytic efficiency and stability.

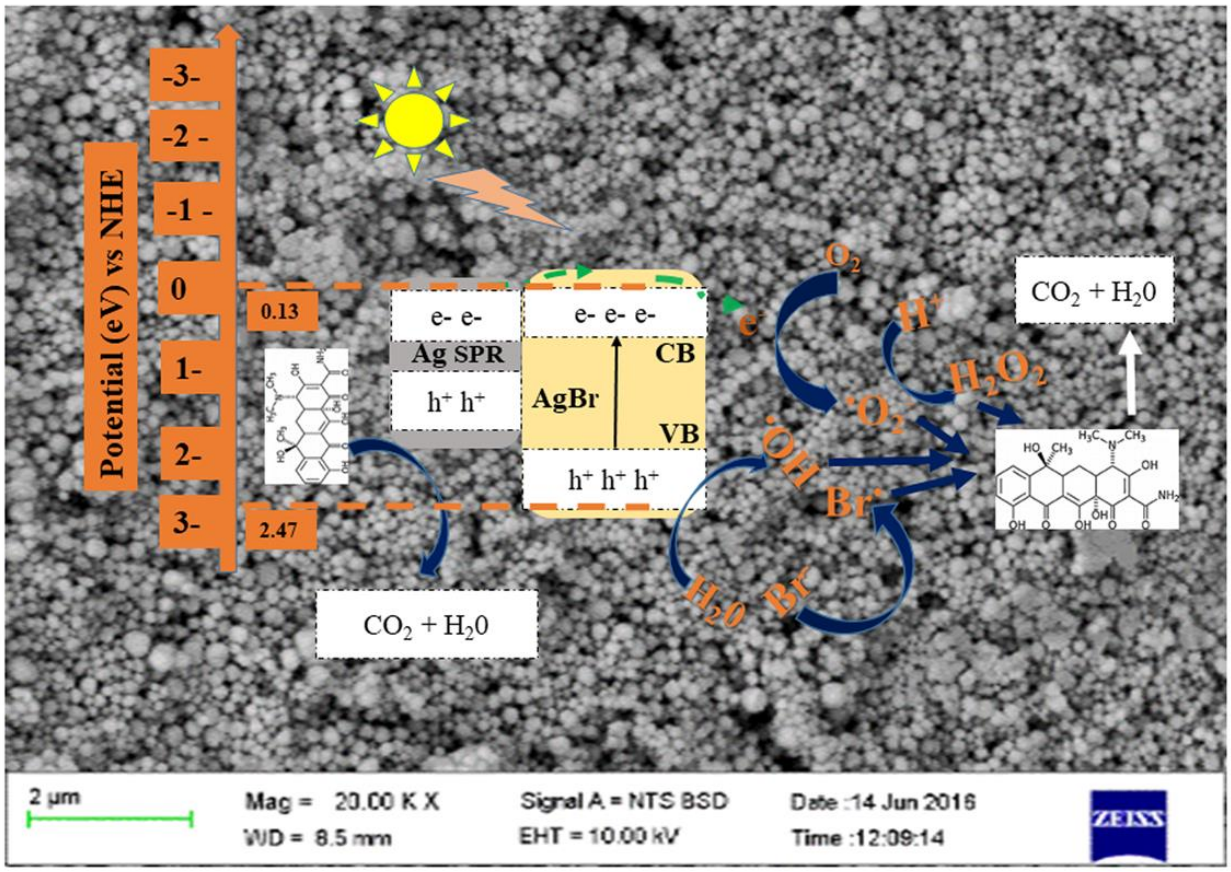

Figure 4.16: The reaction mechanism for the degradation of TC over the AABR-ACK 11 composite under visible light irradiation.

4.5. Summary and concluding remarks

AABR-ACK nanocomposites with close interfacial contact between the AABR particles and carbon were synthesized through the thermal polyol route. The synthesis variables (time, temperature, mass of PVP and activated carbon) were optimized using RSM experimental design to obtain the highest degradation of tetracycline (TC) antibiotic under visible light irradiation. The time and temperature as synthesis parameters play a major role in improving the catalyst properties to enhance the degradation of TC using the AABR-ACK composites. The characterization techniques showed that the optimized AABR-ACK 11 composite had an ordered nanospheres morphology with reduced particle diameter (162 nm), enhanced visible light harvesting along with high separation of photo-induced electron-hole pairs, which explains its high catalytic activity on TC removal in comparison to the other composites. The coupling of AABR into the ACK interconnected carbon network, significantly aid in uniform distribution of AABR particles, which furthers promotes interfacial charge separation and prolongs the lifetime of photo-carriers. The AABR-ACK 11 catalyst had a significantly higher visible light photocatalytic activity for TC removal (92%) than those of AABR, AgBr and reference TiO_2/HCP photocatalysts. The phosphate inorganic anion decreases the performance of AABR-ACK 11 more than other inorganic ions such as sulfate, sulphite, bicarbonate, and chloride. The quenching experiments with scavengers indicated that h^+ and $^{\bullet}O_2^-$ were the main radical responsible for the degradation process. The ordered nanospheres structure of AABR-ACK 11 with enhanced charge carriers separation efficiency is the most important factor that enhanced the activity for TC removal by oxidation degradation under visible light irradiation. This active AABR-ACK 11 photocatalyst property will further be compared with carbon material from different sources as presented in **Chapter 5**.

4.6 References

A. UYGUR. 1997. An overview of oxidative and photooxidative decolorisation treatments of textile waste-waters. *Journal of the Society of Dyers and Colourists,* 113, 211-217.

AN, C., PENG, S. & SUN, Y. 2010. Facile Synthesis of Sunlight-Driven AgCl: Ag Plasmonic Nanophotocatalyst. *Advanced Materials,* 22, 2570-2574.

BAFAQEER, A., TAHIR, M. & AMIN, N.A.S. 2019. Well-designed ZnV_2O_6/g-C_3N_4 2D/2D nanosheets heterojunction with faster charges separation via pCN as mediator towards enhanced photocatalytic reduction of CO_2 to fuels. *Applied Catalysis B: Environmental,* 242, 312-326.

BEGUM, G., MANNA, J. & RANA, R.K. 2012. Controlled orientation in a bio-Inspired assembly of Ag/AgCl/ZnO nanostructures enables enhancement in visible-light-induced photocatalytic performance. *Chemistry–A European Journal,* 18, 6847-6853.

CAO, J., LUO, B., LIN, H. & CHEN, S. 2011. Synthesis, characterization and photocatalytic activity of AgBr/H_2WO_4 composite photocatalyst. *Journal of Molecular Catalysis A: Chemical,* 344, 138-144.

CHEN, D., LI, T., CHEN, Q., GAO, J., FAN, B., LI, J., LI, X., ZHANG, R., SUN, J. & GAO, L. 2012. Hierarchically plasmonic photocatalysts of Ag/AgCl nanocrystals coupled with single-crystalline WO_3 nanoplates. *Nanoscale,* 4, 5431-5439.

CHEN, D., LIU, M., CHEN, Q., GE, L., FAN, B., WANG, H., LU, H., YANG, D., ZHANG, R. & YAN, Q. 2014. Large-scale synthesis and enhanced visible-light-driven photocatalytic performance of hierarchical Ag/AgCl nanocrystals derived from freeze-dried PVP–Ag^+ hybrid precursors with porosity. *Applied Catalysis B: Environmental,* 144, 394-407.

CHEN, F., YANG, Q., NIU, C., LI, X., ZHANG, C., ZHAO, J., XU, Q., ZHONG, Y., DENG, Y. & ZENG, G. 2016. Enhanced visible light photocatalytic activity and mechanism of $ZnSn(OH)_6$ nanocubes modified with AgI nanoparticles. *Catalysis Communications,* 73, 1-6.

CHEN, G., LI, F., HUANG, Z., GUO, C.-Y., QIAO, H., QIU, X., WANG, Z., JIANG, W. & YUAN, G. 2015. Facile synthesis of Ag/AgBr/RGO nanocomposite as a highly efficient sunlight plasmonic photocatalyst. *Catalysis Communications,* 59, 140-144.

CHEN, H., JING, L., TENG, Y. & WANG, J. 2018. Characterization of antibiotics in a large-scale river system of China: occurrence pattern, spatiotemporal distribution and environmental risks. *Science of The Total Environment,* 618, 409-418.

CHEN, W.-R. & HUANG, C.-H. 2011. Transformation kinetics and pathways of tetracycline antibiotics with manganese oxide. *Environmental Pollution,* 159, 1092-1100.

CHEN, Y. & LIU, K. 2017. Fabrication of Ce/N co-doped TiO_2/diatomite granule catalyst and its improved visible-light-driven photoactivity. *Journal of Hazardous Materials,* 324, 139-150.

CHENG, F., YAN, J., ZHOU, C., CHEN, B., LI, P., CHEN, Z. & DONG, X. 2016. An alkali treating strategy for the colloidization of graphitic carbon nitride and its excellent photocatalytic performance. *Journal of Colloid and Interface Science,* 468, 103-109.

CHOI, S.H. & KANG, Y.C. 2014. Fe_3O_4-decorated hollow graphene balls prepared by spray pyrolysis process for ultrafast and long cycle-life lithium ion batteries. *Carbon,* 79, 58-66.

CHOI, W.S., BYUN, G.Y., BAE, T.S. & LEE, H.-J. 2013. Evolution of AgX Nanowires into Ag Derivative Nano/microtubes for Highly Efficient Visible-Light Photocatalysts. *ACS Applied Materials and Interfaces,* 5, 11225-11233.

CONG-WEN, X., HAI-TAO, Y., CHENG-MIN, S., ZI-AN, L., HUAI-RUO, Z., FEI, L., TIAN-ZHONG, Y., SHU-TANG, C. & HONG-JUN, G. 2005. Controlled growth of large-scale silver nanowires. *Chinese Physics,* 14, 2269.

DA SILVA, G.T., CARVALHO, K.T., LOPES, O.F. & RIBEIRO, C. 2017. g-C_3N_4/Nb_2O_5 heterostructures tailored by sonochemical synthesis: Enhanced photocatalytic performance in oxidation of emerging pollutants driven by visible radiation. *Applied Catalysis B: Environmental,* 216, 70-79.

DAI, K., LU, L., DONG, J., JI, Z., ZHU, G., LIU, Q., LIU, Z., ZHANG, Y., LI, D. & LIANG, C. 2013. Facile synthesis of a surface plasmon resonance-enhanced Ag/AgBr heterostructure and its photocatalytic performance with 450 nm LED illumination. *Dalton Transactions,* 42, 4657-4662.

DENG, H., LI, G., YANG, H., TANG, J. & TANG, J. 2010. Preparation of activated carbons from cotton stalk by microwave assisted KOH and K_2CO_3 activation. *Chemical Engineering Journal,* 163, 373-381.

DONG, H., ZENG, G., TANG, L., FAN, C., ZHANG, C., HE, X. & HE, Y. 2015. An overview on limitations of TiO_2-based particles for photocatalytic degradation of organic pollutants and the corresponding countermeasures. *Water Research,* 79, 128-146.

ESMAEILI, A. & ENTEZARI, M.H. 2015. Cubic Ag/AgBr–graphene oxide nanocomposite: Sono-synthesis and use as a solar photocatalyst for the degradation of DCF as a pharmaceutical pollutant. *RSC Advances,* 5, 97027-97035.

GAIKWAD, S.H., KORATTI, A. & MUKHERJEE, S.P. 2019. Facile tuning of Ag@ AgCl cubical hollow nanoframes with efficient sunlight-driven photocatalytic activity. *Applied Surface Science,* 465, 413-419.

GAO, N., LU, Z., ZHAO, X., ZHU, Z., WANG, Y., WANG, D., HUA, Z., LI, C., HUO, P. & SONG, M. 2016. Enhanced photocatalytic activity of a double conductive C/Fe_3O_4/Bi_2O_3 composite photocatalyst based on biomass. *Chemical Engineering Journal,* 304, 351-361.

GAO, Y., SONG, L., JIANG, P., LIU, L., YAN, X., ZHOU, Z., LIU, D., WANG, J., YUAN, H. & ZHANG, Z. 2005. Silver nanowires with five-fold symmetric cross-section. *Journal of Crystal Growth,* 276, 606-612.

HOU, J., WANG, Z., YANG, C., ZHOU, W., JIAO, S. & ZHU, H. 2013. Hierarchically plasmonic Z-scheme photocatalyst of Ag/AgCl nanocrystals decorated mesoporous single-crystalline metastable $Bi_{20}TiO_{32}$ nanosheets. *The Journal of Physical Chemistry C,* 117, 5132-5141.

HOU, Y., LI, X., ZHAO, Q., CHEN, G. & RASTON, C.L. 2012a. Role of hydroxyl radicals and mechanism of Escherichia coli inactivation on Ag/AgBr/TiO_2 nanotube array electrode under visible light irradiation. *Environmental Science and Technology,* 46, 4042-4050.

HU, C., PENG, T., HU, X., NIE, Y., ZHOU, X., QU, J. & HE, H. 2009. Plasmon-induced photodegradation of toxic pollutants with Ag− AgI/Al_2O_3 under visible-light irradiation. *Journal of the American Chemical Society,* 132, 857-862.

HUANG, H.-B., WANG, Y., JIAO, W.-B., CAI, F.-Y., SHEN, M., ZHOU, S.-G., CAO, H.-L., LÜ, J. & CAO, R. 2018. Lotus-leaf-derived activated-carbon-supported nano-CdS as energy-efficient photocatalysts under visible irradiation. *ACS Sustainable Chemistry Engineering,* 6, 7871-7879.

INOUE, H., NAKAZAWA, T., MITSUHASHI, T., SHIRAI, T. & FLUCK, E. 1989. Characterization of Prussian blue and its thermal decomposition products. *Hyperfine Interactions,* 46, 723-731.

JIANG, J. & ZHANG, L. 2011. Rapid Microwave-Assisted Nonaqueous Synthesis and Growth Mechanism of AgCl/Ag, and Its Daylight-Driven Plasmonic Photocatalysis. *Chemistry-A European Journal,* 17, 3710-3717.

JIANG, L., YUAN, X., ZENG, G., CHEN, X., WU, Z., LIANG, J., ZHANG, J., WANG, H. & WANG, H. 2017. Phosphorus-and sulfur-codoped g-C_3N_4: facile preparation, mechanism insight, and application as efficient photocatalyst for tetracycline and methyl orange degradation under visible light irradiation. *ACS Sustainable Chemistry Engineering,* 5, 5831-5841.

KAKAVANDI, B., BAHARI, N., KALANTARY, R.R. & FARD, E.D. 2019. Enhanced sono-photocatalysis of tetracycline antibiotic using TiO_2 decorated on magnetic activated carbon (MAC@ T) coupled with US and UV: A new hybrid system. *Ultrasonics Sonochemistry,* 55, 75-85.

KANDI, D., MARTHA, S., THIRUMURUGAN, A. & PARIDA, K. 2017. Modification of BiOI microplates with CdS QDs for enhancing stability, optical property, electronic behavior toward rhodamine B decolorization, and photocatalytic hydrogen evolution. *The Journal of Physical Chemistry C,* 121, 4834-4849.

KHAN, J.H., MARPAUNG, F., YOUNG, C., LIN, J., ISLAM, M.T., ALSHERI, S.M., AHAMAD, T., ALHOKBANY, N., ARIGA, K. & SHRESTHA, L.K. 2019. Jute-derived microporous/mesoporous carbon with ultra-high surface area using a chemical activation process. *Microporous and Mesoporous Materials,* 274, 251-256.

KONSTANTINOU, I.K. & ALBANIS, T.A. 2004. TiO_2-assisted photocatalytic degradation of azo dyes in aqueous solution: kinetic and mechanistic investigations: a review. *Applied Catalysis B: Environmental,* 49, 1-14.

KUAI, L., GENG, B., CHEN, X., ZHAO, Y. & LUO, Y. 2010. Facile subsequently light-induced route to highly efficient and stable sunlight-driven Ag− AgBr plasmonic photocatalyst. *Langmuir,* 26, 18723-18727.

LEI, Y., WANG, G., SONG, S., FAN, W., PANG, M., TANG, J. & ZHANG, H. 2010. Room temperature, template-free synthesis of BiOI hierarchical structures: visible-light photocatalytic and electrochemical hydrogen storage properties. *Dalton Transactions,* 39, 3273-3278.

LI, B., WANG, H., ZHANG, B., HU, P., CHEN, C. & GUO, L. 2013. Facile synthesis of one dimensional AgBr@ Ag nanostructures and their visible light photocatalytic properties. *ACS Applied Materials and Interfaces,* 5, 12283-12287.

LI, D., CHEN, Y., YIN, F., ZHU, L., LI, J. & MA, X. 2018. Facile synthesis of Mn/N-doped TiO_2 on wood-based activated carbon fiber as an efficient visible-light-driven photocatalyst. *Journal of Materials Science,* 53, 11671-11683.

LI, J., MA, Y., YE, Z., ZHOU, M., WANG, H., MA, C., WANG, D., HUO, P. & YAN, Y. 2017. Fast electron transfer and enhanced visible light photocatalytic activity using multi-dimensional components of carbon quantum dots@ 3D daisy-like In_2S_3/single-wall carbon nanotubes. *Applied Catalysis B: Environmental,* 204, 224-238.

LINARES, N., SILVESTRE-ALBERO, A.M., SERRANO, E., SILVESTRE-ALBERO, J. & GARCÍA-MARTÍNEZ, J. 2014. Mesoporous materials for clean energy technologies. *Chemical Society Reviews,* 43, 7681-7717.

LINIC, S., CHRISTOPHER, P. & INGRAM, D.B. 2011. Plasmonic-metal nanostructures for efficient conversion of solar to chemical energy. *Nature Materials,* 10, 911.

LIU, X., LV, P., YAO, G., MA, C., HUO, P. & YAN, Y. 2013. Microwave-assisted synthesis of selective degradation photocatalyst by surface molecular imprinting method for the degradation of tetracycline onto Cl-TiO_2. *Chemical Engineering Journal*, 217, 398-406.

LIU, C., DONG, X., HAO, Y., WANG, X., MA, H. & ZHANG, X. 2017. Efficient photocatalytic dye degradation over Er-doped BiOBr hollow microspheres wrapped with graphene nanosheets: enhanced solar energy harvesting and charge separation. *RSC Advances,* 7, 22415-22423.

LÓPEZ-PEÑALVER, J.J., SÁNCHEZ-POLO, M., GÓMEZ-PACHECO, C.V. & RIVERA-UTRILLA, J. 2010. Photodegradation of tetracyclines in aqueous solution by using UV and UV/H_2O_2 oxidation processes. *Journal of Chemical Technology and Biotechnology,* 85, 1325-1333.

LOU, Z., HUANG, B., QIN, X., ZHANG, X., CHENG, H., LIU, Y., WANG, S., WANG, J. & DAI, Y. 2012. One-step synthesis of AgCl concave cubes by preferential overgrowth along< 111> and< 110> directions. *Chemical Communications,* 48, 3488-3490.

LUO, B., XU, D., LI, D., WU, G., WU, M., SHI, W., CHEN, M.J.A.A.M. & INTERFACES. 2015. Fabrication of a Ag/Bi_3TaO_7 plasmonic photocatalyst with enhanced photocatalytic activity for degradation of tetracycline. *ACS Applied Materials and Interfaces,* 7, 17061-17069.

LUO, Y., XU, L., RYSZ, M., WANG, Y., ZHANG, H. & ALVAREZ, P.J. 2011. Occurrence and transport of tetracycline, sulfonamide, quinolone, and macrolide antibiotics in the Haihe River Basin, China. *Environmental Science Technology,* 45, 1827-1833.

MAHAMALLIK, P., SAHA, S. & PAL, A. 2015. Tetracycline degradation in aquatic environment by highly porous MnO_2 nanosheet assembly. *Chemical Engineering Journal,* 276, 155-165.

MCEVOY, J.G. & ZHANG, Z. 2014. Synthesis and characterization of magnetically separable Ag/AgCl–magnetic activated carbon composites for visible light induced photocatalytic detoxification and disinfection. *Applied Catalysis B: Environmental*, 160, 267-278.

MCEVOY, J.G. & ZHANG, Z. 2016. Synthesis and characterization of Ag/AgBr–activated carbon composites for visible light induced photocatalytic detoxification and disinfection. *Journal of Photochemistry and Photobiology A: Chemistry*, 321, 161-170.

MOU, H., SONG, C., ZHOU, Y., ZHANG, B. & WANG, D. 2018. Design and synthesis of porous Ag/ZnO nanosheets assemblies as super photocatalysts for enhanced visible-light degradation of 4-nitrophenol and hydrogen evolution. *Applied Catalysis B: Environmental*, 221, 565-573.

NAYAK, S., MOHAPATRA, L. & PARIDA, K. 2015. Visible light-driven novel gC_3N_4/NiFe-LDH composite photocatalyst with enhanced photocatalytic activity towards water oxidation and reduction reaction. *Journal of Materials Chemistry A*, 3, 18622-18635.

POLESEL, F., ANDERSEN, H.R., TRAPP, S. & PLÓSZ, B.G. 2016. Removal of Antibiotics in Biological Wastewater Treatment Systems - A Critical Assessment Using the Activated Sludge Modeling Framework for Xenobiotics (ASM-X). *Environmental Science Technology*, 50, 10316-10334.

RINCON, A.-G. & PULGARIN, C. 2004. Effect of pH, inorganic ions, organic matter and H_2O_2 on E. coli K12 photocatalytic inactivation by TiO_2: implications in solar water disinfection. *Applied Catalysis B: Environmental*, 51, 283-302.

SAHEED, S.O., MODISE, S.J. & SIPAMLA, A.M. 2013. TiO_2 supported clinoptilotile: characterization and optimization of operational parameters for methyl orange removal. *In Advanced Materials Research, Trans Tech Publication*, 2249-2252.

SHAHZAD, A., KIM, W.-S. & YU, T. 2016. A facile synthesis of Ag/AgCl hybrid nanostructures with tunable morphologies and compositions as advanced visible light plasmonic photocatalysts. *Dalton Transactions,* 45, 9158-9165.

SHI, H., LI, G., SUN, H., AN, T., ZHAO, H. & WONG, P.-K. 2014. Visible-light-driven photocatalytic inactivation of E. coli by Ag/AgX-CNTs (X= Cl, Br, I) plasmonic photocatalysts: Bacterial performance and deactivation mechanism. *Applied Catalysis B: Environmental,* 158, 301-307.

SUN, Y. & XIA, Y. 2002. Shape-controlled synthesis of gold and silver nanoparticles. *Science,* 298, 2176-2179.

TIAN, C., ZHAO, H., SUN, H., XIAO, K. & WONG, P.K. 2020. Enhanced adsorption and photocatalytic activities of ultrathin graphitic carbon nitride nanosheets: Kinetics and mechanism. *Chemical Engineering Journal*, 381, 122760.

UPADHYAY, R.K., SOIN, N. & ROY, S.S. 2014. Role of graphene/metal oxide composites as photocatalysts, adsorbents and disinfectants in water treatment: a review. *RSC Advances,* 4, 3823-3851.

WANG, P., HUANG, B., ZHANG, X., QIN, X., JIN, H., DAI, Y., WANG, Z., WEI, J., ZHAN, J. & WANG, S. 2009. Highly Efficient Visible-Light Plasmonic Photocatalyst Ag@AgBr. *Chemistry-A European Journal,* 15, 1821-1824.

WANG, W., FANG, H.-B., ZHENG, Y.-Z., CHE, Y., TAO, X. & CHEN, J.-F. 2015. In situ template-free synthesis of a novel 3D p–n heteroarchitecture Ag_3PO_4/Ta_3N_5 photocatalyst with high activity and stability under visible radiation. *RSC Advances,* 5, 62519-62526.

WEN, X.-J., NIU, C.-G., ZHANG, L., LIANG, C. & ZENG, G.-M. 2018. A novel Ag_2O/CeO_2 heterojunction photocatalysts for photocatalytic degradation of enrofloxacin: possible degradation

pathways, mineralization activity and an in depth mechanism insight. *Applied Catalysis B: Environmental,* 221, 701-714.

WEN, X.-J., NIU, C.-G., ZHANG, L. & ZENG, G.-M. 2017. Novel p–n heterojunction BiOI/CeO_2 photocatalyst for wider spectrum visible-light photocatalytic degradation of refractory pollutants. *Dalton Transactions,* 46, 4982-4993.

WU, S., SHEN, X., JI, Z., ZHU, G., ZHOU, H., ZANG, H., YU, T., CHEN, C., SONG, C. & FENG, L. 2017. Morphological syntheses and photocatalytic properties of well-defined sub-100 nm Ag/AgCl nanocrystals by a facile solution approach. *Journal of Alloys Compounds,* 693, 132-140.

XIANG XU, SHEN, X., HU ZHOU, DEZHOU QIU, GUOXING ZHU & CHEN, K. 2013. Facile microwave-assisted synthesis of monodispersed ball-like Ag@AgBr photocatalyst with high activity and durability. *Applied Catalysis A: General,* 455, 183–192.

XIAO, X., GE, L., HAN, C., LI, Y., ZHAO, Z., XIN, Y., FANG, S., WU, L. & QIU, P. 2015. A facile way to synthesize Ag@ AgBr cubic cages with efficient visible-light-induced photocatalytic activity. *Applied Catalysis B: Environmental,* 163, 564-572.

XU, H., LI, H., XIA, J., YIN, S., LUO, Z., LIU, L. & XU, L. 2010. One-pot synthesis of visible-light-driven plasmonic photocatalyst Ag/AgCl in ionic liquid. *ACS Applied Materials and Interfaces,* 3, 22-29.

XU, H., YAN, J., XU, Y., SONG, Y., LI, H., XIA, J., HUANG, C. & WAN, H. 2013. Novel visible-light-driven AgX/graphite-like C_3N_4 (X= Br, I) hybrid materials with synergistic photocatalytic activity. *Applied Catalysis B: Environmental,* 129, 182-193.

XU, X., SHEN, X., ZHOU, H., QIU, D., ZHU, G. & CHEN, K. 2013. Facile microwave-assisted synthesis of monodispersed ball-like Ag@ AgBr photocatalyst with high activity and durability. *Applied Catalysis A: General,* 455, 183-192.

XU, Y., XU, H., YAN, J., LI, H., HUANG, L., ZHANG, Q., HUANG, C. & WAN, H. 2013. A novel visible-light-response plasmonic photocatalyst CNT/Ag/AgBr and its photocatalytic properties. *Physical Chemistry Chemical Physics,* 15, 5821-5830.

YAN, T., ZHANG, H., LUO, Q., MA, Y., LIN, H. & YOU, J. 2013. Controllable synthesis of plasmonic Ag/AgBr photocatalysts by a facile one-pot solvothermal route. *Chemical Engineering Journal,* 232, 564-572.

YU, J., DAI, G. & HUANG, B. 2009. Fabrication and characterization of visible-light-driven plasmonic photocatalyst Ag/AgCl/TiO_2 nanotube arrays. *The Journal of Physical Chemistry C,* 113, 16394-16401.

YU, Y., ZHU, Z., FAN, W., LIU, Z., YAO, X., DONG, H., LI, C. & HUO, P. 2018. Making of a metal-free graphitic carbon nitride composites based on biomass carbon for efficiency enhanced tetracycline degradation activity. *Journal of the Taiwan Institute of Chemical Engineers,* 89, 151-161.

YUAN, A., LEI, H., XI, F., LIU, J., QIN, L., CHEN, Z. & DONG, X. 2019. Graphene quantum dots decorated graphitic carbon nitride nanorods for photocatalytic removal of antibiotics. *Journal of Colloid and Interface Science,* 548, 56-65.

ZENG, C., TIAN, B. & ZHANG, J. 2013. Silver halide/silver iodide@ silver composite with excellent visible light photocatalytic activity for methyl orange degradation. *Journal of Colloid and Interface Science,* 405, 17-21.

ZHANG, C., AI, L., LI, L. & JIANG, J. 2014. One-pot solvothermal synthesis of highly efficient, daylight active and recyclable Ag/AgBr coupled photocatalysts with synergistic dual photoexcitation. *Journal of Alloys Compounds,* 582, 576-582.

ZHANG, H., FAN, X., QUAN, X., CHEN, S. & YU, H. 2011. Graphene sheets grafted Ag@ AgCl hybrid with enhanced plasmonic photocatalytic activity under visible light. *Environmental Science and Technology,* 45, 5731-5736.

ZHANG, H., HAN, X., YU, H., ZOU, Y. & DONG, X. 2019. Enhanced photocatalytic performance of boron and phosphorous co-doped graphitic carbon nitride nanosheets for removal of organic pollutants. *Separation and Purification Technology*, 226, 128-137.

ZHANG, L., SHI, Y., WANG, L. & HU, C. 2018. AgBr-wrapped Ag chelated on nitrogen-doped reduced graphene oxide for water purification under visible light. *Applied Catalysis B: Environmental,* 220, 118-125.

ZHANG, L., WONG, K.-H., CHEN, Z., JIMMY, C.Y., ZHAO, J., HU, C., CHAN, C.-Y. & WONG, P.-K. 2009. AgBr-Ag-Bi_2WO_6 nanojunction system: a novel and efficient photocatalyst with double visible-light active components. *Applied Catalysis A: General,* 363, 221-229.

ZHANG, S., LI, J., WANG, X., HUANG, Y., ZENG, M. & XU, J. 2014. In situ ion exchange synthesis of strongly coupled Ag@ AgCl/g-C_3N_4 porous nanosheets as plasmonic photocatalyst for highly efficient visible-light photocatalysis. *ACS Applied Materials and Interfaces*, 6, 22116-22125.

ZHANG, W., XU, J., HOU, D., YIN, J., LIU, D., HE, Y. & LIN, H. 2018. Hierarchical porous carbon prepared from biomass through a facile method for supercapacitor applications. *Journal of Colloid Interface Science*, 530, 338-344.

ZHOU, C., LAI, C., HUANG, D., ZENG, G., ZHANG, C., CHENG, M., HU, L., WAN, J., XIONG, W. & WEN, M. 2018. Highly porous carbon nitride by supramolecular preassembly of monomers for photocatalytic removal of sulfamethazine under visible light driven. *Applied Catalysis B: Environmental,* 220, 202-210.

ZHU, M., CHEN, P. & LIU, M. 2011. Graphene oxide enwrapped Ag/AgX (X= Br, Cl) nanocomposite as a highly efficient visible-light plasmonic photocatalyst. *ACS Nano,* 5, 4529-4536.

ZHU, M., CHEN, P. & LIU, M. 2012. Ag/AgBr/graphene oxide nanocomposite synthesized via oil/water and water/oil microemulsions: a comparison of sunlight energized plasmonic photocatalytic activity. *Langmuir,* 28, 3385-3390.

ZHU, Q., WANG, W.-S., LIN, L., GAO, G.-Q., GUO, H.-L., DU, H. & XU, A.-W. 2013. Facile synthesis of the novel Ag_3VO_4/AgBr/Ag plasmonic photocatalyst with enhanced photocatalytic activity and stability. *The Journal of Physical Chemistry C,* 117, 5894-5900.

ZHU, X., GAO, Y., YUE, Q., SONG, Y., GAO, B. & XU, X. 2018. Facile synthesis of hierarchical porous carbon material by potassium tartrate activation for chloramphenicol removal. *Journal of the Taiwan Institute of Chemical Engineers,* 85, 141-148.

Chapter 5. Accelerated electron transport and improved photocatalytic activity of Ag/AgBr under visible light irradiation based on conductive carbon derived biomass

Abstract

Ag/AgBr (AABR) catalyst exhibits good photo-oxidative property for organic pollutants degradation under visible light. However, poor separation of photogenerated charge carriers at the catalyst interface, caused by decelerated photoexcited electron migration results in lower photocatalytic activity and limits the practical application of AABR. In this chapter, series of carbonized materials from different sources (potassium hydroxide impregnated pinecone - ACK, commercial activated carbon - CAC and biochar from pinecone - BCR) were employed as conductive carbon support for coupling Ag/AgBr as-synthesized through thermal polyol route. The structural, electrochemical and optical properties of prepared composites were characterized by various techniques. ACK from microwave pyrolysis of chemically impregnated pinecone exhibited fast electron transfer as compared to BCR and commercial activated carbon (CAC) from the Nyquist EIS plot, due to its interconnected conductive carbon structures. The resulting AABR-ACK exhibit improved degradation efficiency of 92% on tetracycline (TC) antibiotic in a

neutral solution after 180 min, which is better than AABR-BCR and AABR-CAC under visible LED light irradiation. The superior degradation efficiency of AABR-ACK is ascribed to the accelerated transport and enhances separation of photogenerated charge carriers upon introduction of conductive ACK. The degradation intermediates and possible decomposition pathways of TC by AABR-ACK catalyst were identified by LC-MS in this chapter.

Keywords: Ag/AgBr, Conductive carbon, Biomass, Visible light degradation, Tetracycline.

5.1 Introduction

The discharge of industrial effluents such as pharmaceuticals into the water resources over the decade possesses perilous impact on the ecosystem, due to their physiological toxicity and corrosive attributes (La Farre, Pérez, Kantiani & Barceló 2008; Song, Sun, Wang, Xia, Yuan, Li & Wang 2016). Complete removal of these pharmaceutical components such as tetracycline (TC) is crucial, in other to avoid adaptable multi-resistant bacterial strains and other environmental issues (Sun, Shi, Mao & Zhu 2010; Chen & Liu 2016). This imperious situation warrants the motivation in the development of cost-effective and highly efficient technologies for complete degradation of TC antibiotics. The visible-light photocatalytic approach is attractive for the elimination of these TC antibiotics in wastewater since it is cost-effective as compared to conventional approaches (Zhu, Wang, Sun & Zhou 2013; Jiang, Wang, Xu, Li, Meng & Chen 2017). Commonly used photocatalyst such as ZnO and TiO_2 are inactive under visible light and requires ultraviolet light to be active. These catalysts can therefore not harness the solar efficiency effectively (Reyes, Fernandez, Freer, Mondaca, Zaror, Malato & Mansilla 2006; Palominos, Mondaca, Giraldo, Peñuela, Pérez-Moya & Mansilla 2009). Therefore, the development of highly efficient visible light-driven (VLD) photocatalysts is necessitated.

Previous studies have shown that the surface plasmon resonance (SPR) properties of Ag with AgX (X-Cl, Br, I) material yielded active VLD photocatalyst properties for environmental remediation (Hou, Li, Zhao, Chen & Raston 2012; Shi, Li, Sun, An, Zhao & Wong 2014). Ag/AgX plasmonic catalyst has a limitation of poor separation of photogenerated charge carriers that results in lower photocatalytic activity (Zhang, Fan, Quan, Chen & Yu 2011). Techniques such as microstructures control (Xiao, Ge, Han, Li, Zhao, Xin, Fang, Wu & Qiu 2015), formation of heterogeneous hybrid with other semiconductors (Yang, Guo, Guo, Zhao, Yuan & Guo 2014; Yan,

Wang, Gu, Wu, Yan, Hu, Che, Han, Yang & Fan 2015) and carbonaceous materials (Xu, Xu, Yan, Li, Huang, Zhang, Huang & Wan 2013; Shi, Lv, Yuan, Huang, Liu & Kang 2017) have been utilized to enhance separation of photogenerated charge carriers of Ag/AgBr. Coupling Ag/AgBr with carbonaceous materials exhibited better improvement in photocatalytic activity of the photocatalyst more than other methods described above. Over the past few years, photocatalysts combined with carbonaceous materials such as graphene, graphene oxide, carbon nanotubes and carbon dots with high conductivity for electron transport have significantly suppressed the recombination of electron-hole pairs in the photocatalyst and enhanced the photocatalytic activity (Chen, Li, Huang, Zhang, Zhao & An 2012; Yang, Weng & Xu 2013; Vinoth, Karthik, Muthamizhchelvan, Neppolian & Ashokkumar 2016; Shi et al. 2017). Among the known carbonaceous materials, activated carbon (AC) from biomass known as an eco-friendly material has aroused interest in several applications Activated carbon have been applied in supercapacitors and photocatalysis as a result of their sustainability, renewable, cheap, stable and good electrical conductivity properties (Trogadas, Fuller & Strasser 2014; Song, Ma, Wu, Ma, Geng & Wan 2015; Li, Tie, Li, Guo, Liu, Liu, Liu, Feng & Zhao 2018; Lu, Jin, Zhang, Niu, Gao & Li 2018).

The coupling of Ag/AgBr photocatalyst with commercial activated carbon as support has been investigated widely (McEvoy, Joanne Gamage & Zhang, Zisheng 2016; Yang, Jin, Liu, Gan & Wei 2019). These studies described above have not considered the possibility of enhancing the properties of activated carbon to improve photo-excited electron transfer from the photocatalyst. Since, the abundance of sp^2-hybridized C-C with the activated carbon can facilitate the fast transfer of electron from the catalyst material (Gupta, Dimitratos, Su & Villa 2019). The utilization of activated carbon derived from biomass as catalyst support for Ag/AgBr (AABR) is an inspiring perspective in accelerating the transfer of photoinduced electron and boosting interfacial charge

separation, whilst improving the photocatalytic performance of Ag/AgBr. Pinecone biomass is a widely available resource worldwide, it's high lignin content as compared to other biomass favor its utilization for ACs production (Bello, Manyala, Barzegar, Khaleed, Momodu & Dangbegnon 2016). However, AC derived from pinecone biomass potential as catalyst support for transport of photoexcited electron from photocatalyst interface is still under-explored. As far as we know there are no published reports on the use of pinecone activated carbon as catalyst support for Ag/AgBr photocatalyst dispersion, or its application for environmental remediation.

In this chapter, an eco-friendly ACK with improved electron conductive was prepared by the charring pinecone (under inert atmosphere) coupled by potassium hydroxide (KOH) impregnation and microwave pyrolysis (ACK). The Ag/AgBr (AABR) was then coupled with biochar (BCR), ACK, and commercial activated carbon (CAC) through a modified thermal polyol route. The electron conductive properties of ACK, CAC and BCR were evaluated using nyquist electrochemical impedance spectroscopy (EIS). The photocatalytic activity of prepared composites was evaluated by the degradation of tetracycline hydrochloride (TC) antibiotic under visible light irradiation. The influence of operational parameters such as pH, different LED light, degradation temperature with the most active catalyst were carried out in this chapter. The physicochemical and electrical properties were discussed in details, while a new perspective regarding the influence of ACK on the superior photocatalytic activity was proposed.

5.2 Experimental

5.2.1 Preparation of photocatalyst materials

The preparation of optimized activated carbon (ACK-2.24-16) from KOH impregnated pinecone and biochar have been described properly in **Chapter 3** (**Section 3.2.2**). The synthesis

of Ag/AgBr on activated carbon (AABR-ACK) was carried out through a modified thermal polyol route (Chen, Li, Huang, Guo, Qiao, Qiu, Wang, Jiang & Yuan 2015), and already optimized in **Chapter 4** (**Section 4.2.4**). In a typical preparation of the AABR-ACK, 18 mL of ethylene glycol (EG, 99%, Acros) was poured into a round-bottom flask which was heated at 60℃ for 30 min. Polyvinylpyrrolidone (0.26g, PVP, M.W. 58000, K 29-32 Acros) and 480 mg of hexadecyltrimethylammonium bromide (HTAB, Acros, 99%) were sequentially added to the solution, and then 0.03 g of ACK as the catalyst support were further then added to the reaction mixture. After proper mixing to completely dissolve the PVP and HTAB, 3 ml EG solution containing 200 mg silver nitrate (Merck, 98%) was slowly added drop-wise to the stirred solution. The solution was maintained at 60 °C for an additional 30 min, and thereafter the stirred solution was then heated to a temperature of 140 °C. After reaching the desired temperature, the reaction was further stirred for 18 min. Thereafter the reaction mixture was cooled down to room temperature in the air. The resulting precipitate were separated by centrifugation at 6000 rpm for 10 mins (REMI bench top centrifuge-R-8 D), washed thoroughly with ethanol, and dried in an oven for 12 hr. For comparison purpose, AABR - CAC and AABR - BCR were also prepared via the same route (**Section 4.2.4**) in the presence of CAC (DARCO, Sigma Aldrich, 100 mesh) and BCR as carbonaceous catalyst support respectively. In addition, silver bromide and silver dispersed on ACK (AgBr/ACK and Ag/ACK) was prepared as described route (**Section 4.2.4)** in the dark environment and without addition of HTAB in the dark.

5.2.2 Characterization of the synthesized materials

Shimadzu X-ray 700 with Cu Kαradiation recorded the X-ray diffraction (XRD) pattern of the samples in the 2θ range of 20–80º at 40 KV and 40 MA. The crystallite size of the prepared samples

was estimated from the Scherrer equation by using the most intense reflection peak (Amin, Pazouki & Hosseinnia 2009). The microstructures of the prepared products were observed through scanning electron microscopy (Zeiss Leo 1430 VP) and energy dispersive X-ray spectrometer (EDS, INCA). Ultraviolet-visible (UV−vis) diffuse reflectance spectroscopy (DRS) was conducted via an Ocean Optics high-resolution spectrometer (Maya 2000) equipped with an integrating sphere accessory, using $BaSO_4$ as a reference within the wavelength range of 350 to 800 nm. Photoluminescence (PL) spectra of the produced samples were collected using Fluorescence spectrophotometer (FP-8600 Spectrofluorometer, Jasco) with an excitation wavelength at 365 nm. The produced photocatalyst were characterized using Fourier Transform Infrared Spectroscopy (FTIR) on a PerkinElmer spectrometer (spectrum 400 FT-IR/NIR) in the range of 4000-400 cm^{-1}. The linear sweep voltammetry (LSV) and electrochemical impedance spectroscopy (EIS) were performed using a Biologic SP 240 potentiostat workstation in a standard three-electrode system with the prepared samples as the glassy carbon electrode (GCE). A platinum wire and Ag/AgCl (in saturated KCl) were used as the counter electrode and a reference electrode, respectively. The working electrode was prepared as follows: 5 mg were dispersed into 0.5 ml DMF solution using ultrasonication machine to obtain a homogenous solution and 20 µL of it is drop cast on the clean GCE. The LSV was carried out using 0.2 M sodium sulphate solution at 50 Mv/S. The EIS experiments were carried out between frequency ranges of 100 KHz to 40 mHz with a perturbation amplitude of 5 mV in 5 mM Ferrocyanide containing 0.1 M KCl solution as an electrolyte.

5.2.3 Photocatalytic activity evaluation

The photocatalytic activity of prepared samples was evaluated by degradation of tetracycline hydrochloride (TC, Sigma Aldrich, 99%) under a 36 W white visible RGB LED light (Oseghe & Ofomaja 2018). The initial TC concentration was 15 mg/L and the photocatalyst loading was 0.3

g/L in 150 mL of TC solution. Prior to irradiation, the mixed solution was sonicated, mildly stirred in the reactor for 60 min in the dark (D) to achieve adsorption/desorption equilibrium of TC on the surface of the sample. The adsorbed solution was subjected to degradation by switching on the visible light (VL) LED under stirring for 3 hr, while 3 mL of suspension was withdrawn at time intervals (30 min), centrifuged and analyzed by a UV-visible spectrophotometer (T80 model, PG Instrument Limited, USA) at 376 nm. In this work, the photocatalytic performance of optimized AABR-ACK composite unto TC degradation was further assessed as a function of solution pH, different temperatures and LED light to determine the optimum conditions.

The by-products of TC and other aromatic organic pollutants (4-Nitrophenoll and Rhodamine B) degradation were analyzed by Dionex Ultimate 3000 UHPLC system (Thermo Scientific, Dionex, Sunnyvale, California, USA) coupled to a Bruker Compact Q-TOF mass spectrometer (Bruker Daltonics, Bremen, Germany). Injection volume was 10 µL, which was run through a loop for one minute at 50% Solvent A consisting of 0.1 % formic acid in H_2O (v/v) and 50% solvent B consisting of 0.1 % formic acid in Acetonitrile (v/v) at a flow rate of 0.3 mL/min.

5.3 Results and discussions

5.3.1 Characterization

The formation process of AABR composite with the carbon materials is presented in **Figure 5.1**. When the $AgNO_3$ solution is added dropwise to the suspension mixture of HTAB and PVP in the presence of the carbon samples at initial temperature of 60 °C, AgBr nanoparticles are generated via ion exchange reaction. Moreover, the partial reduction of Ag^+ from formed AgBr to metallic Ag occurs upon ramping up the temperature to desired target under ambient light condition to form the Ag/AgBr. The increased reaction temperature, PVP and carbon materials

significantly strain the fast diffusion rate of generated AgBr, thus resulting in controlled microstructure of Ag/AgBr nanoparticles on the carbon materials surface.

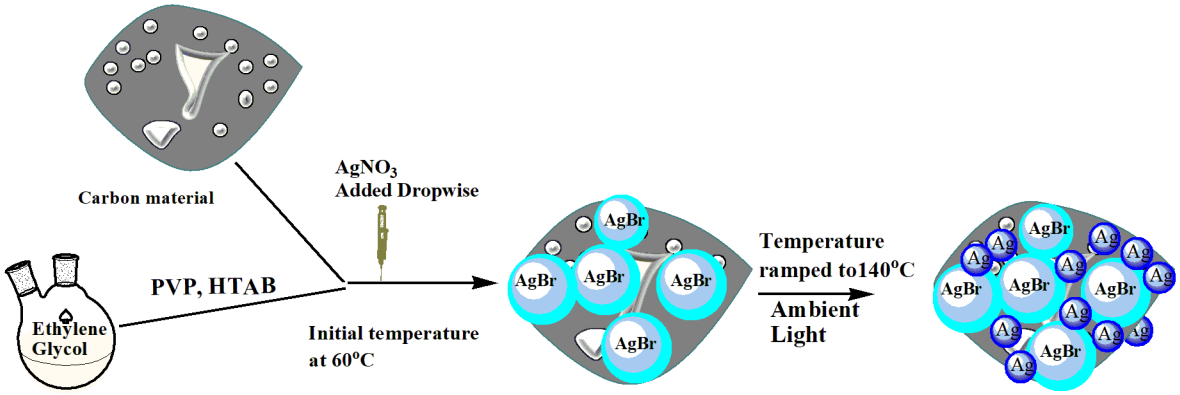

Figure 5 1: Schematic illustration of formation process for the AABR composites with the carbon materials.

The synergistic interaction of AABR with ACK, CAC, and BCR were investigated with XRD as shown in **Figure 5.2**. The diffraction peaks on the prepared composites are consistent with pure face center cubic phase of AgBr (JPCDS 079-0148) and metallic Ag (JCPDS 071-3762) with space group: Fm-3m (225) (Zhu, Wang, Lin, Gao, Guo, Du & Xu 2013). The peaks at 2θ values of 26.6, 31.1, 44.3, 54.8, 64.8, and 73.4° corresponds with the diffraction peaks of (111), (200), (220), (222), (400) and (420) crystal planes of AgBr and the diffraction peaks at 38.1, 44.2, 64.4 and 77.8^{o} which belongs to (111), (200), (220) and (311) assigned to metallic cubic Ag. The characteristic diffraction peak of Ag^{o} at 38.1 ^{o} has low intensity for AABR-ACK, which signifies good dispersion, low Ag metallic content and reduced particle size (Hou, Li, Zhao, Quan & Chen

2011). Though, the diffraction peaks 2θ of AgBr and Ag particles left-shifted by 0.2° as compared to the data card peaks, and this attributed to the strong interaction between AgBr and Ag nanoparticles (Lin, Xiao, Yan, Liu, Li & Yang 2015).The characteristic peaks of carbon for ACK, CAC, and BCR were not visible in the composites due to low content and being amorphous. The XRD results show that the as-prepared composites are composed of Ag particles and AgBr crystal. The calculated crystallite size from the peak (220) using the Scherrer formula for AABR-ACK, AABR-CAC, and AABR-BCR, and AABR are 25, 18, 12 and 65 nm.

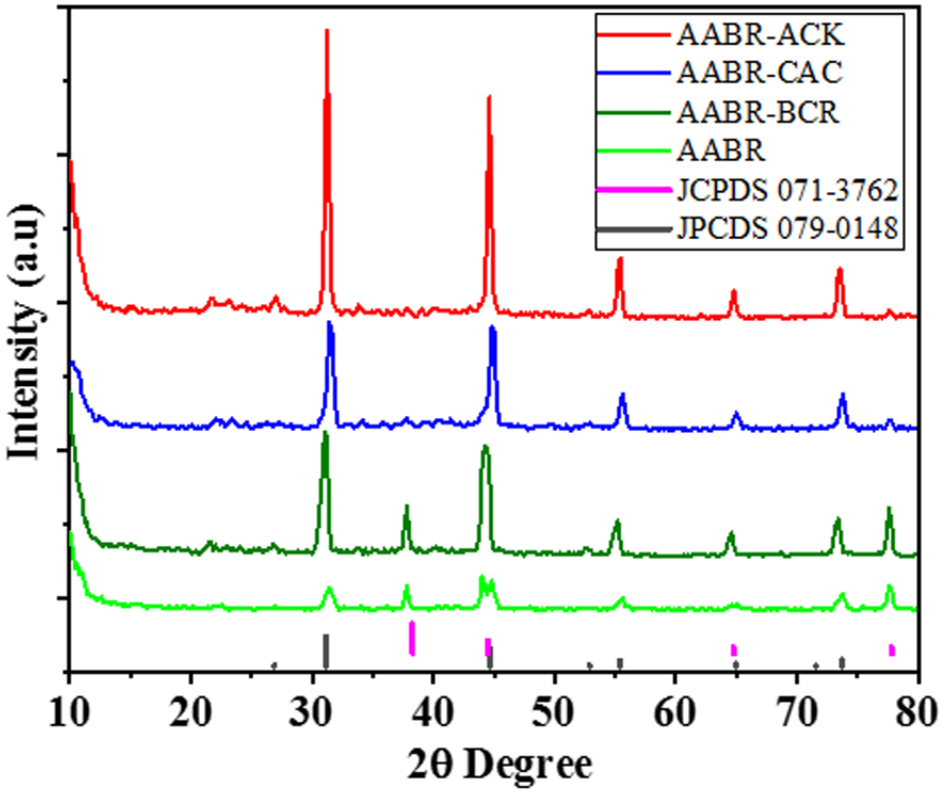

Figure 5 2: XRD pattern of AABR, AABR-BCR, AABR-CAC and AABR-ACK.

The hybridization of AABR with the carbon materials was investigated by FT-IR analysis. **Figure 5.3** shows the FT-IR spectra of the AABR and AABR with the different carbon material. The absorption regions at 3333, 1565 and 1035 cm^{-1} could be observed with AABR with different carbon support, which are attributed to OH stretching group (López-Peñalver, Sánchez-Polo, Gómez-Pacheco & Rivera-Utrilla), carboxylic (-COO) symmetrical stretching vibration and C-0-C stretching respectively. The peaks at 1565 and 1035 cm^{-1} confirm the existence of carbon in the prepared composites. The carboxylic-stretching band weakens (ACK < CAC < BCR), most especially a lower wavenumber for AABR-ACK, which indicates good dispersion and synergistic interplay between AABR with the ACK (Petroski & El-Sayed 2003; Zhu, Chen & Liu 2011). The formation of close connected interface between AABR and conductive ACK will promotes high photocurrent density (as explained in **Figure 5.8b**). The bands at 2918 and 2839 cm^{-1} are ascribed to the stretching vibration of C-H bonds in $-CH_3$ and $-CH_2$ groups from the PVP molecules (Gao, Song, Jiang, Liu, Yan, Zhou, Liu, Wang, Yuan & Zhang 2005). The band at 1450 cm^{-1} correspond to antisymmetric deformation vibration of $-CH_3$ group of the PVP molecules (Cong-Wen, Hai-Tao, Cheng-Min, Zi-An, Huai-Ruo, Fei, Tian-Zhong, Shu-Tang & Hong-Jun 2005).

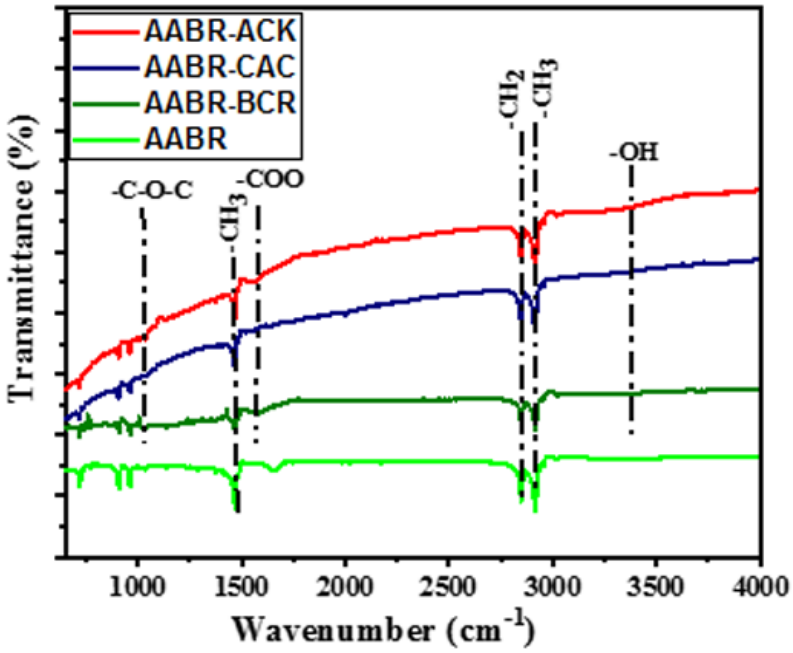

Figure 5 3: FTIR spectra of AABR-BCR, AABR-CAC, AABR-ACK and AABR.

The EIS plot in **Figure 5.4** shows the conductive abilities of ACK, CAC, and BCR. The arc radius of ACK (inset of Fig. 4b) is smaller than CAC and BCR, indicating a reduced charge transfer resistance (Rct). The Rct value for ACK (6062 Ω) is lower than CAC (6763 Ω) and BCR (8747 Ω), which correlates with better conductive capability for photoexcited electron transfer, thus further promoting charge separation during photocatalysis. The 3D hierarchical interconnected porous for ACK (SEM image, **Figure 5.5a**) promotes good interfacial charge transfer resistance (Rct) in comparison to well developed porous structure of CAC and BCR as presented in **Figure 5.5b-c**.

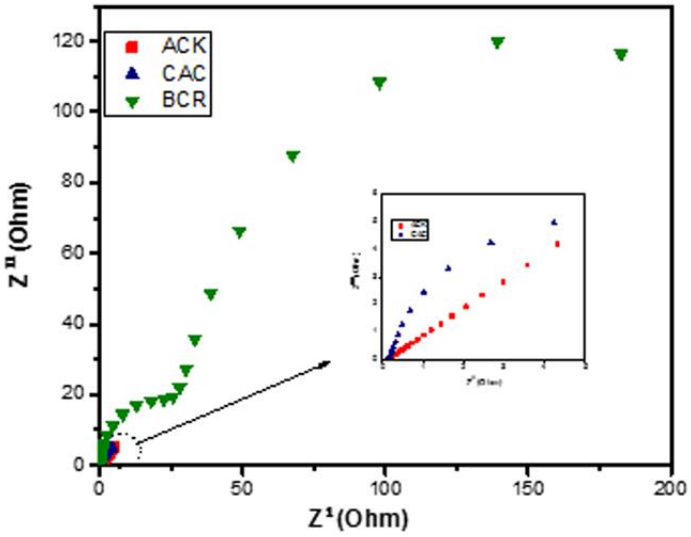

Figure 5 4: EIS Nyquist plot of BCR, CAC and ACK.

The morphology of ACK, BCR, CAC, AABR, and AABR-ACK was investigated by SEM. As shown in **Figure 5.5a**, ACK morphology is irregular and heterogeneous surface, with formation of interconnected conductive carbon structures. The porous structure is more developed in comparison to CAC and BCR morphology as presented in **Figure 5.5b –c**.

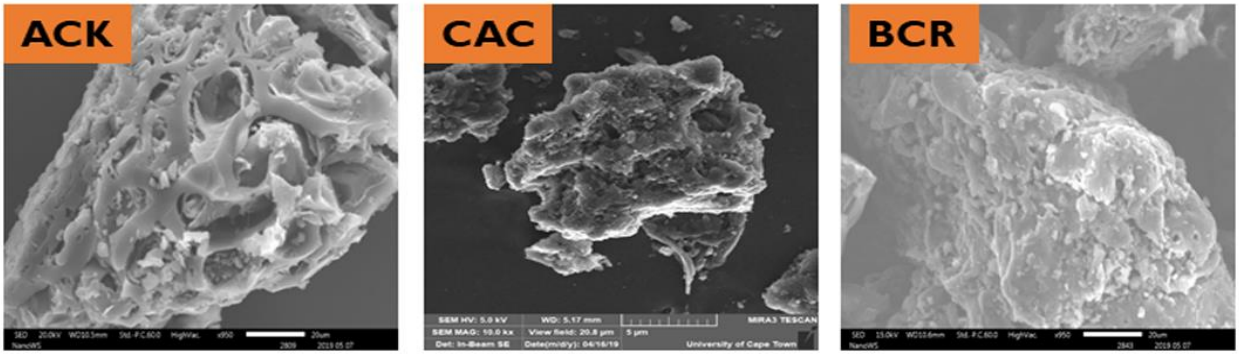

Figure 5 5: SEM images of ACK, CAC and BCR.

AABR image as shown in **Figure 5.6a**, constitute of clustered polyhedral shape with an average particle diameter between 1.0–1.2 μm. However, a uniform nanospheres morphology without agglomeration and aggregation is evident with AABR-ACK (**Figure 5.6b**) with particle diameter around 195–205 nm. The particle diameter of AABR-ACK is smaller in comparison to Ag/AgBr dispersed on commercial activated carbon (McEvoy, Joanne Gamage & Zhang, Zisheng 2016; Wang, Zhao, Luo, Yin, An & Li 2016) from previous work. The ACK significantly utilizes its oxygenated functional groups in the controlled microstructure of the material (AABR-ACK) with fine dispersion and agglomeration prevention of Ag/AgBr particles on ACK 3D hierarchical structure. The different magnification of AABR-ACK is presented in **Figure 5.6b-d**. The composite has uniform morphologies without agglomeration, as ACK was beneficial for the formation of smaller AABR particles, which favors the catalytic activity. The SEM-EDS line scan and elemental mapping spectra were carried out to gain insight of the surface element composition and distribution of the as prepared composite. **Figure 5.6e** depicts the SEM-EDS spectrum of AABR-ACK, indicating that Ag, Br and C elements distributed throughout the composite. The elemental mapping as observed in **Figure 5.6f - h**, for Ag, Br, and C element, which justify the presence of carbon and silver along with bromide hybridized onto the structure of ACK. The nanospheres morphology and reduced particle diameter of AABR-ACK will significantly influence the degradation of TC, which is coherent with tailored SPR attributes of Ag (Yan, Zhang, Luo, Ma, Lin & You 2013; Wu, Shen, Ji, Zhu, Zhou, Zang, Yu, Chen, Song & Feng 2017) anchor on AgBr. The synergistic interplay between AABR (Ag/AgBr) and ACK (An, Wang, Sun, Zhang, Zhang, Wang & Fang 2016) in the composite also aid enhanced photo-generated charge carriers separation.

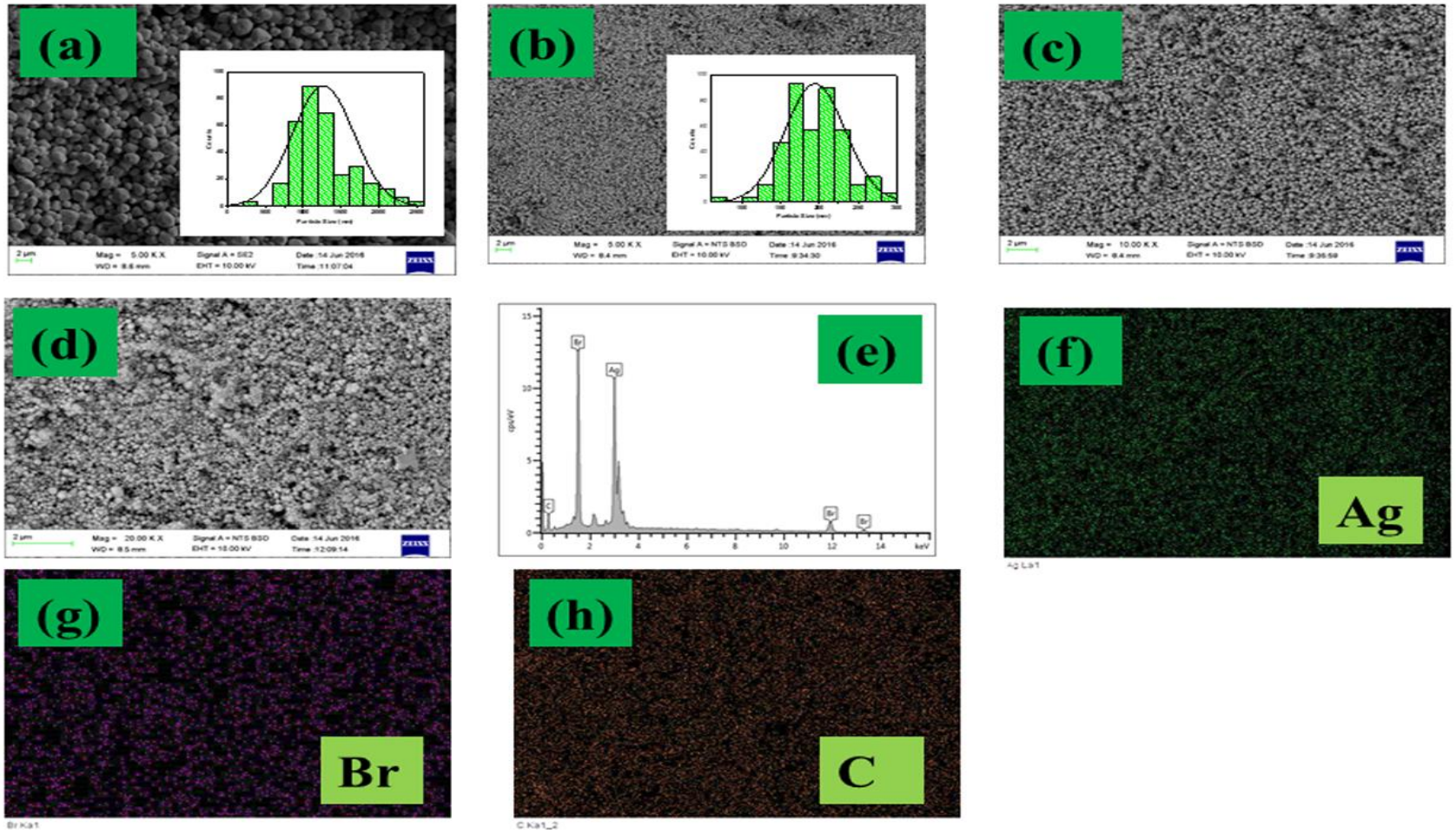

Figure 5 6: SEM images of (a) AABR, (b) AABR-ACK, (c and d) AABR-ACK at different magnification, (e) SEM-EDS spectrum, EDX mapping images for (f) silver, (g) bromine and (h) carbon.

The UV-DRS spectra of the prepared composites are shown in **Figure 5.7a**, exhibit strong absorption in the range of 450 to 800 nm in the visible light (VL) region which is ascribed to the surface plasmon resonance (SPR) of metallic Ag NPs nucleated on the surface of AgBr (Dai, Lu, Dong, Ji, Zhu, Liu, Liu, Zhang, Li & Liang 2013; Jiang, Wen, Xu, Gao, Li & Chen 2018). The prepared composite (AABR-ACK, AABR-CAC, and AABR-BCR) exhibited stronger absorption in the VL region than AABR upon introduction of carbon materials. The AABR-ACK was slight red-shifted and showed stronger absorption in the VL region than other prepared composites. The extended VL light absorption of AABR by ACK empower the prepared composite (AABR-ACK) to produce more photogenerated charge carriers for improved photocatalytic activity (Deng, Tang, Zeng, Wang, Zhou, Wang, Tang, Liu, Peng & Chen 2016). The energy band gaps (Eg) of AABR-ACK and other AABR relatives were obtained using the formular as shown in Eq. 5.1.

$$\alpha h\nu = A(h\nu - Eg)^{\frac{n}{2}} \qquad 5.1$$

Where α, h, υ, Eg and A are the optical absorption coefficient, Plank's constant, light frequency, band gap and a proportionality constant. Additionally, n depends on the attributes of the optical transition in a semiconductor (for direct transition, n=1, and for indirect transition, n=4). In the present work, AABR catalyst allowed direct transition and the corresponding band gap for AABR-ACK, AABR-CAC, AABR-BCR and AABR are 2.34 eV, 2.36 eV, 2.40 eV and 2.4 eV respectively (**Figure 5.7b**).

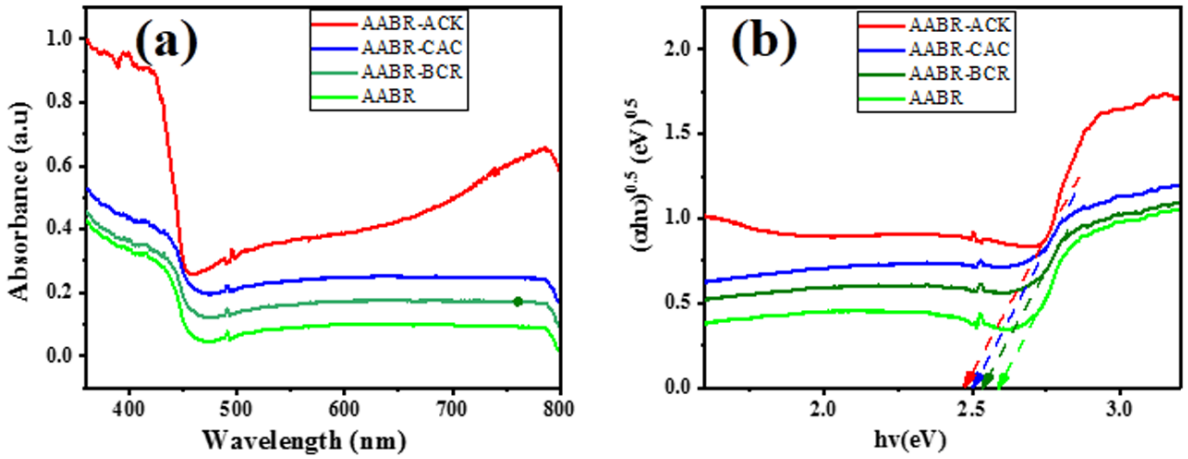

Figure 5 7: (a) UV–Vis diffuse reflectance spectra and (b) corresponding band gap (Tauc plots) of AABR, AABR-BCR, AABR-CAC and AABR-ACK.

The PL spectra of the prepared samples excited at 365 nm, with an emission band around 400 – 600 nm are shown in **Figure 5.8**. The PL intensity of AABR-ACK has weaker intensities as compared to AABR-CAC, AABR-BCR, and AABR. This low intensity of AABR-ACK highlights the hindrance of recombination of photogenerated electron-hole pairs (Lu, Zeng, Song, Qin, Zeng & Xie 2017). This also signifies an enhanced transport of photoexcited electron and charge carriers separation from AABR conduction band by the ACK (An et al. 2016) which subsequently results in high photocatalytic activity for TC degradation (Obregón, Zhang & Colón 2016).

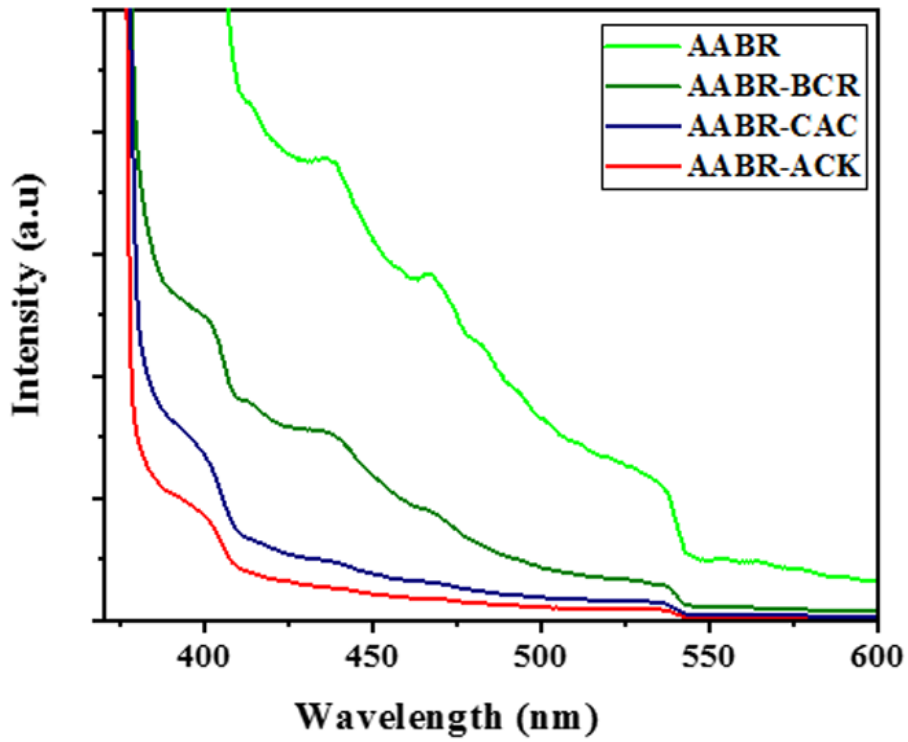

Figure 5 8: Photoluminescence spectra for AABR-ACK, AABR-CAC, AABR-BCR and AABR.

5.3.2 Charge carrier separation properties

The separation of charge carriers would influence superior degradation activities; hence the investigation of charge migration properties was verified with EIS and LSV respectively. The AABR-ACK composite from EIS Nyquist plot (**Figure 5.9a**) show a smaller arc radius and reduced charge transfer resistance value (**Table 5.1**) as compared to other composites and AABR. The Z-fit software was utilized for the fitting of charge resistance transfer (Rct) and other resistance values, based on the equivalent circuit illustrated in the inset of **Figure 5.9a**. This finding shows a better conductivity of ACK for an efficient photoinduced electron transfer and interfacial charge separation in the AABR-ACK as compared to other composites. This

fast separation of the photogenerated charge carriers by AABR-ACK also correlates to the PL spectra discussed above (**Figure 5.8**) and with their improved photocatalytic activities on TC in this study.

From **Figure 5.9b**, the photocurrent density of AABR-ACK (1.06 and 0.93 mA cm^{-2}) was much higher than the AABR (0.94 and 0.68 mA cm^{-2}) under visible light (VL) and dark (D) condition. The high photocurrent density of AABR-ACK highlights an effective charge separation and a longer lifetime of photogenerated charge carriers taking place at the surface of the photocatalyst under the VL. The photocurrent density result also confirms the conductive attributes of ACK in AABR-ACK composite for speedier transfer of photoexcited electrons and separation of charge carriers, which yielded reactive oxidative species for improved photocatalytic activity.

Table 5.1 : The fitted resistance values of prepared photocatalyst in accordance with series circuit.

Samples	**[a]Rs (Ω)**	**[b]Rd (Ω)**	**[c]Rct (Ω)**
AABR-ACK	80.5	270.6	504.9
AABR-CAC	101.7	612.5	892.6
AABR-BCR	89.3	725.4	14788
AABR	554.4	90642	4110000

[a]Rs is series resistance, **[b]Rd** is diffusion resistance, **[c]Rct** is charge transfer resistance.

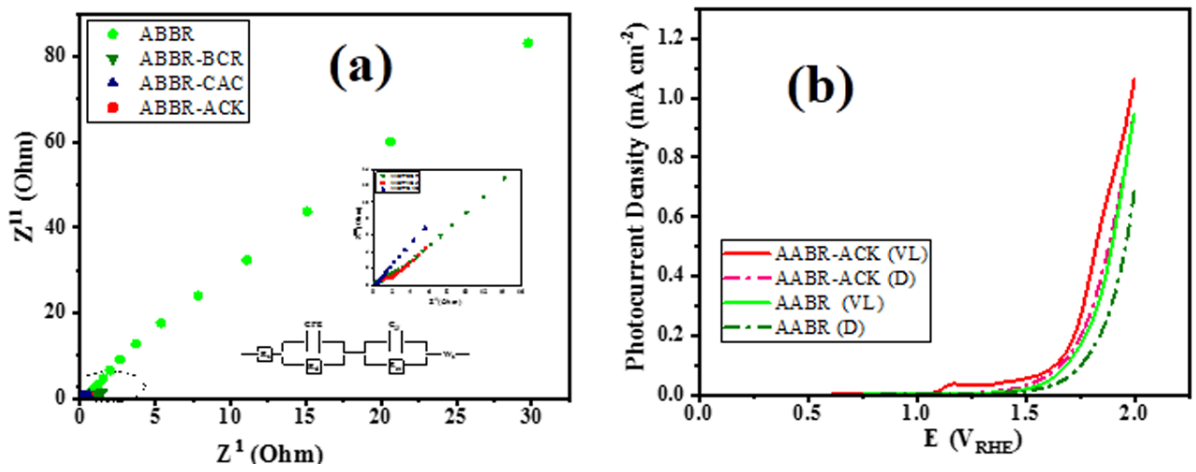

Figure 5 9: (a) EIS Nyquist plot for AABR, AABR-CAC, AABR-ACK and AABR-BCR; (b) linear sweep voltammogram curves for AABR-ACK and AABR.

5.3.3 Photocatalytic activities

The photocatalytic activities of the as-prepared samples were further investigated on the degradation of TC (15 mg/L) under VL LED irradiation, as shown in **Figure 5.10a**. The degradation of TC without photocatalyst shows that direct photolysis of TC will not proceed under visible light condition. The degradation efficiency of AABR-ACK was 92% after 180 min, which is much higher than AABR-CAC, AABR-BCR, AABR, ACK, and photolysis at 80%, 74%, 60%, 32% and 14% respectively. The addition of carbon materials to AABR significantly enhance the photocatalytic performance of the composite than that of AABR due to enhanced interfacial charge separation by the carbon supports from the AABR conduction band (CB) interface. The improved activity of AABR-ACK as compared to other composites is ascribed to ACK conductive attributes for fast transfer of photoexcited electrons from AABR CB interface. The accelerated electron transfer of ACK ascribed to its interconnected conductive carbon structure (Liu, Chen, Cui, Yin & Zhang 2018) is responsible for interfacial charge separation, which further results in the production of reactive oxidative species for high

degradation of TC.

To quantitatively evaluate the photodegradation kinetics of TC over the prepared samples, the pseudo-second and first-order kinetic fitting (**as described in eqn. 4.6 and 4.7 in Chapter 4**) were used and shown in **Figure 5.10 b and c**. The pseudo-second (**Figure 5.10b**) fits better as compared to the first order, while degradation rate constant for TC by ACK, AABR, AABR -BCR, AABR -CAC, and AABR PLAS-ACK composites are 0.0004 L mg^{-1} min^{-1}, 0.0005 L mg^{-1} min^{-1}, 0.0009 L mg^{-1} min^{-1}, 0.0015 L mg^{-1} $min^{-1}$and 0.0044 L mg^{-1} min^{-1} respectively. In this photocatalytic system using AABR-ACK, adsorption and photocatalytic activity was the major reason for the degradation kinetics of TC molecule.

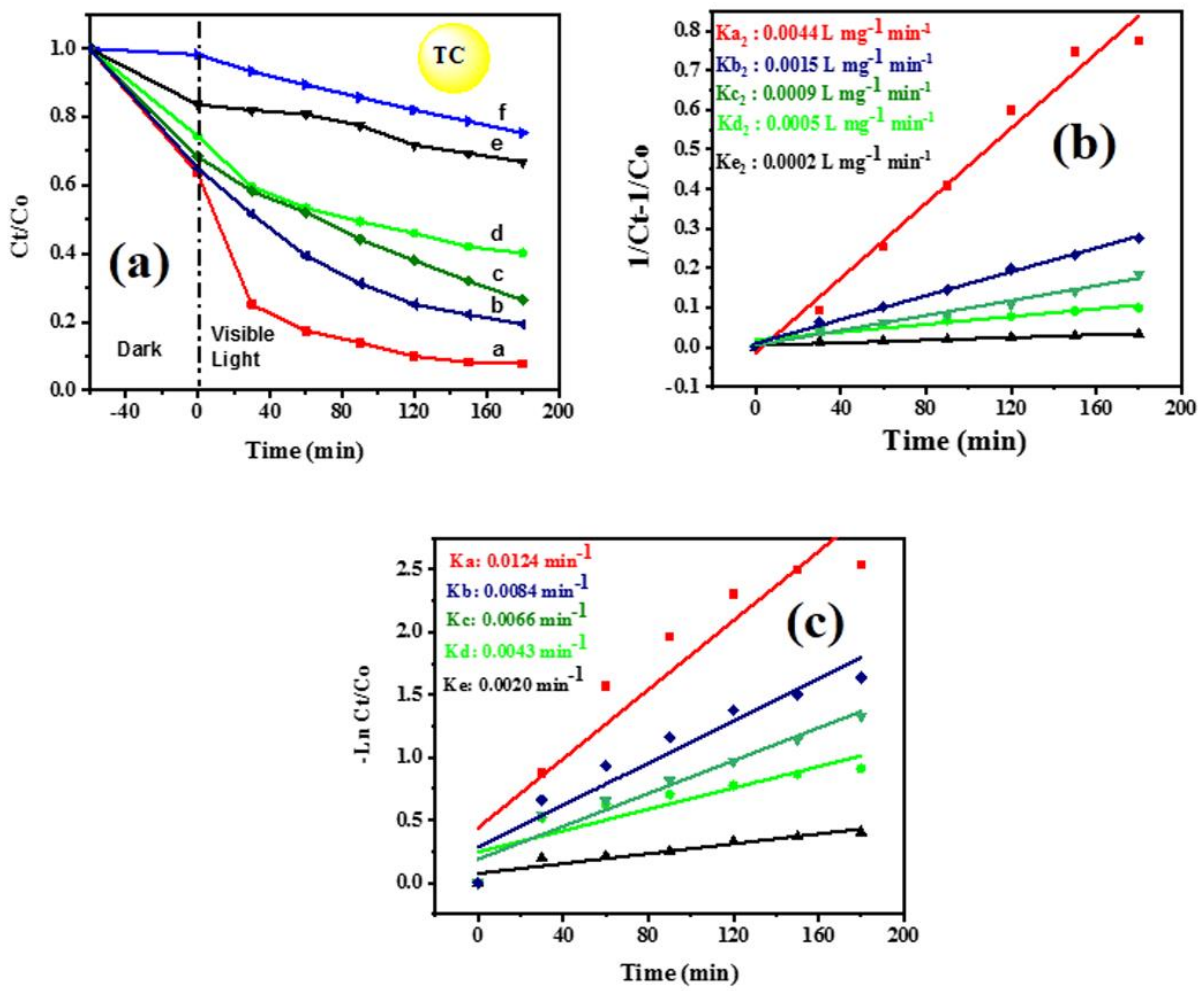

Figure 5 10: (A) Photodegradation of TC under visible irradiation (λ > 420 nm) a-AABR-ACK, b-AABR-CAC, c-AABR-BCR, d-AABR and e-Photolysis; (B) pseudo second and (C) pseudo first order kinetics of TC degradation.

With Ag-ACK and AgBr–ACK, the degradation efficiency of TC solution reached 51% and 46% after 180 min irradiation time as compared to 92% removal for PLAS-ACK in **Fig**ure **5.11.** Significantly, the ACK synergistic interaction with SPR Ag particles and photoexcited AgBr played a crucial role in the enhanced activity of PLAS-ACK as compared to Ag-ACK and AgBr-ACK. The corresponding kinetic fits are presented in **Figure 5.12**.

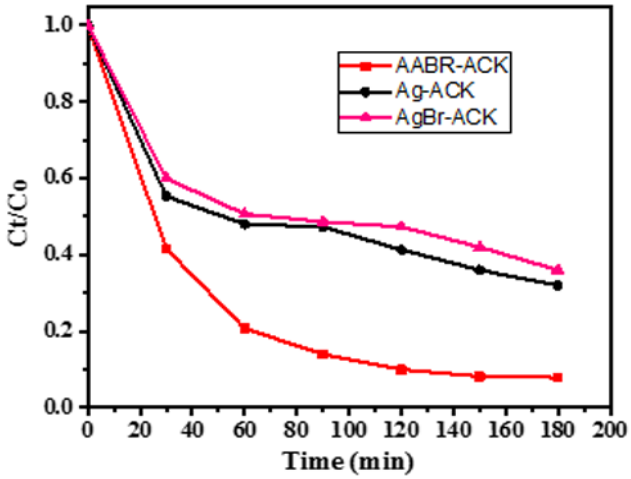

Figure 5 11: Degradation efficiency of AgBr-ACK, Ag-ACK and AABR-ACK on TC removal.

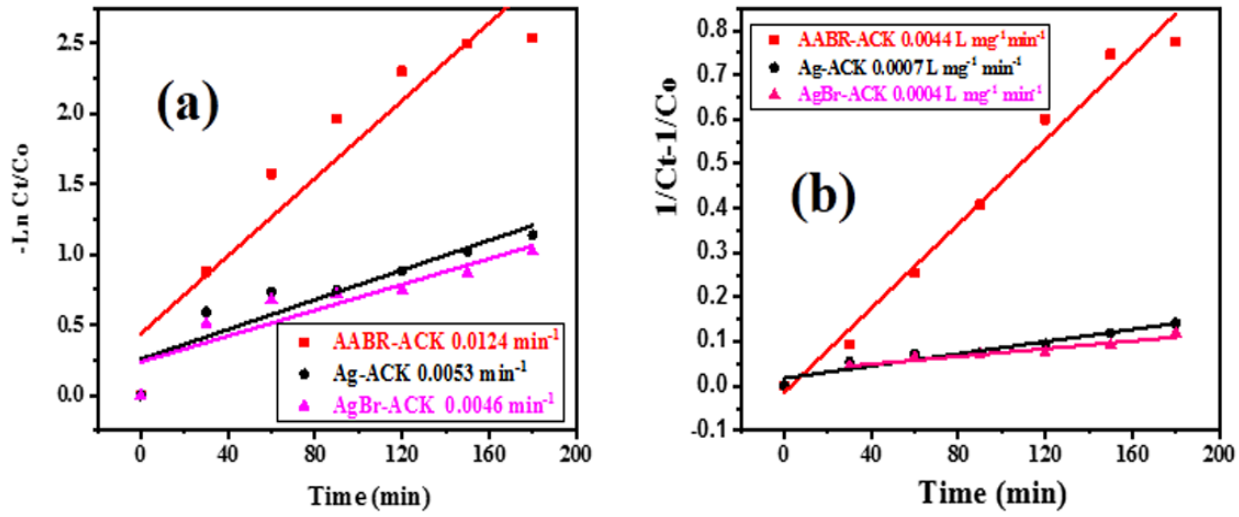

Figure 5 12: Pseudo first and second order kinetics of AgBr-ACK, Ag-ACK and AABR-ACK on TC removal.

The photocatalytic activities of AABR-ACK and AABR on oxidation of 4-nitrophenol (4-NP; 5 ppm) and Rhodamine b dye (RhB; 5 ppm) were evaluated, exploring the same degradation conditions used for TC. As shown in **Figure 5.13**, AABR-ACK exhibited good photocatalytic performance for 4-NP and Rhb (74 and 94%) degradation compared with AABR (38 and 50%). Corresponding absorbance spectra decrease of RhB and 4-NP degradation using AABR-ACK is presented in **Figure 5.14.** This result of photocatalytic degradation indicate the AABR-ACK composite was an effective photocatalyst for the removal of different pollutants in wastewater. This is attributed to the controlled microstructure of AABR-ACK, the ACK material as a mediator for higher transportation of photoexcited electrons and interfacial charge separation, and from strong synergistic interaction between elements of the composite.

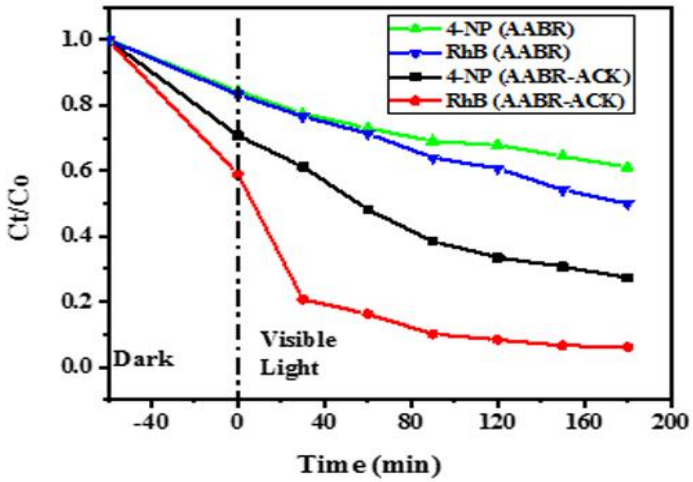

Figure 5 13: Photocatalytic degradation of 4-Nitrophenol and Rhodamine using AABR and AABR-ACK composite.

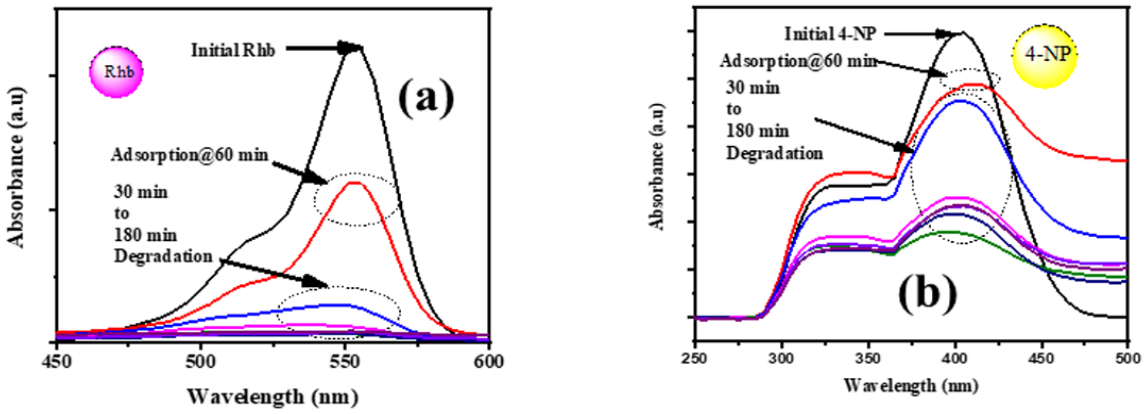

Figure 5 14: UV absorbance spectra decrease of Rhodamine b dye and 4-nitrophenol degradation using AABR-ACK composite.

Figure 5.15a shows the reaction of different solution pH on the TC photocatalytic degradation in the presence of AABR-ACK under LED visible light. An increase in the pH from 3 to 7 resulted to increase removal of TC from 38 to 92%, then decrease slightly to 75% at pH 10, which is ascribed to surface adsorption in the reaction system. It's observed that TC molecules degrade efficiently at neutral pH as compared to basic and acidic conditions in this study. The pH at a point of zero charge (pH-pzc) for AABR-ACK is 6.42 as depicted in **Figure 5.15b**. The photocatalyst surface will be positively charged at pH less than pH-pzc, while negatively charged at higher pH (Barakat, Schaeffer, Hayes & Ismat-Shah 2005). Moreover, TC molecules exist at three different speciations: positively charged at acidic medium, non-charged at a neutral form and negatively charge at basic conditions. At pH values different to the pH-pzc of the material, electrostatic repulsion will occur between the photocatalyst and TC molecules with the same charge (Liu, Zheng, Zhong & Cheng 2015; Safari, Hoseini, Seyedsalehi, Kamani, Jaafari & Mahvi 2015), thus lessen the catalytic performance of the composite.

The TC catalytic performance by the AABR-ACK was also carried out on the variation of LED light with a different wavelength as shown in **Figure 5.15c**. The highest TC degradation efficiency was observed with a white light source since the white light is the sum of the other three LED lights (Sacco, Vaiano, Sannino & Ciambelli 2017).

The temperature effect on TC degradation over AABR-ACK at pH 7 was investigated from 25 to 40 ^{o}C. TC degradation efficiency increases from 92 to 94% with increasing temperature investigated from 25 to 40 ^{o}C after 180 min (**Figure 5.15d**). The activation energy (Ea) was determined using the Arrhenius calculation (Eq. 5.2) and corresponding plot of In k_{obs} versus T^{-1} is shown in **Figure 5.15e.**

$$Ink_{obs} = InA - \frac{E_a}{RT} \qquad 5.2$$

where A is the pre-exponential factor (h^{-1}); R is the universal gas constant (8.314 J/mol·K); T is temperature (K) (Wang, Wang & Cao 2019).

The activation energy (Ea) of AABR-ACK on TC degradation was calculated to be 15.42 kJ/mol. The Ea was lower than the expected activation energy of surface-controlled reactions, which is typically about 29 kJ/mol. This indicates that the apparent rate constant is influenced by diffusion-controlled reactions where the activation energies are expected to be between 8 to 21 kJ/mol (Feng, Wu, Deng, Zhang & Shih 2016). The obtained value of 15.42 kJ/mol for AABR-ACK in this study is much lower compared to Ag/AgI photocatalyst (Liang, Wang, Liu, Wu, Cui, McEvoy & Zhang 2015), highlighting that TC degradation requires lower activation energy.

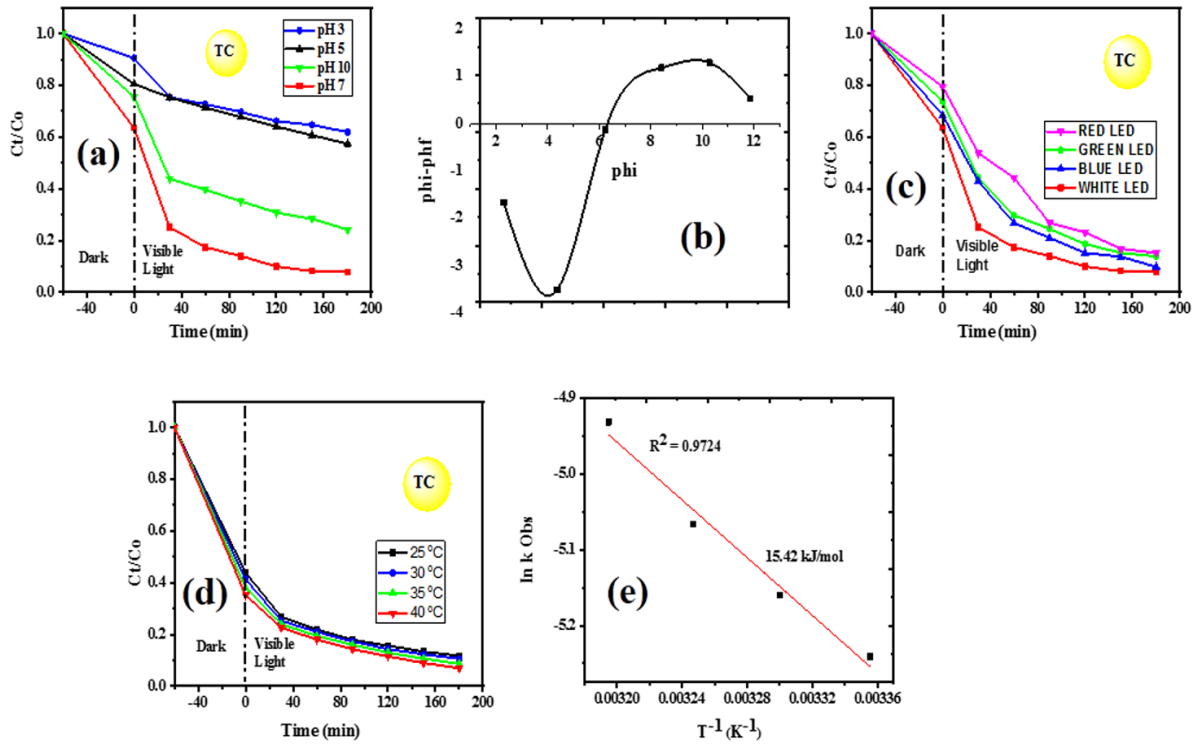

Figure 5 15: (a) pH effect; (b) pH-pzc of AABR-ACK; (c) different LED light (d) temperature effect on TC Degradation and (e) the relationship between ln k obs and T^{-1}.

5.4 Mass spectra of TC and other organic pollutants intermediates

The main reactive oxidative species in the photocatalytic degradation of TC under visible LED light using AABR-ACK and corresponding reaction mechanism has been discussed in **Chapter 4** (**Section 4.4.4**). The mass spectra view and zoomed in spectra of TC solution before degradation and all intermediate products formed from TC molecule after degradation using AABR-ACK are displayed in **Figure 5.16**. Based on products transformed and in line with previous reports (Barhoumi, Olvera-Vargas, Oturan, Huguenot, Gadri, Ammar, Brillas & Oturan 2017; Deng, Tang, Zeng, Wang, Zhou, Wang, Tang, Wang & Feng 2018), the TC molecules are broken down by the reactive oxidative species via three pathways and their respective molecular formulas are displayed in **Figure 5.17**. Products such as PD 1 (*m/z* 391.3), PD 2 (*m/z* 344.2) and PD 3 (*m/z* 279.1) were transformed because of hydroxylation, deamination, and demethylation from the TC molecule (Zhou, Li, Ye, Ma, Wang, Huo, Shi & Yan 2015). However, dehydration and ring opening products such as PD 4 (*m/z* 211.1), PD 5(*m/z* 167) and PD 6 (*m/z* 149) are also formed from PD 3, and while PD 7 (*m/z* 113) were assigned to be further oxidation products from PD 5 and PD 6. Finally, other oxidation products are further mineralized into CO_2 and H_2O from PD 7.

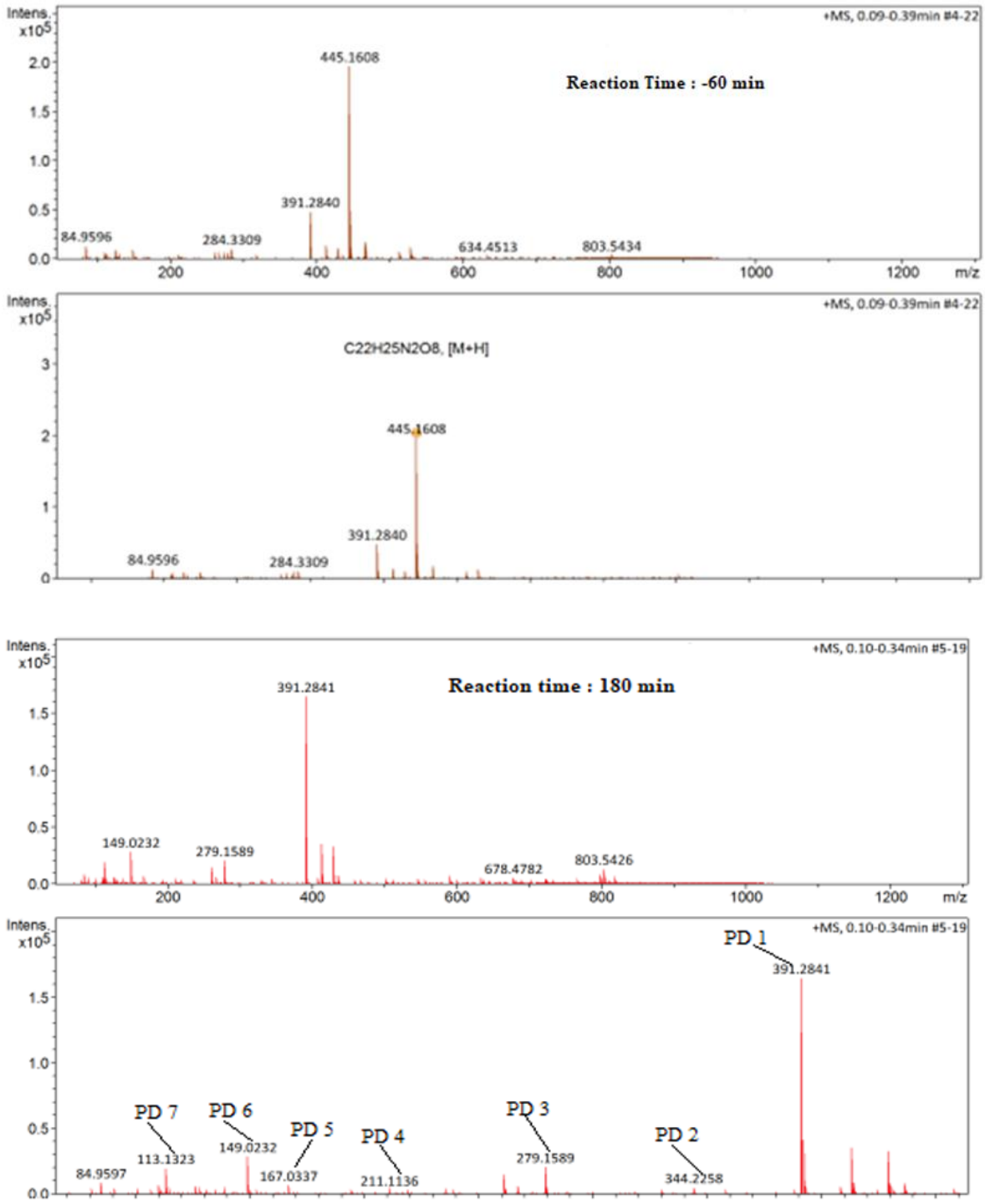

Figure 5 16: LC-MS spectra of TC degradation intermediates in the photodegradation reaction process using AABR-ACK.

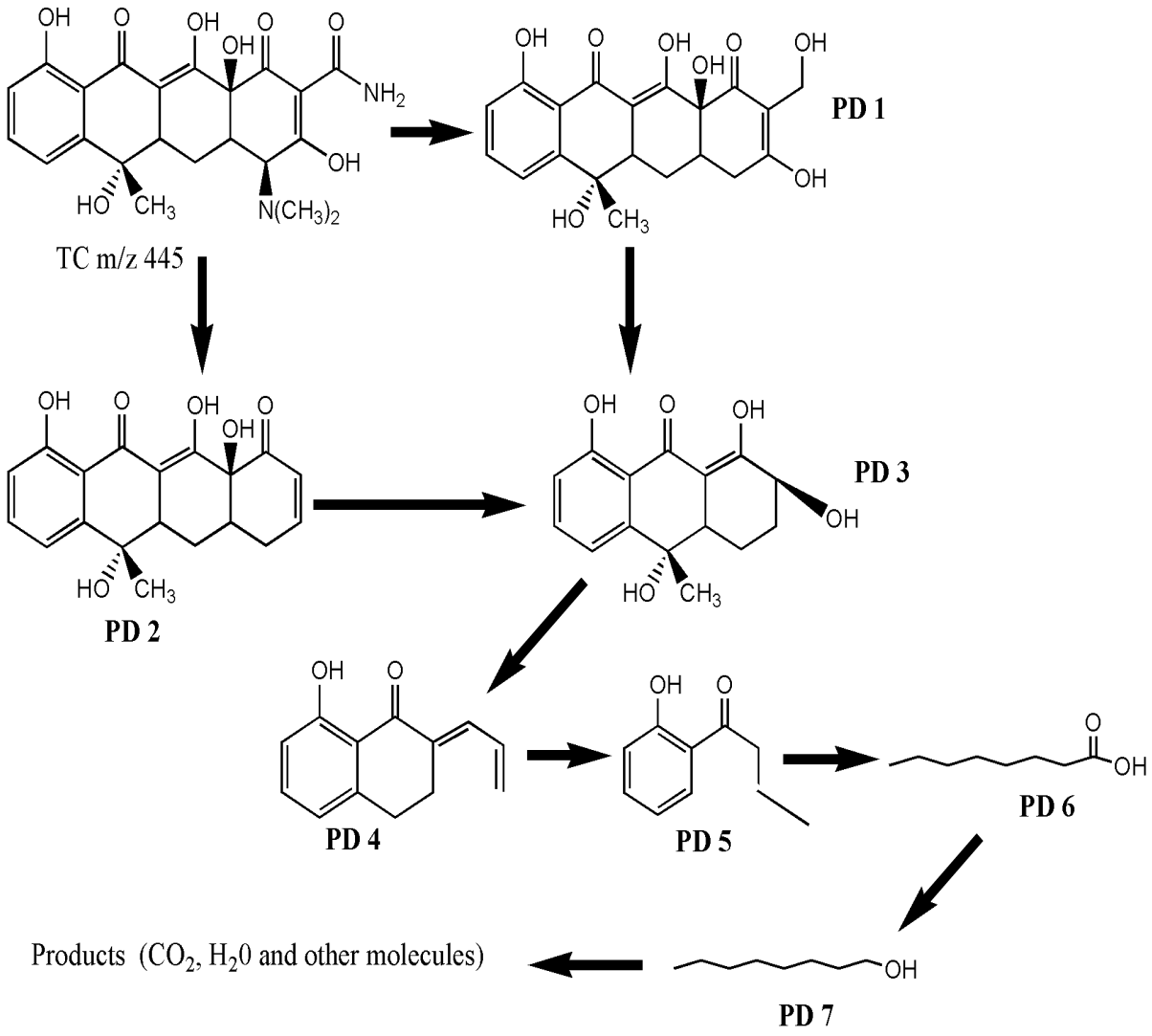

Figure 5 17: The proposed intermediate products from TC photodegradation under visible light.

The LC-MS spectra of degradation pathways and intermediates products for other organic pollutants (4-Nitrophenol and Rhodamine B) by LED visible-light photocatalysis over AABR-ACK are also presented from **Figure 5.18 - 21**. LC–MS analysis was employed and the corresponding 4-NP along with the products from 4-NP extract after 180 min degradation were summarized in **Figure 5.18**. As observed from **Figure 5.19**, the major intermediate products includes hydroquinone, p-benzoquinone, fumaric acid, maleic acid and oxalic acid are detected during 4-NP degradation and consistent with other studies (Zhou, Hu, Wan, Yang, Yu, Li, Chen, Wang & Lu 2016; Wei, Cao & Fang 2018; Verma, Jaihindh & Fu 2019). These intermediate products further undergo attack by the superoxide anions and photo-induced hole radicals resulting in the formation of carbon dioxide and water (Xie, Xu, Xia, Jia & Zhang 2016; Verma, Jaihindh & Fu 2019).

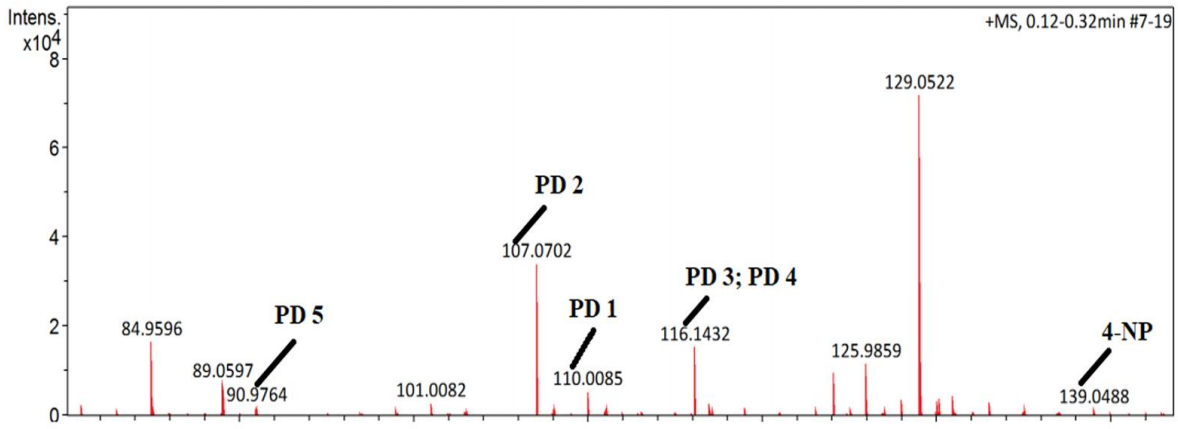

Figure 5 18: LC-MS spectra of the 4-NP degradation products after the reaction time of 180 min.

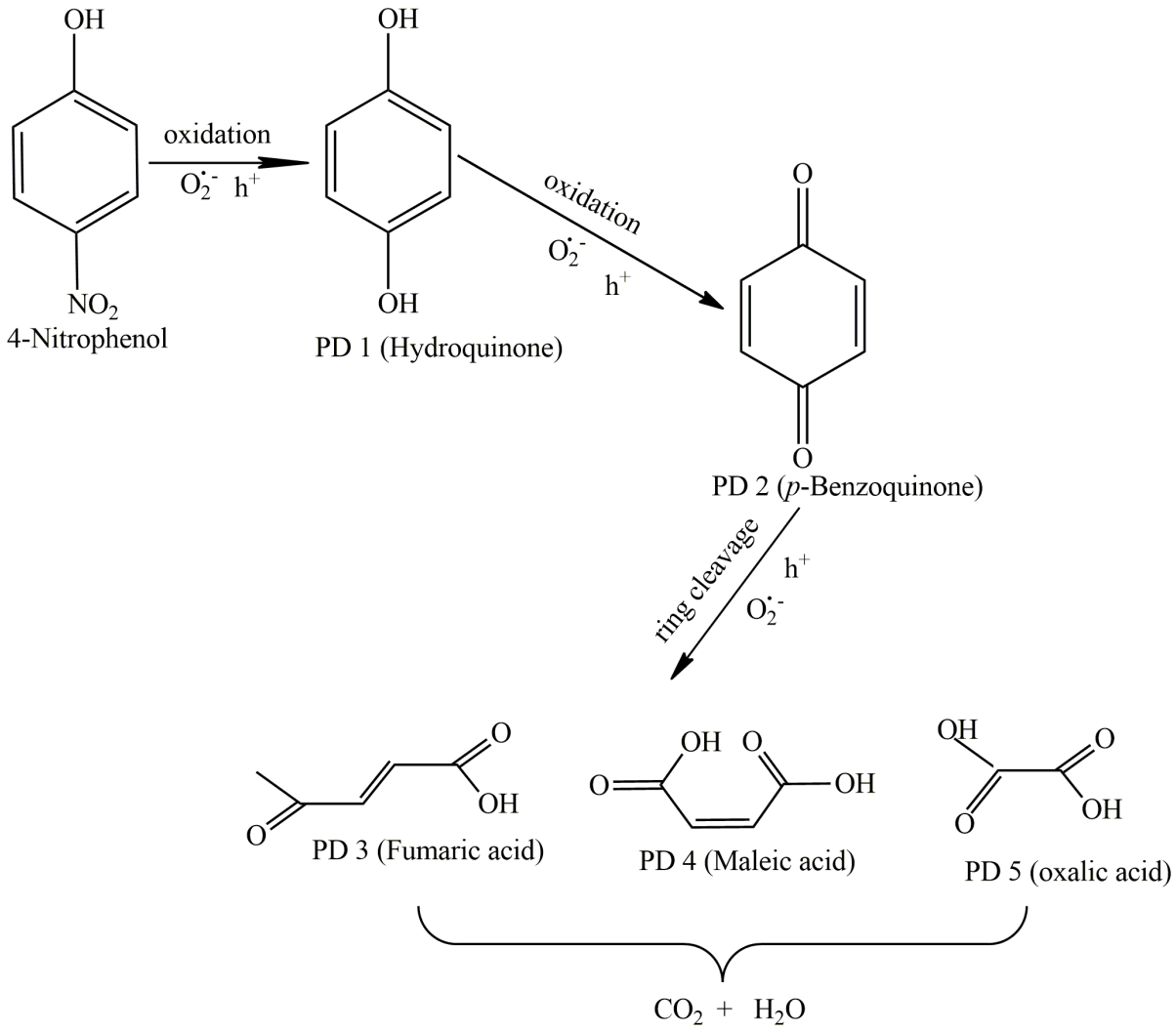

Figure 5 19**:** Proposed reaction pathway for the degradation of 4-Nitrophenol in the AABR-ACK photocatalytic process.

The intermediate products were analyzed by LC-MS, after the degradation of RhB using AABR-ACK as the catalyst. The signal of RhB is assigned to 443.2 as shown in **Figure 5.20**, whilst the mass spectra at m/z 415.2, 387.2, 359.1, 223.1, 149, and 129.1 all corresponds to RhB intermediates products. The degradation of RhB under the attack of reactive oxidative radicals (especially superoxide anion and photo-induced hole) generated from the surface of AABR-ACK undergoes four stages(De-ethylation, chromophore cleavage, ring opening and mineralization) in **Figure 5.21** which is consistent with other reports (Ahmed, Li, Tan & Huang 2013; Nidheesh & Gandhimathi 2014; Huang, He, Yang, Tian, Hu & Wen 2019). Simultaneous formation of de-ethylated products from RhB dye (443 m/z) to PD 3 (359.2 m/z) shows the beginning of degradation, without breaking down the chromophore group. Further, chromophore cleavage and ring opening intermediates (PD 4, PD 5 and PD 6) occurs from de-ethylated product by the cleavage reaction of PD 3 (Cai, Luo, Sun, Fan, Chu & Chen 2019). During the catalytic process, these intermediate products are further attacked by the active species and decomposed to the smaller organic fragments. Therefore in this chapter, 4-NP and RhB were effectively degraded in the AABR-ACK photocatalytic process.

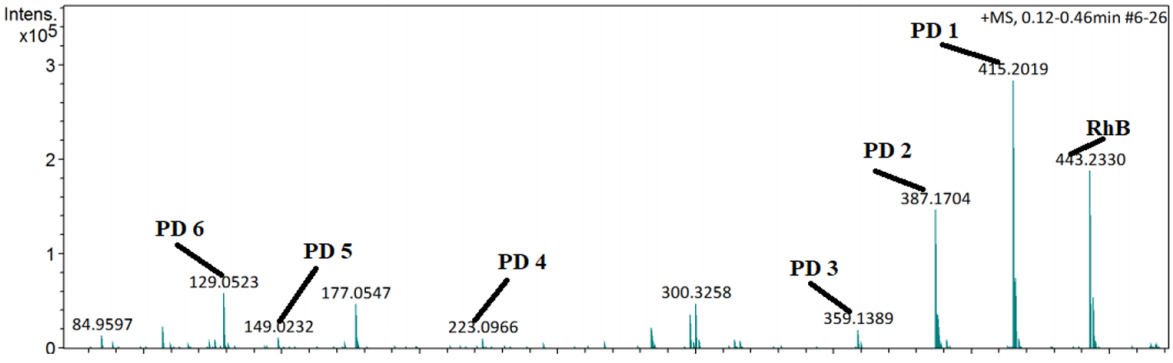

Figure 5 20: LC-MS spectra of RhB by visible-light photocatalysis over AABR-ACK after 180 min.

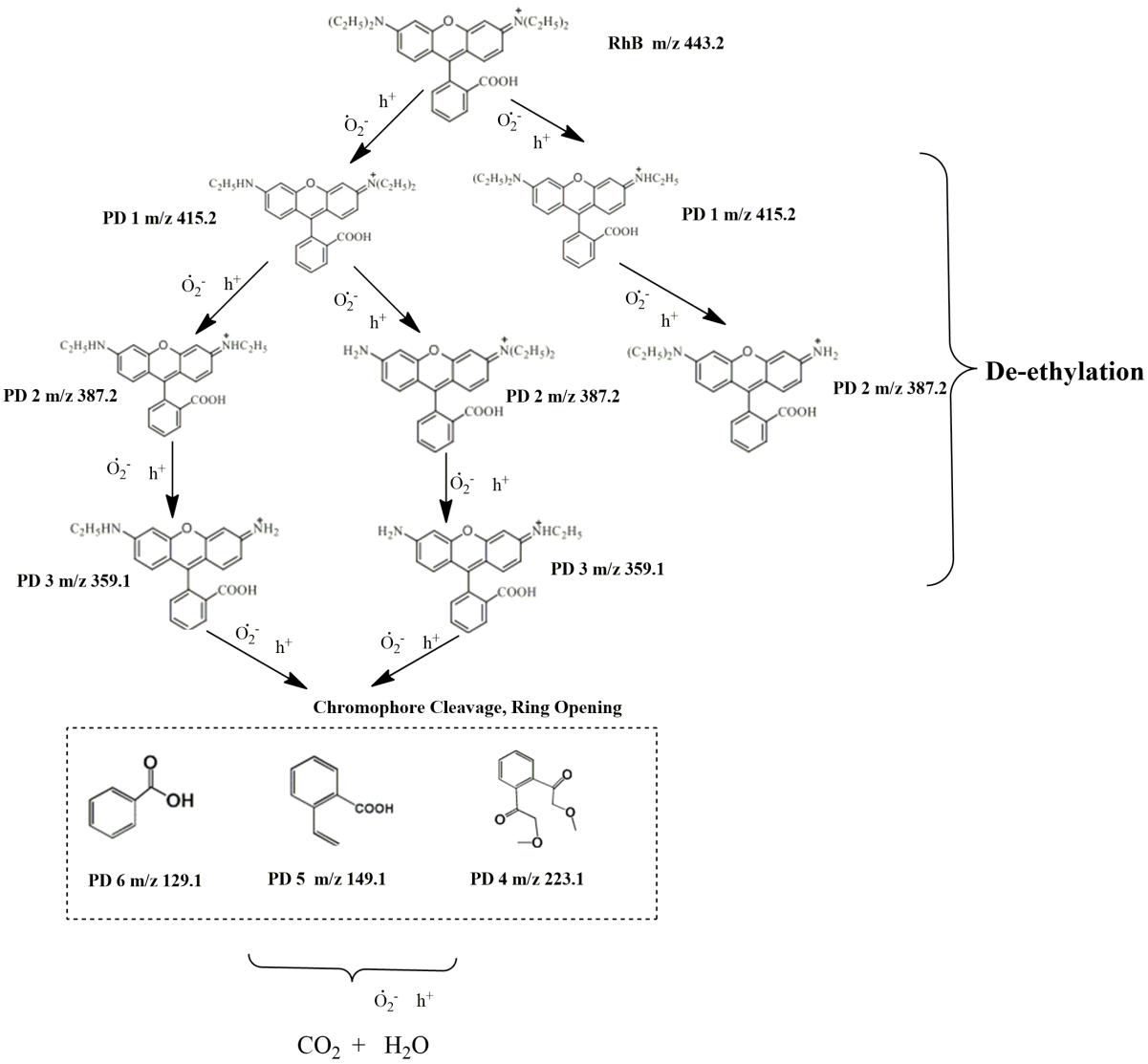

Figure 5 21: Proposed degradation pathway of RhB by visible-light photocatalysis over AABR-ACK.

5.5 Summary and concluding remarks

In this chapter, Ag/AgBr composites with carbon materials (activated carbon from KOH impregnated pinecone - ACK, commercial source - CAC and biochar -BCR) were prepared through thermal polyol route. The prepared composites were applied as photocatalyst for degradation of tetracycline (TC) under visible LED light irradiation. ACK possesses better conductive property for accelerated transfer of photo-induced electron in comparison to CAC and BCR, based on the electrochemical properties. This ascribed to the interconnected hierarchical carbon structures present in the ACK. The hierarchical carbon structure for ACK prevents agglomeration and aggregation of AABR, also enhance more visible light absorption for generation of charge carriers. Improved photocatalytic degradation of TC (92%) was achieved at neutral pH of the aqueous solution (15 mg/L) for AABR-ACK after 180 min in comparison to AABR-CAC (80%) and AABR-BCR (74%). The enhanced photocatalytic performance is ascribed to fast transport of photoexcited electrons and separation of photogenerated charge carriers from AABR by the conductive ACK in comparison to CAC and BCR. The AABR-ACK photocatalyst has potential application for environmental purification of other organic contaminant (Rhodamine B – 94%, and 4-Nitrophenol -74%) under LED visible light. With the help of LC-MS, it was found that hydroxylation, demethylation, deamination, dehydration and ring-opening process were the main degradation pathway for TC using AABR-ACK in this reaction system. This study provides a new insight on the utilization of different carbon based Ag/AgBr composite in photocatalytic water purification. The catalytic properties of AABR-ACK from this chapter will be further compared with AABR-ACK through another synthetic approach (deposition precipitation route) as presented in **Chapter 6**.

5.6 References

AHMED, K.A.M., LI, B., TAN, B. & HUANG, K. 2013. Urchin-like cobalt incorporated manganese oxide OMS-2 hollow spheres: synthesis, characterization and catalytic degradation of RhB dye. *Solid State Sciences*, 15 66-72.

AMIN, S.A., PAZOUKI, M. & HOSSEINNIA, A. 2009. Synthesis of TiO_2–Ag nanocomposite with sol–gel method and investigation of its antibacterial activity against E. coli. *Powder Technology*, 196, 241-245.

AN, C., WANG, S., SUN, Y., ZHANG, Q., ZHANG, J., WANG, C. & FANG, J. 2016. Plasmonic silver incorporated silver halides for efficient photocatalysis. *Journal of Materials Chemistry A*, 4, 4336-4352.

BARAKAT, M., SCHAEFFER, H., HAYES, G. & ISMAT-SHAH, S. 2005. Photocatalytic degradation of 2-chlorophenol by Co-doped TiO_2 nanoparticles. *Applied Catalysis B: Environmental*, 57, 23-30.

BARHOUMI, N., OLVERA-VARGAS, H., OTURAN, N., HUGUENOT, D., GADRI, A., AMMAR, S., BRILLAS, E. & OTURAN, M.A. 2017. Kinetics of oxidative degradation/mineralization pathways of the antibiotic tetracycline by the novel heterogeneous electro-Fenton process with solid catalyst chalcopyrite. *Applied Catalysis B: Environmental*, 209, 637-647.

BELLO, A., MANYALA, N., BARZEGAR, F., KHALEED, A.A., MOMODU, D.Y. & DANGBEGNON, J.K. 2016. Renewable pinecone biomass derived carbon materials for supercapacitor application. *RSC Advances*, 6, 1800-1809.

CAI, Y., LUO, Y., SUN, B.-C., FAN, T.-X., CHU, G.-W. & CHEN, J.-F. 2019. A novel plasma-assisted rotating disk reactor: Enhancement of degradation efficiency of rhodamine B. *Chemical Engineering Journal*, 377, 119897.

CHEN, G., LI, F., HUANG, Z., GUO, C.-Y., QIAO, H., QIU, X., WANG, Z., JIANG, W. & YUAN, G. 2015. Facile synthesis of Ag/AgBr/RGO nanocomposite as a highly efficient sunlight plasmonic photocatalyst. *Catalysis Communications,* 59, 140-144.

CHEN, J., LI, G., HUANG, Y., ZHANG, H., ZHAO, H. & AN, T. 2012. Optimization synthesis of carbon nanotubes-anatase TiO_2 composite photocatalyst by response surface methodology for photocatalytic degradation of gaseous styrene. *Applied Catalysis B: Environmental,* 123, 69-77.

CHEN, Y. & LIU, K. 2016. Preparation and characterization of nitrogen-doped TiO_2/diatomite integrated photocatalytic pellet for the adsorption-degradation of tetracycline hydrochloride using visible light. *Chemical Engineering Journal,* 302, 682-696.

CONG-WEN, X., HAI-TAO, Y., CHENG-MIN, S., ZI-AN, L., HUAI-RUO, Z., FEI, L., TIAN-ZHONG, Y., SHU-TANG, C. & HONG-JUN, G. 2005. Controlled growth of large-scale silver nanowires. *Chinese Physics,* 14, 2270-2275.

DAI, K., LU, L., DONG, J., JI, Z., ZHU, G., LIU, Q., LIU, Z., ZHANG, Y., LI, D. & LIANG, C. 2013. Facile synthesis of a surface plasmon resonance-enhanced Ag/AgBr heterostructure and its photocatalytic performance with 450 nm LED illumination. *Dalton Transactions,* 42, 4657-4662.

DENG, Y., TANG, L., ZENG, G., WANG, J., ZHOU, Y., WANG, J., TANG, J., LIU, Y., PENG, B. & CHEN, F. 2016. Facile fabrication of a direct Z-scheme Ag_2CrO_4/g-C_3N_4 photocatalyst with enhanced visible light photocatalytic activity. *Journal of Molecular Catalysis A: Chemical,* 421, 209-221.

DENG, Y., TANG, L., ZENG, G., WANG, J., ZHOU, Y., WANG, J., TANG, J., WANG, L. & FENG, C. 2018. Facile fabrication of mediator-free Z-scheme photocatalyst of phosphorous-doped ultrathin graphitic carbon nitride nanosheets and bismuth vanadate composites with enhanced tetracycline degradation under visible light. *Journal of Colloid and Interface Science,*

509, 219-234.

FENG, Y., WU, D., DENG, Y., ZHANG, T. & SHIH, K. 2016. Sulfate radical-mediated degradation of sulfadiazine by $CuFeO_2$ rhombohedral crystal-catalyzed peroxymonosulfate: synergistic effects and mechanisms. *Environmental Science and Technology,* 50, 3119-3127.

GAO, Y., SONG, L., JIANG, P., LIU, L., YAN, X., ZHOU, Z., LIU, D., WANG, J., YUAN, H. & ZHANG, Z. 2005. Silver nanowires with five-fold symmetric cross-section. *Journal of Crystal Growth,* 276, 606-612.

GUPTA, N., DIMITRATOS, N., SU, D. & VILLA, A. 2019. Valorisation of Biomass Derived Furfural and Levulinic Acid by Highly Efficient Pd@ ND Catalyst. *Energy Technology*, 7, 269-276.

HOU, Y., LI, X., ZHAO, Q., QUAN, X. & CHEN, G. 2011. TiO_2 nanotube/Ag–AgBr three-component nanojunction for efficient photoconversion. *Journal of Materials Chemistry*, 21, 18067-18076.

HOU, Y., LI, X., ZHAO, Q., CHEN, G. & RASTON, C.L. 2012. Role of hydroxyl radicals and mechanism of Escherichia coli inactivation on Ag/AgBr/TiO_2 nanotube array electrode under visible light irradiation. *Environmental Science and Technology,* 46, 4042-4050.

HUANG, H., HE, M., YANG, X., TIAN, Z., HU, J. & WEN, B. 2019. One-pot hydrothermal synthesis of TiO_2/RCN heterojunction photocatalyst for production of hydrogen and rhodamine B degradation. *Applied Surface Science*, 493, 202-211.

JIANG, D., WANG, T., XU, Q., LI, D., MENG, S. & CHEN, M. 2017. Perovskite oxide ultrathin nanosheets/g-C_3N_4 2D-2D heterojunction photocatalysts with significantly enhanced photocatalytic activity towards the photodegradation of tetracycline. *Applied Catalysis B: Environmental*, 201, 617-628.

JIANG, D., WEN, B., XU, Q., GAO, M., LI, D. & CHEN, M. 2018. Plasmonic Au Nanoparticles/$KCa_2Nb_3O_{10}$ nanosheets 0D/2D heterojunctions with enhanced photocatalytic

activity towards the degradation of tetracycline hydrochloride. *Journal of Alloys Compounds,* 762, 38-45.

LA FARRE, M., PÉREZ, S., KANTIANI, L. & BARCELÓ, D. 2008. Fate and toxicity of emerging pollutants, their metabolites and transformation products in the aquatic environment. *Trends in Analytical Chemistry,* 27, 991-1007.

LI, X., TIE, K., LI, Z., GUO, Y., LIU, Z., LIU, X., LIU, X., FENG, H. & ZHAO, X.S. 2018. Nitrogen-doped hierarchically porous carbon derived from cherry stone as a catalyst support for purification of terephthalic acid. *Applied Surface Science,* 447, 57-62.

LIANG, Y., WANG, H., LIU, L., WU, P., CUI, W., MCEVOY, J.G. & ZHANG, Z.J. 2015. Microwave-assisted synthesis of a superfine Ag/AgI photocatalyst with high activity and excellent durability. *Journal of Materials Science,* 50, 6935-6946.

LIN, Z., XIAO, J., YAN, J., LIU, P., LI, L. & YANG, G. 2015. Ag/AgCl plasmonic cubes with ultrahigh activity as advanced visible-light photocatalysts for photodegrading dyes. *Journal of Materials Chemistry A,* 3, 7649-7658.

LIU, Q., ZHENG, Y., ZHONG, L. & CHENG, X. 2015. Removal of tetracycline from aqueous solution by a Fe_3O_4 incorporated PAN electrospun nanofiber mat. *Journal of Environmental Sciences,* 28, 29-36.

LIU, Y., CHEN, J., CUI, B., YIN, P. & ZHANG, C. 2018. Design and preparation of biomass-derived carbon materials for supercapacitors: A review. *Carbon,* 4, 53.

LÓPEZ-PEÑALVER, J.J., SÁNCHEZ-POLO, M., GÓMEZ-PACHECO, C.V. & RIVERA-UTRILLA, J. 2010. Photodegradation of tetracyclines in aqueous solution by using UV and UV/H_2O_2 oxidation processes. *Journal of Chemical Technology and Biotechnology,* 85, 1325-1333.

LU, S.Y., JIN, M., ZHANG, Y., NIU, Y.B., GAO, J.C. & LI, C.M. 2018. Chemically Exfoliating Biomass into a Graphene-like Porous Active Carbon with Rational Pore Structure,

Good Conductivity, and Large Surface Area for High-Performance Supercapacitors. *Advanced Energy Materials*, 8, 1702545.

LU, Z., ZENG, L., SONG, W., QIN, Z., ZENG, D. & XIE, C. 2017. In situ synthesis of C-TiO_2/g-C_3N_4 heterojunction nanocomposite as highly visible light active photocatalyst originated from effective interfacial charge transfer. *Applied Catalysis B: Environmental*, 202, 489-499.

MCEVOY, J.G. & ZHANG, Z. 2016. Synthesis and characterization of Ag/AgBr–activated carbon composites for visible light induced photocatalytic detoxification and disinfection. *Journal of Photochemistry Photobiology A: Chemistry*, 321, 161-170.

NIDHEESH, P.V. & GANDHIMATHI, R. 2014. Comparative removal of rhodamine B from aqueous solution by electro-fenton and electro-fenton-like processes. *CLEAN–Soil, Air, Water*, 42, 779-784.

OBREGÓN, S., ZHANG, Y. & COLÓN, G. 2016. Cascade charge separation mechanism by ternary heterostructured $BiPO_4/TiO_2/gC_3N_4$ photocatalyst. *Applied Catalysis B: Environmental*, 184, 96-103.

OSEGHE, E.O. & OFOMAJA, A.E. 2018. Study on light emission diode/carbon modified TiO_2 system for tetracycline hydrochloride degradation. *Journal of Photochemistry and Photobiology A: Chemistry*, 360, 242-248.

PALOMINOS, R.A., MONDACA, M.A., GIRALDO, A., PEÑUELA, G., PÉREZ-MOYA, M. & MANSILLA, H. 2009. Photocatalytic oxidation of the antibiotic tetracycline on TiO_2 and ZnO suspensions. *Catalysis Today*, 144, 100-105.

PETROSKI, J. & EL-SAYED, M.A. 2003. FTIR study of the adsorption of the capping material to different platinum nanoparticle shapes. *The Journal of Physical Chemistry A*, 107, 8371-8375.

REYES, C., FERNANDEZ, J., FREER, J., MONDACA, M., ZAROR, C., MALATO, S. &

MANSILLA, H. 2006. Degradation and inactivation of tetracycline by TiO_2 photocatalysis. *Journal of Photochemistry and Photobiology A: Chemistry,* 184, 141-146.

SACCO, O., VAIANO, V., SANNINO, D. & CIAMBELLI, P. 2017. Visible light driven mineralization of spiramycin over photostructured N-doped TiO_2 on up conversion phosphors. *Journal of Environmental Sciences,* 54, 268-276.

SAFARI, G., HOSEINI, M., SEYEDSALEHI, M., KAMANI, H., JAAFARI, J. & MAHVI, A. 2015. Photocatalytic degradation of tetracycline using nanosized titanium dioxide in aqueous solution. *International Journal of Environmental Science and Technology,* 12, 603-616.

SHI, H., LI, G., SUN, H., AN, T., ZHAO, H. & WONG, P.-K. 2014. Visible-light-driven photocatalytic inactivation of E. coli by Ag/AgX-CNTs (X= Cl, Br, I) plasmonic photocatalysts: Bacterial performance and deactivation mechanism. *Applied Catalysis B: Environmental,* 158, 301-307.

SHI, W., LV, H., YUAN, S., HUANG, H., LIU, Y. & KANG, Z. 2017. Near-infrared light photocatalytic ability for degradation of tetracycline using carbon dots modified Ag/AgBr nanocomposites. *Separation and Purification Technology,* 174, 75-83.

SONG, C., SUN, X.F., WANG, Y.K., XIA, P.F., YUAN, F.H., LI, J.J. & WANG, S.G. 2016. Fate of tetracycline at high concentrations in enriched mixed culture system: biodegradation and behavior. *Journal of Chemical Technology and Biotechnology,* 91, 1562-1568.

SONG, S., MA, F., WU, G., MA, D., GENG, W. & WAN, J. 2015. Facile self-templating large scale preparation of biomass-derived 3D hierarchical porous carbon for advanced supercapacitors. *Journal of Materials Chemistry A,* 3, 18154-18162.

SUN, H., SHI, X., MAO, J. & ZHU, D. 2010. Tetracycline sorption to coal and soil humic acids: An examination of humic structural heterogeneity. *Environmental Toxicology Chemistry,* 29, 1934-1942.

TROGADAS, P., FULLER, T.F. & STRASSER, P. 2014. Carbon as catalyst and support for electrochemical energy conversion. *Carbon,* 75, 5-42.

VERMA, A., JAIHINDH, D.P. & FU, Y.-P. 2019. Photocatalytic 4-nitrophenol degradation and oxygen evolution reaction in CuO/gC_3N_4 composites prepared by deep eutectic solvent-assisted chlorine doping. *Dalton Transactions*, 48 8594-8610.

VINOTH, R., KARTHIK, P., MUTHAMIZHCHELVAN, C., NEPPOLIAN, B. & ASHOKKUMAR, M. 2016. Carrier separation and charge transport characteristics of reduced graphene oxide supported visible-light active photocatalysts. *Physical Chemistry Chemical Physics,* 18, 5179-5191.

WANG, C., WANG, H. & CAO, Y. 2019. Waste printed circuit boards as novel potential engineered catalyst for catalytic degradation of orange II. *Journal of Cleaner Production,* 221, 234-241.

WANG, D., ZHAO, M., LUO, Q., YIN, R., AN, J. & LI, X. 2016. An efficient visible-light photocatalyst prepared by modifying AgBr particles with a small amount of activated carbon. *Materials Research Bulletin,* 76, 402-410.

WEI, X., CAO, J. & FANG, F. 2018. A novel multifunctional Ag and Sr^{2+} co-doped TiO_2@ rGO ternary nanocomposite with enhanced p-nitrophenol degradation, and bactericidal and hydrogen evolution activity. *RSC Advances,* 8 31822-31829.

WU, S., SHEN, X., JI, Z., ZHU, G., ZHOU, H., ZANG, H., YU, T., CHEN, C., SONG, C. & FENG, L. 2017. Morphological syntheses and photocatalytic properties of well-defined sub-100 nm Ag/AgCl nanocrystals by a facile solution approach. *Journal of Alloys and Compounds,* 693, 132-140.

XIAO, X., GE, L., HAN, C., LI, Y., ZHAO, Z., XIN, Y., FANG, S., WU, L. & QIU, P. 2015. A facile way to synthesize Ag@ AgBr cubic cages with efficient visible-light-induced photocatalytic activity. *Applied Catalysis B: Environmental,* 163, 564-572.

XIE, F., XU, Y., XIA, K., JIA, C. & ZHANG, P. 2016. Alternate pulses of ultrasound and electricity enhanced electrochemical process for p-nitrophenol degradation. *Ultrasonics Sonochemistry,* 28 199-206.

XU, Y., XU, H., YAN, J., LI, H., HUANG, L., ZHANG, Q., HUANG, C. & WAN, H. 2013. A novel visible-light-response plasmonic photocatalyst CNT/Ag/AgBr and its photocatalytic properties. *Physical Chemistry Chemical Physics,* 15, 5821-5830.

YAN, T., ZHANG, H., LUO, Q., MA, Y., LIN, H. & YOU, J. 2013. Controllable synthesis of plasmonic Ag/AgBr photocatalysts by a facile one-pot solvothermal route. *Chemical Engineering Journal,* 232, 564-572.

YAN, X., WANG, X., GU, W., WU, M., YAN, Y., HU, B., CHE, G., HAN, D., YANG, J. & FAN, W. 2015. Single-crystalline AgIn $(MoO_4)_2$ nanosheets grafted Ag/AgBr composites with enhanced plasmonic photocatalytic activity for degradation of tetracycline under visible light. *Applied Catalysis B: Environmental,* 164, 297-304.

YANG, M.-Q., WENG, B. & XU, Y.-J. 2013. Improving the visible light photoactivity of In_2S_3–graphene nanocomposite via a simple surface charge modification approach. *Langmuir,* 29, 10549-10558.

YANG, Y., GUO, W., GUO, Y., ZHAO, Y., YUAN, X. & GUO, Y. 2014. Fabrication of Z-scheme plasmonic photocatalyst Ag@ AgBr/g-C_3N_4 with enhanced visible-light photocatalytic activity. *Journal of Hazardous Materials,* 271, 150-159.

YANG, Y., JIN, H., LIU, R., GAN, H. & WEI, X. 2019. Dispersion of Ag–AgBr particles in activated carbon as a recyclable photocatalyst for adsorption and degradation of pollutants. *Journal of Dispersion Science Technology,* 1-11.

ZHANG, H., FAN, X., QUAN, X., CHEN, S. & YU, H. 2011. Graphene sheets grafted Ag@ AgCl hybrid with enhanced plasmonic photocatalytic activity under visible light. *Environmental Science and Technology,* 45, 5731-5736.

ZHOU, M., LI, J., YE, Z., MA, C., WANG, H., HUO, P., SHI, W. & YAN, Y. 2015. Transfer Charge and Energy of Ag@ CdSe QDs-rGO Core–Shell Plasmonic Photocatalyst for Enhanced Visible Light Photocatalytic Activity. *ACS Applied Materials and Interface,* 7, 28231-28243.

ZHOU, H., HU, L., WAN, J., YANG, R., YU, X., LI, H., CHEN, J., WANG, L. & LU, X. 2016. Microwave-enhanced catalytic degradation of p-nitrophenol in soil using MgFe2O4. *Chemical Engineering Journal*, 284 54-60.

ZHU, M., CHEN, P. & LIU, M. 2011. Graphene oxide enwrapped Ag/AgX (X= Br, Cl) nanocomposite as a highly efficient visible-light plasmonic photocatalyst. *ACS Nano,* 5, 4529-4536.

ZHU, Q., WANG, W.-S., LIN, L., GAO, G.-Q., GUO, H.-L., DU, H. & XU, A.-W. 2013. Facile synthesis of the novel Ag_3VO_4/AgBr/Ag plasmonic photocatalyst with enhanced photocatalytic activity and stability. *The Journal of Physical Chemistry C*, 117, 5894-5900.

ZHU, X.-D., WANG, Y.-J., SUN, R.-J. & ZHOU, D.-M. 2013. Photocatalytic degradation of tetracycline in aqueous solution by nanosized TiO_2. *Chemosphere,* 92, 925-932.

Chapter 6. Controlled microstructure of Ag/AgBr-activated carbon and synergistic enhancement on photocatalytic degradation of tetracycline: A synthesis approach comparison

Abstract

The controlled microstructure of plasmonic Ag/AgBr has enormously influenced its potential application in environmental remediation. On this basis, thermal polyol and deposition-precipitation routes synthesized Ag/AgBr nanoparticles immobilized on activated carbon (AABR-ACK) nanocomposites. Their photocatalytic activities on the degradation of tetracycline (TC) under visible light were further investigated. The synthesized nanocomposites microstructure, structural, optical and electrochemical properties were determined using analytical techniques. From the analysis results, the Ag/AgBr nanoparticles were distributed evenly on the ACK surface without agglomeration with an average particle size between 160 to 190 nm and possess {111} exposed facets of AgBr NPs. The controlled microstructure of TP-AABR-ACK along with the speedier interfacial separation of photogenerated charge carriers boosted the superior catalytic performance on tetracycline (92%) as compared to other nanocomposites in this study. ACK synergistic interaction with AABR NPs in this chapter significantly enhances charge carriers transfer, the creation of active sites for the generation of reactive oxygen species and thus a higher photoactivity under LED light irradiation conditions. Reactive species scavenging experiments revealed that photogenerated holes and superoxide anions are the main active species during the

photocatalytic process. Furthermore, total organic carbon (TOC) removal of TC and the reactive superoxide anion generation with the prepared composites were investigated in this chapter.

Keywords: Controlled Microstructure, Thermal polyol, Deposition-precipitation route, Tetracycline, Visible light, Reactive oxygen species

6.1 Introduction

The prevalence of antibiotics in the surface and municipal water poses huge risks to our environment and human health at large. Although trace level and long accumulation of these antibiotics in the environment have adverse effects on both aquatic and terrestrial organisms (Zhang, Liu, Feng & Yang 2013). Tetracycline is a commonly used antibiotic that has been detected in the ecosystem (Chao, Zhu, Yan, Lin, Xun, Ji, Wu, Li & Han 2014). The complete removal of this antibiotic using conventional techniques still have their pitfalls, hence the need for effective treatment method that can be applied on a large scale is required (Chao et al. 2014). Semiconductor photocatalysis under advanced oxidation processes (AOPs) using conventional TiO_2 photocatalyst has shown promising attributes for antibiotic removal (Lu, Chen, He, Song, Ma, Shi, Yan, Lan, Li & Xiao 2014). However, the development of efficient and sustainable visible-light-driven photocatalysts that can fully explore the potential of the solar spectrum is considered as one of the promising strategies toward solving the pitfall of conventional TiO_2 photocatalyst (Simsek, Balta & Demircivi 2019). Host of visible light photocatalyst have shown potential for degradation of TC antibiotic effectively (Guan, Yuan, Wu, Wang, Jiang, Zhang, Li, Zeng & Mo 2018; Liu, Kong, Yuan, Zhao, Zhu, Sun & Xie 2018; Jiang, Yuan, Zeng, Liang, Wu, Yu, Mo, Wang, Xiao & Zhou 2019). Huge attention is channeled towards the design of Ag-based photocatalysts (Ag/AgX, X=Cl, Br, I), which respond intensively to the visible light due to surface plasmon resonance (SPR) of Ag nanoparticles (NPs) anchored on the large bandgap of the photocatalysts (Kuai, Geng, Chen, Zhao & Luo 2010; Xiao, Ge, Han, Li, Zhao, Xin, Fang, Wu & Qiu 2015).

Ag/AgBr is an important photocatalyst with exceptional attributes as compared to Ag/AgX (X=Cl, I) (Wang, Huang, Zhang, Qin, Jin, Dai, Wang, Wei, Zhan & Wang 2009; Zhu, Chen & Liu 2012), with less emphasis on the synthetic approach for well-defined Ag/AgBr

nanostructures. The synthetic approach plays a huge role in the development of this highly efficient photocatalyst. However, the rapid reaction in the formation of AgBr nanospecies from conventional post-treatment route (photoinduced reduction) is still challenging for effective distribution and growth of the metallic silver nanoparticles (Ag NPs) (Kuai et al. 2010). The well tailor surface plasmon resonance properties (SPR) of Ag NPs are dependent on controlled microstructure (shape, size, and composition) of Ag/AgX nanocomposite. The controlled microstructure of Ag/AgBr (AABR) nanospecies with different sizes and defined morphologies have been achieved through a host of approaches (Wang et al. 2009; Li, Wang, Zhang, Hu, Chen & Guo 2013; Yan, Zhang, Luo, Ma, Lin & You 2013). However, the SPR attributes of produced Ag NPs anchored on AgBr NPs from these preceding works (Wang et al. 2009; Xu, Song, Liu, Li, Xu, Xia, Wu & Zhao 2012; Li et al. 2013; Yan et al. 2013) have limited significance on separation of charge carriers and as such high recombination rate of electron and holes is still evident. Therefore, there is a need to disperse Ag/AgBr NPs on the clean surface material, which can participate in the controlled microstructure of Ag/AgBr NPs. This material should also accelerate the separation efficiency of charge carriers and boosts the overall stability of formed composite in the catalytic process.

The application of carbonaceous materials with abundant oxygenated functional groups as a catalyst promoter and support in the dispersion of Ag/AgBr nanoparticles (Zhu et al. 2012; Chen, Li, Huang, Guo, Qiao, Qiu, Wang, Jiang & Yuan 2015; Esmaeili & Entezari 2015, 2016), has shown exceptional attributes to overcome the challenges of previous works (Wang et al. 2009; Li et al. 2013; Yan et al. 2013). In view of the outstanding properties of these carbonaceous materials, this work focuses on the utilization of activated carbon derived from microwave pyrolysis of impregnated pinecone as a catalyst support in the controlled microstructure of Ag/AgBr nanoparticles. The AABR-ACK nanocomposites were prepared through two different approaches (thermal polyol - TP-AABR-ACK and deposition-

precipitation method - DP-AABR-ACK), which has never been reported so far to the best of our knowledge. The synthesis influence of the prepared AABR-ACKs composite on the degradation of tetracycline (TC) antibiotic removal under visible light irradiation was also carried out. TP-AABR-ACK nanocomposite displays higher photocatalytic activity on TC than the DP-AABR-ACK nanocomposite and corresponding AABR nanoparticles under visible LED light irradiation.

6.2 Experimental section

6.2.2 Activated carbon synthesis

The experimental description of optimized activated carbon produced from pinecone biomass has been described in **Chapter 3** (**Section 3.2.2)**.

6.2.3 Preparation of TP-AABR-ACK through thermal polyol route

The experimental detail of optimized TP-AAABR-ACK synthesis has been described in **Chapter 5** (**Section 5.2.1)** and corresponding TP-AABR catalysts was prepared via the same route without addition of ACK.

6.2.4 Preparation of DP-AABR-ACK through deposition-precipitation route

The Ag/AgBr coupled ACK (AABR-ACK) composite were synthesized using the deposition-precipitation method (Zhu, Chen & Liu 2013). Typically, 12 mL ethylene glycol solution (EG, Acros, 99 %) was heated in a round-bottom flask for 30 min at a temperature of 65 ºC. Hexadecyltrimethylammonium bromide (HTAB, Acros, 99%;0.26 g) and ACK 0.09 g were sequentially added to the EG stirred solution. After homogenization, 0.2 g of silver nitrate ($AgNO_3$, Merck, 98%) mixed with 1M ammonium water volume (2.5 ml) was added dropwise while stirring. The mixture was stirred for 6 hr under ambient light for the formation of Ag° NPs on nucleated AgBr. The precipitated solution was allowed to cool down, separated by centrifugation (6000 rpm, 10 min), further washed with ethanol and deionized water repeatedly, then dried in a vacuum oven at 60 ℃ overnight. A reference Ag/AgBr (DP - AABR) was

synthesized using the same route without ACK in the synthesis process.

6.2.5 Characterization of the synthesized materials

Detailed descriptions of the analytical procedures (SEM, TEM, XRD, FTIR, UV-DRS, and electrochemical studies) carried out on characterization of TP-AAABR-ACK, DP-AABR-ACK, TP-AABR, and DP-AABR nanocomposites during this work can be found in **Chapter 4** (**Section 4.2.3).**

6.2.6 Photocatalytic activity evaluation

The photocatalytic activity of the prepared samples was evaluated on the degradation of tetracycline (TC) in aqueous solution under the irradiation of 36 W white visible LED light strips. The initial TC concentration was 15 mg/L with a catalyst loading of 0.3 g/L in 150 mL of TC solution. Prior to irradiation, the mixed solution was ultrasonicated, then stirred in the reactor for 1 h in the dark to reach the adsorption/desorption equilibrium of TC on the photocatalyst surface. The adsorbed solution was further subjected to degradation by switching on the LED light under stirring for 3 h, while 3 mL of the sample solution was withdrawn at given time intervals (30 min) and centrifuged to remove suspended particles. The concentration of TC left was determined by measuring the absorbance of the solution in a UV-visible spectrophotometer at 356 nm. Moreover, the effect of sacrificial agents such as Benzoquinone (BQ), isopropanol (IPA) and disodium ethylenediaminetetraacetic acid (EDTA-Na_2) on the degradation rate of TC over-TP-AABR-ACK and DP-AABR-ACK were evaluated.

Similar to the photodegradation experiments the measurement of superoxide radicals generated was carried out in this studies using nitroblue tetrazolium molecules. The nitroblue tetrazolium (NBT) can be specifically reduced by the superoxide ion to form the insoluble purple formazan in the aqueous solution. A 20 mg/L Nitroblue Tetrazolium solution (Sigma

Aldrich, 99%) with 0.3 g/L of photocatalysts were degraded under LED visible light and the change in concentration was measured at maximum absorbance wavelength of 259 nm. Total organic carbon (TOC) analysis was performed to determine the mineralization degree of the TC reached after the photocatalytic process.

6.3 Characterization

6.3.1 Morphology, size and composition analysis

The SEM micrographs, particle diameter and elemental compositions of plasmon TP-AABR-ACK and DP-AABR-ACK are shown in **Figure 6.1a - f**, where the formation of ordered nanospheres morphology is pronounced for plasmon TP-AABR-ACK (**Figure 6.1a and b**) with an average diameter of 162 nm. However, the morphologies of plasmon DP-AABR-ACK are near spheres nanostructure with an average particle size of 180 nm (**Figure 6.1d and e**). The reduced particle size and uniform morphologies for plasmon TP-AABR-ACK as compared to plasmon DP-AABR-ACK are ascribed to reaction time, synthesis temperature and PVP influence, as these parameters significantly hamper irregular growth of Ag/AgBr (AABR) nanoparticles yielding formation of uniform nanostructures. The synthesis temperature from previous work has resulted in the formation of isotropically shaped Ag/AgBr nanoparticles (Chen et al. 2015; Wu, Shen, Ji, Zhu, Zhou, Zang, Yu, Chen, Song & Feng 2017), whilst PVP acts as a capping agent (Yan et al. 2013) in particle size reduction and formation of well-defined shaped nanoparticles. Plasmon TP-AABR-ACK with small particle size and uniform nanospheres morphology will have speedier charge transfer, facilitating adsorption of the pollutant on the surface of catalyst and creation of active sites in the catalytic system for enhanced degradation of tetracycline pollutant in this study.

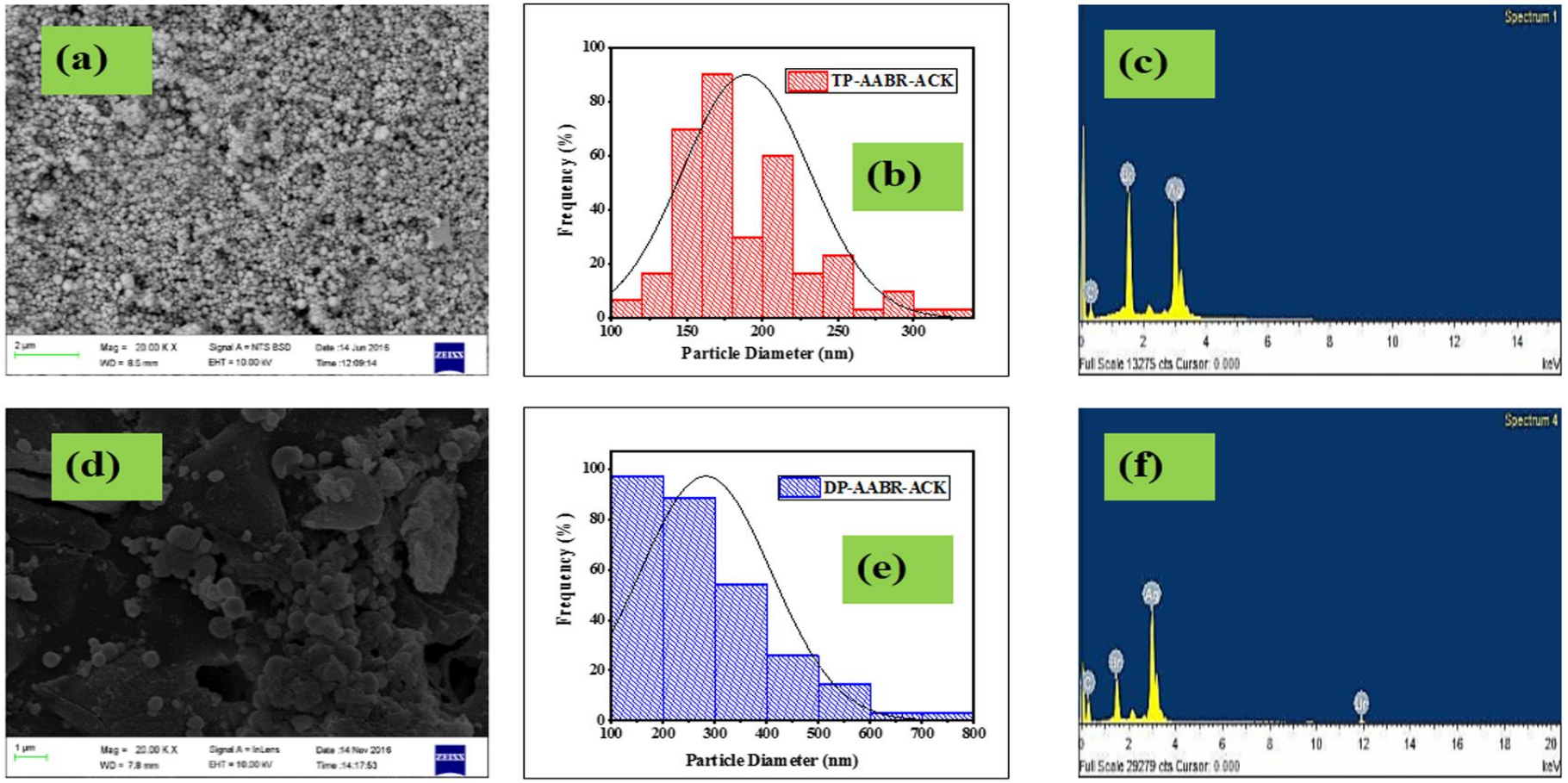

Figure 6.1: SEM images and EDX spectrum of plasmon TP-AABR-ACK (a, b and c) and plasmon DP-AABR-ACK (d, e and f).

The elemental components of the plasmon nanocomposites (TP-AABR-ACK and DP-AABR-ACK) were further investigated by energy dispersive X-ray spectroscopy (EDX) analysis. As depicted in **Figure 6.1c and f**, Ag, Br from AABR and presence of C element from activated carbon are identified in the AABR-ACK nanocomposites. The EDX analysis also show no other elements in the prepared AABR-ACK photocatalyst, which confirms the high purity of the prepared products. The atomic ratio between Ag and Br was more than 1:1 for the DP- AABR-ACK compared to TP-AABR-ACK composite based on the semi-quantitative analysis (**Table 6.1**). This further confirms the formation of metallic Ag NPs anchored on AgBr in the nanocomposite. Also, the plasmon DP-AABR-ACK possesses more content of Ag NPs ratio and high percentage reduction of Ag NPs as compared to TP-AABR-ACK. This is ascribed to ammonium hydroxide ionizing the carboxylic functional groups on ACK surface leading to the formation of more carboxylate anions. The formed carboxylate anions act as additional capping sites for AgBr NPs dispersion and growth through electrostatic interactions between the carboxylate anions and silver cations (Zhu et al. 2013). The high Ag content on surface of AgBr for DP-AABR-ACK might results to reduced photocatalytic activity (Guo, Niu, Wen, Zhang, Liang, Zhang, Guan, Tang & Zeng 2018), while TP-AABBR-ACK with low content and order dispersion of AABR NPs will enhance TC removal efficiently in this study (Zhang, Tang, Fu & Xu 2011; Guo et al. 2018). The three-dimensional network structure of ACK favored uniform distribution of AABR nanoparticles in the formed nanocomposites.

Table 6.1: EDX analyses of AABR-ACK nanocomposites synthesized from both methods.

Sample	Atomic ratio (C)	Atomic ratio (Br)	Atomic ratio (Ag)	[a]Atomic ratio (Ag:AgBr)	[b]Reduction % of Ag
TP-AABR-ACK	20.50	28.73	50.77	0.77:1	43.41
DP-AABR-ACK	72.44	7.13	20.43	1.86:1	65.10

$a = \frac{A-B}{B}; b = \frac{A-B}{A}$ (A-is atomic ratio of Ag and B is atomic ratio of Br) (Shahzad, Yu & Kim 2016)

Figure 6.2a shows the TEM image for TP-AAABR-ACK is spheres shaped like nanoparticles, in which the PLAS particles with diameter around 3-5 nm (**Figure 6.2c**) uniformly distributed on the ACK surface. The formation of near spheres nanostructure in DP-AABR-ACK is further ascertained by TEM (**Figure 6.2d**), with particle diameter between 4 to 10 nm (Figure 6.2f) sparsely distributed on the ACK surface with little agglomeration. **Figure 6.2b** and **e** from the HRTEM image show d-spacing of 0.237 nm ascribed to (111) planes of metallic silver, while d-spacing of 0.286 nm belongs to (200) planes of AgBr. The average particle size of TP-AABR-ACK is smaller than that of TP-AABR-ACK, which could also contribute partially to enhanced photocatalytic performance. The TEM and HRTEM image for both TP-AAABR-ACK and DP-AAABR-ACK remarkably evidence the co-existence of metallic Ag and AgBr in the composites, as direct contact among the components with ACK is favorable for the formation of strong heterostructure for enhanced charge carrier separation.

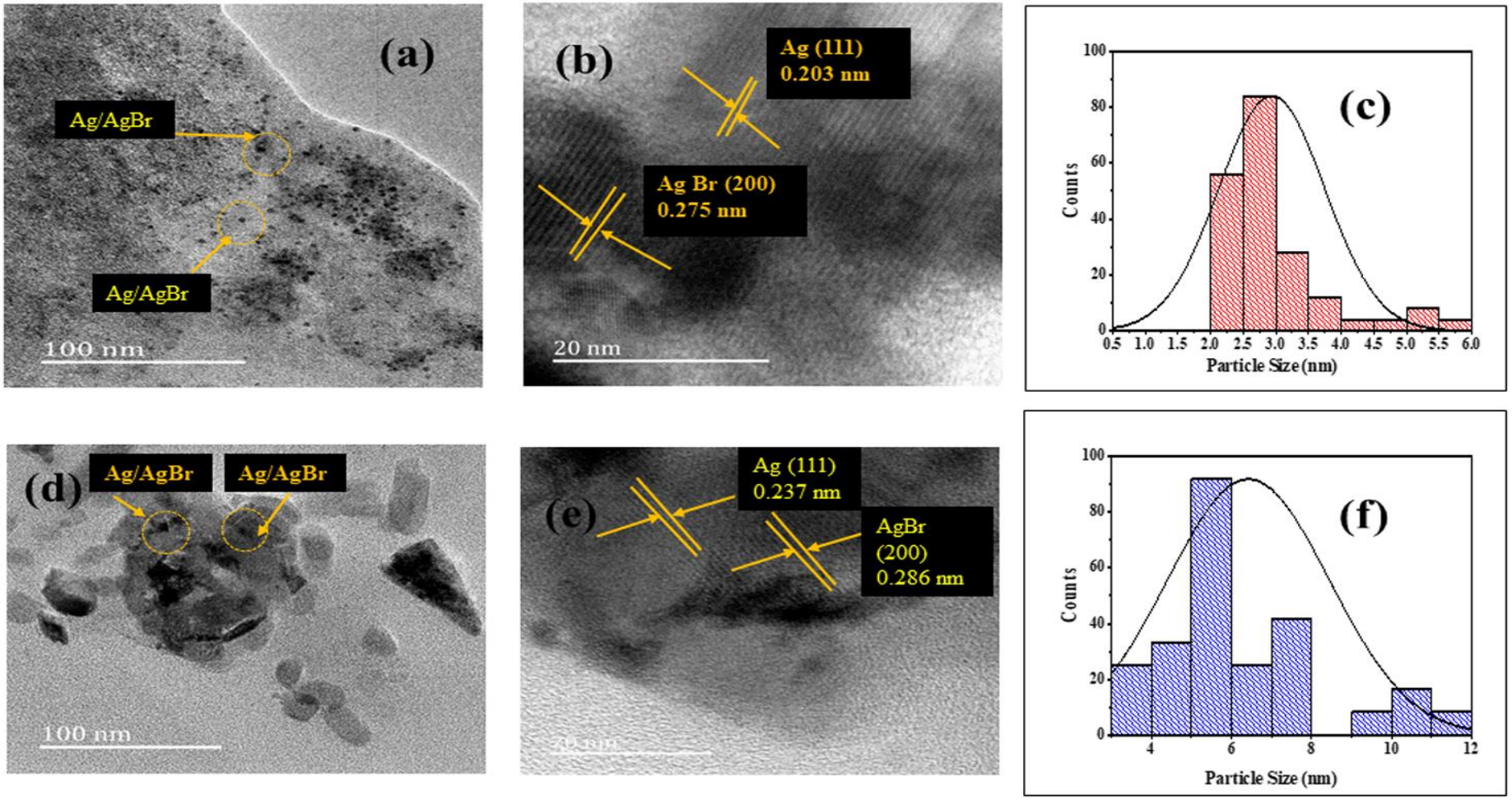

Figure 6.2: (a, d) TEM image, (b, d) HRTEM image and (c, f) particle diameter of TP-AABR-ACK and DP-AABR-ACK photocatalyst.

6.3.2 X-ray diffraction analysis

The crystal structures and the existence of metallic Ag and AgBr in the prepared nanocomposites were established with XRD investigation. As shown in **Figure 6.3**, the XRD pattern of the AABR-ACK and AABR nanocomposites indicated distinct diffraction peaks that are ascribed to face centered cubic phase of AgBr (JPCDS 079-0148) and metallic Ag NPs (JCPDS 071-3762) (Zhu, Wang, Lin, Gao, Guo, Du & Xu 2013). These peaks at the 2θ include 26.6° (111), 31.1° (200), 44.3° (220), 54.8° (222), 64.8° (400), 73.4° (420) for AgBr and 38.2° (111), 44.2° (200), 64.4° (220) and 77.8° (311) all belong to Ag NPs (Lou, Huang, Qin, Zhang, Cheng, Liu, Wang, Wang & Dai 2012). Low intensity of diffraction peak for Ag^{o} at 38.2° in TP-AABR-ACK is assigned to its high dispersion, low content and ultrafine particle size. The intensity ratio of $I_{(200)}/I_{(220)}$ of AgBr peaks for plasmon TP-AABR-ACK and DP-AABR-ACK are about 1.06 and 0.68, which are higher than that of TP-AABR and DP-AABR NPs at 0.42 and 0.31. This observation confirms that synthesized Ag/AgBr materials growth directions are <100> direction with high exposed facet of {111} AgBr NPs (Lin, Xiao, Yan, Liu, Li & Yang 2015). This {111} facets of AgBr from previous work describe the facets with higher surface energy than facets of {100} and {110} with enhanced catalytic activities (Ma, Dai, Lu, Guo & Huang 2012). As a result, the plasmon TP-AABR-ACK with a high ratio of the {111} facet AgBr NPs will exhibit higher catalytic activity as compared to plasmon DP-AABR-ACK and corresponding AABR with lower ratios. In addition, TP-AABR-ACK and DP-AABR-ACK diffraction peaks for AgBr and metallic Ag were right shifted by 0.2˚, which arises from the strong interaction between AgBr, Ag and ACK support (Lin et al. 2015), and which will promotes fast separation of photogenerated charge carriers.

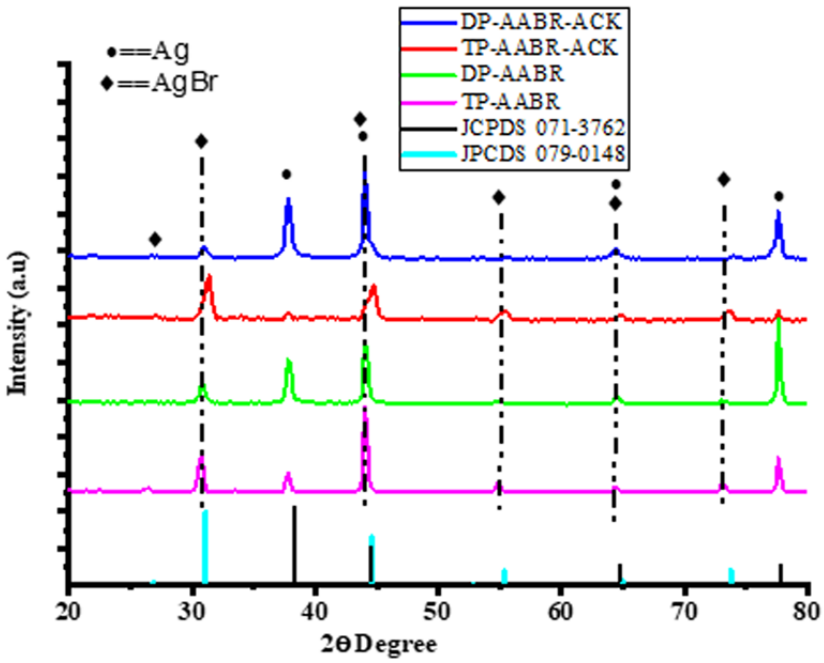

Figure 6.3: XRD patterns of the synthesized AABR-ACK nanocomposites and corresponding AABR.

6.3.3 Fourier-Transform Infrared (FTIR) analysis

The FTIR analysis confirms the synergistic interaction between ACK and AABR NPs. The ACK (López-Peñalver, Sánchez-Polo, Gómez-Pacheco & Rivera-Utrilla) displays a broad peak at 3343 cm^{-1}which corresponds to O-H stretching, while the carbonyl stretching peak is at 1692 cm^{-1} (Feng, Zhou, Liu, Qiao, Wang, Lu, Yang & Wu 2012) and the peak at 1583 cm^{-1} is ascribed to the carboxylic (-COO) stretching vibration (**Figure 6.4**). The characteristic peaks of C-OH and C-O-C at 1288, 1127and 1026 cm^{-1} respectively are also present in the ACK material. The carbonyl and carboxyl stretching band shifted to high intensity in the AABR-ACK nanocomposites (**Figure 6.4**), which confirms the formation of firm bonding as observed with other reports (Petroski & El-Sayed 2003; Zhu, Chen & Liu 2011) using carbonaceous material in hybridization of plasmonic Ag/AgX (X = Cl, Br) materials. In addition, the aliphatic

bands of the capped surfactants (PVP and HTAB) at 2912 and 2842 cm^{-1} appear with high and low intensity for TP-AAABR-ACK and DP-AABR-ACK. The high intensity of aliphatic bands in TP-AAABR-ACK highlights formation of ordered AABR nanoparticles with small particle diameter (*evidenced from SEM and TEM analysis in* ***Figure 6.1a and 6.2a***). Overall, reduction in the rapid growth of AABR particles, agglomeration prevention and decrease in size distribution is evident for both TP-AABR-ACK and DP AABR-ACK composites based on FTIR analysis (**Figure 6.4**).

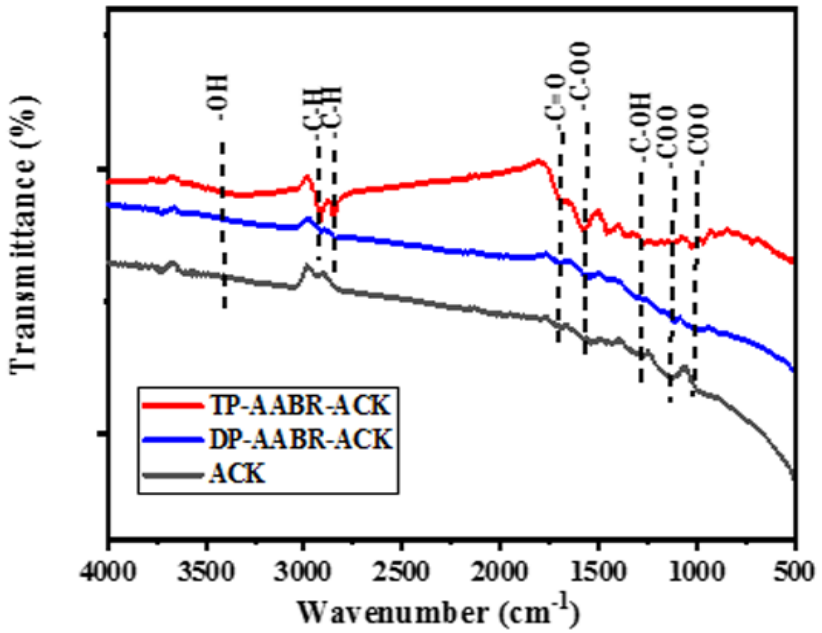

Figure 6.4: FTIR spectrum of ACK, TP-AABR-ACK and DP-AABR-ACK composites.

6.3.4 Optical properties of AABR-ACK

The as-prepared nanocomposites (TP-AABR-ACK, DP-AABR-ACK, TP-AABR and DP-AABR) display strong absorption both in the visible region as shown in **Figure 6.5**. This further confirms the presence of metallic Ag NPs in both nanocomposites, which generates surface plasmon resonance (SPR) absorption in the visible region (Jiang, Li & Zhang 2012). As the tailored SPR properties of Ag NPs anchored on AgBr are influenced by controlled microstructure (size, morphology, and composition) (Wang et al. 2009). TP-AABR-ACK nanocomposite exhibits more intense absorption in the visible region as compared with DP-AABR-ACK, which can be ascribed to oriented SPR properties of Ag NPs. The excessive Ag content in DP-AABR-ACK (from **Table 6.1**) will cover up the actives sites of the material and reduces the visible light absorption for generation of reactive species (Deng, Zhao, Luo, Luo & Dionysiou 2018; Bhatt & Patel 2019). The 3D hierarchical structure of ACK also aids light transmittance within the TP-AABR-ACK and DP-AABR-ACK composite, thus enhancing the absorption edge of AABR for higher activity compared to TP-AABR and DP-AABR. The as-prepared TP-AABR-ACK with controlled microstructures will possess higher photocatalytic activity than plasmon DP-AABR-ACK in the whole solar spectrum region.

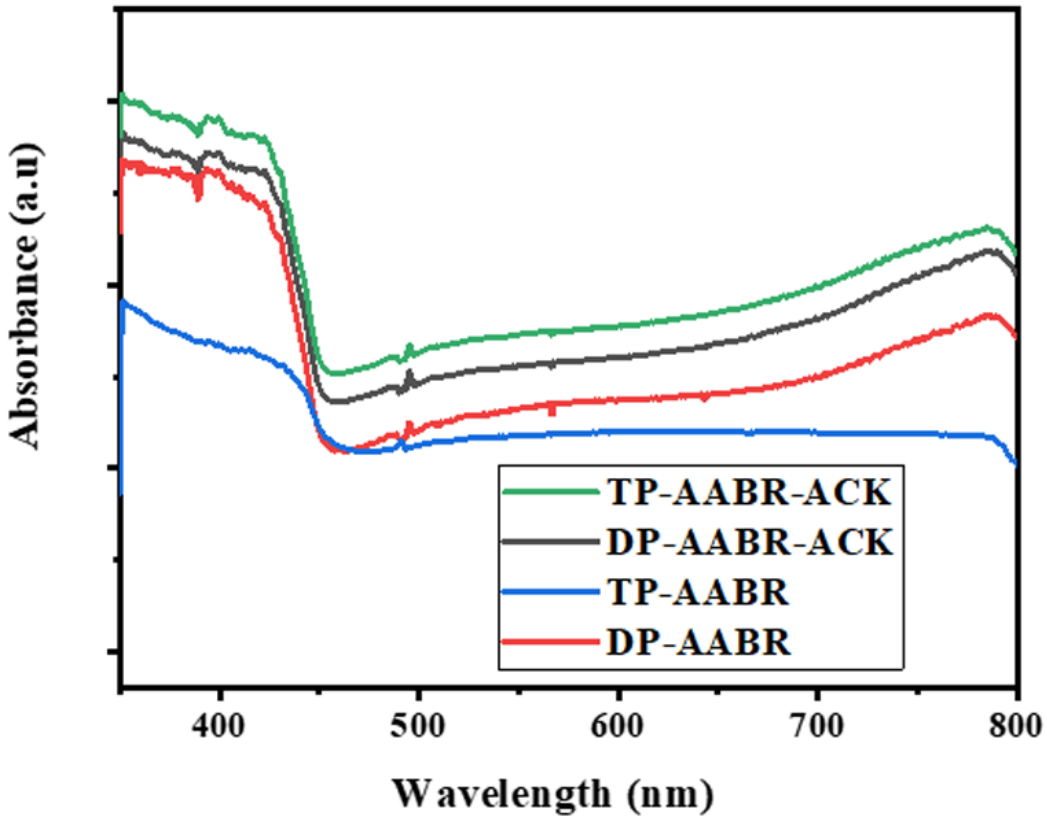

Figure 6.5: UV–Vis diffusive reflectance spectra of as prepared nanocomposites.

6.3.5 Electrochemical Properties

The electrochemical impedance spectra (EIS) Nyquist plots and equivalent circuit utilized in fitting the curve are shown in **Figure 6.6**, where R_s denotes the series resistance of electrolyte, R_d is the diffusion resistance, R_{ct} is the charge transfer resistance, while CPE, $C_{f,}$ and W_s are the constant phase element, chemical capacitance and Warburg resistance between the photoanode and electrolyte respectively. The TP-AABR-ACK displays a smaller arc radius as compared to DP-AABR-ACK, TP-AABR and DP-AABR in the EIS Nyquist plots (**Figure 6.6**) which signify a reduced charge transfer resistance with enhanced interfacial separation of charge carriers. Plasmon TP-AABR-ACK has least R_{ct} values with the highest efficiency for electron-hole separation, which further enhances the generation of reactive active species for

tetracycline (TC) degradation. This is ascribed to the well-controlled microstructure of AABR nanoparticles with exposed active sites and the synergetic coupling of AABR nanoparticles with activated carbon support. The activated carbon support behaves as a transport medium in the separation of photo-induced charge carriers from the Ag/AgBr nanoparticles, which further boost the catalytic attributes of TP-AABR-ACK in this study.

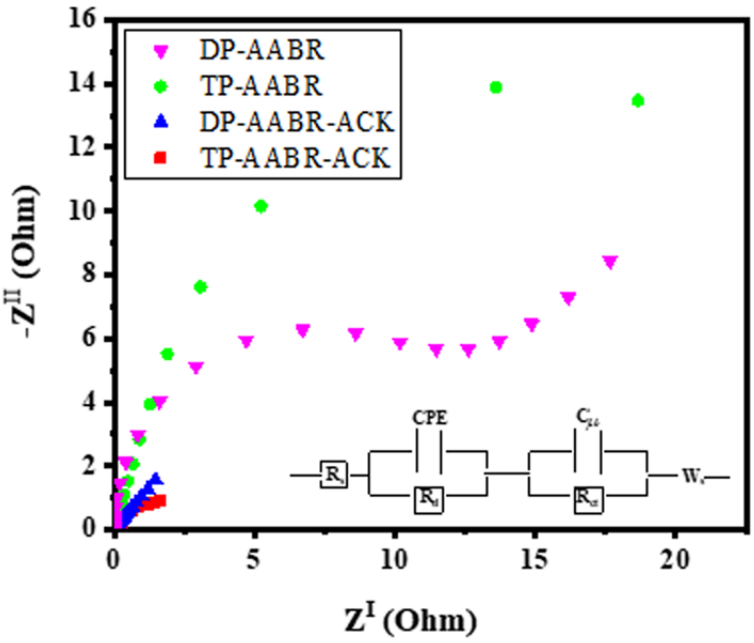

Figure 6.6: EIS Nyquist plots of TP-AABR-ACK, DP-AABR-ACK, TP-AABR and DP-AABR with an equivalent circuit diagram.

6.3.6 Photocatalytic Degradation of Tetracycline

The photocatalytic activities of the as-prepared samples were assessed by degradation of tetracycline (TC) under visible light irradiation. As shown in **Figure 6.7a**, after 180 min of degradation of TC, only 14.66% removal was achieved in the absence of the photocatalyst, indicating that TC molecule is highly stable under visible light irradiation. However, with other photocatalysts prepared in this work, the decrease in concentration of TC as a function of time is evident in **Figure 6.7a**. The TP-AABR and DP-AABR showed visible light activity on the degradation of TC (59.72 and 57.10%), while the dispersion of ordered shaped AABR on ACK improves the degradation rate significantly. Plasmon TP-AABR-ACK induces more degradation rate (92.08%) than DP-AABR-ACK (81.12, %) due to the ordered morphology of AABR nanoparticles with reduced particle diameter. The excessive Ag content in DP-AABR-ACK compared to TP-AABR-ACK (as evidenced from EDX analysis in **Figure 6.1**) can be a recombination center and hasten the recombination of charge carrier pair, resulting to reduced activity (Hu & Cao 2012; Deng et al. 2018). Overall, the TP-AABR-ACK photocatalytic performance was higher than that of DP-AABR-ACK, AABR NPs and photolysis in the degradation of TC. The superior photocatalytic performance for TP-AABR-ACK could also be ascribed to the formation of effective heterojunction among the three components as well as the promotion of interfacial charge transfer process.

The catalytic degradation rates of TC over the as-prepared nanocomposites were fitted using the pseudo-first-order (Eq. 6.1) (Xu, Wang, Shang, Sun, Ren & Zhang 2010) and pseudo second order kinetics (Eq. 6.2) as presented below:

$$-In\frac{C_t}{C_o} = kt \qquad 6.1$$

$$\frac{1}{C_t} - \frac{1}{C_o} = k_2 t \qquad 6.2$$

Here, t is reaction time, Co and Ct are the TC concentrations at reaction time of 0 and t min, k and k2 are the apparent rate constant of pseudo first order and pseudo second order kinetics.

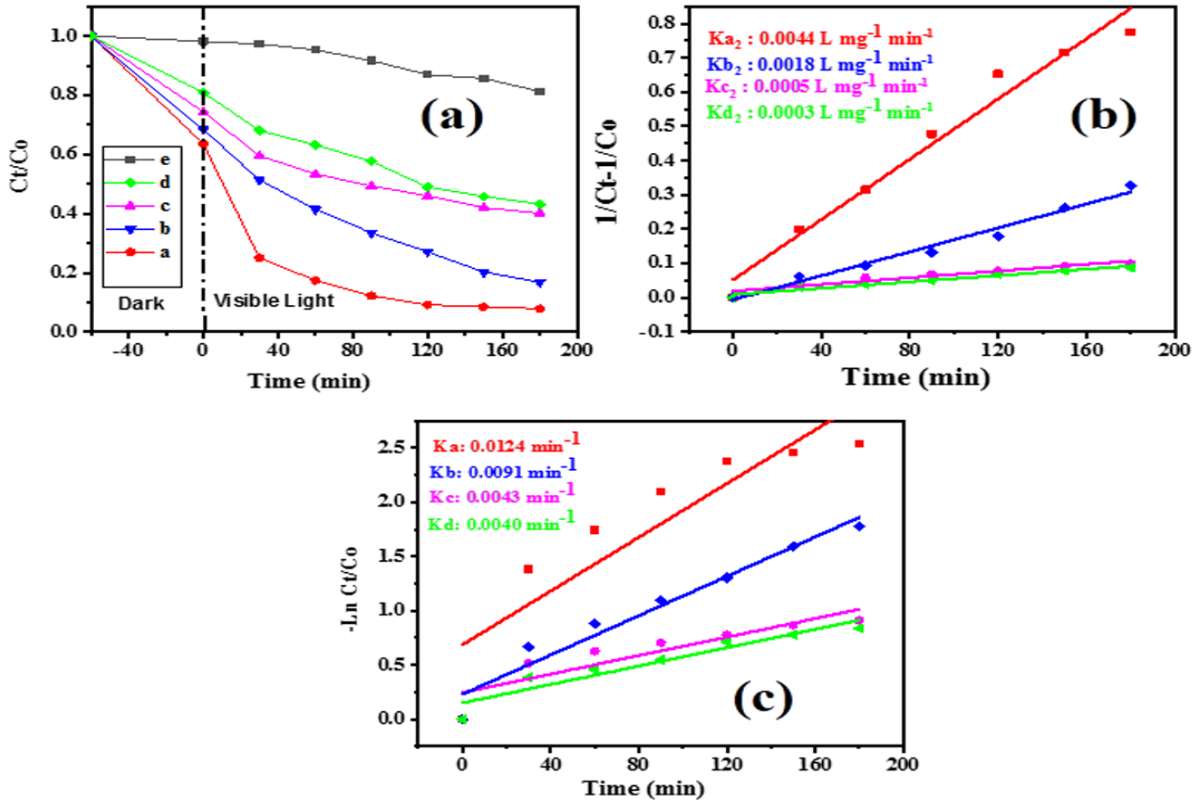

Figure 6.7: (A) Photocatalytic activity of as-prepared nanocomposites on TC degradation under visible light; (a) TP-AABR-ACK, (b) DP-AABR-ACK, (c) TP-AABR, (d) DP-AABR and (e) photolysis; (B) pseudo second and (C) pseudo first order kinetics.

The pseudo second order fits the degradation of TC better compared to pseudo first order kinetic (**Figure 6.7b and c)**. The k_{a2} rate constant for plasmon TP-AABR-ACK is largest compared to plasmon DP-AABR-ACK, TP-AABR, and DP-AABR respectively in this work.

Figure 6.8a and b shows the UV–Vis absorption plot of TC degradation in the presence of plasmon TP-AABR-ACK and DP-AABR-ACK under visible light irradiation. The characteristic maximum absorption peak of TC (376 nm) decreases rapidly as the degradation time increases, highlighting the destruction of aromatic ring in TC. This analysis shows that photocatalytic degradation efficiency of TP-AABR-ACK is better compared to DP-AABR-ACK. The TP-AABR-ACK and DP-AABR-ACK exhibits superior photocatalytic degradation of TC in comparison with other previously reported photocatalysts as depicted in **Table 6.2**.

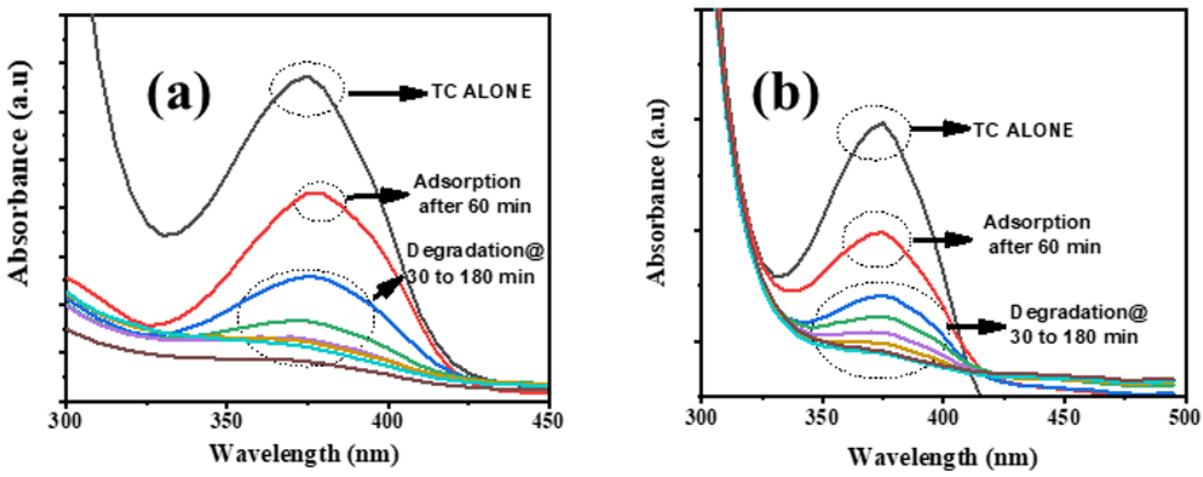

Figure 6.8: Decrease in maximum absorption peak of TC at different irradiation times using (a) plasmon TP-AABR-ACK and (b) DP-AABR-ACK as a photocatalyst.

Table 6.2: Comparison of degradation efficiency with different Ag/AgBr heterostructure composites on tetracycline removal.

Catalyst	Catalyst mass (g), TC concentration (mg/L)	Light Source	% Degradation	References
Ag/AgBr/$AgIn(MoO_4)_2$	0.1, 10	500 W Xe lamp	42 after 40 min	(Yan, Wang, Gu, Wu, Yan, Hu, Che, Han, Yang & Fan 2015)
Ag-$K_2Ta_2O_6$	0.1, 20	300 W Xe lamp	50 after 270 min	(Yang, Niu, Huang, Zhang & Zeng 2017)
AgI-WO_3	0.04, 35	300 W Xe lamp	75 after 60 min	(Xu, Liu, Shi, Chen, Luo, Xiao & Gu 2015)
Ag_2CO_3/Ag/WO_3	0.1, 10	300 W Xe lamp	81 after 90 min	(Wang, Quan, Jiang, Chen, Li, Meng & Chen 2016)
Ag/Bi_3TaO_7	0.05, 10	250 W Xe lamp	85 after 60 min	(Yuan, Jiang, Chen, Leng, Wang, Wu, Xiong, Liang & Zeng 2017)
graphene-like BN/BiOBr	0.05, 20	300 W Xe lamp	75 after 80 min	(Di, Xia, Ji, Wang, Yin, Zhang, Chen & Li 2016)
Bi_4NbO_8Cl perovskite	0.01, 20	18-W LED bulb	79 after 60 min	(Majumdar & Pal 2019)
GO/CN/BiOI	0.03, 20	35W LED track light	74 after 100 min	(Wang, Li, Huang, Zhang, Wang, Wang, Zhang, Xie & Li 2019)
TP-AABR-ACK	**0.045, 15**	**36 W Visible LED Light**	**92 after 180 min**	***This Study***
DP-AABR-ACK			**81 after 180 min**	

TOC Teledyne Tekmar analyzer evaluated the mineralization ability of the prepared composites on TC, and the result are presented in **Figure 6.9**. The total carbon content of TC molecules gradually decreased, as the TP-AABR-ACK sample gave a total TOC removal efficiency of 87.5% after 180 min, which is higher than that of DP-AABR-ACK, TP-AABR and DP-AABR (78.5%, 19% and 15.4%) under same conditions. This further indicates that the TP-AABR-ACK composite present enhanced mineralization ability in TC antibiotic degradation, indicating the formation of inorganic ions and CO_2. It also indicates that AABR NPs decorated on the ACK porous structure enhances mineralization of TC 5 times fold than corresponding AABR without activated carbon.

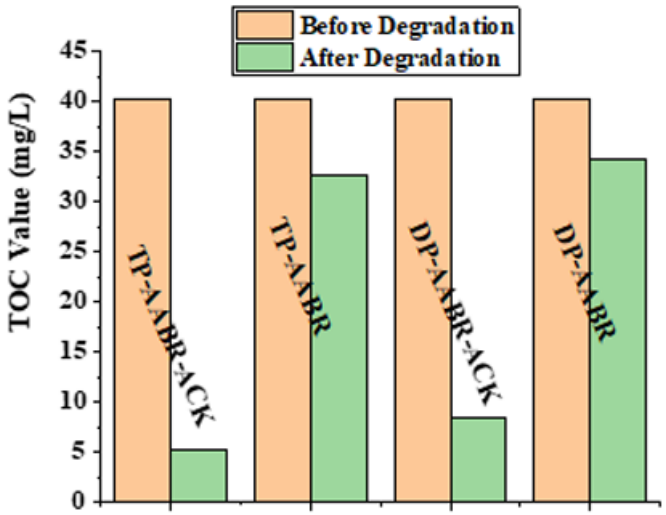

Figure 6.9: TOC changes of TC before and after photocatalytic reaction using as prepared samples.

For further confirmation of active species responsible for enhanced photodegradation of TC using the TP-AABR-ACK and DP-AABR-ACK under visible light irradiation. A host of different scavenger solution (1 mmol) such as benzoquinone (BQ), isopropanol (IPA) and ethylenediaminetetraacetic acid disodium (EDTA-Na_2) were added to TC solution to quench superoxide ($^{\bullet}O_2^-$), hydroxyl ($^{\bullet}OH$), and hole (h^+) radicals in the degradation process. The degradation rate of TC decreases significantly to 9-14% and 32-40% in the presence of BQ and EDTA-Na_2 respectively (**Figure 6.10**), which indicates that $^{\bullet}O_2^-$ and h^+ greater influence in the removal of TC. However, the degradation rate of TC was not so much affect2%) ed by the addition of IPA, indicating that $^{\bullet}OH$ is not the major reactive radical and combination of all the scavengers as mixture highlights their participation in TC degradation. However, the combination of these radicals' species as mixture significantly affect the degradation activities of TP-AABR-ACK and DP-AABR-ACK. Overall, the $^{\bullet}O_2^-$ and h^+ are responsible for enhanced TC degradation, while the significant role of superoxide radical is further explored in this study.

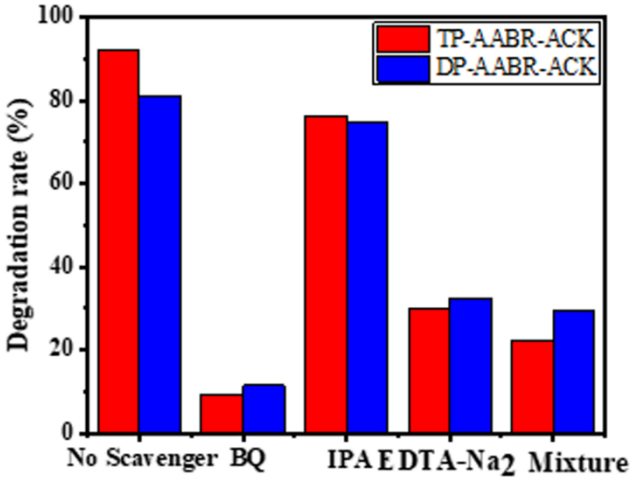

Figure 6.10: Photocatalytic degradation of TC solution over TP-AABR-ACK and DP-AABR-ACK with different scavengers.

To confirm the rate of formation of superoxide radical ($^{\bullet}O_2^-$) in this study, degradation of nitroblue tetrazolium (NBT) to diformazan (Obregón, Zhang & Colón 2016) under visible light irradiation was carried out. The generation rate of $^{\bullet}O_2^-$ is measured by the decrease in absorbance wavelength of NBT (259 nm) with degradation time as presented in **Figure 6.11a –d**. A higher amount of reactive $^{\bullet}O_2^-$is produced more with plasmon TP-AABR-ACK (**Figure 6.10d**) with faster decline in absorbance wavelength of NBT, which is in tune with its enhanced degradation rate on TC as compared to plasmon DP-AABR-ACK, TP-AABR, and DP-AABR. Among the photocatalyst employed, the highest generation of superoxide radical based on highest NBT disappearance follows the order TP-AABR-ACK > DP-AABR-ACK > TP-AABR > DP-AABR in this study. The production of reactive oxygen species is strongly related to the separation efficiency of the photogenerated charge carriers in the photocatalyst (as evidenced from EIS spectra in **Figure 6.6**).

From the analysis and discussion described above, the tailored SPR properties of Ag NPs from the controlled microstructure of AABR-ACK nanocomposite, more exposed facet of AgBr and speedier interfacial separation of photogenerated charge carriers in plasmon TP-AABR-ACK all resulted in higher photocatalytic activity on TC removal in this study.

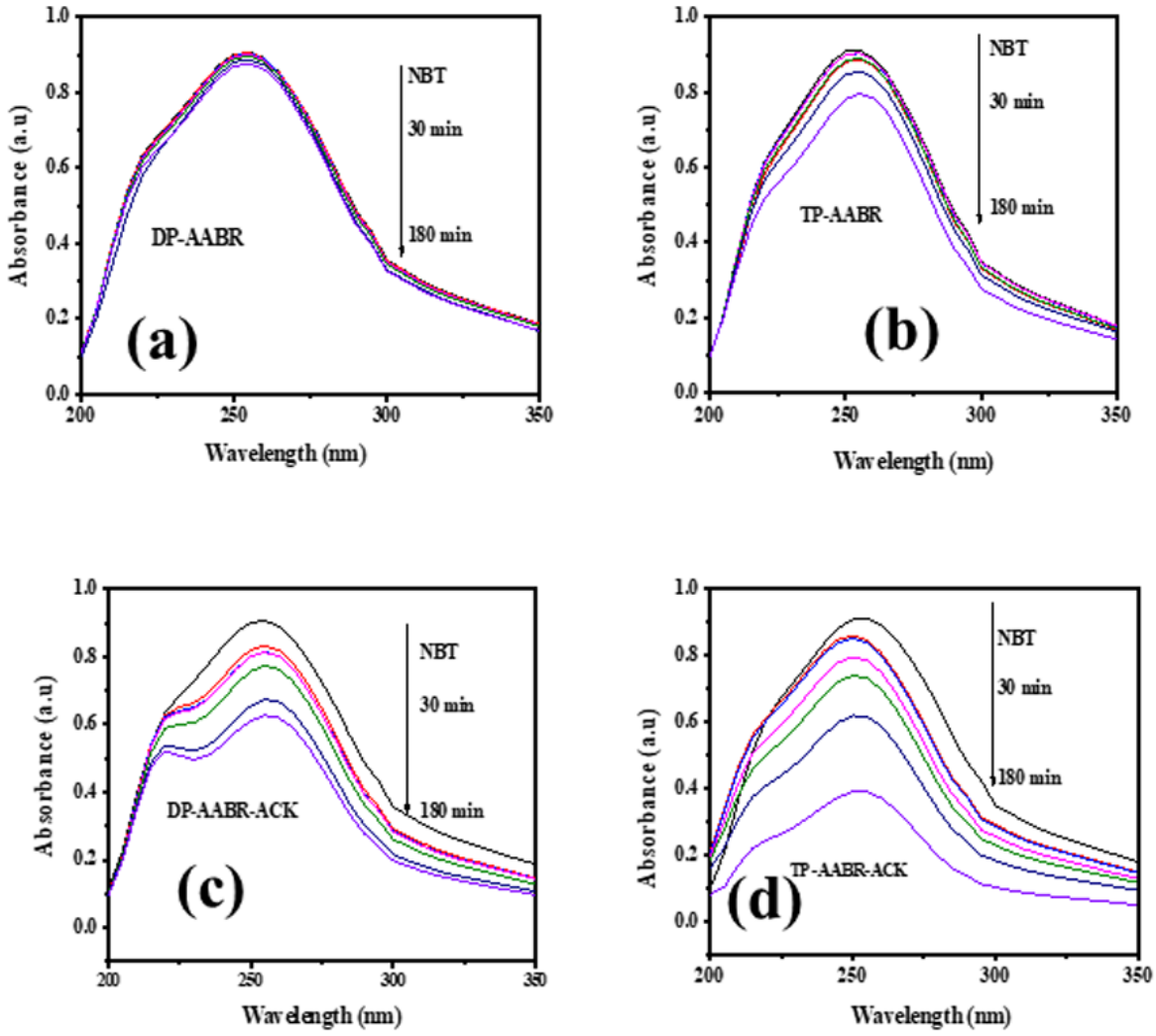

Figure 6.11: UV-Vis absorption spectra of NBT reduction with (a) DP-AABR, (b) TP-AABR, (c) DP-AABR-ACK and (d) TP-AABR-ACK.

6.4 Summary and concluding remarks

The microstructure of AABR-ACK nanocomposites (TP-AABR-ACK and DP-AABR-ACK) were effectively controlled in this chapter through two different synthetic approaches (thermal polyol and deposition-preciptation method), then subsequently utilized in the degradation of tetracycline under visible light irradiation. Both plasmon TP-AABR-ACK and DP-AABR-ACK have uniform distribution of Ag/AgBr nanoparticles on the surface of activated carbon with an average particle size between 160 to 190 nm. However, based on ordered nanospheres morphology, smaller particle size, a more exposed facet of AgBr and along with restrained recombination of charge carriers in the generation of reactive species. Plasmon TP-AABR-ACK displays enhanced photocatalytic degradation of tetracycline as compared to plasmon DP-AABR-ACK and corresponding AABR NPs under visible light. The activated carbon presence in the composites (TP-AABR-ACK and DP-AABR-ACK) significantly boosted the absorption edge of AABR NPs into the visible region for more production of reactive species. The transport and separation efficiency of photogenerated charge carrier in the catalytic process was also enhanced by ACK. In addition, both TP-AABR-ACK and DP-AABR-ACK composites are capable of producing reactive oxygen species (ROS) such as superoxide anions through the selective interaction of the photocatalyst with nitroblue tetrazolium molecules. The AABR-ACKs exhibited improved performance on TC removal when compared to previously reported photocatalysts in literature.

6.5 References

BHATT, D.K. & PATEL, U.D. 2019. Mechanism underlying visible-light photocatalytic activity of Ag/AgBr: Experimental and theoretical approaches. *Journal of Physics Chemistry of Solids,* 135, 109118.

CHAO, Y., ZHU, W., YAN, B., LIN, Y., XUN, S., JI, H., WU, X., LI, H. & HAN, C. 2014. Macroporous polystyrene resins as adsorbents for the removal of tetracycline antibiotics from an aquatic environment. *Journal of Applied Polymer Science,* 131, 40561.

CHEN, G., LI, F., HUANG, Z., GUO, C.-Y., QIAO, H., QIU, X., WANG, Z., JIANG, W. & YUAN, G. 2015. Facile synthesis of Ag/AgBr/RGO nanocomposite as a highly efficient sunlight plasmonic photocatalyst. *Catalysis Communications,* 59, 140-144.

DENG, F., ZHAO, L., LUO, X., LUO, S. & DIONYSIOU, D.D. 2018. Highly efficient visible-light photocatalytic performance of Ag/$AgIn_5S_8$ for degradation of tetracycline hydrochloride and treatment of real pharmaceutical industry wastewater. *Chemical Engineering Journal,* 333, 423-433.

DI, J., XIA, J., JI, M., WANG, B., YIN, S., ZHANG, Q., CHEN, Z. & LI, H. 2016. Advanced photocatalytic performance of graphene-like BN modified BiOBr flower-like materials for the removal of pollutants and mechanism insight. *Applied Catalysis B: Environmental,* 183, 254-262.

ESMAEILI, A. & ENTEZARI, M.H. 2015. Cubic Ag/AgBr–graphene oxide nanocomposite: sono-synthesis and use as a solar photocatalyst for the degradation of DCF as a pharmaceutical pollutant. *RSC Advances,* 5, 97027-97035.

ESMAEILI, A. & ENTEZARI, M.H. 2016. Sonosynthesis of an Ag/AgBr/Graphene-oxide nanocomposite as a solar photocatalyst for efficient degradation of methyl orange. *Journal of*

Colloid and Interface Science, 466, 227-237.

FENG, Y., ZHOU, H., LIU, G., QIAO, J., WANG, J., LU, H., YANG, L. & WU, Y. 2012. Methylene blue adsorption onto swede rape straw (Brassica napus L.) modified by tartaric acid: equilibrium, kinetic and adsorption mechanisms. *Bioresource Technology,* 125, 138-144.

GUAN, R., YUAN, X., WU, Z., WANG, H., JIANG, L., ZHANG, J., LI, Y., ZENG, G. & MO, D. 2018. Accelerated tetracycline degradation by persulfate activated with heterogeneous magnetic $Nix Fe_{3-} xO_4$ catalysts. *Chemical Engineering Journal,* 350, 573-584.

GUO, H., NIU, C.-G., WEN, X.-J., ZHANG, L., LIANG, C., ZHANG, X.-G., GUAN, D.-L., TANG, N. & ZENG, G.-M. 2018. Construction of highly efficient and stable ternary AgBr/Ag/$PbBiO_2Br$ Z-scheme photocatalyst under visible light irradiation: Performance and mechanism insight. *Journal of Colloid and Interface Science,* 513, 852-865.

HU, P. & CAO, Y. 2012. A new chemical route to a hybrid nanostructure: room-temperature solid-state reaction synthesis of Ag@ AgCl with efficient photocatalysis. *Dalton Transactions*, 41, 8908-8912.

JIANG, J., LI, H. & ZHANG, L. 2012. New insight into daylight photocatalysis of AgBr@ Ag: synergistic effect between semiconductor photocatalysis and plasmonic photocatalysis. *Chemistry-A European Journal,* 18, 6360-6369.

JIANG, L., YUAN, X., ZENG, G., LIANG, J., WU, Z., YU, H., MO, D., WANG, H., XIAO, Z. & ZHOU, C. 2019. Nitrogen self-doped g-C_3N_4 nanosheets with tunable band structures for enhanced photocatalytic tetracycline degradation. *Journal of Colloid and Interface Science,* 536, 17-29.

KUAI, L., GENG, B., CHEN, X., ZHAO, Y. & LUO, Y. 2010. Facile subsequently light-induced route to highly efficient and stable sunlight-driven Ag− AgBr plasmonic photocatalyst. *Langmuir,*

26, 18723-18727.

LI, B., WANG, H., ZHANG, B., HU, P., CHEN, C. & GUO, L. 2013. Facile synthesis of one dimensional AgBr@ Ag nanostructures and their visible light photocatalytic properties. *ACS Applied Materials and Interfaces,* 5, 12283-12287.

LIN, Z., XIAO, J., YAN, J., LIU, P., LI, L. & YANG, G. 2015. Ag/AgCl plasmonic cubes with ultrahigh activity as advanced visible-light photocatalysts for photodegrading dyes. *Journal of Materials Chemistry A,* 3, 7649-7658.

LIU, Y., KONG, J., YUAN, J., ZHAO, W., ZHU, X., SUN, C. & XIE, J. 2018. Enhanced photocatalytic activity over flower-like sphere $Ag/Ag_2CO_3/BiVO_4$ plasmonic heterojunction photocatalyst for tetracycline degradation. *Chemical Engineering Journal,* 331, 242-254.

LÓPEZ-PEÑALVER, J.J., SÁNCHEZ-POLO, M., GÓMEZ-PACHECO, C.V. & RIVERA-UTRILLA, J. 2010. Photodegradation of tetracyclines in aqueous solution by using UV and UV/H2O2 oxidation processes. *Journal of Chemical Technology and Biotechnology,* 85, 1325-1333.

LOU, Z., HUANG, B., QIN, X., ZHANG, X., CHENG, H., LIU, Y., WANG, S., WANG, J. & DAI, Y. 2012. One-step synthesis of AgCl concave cubes by preferential overgrowth along< 111> and< 110> directions. *Chemical Communications,* 48, 3488-3490.

LU, Z., CHEN, F., HE, M., SONG, M., MA, Z., SHI, W., YAN, Y., LAN, J., LI, F. & XIAO, P. 2014. Microwave synthesis of a novel magnetic imprinted TiO_2 photocatalyst with excellent transparency for selective photodegradation of enrofloxacin hydrochloride residues solution. *Chemical Engineering Journal,* 249, 15-26.

MA, X., DAI, Y., LU, J., GUO, M. & HUANG, B. 2012. Tuning of the surface-exposing and photocatalytic activity for AgX (X= Cl and Br): a theoretical study. *The Journal of Physical*

Chemistry C, 116, 19372-19378.

MAJUMDAR, A. & PAL, A. 2019. Optimized synthesis of Bi_4NbO_8Cl perovskite nanosheets for enhanced visible light assisted photocatalytic degradation of tetracycline antibiotics. *Journal of Environmental Chemical Engineering,* 103645.

OBREGÓN, S., ZHANG, Y. & COLÓN, G. 2016. Cascade charge separation mechanism by ternary heterostructured $BiPO_4/TiO_2/gC_3N_4$ photocatalyst. *Applied Catalysis B: Environmental,* 184, 96-103.

PETROSKI, J. & EL-SAYED, M.A. 2003. FTIR study of the adsorption of the capping material to different platinum nanoparticle shapes. *The Journal of Physical Chemistry A,* 107, 8371-8375.

SHAHZAD, A., YU, T. & KIM, W.-S. 2016. Controlling the morphology and composition of Ag/AgBr hybrid nanostructures and enhancing their visible light induced photocatalytic properties. *RSC Advances,* 6, 54709-54717.

SIMSEK, E.B., BALTA, Z. & DEMIRCIVI, P. 2019. Novel shungite based Bi_2WO_6 carbocatalyst with high photocatalytic degradation of tetracycline under visible light irradiation. *Journal of Photochemistry and Photobiology A: Chemistry,* 380, 111849.

WANG, P., HUANG, B., ZHANG, X., QIN, X., JIN, H., DAI, Y., WANG, Z., WEI, J., ZHAN, J. & WANG, S. 2009. Highly Efficient Visible-Light Plasmonic Photocatalyst Ag@ AgBr. *Chemistry-A European Journal,* 15, 1821-1824.

WANG, T., QUAN, W., JIANG, D., CHEN, L., LI, D., MENG, S. & CHEN, M. 2016. Synthesis of redox-mediator-free direct Z-scheme AgI/WO_3 nanocomposite photocatalysts for the degradation of tetracycline with enhanced photocatalytic activity. *Chemical Engineering Journal,* 300, 280-290.

WANG, Q., LI, Y., HUANG, L., ZHANG, F., WANG, H., WANG, C., ZHANG, Y., XIE, M. &

LI, H. 2019. Enhanced photocatalytic degradation and antibacterial performance by GO/CN/BiOI composites under LED light. *Applied Surface Science*, 497, 143753.

WU, S., SHEN, X., JI, Z., ZHU, G., ZHOU, H., ZANG, H., YU, T., CHEN, C., SONG, C. & FENG, L. 2017. Morphological syntheses and photocatalytic properties of well-defined sub-100 nm Ag/AgCl nanocrystals by a facile solution approach. *Journal of Alloys and Compounds*, 693, 132-140.

XIAO, X., GE, L., HAN, C., LI, Y., ZHAO, Z., XIN, Y., FANG, S., WU, L. & QIU, P. 2015. A facile way to synthesize Ag@ AgBr cubic cages with efficient visible-light-induced photocatalytic activity. *Applied Catalysis B: Environmental*, 163, 564-572.

XU, D., LIU, K., SHI, W., CHEN, M., LUO, B., XIAO, L. & GU, W. 2015. Ag-decorated $K_2Ta_2O_6$ nanocomposite photocatalysts with enhanced visible-light-driven degradation activities of tetracycline (TC). *Ceramics International*, 41, 4444-4451.

XU, H., SONG, Y., LIU, L., LI, H., XU, Y., XIA, J., WU, X. & ZHAO, S. 2012. Plasmonic-enhanced visible-light-driven photocatalytic activity of Ag–AgBr synthesized in reactable ionic liquid. *Journal of Chemical Technology and Biotechnology*, 87, 1626-1633.

XU, J., WANG, W., SHANG, M., SUN, S., REN, J. & ZHANG, L. 2010. Efficient visible light induced degradation of organic contaminants by Bi_2WO_6 film on SiO_2 modified reticular substrate. *Applied Catalysis B: Environmental*, 93, 227-232.

YAN, T., ZHANG, H., LUO, Q., MA, Y., LIN, H. & YOU, J. 2013. Controllable synthesis of plasmonic Ag/AgBr photocatalysts by a facile one-pot solvothermal route. *Chemical Engineering Journal*, 232, 564-572.

YAN, X., WANG, X., GU, W., WU, M., YAN, Y., HU, B., CHE, G., HAN, D., YANG, J. & FAN, W. 2015. Single-crystalline $AgIn(MoO_4)_2$ nanosheets grafted Ag/AgBr composites with enhanced

plasmonic photocatalytic activity for degradation of tetracycline under visible light. *Applied Catalysis B: Environmental,* 164, 297-304.

YANG, S.-F., NIU, C.-G., HUANG, D.-W., ZHANG, H. & ZENG, G.-M. 2017. Ag/AgCl nanoparticles-modified $CdSnO_3$ $3H_2O$ nanocubes photocatalyst for the degradation of methyl orange and antibiotics under visible light irradiation. *Journal of Colloid and Interface Science,* 505, 96-104.

YUAN, X., JIANG, L., CHEN, X., LENG, L., WANG, H., WU, Z., XIONG, T., LIANG, J. & ZENG, G. 2017. Highly efficient visible-light-induced photoactivity of Z-scheme Ag_2CO_3/Ag/WO_3 photocatalysts for organic pollutant degradation. *Environmental Science: Nano,* 4, 2175-2185.

ZHANG, H., LIU, P., FENG, Y. & YANG, F. 2013. Fate of antibiotics during wastewater treatment and antibiotic distribution in the effluent-receiving waters of the Yellow Sea, northern China. *Marine Pollution Bulletin,* 73, 282-290.

ZHANG, Y., TANG, Z.-R., FU, X. & XU, Y.-J. 2011. Nanocomposite of Ag–AgBr–TiO_2 as a photoactive and durable catalyst for degradation of volatile organic compounds in the gas phase. *Applied Catalysis B: Environmental,* 106, 445-452.

ZHU, M., CHEN, P. & LIU, M. 2011. Graphene oxide enwrapped Ag/AgX (X= Br, Cl) nanocomposite as a highly efficient visible-light plasmonic photocatalyst. *ACS Nano,* 5, 4529-4536.

ZHU, M., CHEN, P. & LIU, M. 2012. Ag/AgBr/graphene oxide nanocomposite synthesized via oil/water and water/oil microemulsions: a comparison of sunlight energized plasmonic photocatalytic activity. *Langmuir,* 28, 3385-3390.

ZHU, M., CHEN, P. & LIU, M. 2013. High-performance visible-light-driven plasmonic

photocatalysts Ag/AgCl with controlled size and shape using graphene oxide as capping agent and catalyst promoter. *Langmuir*, 29, 9259-9268.

ZHU, Q., WANG, W.-S., LIN, L., GAO, G.-Q., GUO, H.-L., DU, H. & XU, A.-W. 2013. Facile synthesis of the novel Ag_3VO_4/AgBr/Ag plasmonic photocatalyst with enhanced photocatalytic activity and stability. *The Journal of Physical Chemistry C,* 117, 5894-5900.

7.0 Conclusions and Recommendations

7.1 Conclusions

The quest for cost effective and ecofriendly materials to combat the threat of pollutants has continued to attract focus attention. Heterogeneous photocatalysis using metal semiconductors as catalyst along with light source have been extensively utilised worldwide to counteract the threats of these pollutants in the environment. Hence, the pressing need for photocatalyst material that can effectively deal with the challenges of emerging recalcitrant pollutants (antibiotics) in drinking water and capable of operating at low intensity region of visible light. The plasmonic silver-silver bromide (Ag/AgBr) catalyst potential in removal of organic contaminants are limited by irregular morphology, limited visible light absorption, and high recombination of charge carrier pair. However, the major addition to the knowledge under heterogeneous photocatalysis that this doctorate thesis contributes is through utilization of activated carbon generated from waste source as catalyst support. This activated carbon as catalyst support, effectively aid in the dispersion of plasmonic Ag/AgBr nanoparticles, which in turn form firm contact and promotes separation of charge carriers. The catalytic performance of these composite toward tetracycline antibiotics remediation under visible LED light was also studied in this thesis. The major findings that can be inferred from this thesis are as follows:

- Activated carbon from microwave pyrolysis of chemical (KOH) impregnated pinecone, optimized at different microwave pyrolysis time and impregnation ratio of potassium

hydroxide to pinecone mass were prepared and characterized. XRD analysis complemented by FTIR, TEM, TGA, RAMAN, and BET results confirmed the formation of porous carbon as good catalyst support. The carbonized pinecone materials also exhibited good electrochemical properties, which can efficiently transport electrons and separate charge carriers in a photocatalyst. Among the prepared activated carbons (ACKs), ACK-2.24-16 was selected as the best catalyst support due to complex formation of 3D hierarchical porous structure, which was correlated with the high iodine and methylene blue adsorption capacity. This study for the first time, reveal the promising attributes of activated carbon from pinecone biomass as a catalyst support to enhance the properties of catalyst in wastewater remediation.

- Ag/AgBr-activated carbon (AABR-ACK) composites were prepared via a thermal polyol route, through modelling the synthesis parameters using response surface methodology (RSM). RSM model highlights the significant impact of the synthesis time and temperature as reaction parameters, in relation with enhanced activities of AABR-ACK composites on TC removal. AABR-ACK composites HRTEM, XRD and SEM analysis confirmed the deposition of AABR nanoparticles, with strong attachment onto the ACK surface. Optimal AABR-ACK composite was obtained at 0.26 g (PVP), 140 ºC (temperature), 0.03 g (ACK mass) and 17.50 min (time) enhanced the photocatalytic activity under LED visible light more than other AABR-ACK composites and AABR. Ordered morphology with reduced particle diameter for AABR-ACK 11 promotes fast separation of charge carriers. ACK presence in the AABR-ACK 11 composite was responsible for the reduction of band gap energy. This study highlights for the first time, the successful utilization of RSM model to

correlate relevant aspect of synthesis parameters of Ag/AgBr catalysts on enhanced removal of antibiotics. The optimal AABR-ACK catalyst could be reused and maintained high activity after five repeated cycles.

- A series of composites comprising of AABR NPs with carbon from different sources (KOH impregnated pinecone biomass, commercial source and biochar) were synthesized by thermal polyol route. Carbon from KOH impregnated pinecone biomass possesses better conductive property for accelerated transfer of photo-induced electron in comparison to commercial activated carbon and biochar. The interconnected hierarchical carbon structure for carbonized pinecone, significantly enhance AABR NPs catalytic properties on TC removal. Degradation of TC with AABR-ACK nanocomposite generated lower molecular weight intermediates as observed from the LC-MS analysis. The LC-MS analysis of TC degraded solution indicated that generated superoxide radicals executed major roles in the degradation process. The degradation mechanism of TC breakdown via dehydroxylation, deamination, demethylation, dehydration, and ring opening was proposed in this thesis.

- It was also found in this thesis that carbonized pinecone derived from microwave pyrolysis played a role in the controlled microstructure and dispersion of AABR nanoparticles, in accordance to two different synthetic approaches (thermal polyol and deposition precipitation approach). This means that the ACK material simultaneously serve as a stabilizing agent, light transmitting channel for enhancing absorption edge of AABR NPs into the visible region, and accelerate the separation efficiency of photogenerated charge

carrier in the catalytic process for degradation of TC. Overall, the superoxide anion radicals played crucial role in the degradation of TC as evident from scavenging experiment in this study. TP-AABR-ACK generates more superoxide anion radicals in the degradation process in comparison to other photocatalysts from this study, from their selective interaction with nitroblue tetrazolium molecules. The mineralization percentage (TOC value) of TC under LED visible light with TP-AABR-ACK and DP-AABR-ACK were 87.5 and 78.5%, respectively. ACK presence in TP-AABR-ACK and DP-AABR-ACK composite enhance high removal of TOC in TC, which were 5 times fold higher than corresponding AABR NPs. The enhancement can be explained based on efficient charge carriers separation in the interface created by intimate contact between AABR NPs and ACK.

7.2 Recommendations

This thesis has elaborated the preparation of activated carbon as catalyst support from pinecone biomass, which significantly enhanced the photocatalytic properties of Ag/AgBr on degradation and removal of tetracycline antibiotics under visible light irradiation. A number of major challenges for further work have been identified, these includes as described below:

- This thesis focused on the preparation and understanding the potential application of activated carbon from pinecone biomass as catalyst support. In order to improve the surface area of activated carbon produced from pinecone biomass, the microwave power for pyrolysis of the pinecone needs to be optimized for future applications. In this thesis,

microwave pyrolysis of the chemically impregnated carbonized material was done in a static inert environment. This static environment limits the removal of the pyrolysis oils, which may hamper the formation of activated carbon with higher surface areas. The microwave process should have continuous flow of nitrogen. The exploration of other chemical activating agents such as zinc chloride and phosphoric acid with pinecone biomass are suggested for better porosity and increased surface area properties. The adsorption properties of prepared activated carbon on removal of emerging contaminants (Ecs) in environment should be consider for future applications. Photocatalytic activities of activated carbon as catalyst on tetracycline and other recalcitrant antibiotics in the presence of peroxymonosulfate activator (sulfate radical initiator) removal under LED visible light should also be explored for further studies.

- This thesis was focused on the design and application of the Ag/AgBr-ACK composites for the degradation of tetracycline antibiotics only. RSM modelling of Ag/AgBr-ACK composites synthesis parameters from deposition precipitation route on degradation of other recalcitrant antibiotics should be consider for future work. Based on the morphology, band gaps and electrochemical properties of the composites, this photocatalyst should be further applied in photocatalytic water splitting reaction for hydrogen generation. The amount of silver ion (Ag^{+}) concentration leached during the degradation process should also be considered using the inductively coupled plasma mass spectroscopy. The development of Z-scheme ternary composites with other photocatalyst is still required to understand better reduction of recombination rate of charge carriers for enhanced activity.

The antibacterial test and cytotoxicity of prepared Ag/AgBr-ACK composites for water disinfection is also recommended for future purpose.

Appendix A

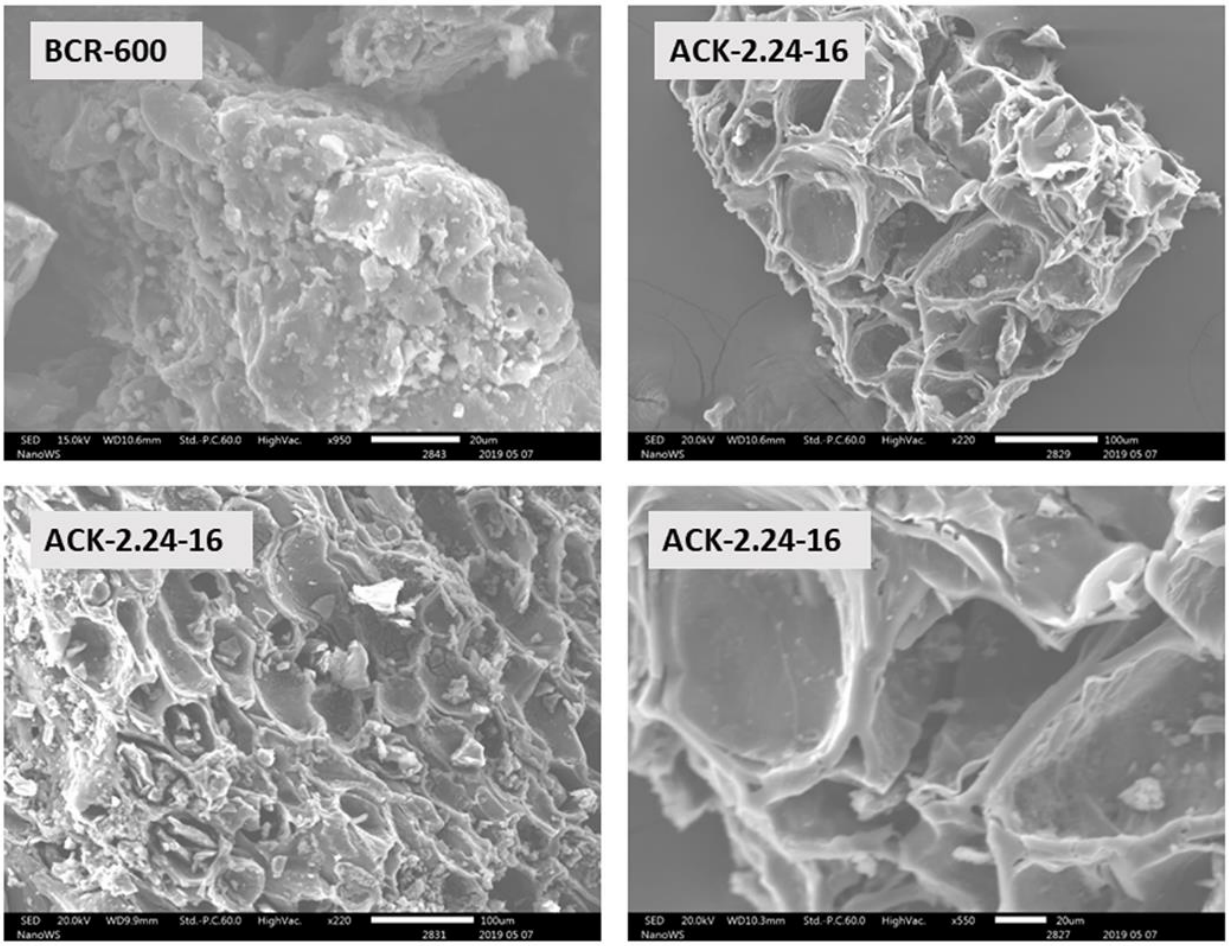

Figure A 1: SEM images of (a) Biochar; (b-d) ACK-2.24-16 sample at different magnification.

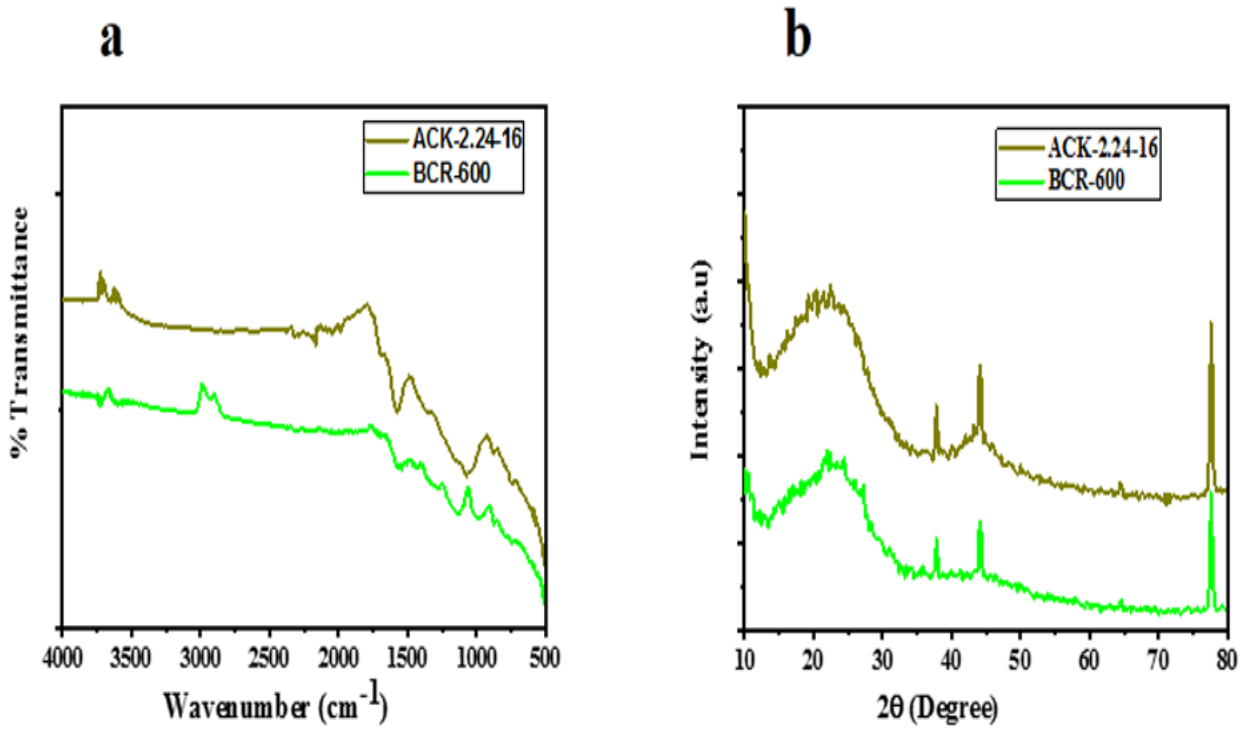

Figure A 2: (a) XRD pattern and (b) FTIR spectrum of optimized ACK-2.24-16 and Biochar.

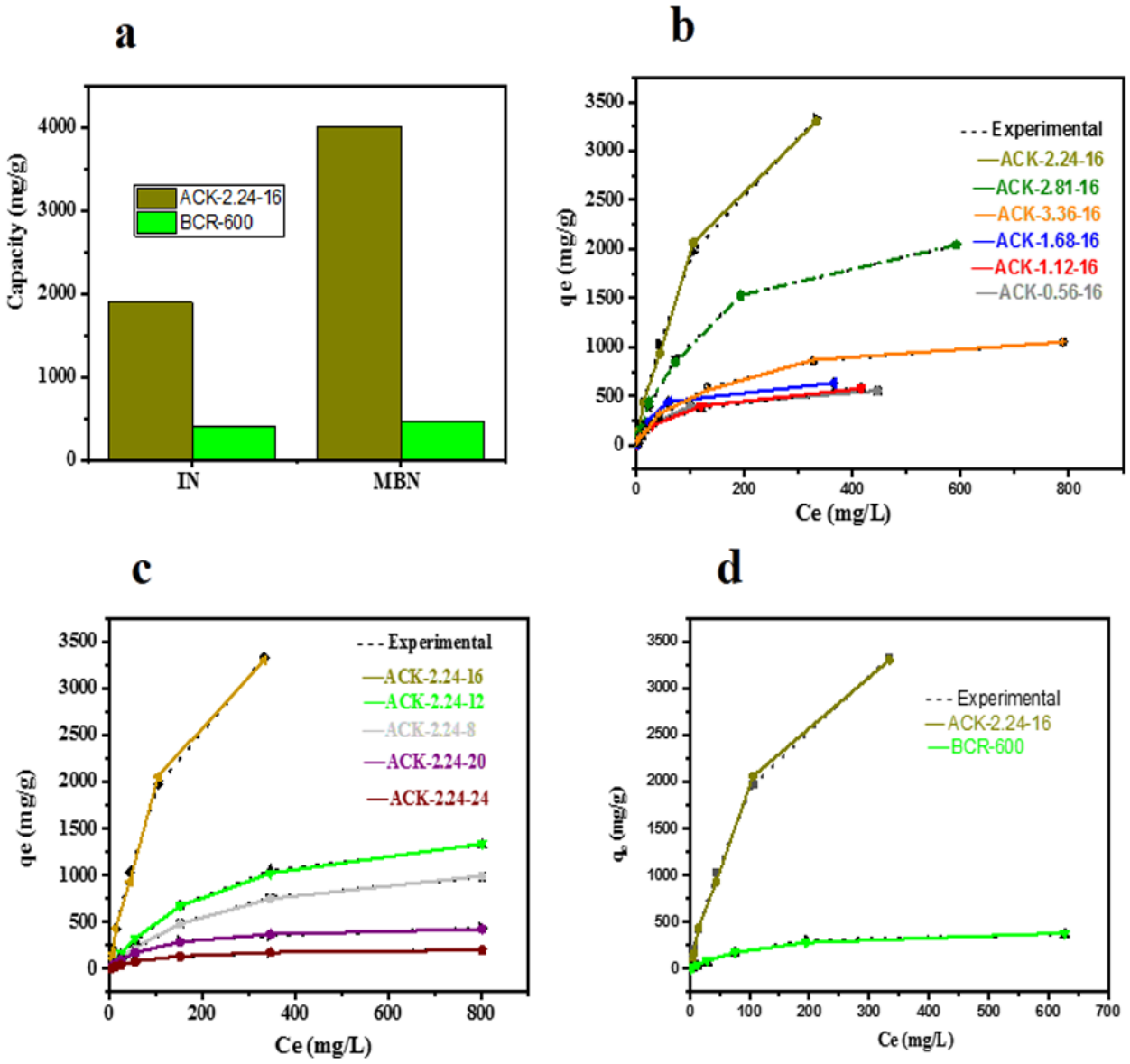

Figure A 3: (a) IN and MBN of optimized ACK-2.24-16 and Biochar; Langmuir isotherm fit for MB adsorption onto ACK samples (b) different IR; (c) different MPT and (d) optimized ACK-2.24-16 and Biochar.

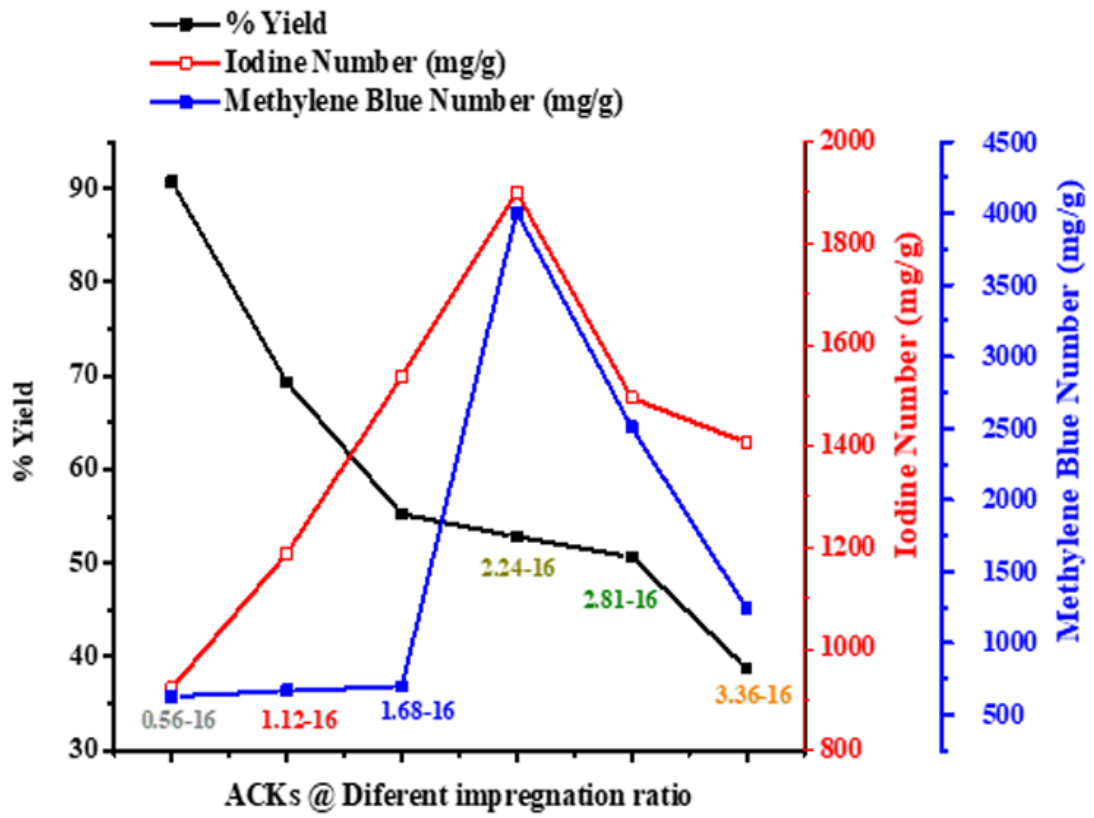

Figure A 4: Effects of different impregnation ratio on the yield, iodine and methylene blue uptake of activated carbons.

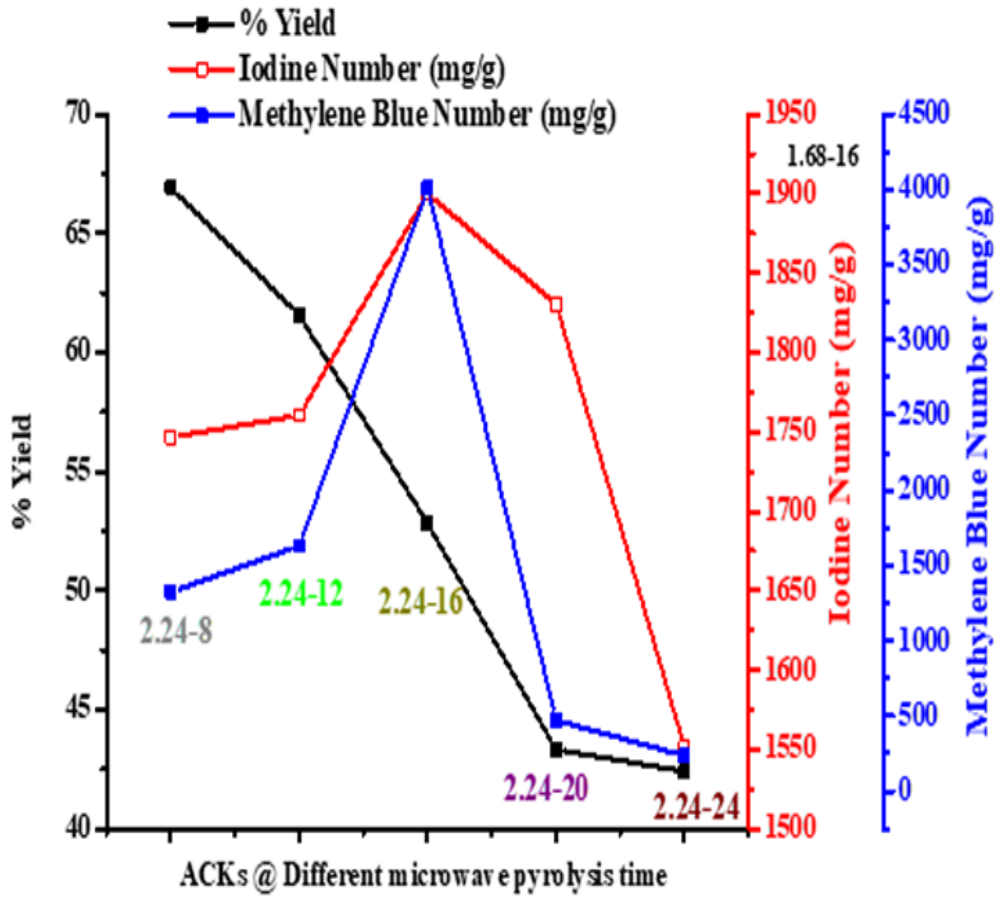

Figure A 5: Effects of different microwave pyrolysis time on the yield, iodine and methylene blue uptake of activated carbons.

Table A 1: Langmuir and Freundlich model of adsorption isotherm on methylene blue unto ACK samples at different impregnation ratio.

Samples	Langmuir model parameters			Freundlich model parameters		
	Qm (mg/g)	K_L (L/mg)	R^2	N	K_F (mg/g)	R^2
BCR	458.8550	0.0081	0.9957	0.0074	0.0105	0.7792
ACK-0.56-16	624.6440	0.0175	0.9983	0.0114	0.0078	0.8105
ACK-1.12-16	663.8616	0.0148	0.9958	1.5386	0.9803	0.8515
ACK-1.68-16	727.9682	0.0152	0.9998	1.1612	0.6060	0.7387
ACK-2.24-16	4006.5380	0.0104	0.9998	1.2584	0.1144	0.9338
ACK-2.81-16	2262.3206	0.0206	0.9997	0.8951	0.2235	0.8312
ACK-3.36-16	1118.6034	0.0346	0.9998	1.1785	0.7332	0.7901

Table A 2: Langmuir and Freundlich model of adsorption isotherm on methylene blue unto ACK samples at different microwave pyrolysis time

Samples	Langmuir model parameters			Freundlich model parameters		
	Qm (mg/g)	K_L (L/mg)	R^2	N	K_F (mg/g)	R^2
ACK-2.24-8	1324.4852	0.0037	0.9996	1.2530	0.8641	0.8779
ACK-2.24-12	1747.5476	0.0040	0.9992	1.3997	0.6543	0.8234
ACK-2.24-16	4006.5380	0.0104	0.9998	1.2584	0.1144	0.9338
ACK-2.24-20	478.3078	0.0100	0.9984	0.5955	1.0136	0.6645
ACK-2.24-24	227.6200	0.0098	0.9996	0.2662	1.0058	0.7115

Table A 3: The concentration of functional groups on the ACK sample as determined by Boehm titration.

Samples	Phenolic (mmol/g)	Lactonic (mmol/g)	Carboxylic (mmol/g)	Total Acid group (mmol/g)	Total Basic group (mmol/g)
Biochar	1.36	0.605	0.35	2.31	4.51
ACK-0.56-16	1.39	0.48	0.54	2.41	4.64
ACK-1.12-16	1.4	0.47	0.57	2.44	4.69
ACK-1.68-16	1.42	0.46	0.59	2.47	4.72
ACK-2.24-16	1.41	0.47	0.61	2.48	4.76
ACK-2.81-16	1.42	0.46	0.58	2.45	4.73
ACK-3.36-16	1.34	0.49	0.55	2.38	4.7
ACK-2.24-8	1.36	0.55	0.51	2.41	4.71
ACK-2.24-12	1.38	0.52	0.55	2.44	4.73
ACK-2.24-20	1.35	0.53	0.53	2.42	4.75
ACK-2.24-24	1.34	0.54	0.52	2.4	4.72

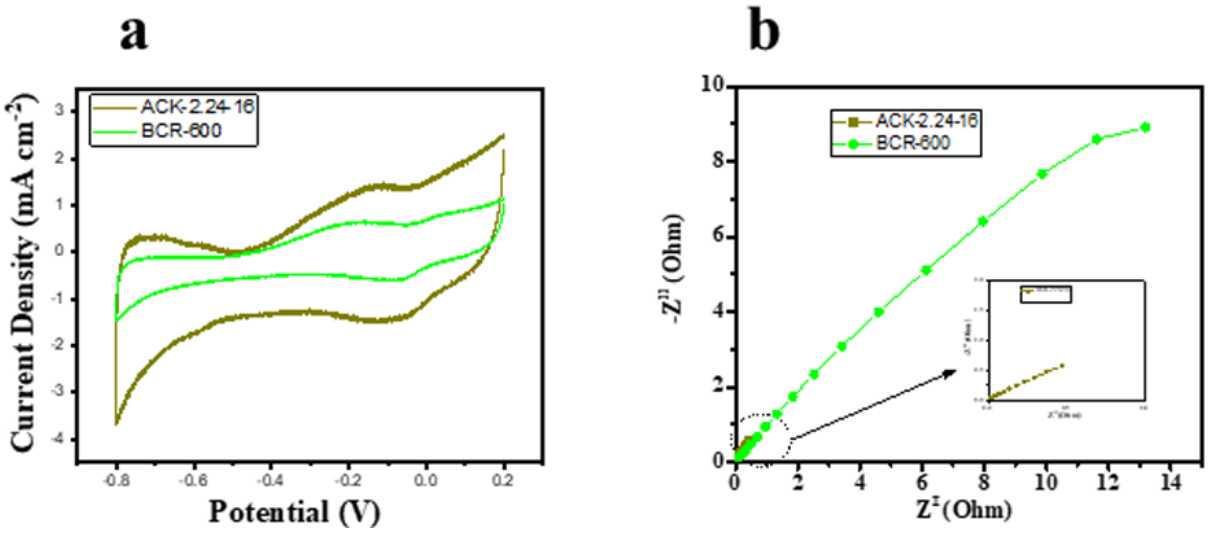

Figure A 6: (a) Cyclic Voltammetry curve and (b) electrochemical impedance spectroscopy of optimized ACK-2.24-16 and Biochar.

Post Tribute to Professor Ofomaja

YOU MEANT SO MUCH

You meant so much to all of us

You were special, and that's no lie

You brightened up the darkest day

And the cloudiest sky.

Your smile alone warmed hearts

Your laugh was like music to hear

I would give absolutely anything

To have you well and standing near.

Not a second passes

When you are not on our minds

Your love we will never forget

The hurt will ease in time.

Many tears I have seen and cried

They have all poured out like rain

I know that you are happy now

And no longer in any pain.

--Cassie Mitchell-